From the Priority Research Area Infections
of the Leibniz-Center for Medicine and Biosciences Borstel
Director: Prof. Dr. Ulrich Schaible
Division of Biophysics
Prof. Dr. Thomas Gutsmann

Biophysical Characterisation of the Fungal Peptide Toxin Ece1-III and its Interaction with Lipid Membranes

Dissertation
for Fulfillment of Requirements
for the Doctoral Degree
of the University of Lübeck
from the Department of Natural Sciences

Submitted by
Julia Wernecke
from Rostock

Lübeck 2016

First referee: Prof. Dr. Thomas Gutsmann
Second referee: Prof. Dr. Lars Redecke
Date of oral examination: 29.09.2016
Approved for printing. Lübeck, 29.09.2016

Abstract

For decades, researchers have been trying to elucidate critical determinants of the pathogenicity of human fungi. Only recently, has an international consortium of scientists succeeded in identifying such a factor – a peptide toxin secreted by the clinically important fungus *Candida albicans*. This peptide, Ece1-III (extent of cell elongation), plays a crucial role during fungal infections of human mucosae. The peptide's virulence manifests in the direct damage of epithelial membranes, in the stimulation of a danger response signalling pathway and in the activation of epithelial immunity [1]. The present work contributed substantially to the pioneering study on the virulence of the opportunistic fungus *C. albicans*, as it provides the first insights into the direct interaction between Ece1-III and lipid membranes. In this thesis, fundamental structural properties of the peptide are examined. Further, its membrane interaction is studied using different analytical approaches to resolve different stages of the peptide's basic mode of action. To lower the biological complexity, which features membranes of living cells and therefore increases the difficulty of unravelling distinct interaction partners, phospholipid model membranes are employed for most of the experiments. Three major aspects are addressed to enlighten the general interaction mechanism leading to the permeabilisation of lipid membranes: (i) the influence of the peptide concentration in terms of the lipid-to-peptide ratio, (ii) the peptide's cell selectivity with the help of four different membrane compositions, and (iii) the peptide's structure-activity relationship with the aid of C-terminal sequence modifications.

Finally, a generalised interaction model is proposed. Therein, the peptide's amphiphilic α-helical structure is described as a fundamental prerequisite for its binding to lipid membranes. In consequence of the initialised binding, the peptide inserts between the lipid headgroups at the polar/apolar interface and aligns parallel to the bilayer surface. Upon increasing surface accumulation, however, the helix starts to penetrate the bilayer with oblique inclination. The lipids have to accommodate the peptide penetration which perturbs the lipid packing and increases the curvature stress. As a result, the bilayer is destabilised and transient local collapses occur. This carpet-like disintegration eventually leads to the disruption of the entire membrane. Such dramatic disturbances of the bilayer integrity entailed by increasing peptide concentrations, are found for all four lipid compositions probed in this thesis. Consequently, no distinct membrane specificity can be recognised. In addition, it becomes evident that the molecular structure at the peptide's C-terminus is critical for its membrane activity. However, the particular details of the structure-activity relationship remain unclear as it is neither explained by solely the C-terminal am-

phiphilicity nor the cationicity. In conclusion, the fundamentals of the fungal toxins' mode of action could be demonstrated. Thus, the thesis provides an important basis for understanding the pathogenic mechanisms of *C. albicans*.

Kurzfassung

Jahrzehntelang haben Forscher versucht, die entscheidenden Faktoren der Pathogenität humaner Pilze zu entschlüsseln. Vor kurzem gelang es einem internationalen Konsortium von Wissenschaftlern, einen dieser Faktoren zu identifizieren – ein toxisches Peptid, das vom klinisch-relevanten Pilz *Candida albicans* sekretiert wird. Dieses Peptid, Ece1-III (*extent of cell elongation*), spielt eine zentrale Rolle bei Candida-Infektionen von humanen Schleimhäuten. Seine Virulenz zeigt sich in der direkten Beschädigung von epithelialen Membranen, in der Stimulation einer Immunantwort und in der Aktivierung epithelialer Immunität [1]. Die vorliegende Arbeit hat maßgeblich zu der wegweisenden Studie der Virulenz des opportunistischen Pilzes *C. albicans* beigetragen, da sie erste Einblicke in die direkte Wechselwirkung zwischen Ece1-III und Lipidmembranen gibt. In der Arbeit werden grundlegende strukturelle Eigenschaften des Peptids untersucht. Seine Wechselwirkung mit Membranen wird mit verschiedenen analytischen Methoden betrachtet, um einzelne Phasen der fundamentalen Peptid-Interaktion zu beleuchten. Die Komplexität, die lebende Zellen kennzeichnet, erschwert es, einzelne Wechselwirkungspartner auszumachen. Für die Mehrheit der Experimente werden daher Phospholipid-Modellmembranen eingesetzt, um die biologische Vielschichtigkeit zu vereinfachen. Der prinzipielle Mechanismus, der zur Permeabilisierung von Lipidmembranen führt, wird unter drei wesentlichen Gesichtspunkten untersucht: (i) dem Einfluss der Peptidkonzentration in Bezug auf das Lipid-zu-Peptid-Verhältnis, (ii) der Zellselektivität des Peptids bezüglich vier verschiedener Membranzusammensetzungen und (iii) dem Zusammenhang zwischen Struktur und Aktivität mittels C-terminaler Sequenzmodifikationen.

Schließlich wird ein verallgemeinertes Modell für den Wirkmechanismus vorgeschlagen. Darin wird die amphiphile α-helikale Struktur des Peptids als elementare Voraussetzung für seine Bindung an Lipidmembranen beschrieben. Bedingt durch diese Bindung baut sich das Peptid zwischen den Kopfgruppen der Lipide an der polaren/apolaren Grenzfläche ein und richtet sich parallel zur Membranoberfläche aus. Mit zunehmender Oberflächenansammlung dringt die Helix in schiefer Orientierung in die Lipiddoppelschicht ein. Die Lipide müssen sich dieser Peptidpenetration anpassen, was ihre strukturelle Organisation stört und die Krümmungsspannung erhöht. Dadurch wird die Lipiddoppelschicht destabilisiert und kurzlebige, lokale Fehlstellen treten auf. Diese „carpet-artigen“ Schäden führen letztlich zum Zusammenbruch der gesamten Membran. Es wird zudem gezeigt, dass eine steigende Peptidkonzentration die Membranintegrität aller vier Lipidzusammensetzungen dramatisch beeinträchtigt. Folglich wird keine ausgeprägte Membranspezifizität

offensichtlich. Darüber hinaus wird deutlich, dass die molekulare Struktur des C-terminalen Peptidabschnitts entscheidend ist für dessen Membranaktivität. Allerdings bleiben die Details der Struktur-Aktivitäts-Relation des Peptids unklar, da sie weder allein durch die C-terminale Amphiphilizität noch durch die Kationizität erklärt werden kann. Zusammenfassend betrachtet, konnten die grundlegenden Wirkprinzipien des humanpathogenen Peptids veranschaulicht werden. Damit liefert diese Arbeit einen wertvollen Beitrag, um die krankheitserregenden Mechansimen von *C. albicans* eines Tages vollständig verstehen und Pilzinfektionen vermeiden zu können.

Contents

1 Introduction **1**

1.1 Aim of the Thesis . . . 1
1.2 Biological Context . . . 3
1.2.1 *Candida albicans* . . . 3
1.2.2 Ece1-III . . . 3
1.3 Fundamentals of Membrane Biophysics . . . 4
1.3.1 Membrane Architecture . . . 4
1.3.2 Membrane Dynamics . . . 5
1.3.3 Membrane Lipids . . . 6
1.3.4 Lipid Polymorphism . . . 11
1.3.5 Interactions between Lipid Bilayers . . . 15
1.4 Membrane-Peptide Interactions . . . 19
1.4.1 Membrane-Active Peptides . . . 19
1.4.2 Mechanisms of Membrane-Disruption by Peptides . . . 20
1.4.3 Lipid Polymorphism in the Presence of Peptides . . . 24
1.4.4 Functional Relevance of C-terminal Peptide Amidation . . . 25

2 Model Systems **27**

2.1 Diversity of Lipid Model Membranes . . . 27
2.2 Sample Preparation . . . 36
2.2.1 Lipids . . . 36
2.2.2 Buffer . . . 37
2.2.3 Lipid Membrane Systems . . . 37
2.3 Peptides . . . 41
2.3.1 Synthesis . . . 41
2.3.2 Peptide Stock Solutions . . . 42
2.3.3 Solubility . . . 42

3 Applied Biophysical Methods **43**

3.1 Techniques based on Light Scattering . . . 43
3.1.1 Dynamic Light Scattering . . . 43
3.1.2 Zeta Potential . . . 46

3.2 Spectroscopic Techniques 49
3.2.1 (O)CD Spectropolarimetry 49
3.2.2 Fourier Transformation Infrared Spectroscopy 55
3.2.3 Förster Resonance Energy Transfer Assays 56
3.2.4 Haemolysis Assay 60
3.3 Electrochemical Techniques 61
3.3.1 Electrochemical Impedance Spectroscopy of tBLMs 61
3.3.2 Electrophysiological Characterisation of BLMs 63
3.4 Techniques Based on Force Interactions 65
3.4.1 Film Balance Experiments 65
3.4.2 Atomic Force Microscopy 67
3.5 X-Ray Diffraction 70
3.5.1 Fundamental Aspects of X-ray Diffraction 70
3.5.2 X-Ray Reflectivity of Oriented Lipid Model Membranes 80
3.5.3 Grazing Incidence X-Ray Diffraction on Lipid Multilayers . . . 81
3.5.4 Experimental Setups 83
3.5.5 XRR Data Analysis 88
3.5.6 GID Data Analysis 95

4 Biological Peptide Activity 99
4.1 Cytotoxic Activity 99
4.2 Microscopically Visible Effects on Erythrocytes 101

5 Peptide Characteristics 103
5.1 Theoretical Analysis of the Peptide Sequence 103
5.1.1 Net Charge 103
5.1.2 Secondary Structure Prediction 104
5.1.3 Classification of Amphipathic Helix 108
5.1.4 Effect C-terminal Amidation 111
5.2 Experimental Analysis of the Secondary Structure 111
5.2.1 Isotropic Circular Dichroism 111
5.2.2 Evidence for the Amphiphilicity of Ece1-III 115

6 The Lipid-Peptide Interaction 119
6.1 Peptide Binding to Lipid Membranes 119
6.1.1 FRET Binding Assay 119
6.1.2 Zeta Potential 121
6.1.3 Discussion of the Binding Data 123

6.2 Peptide Intercalation into Lipid Membranes . . . 124
6.2.1 Peptide Integration into Lipid Monolayers . . . 124
6.2.2 Dynamic Light Scattering . . . 125
6.2.3 FRET Intercalation Assay . . . 129
6.2.4 Peptide Orientation in Aligned Lipid Bilayers (OCD) . . . 132
6.2.5 Discussion of the Integration Data . . . 137
6.3 Peptide-induced Structural Changes in Bilayers . . . 140
6.3.1 Microscopically Visible Impact on Multilayer Membranes . . . 140
6.3.2 Peptide Influence on the Vertical Bilayer Structure . . . 144
6.3.3 Peptide Influence on the Lateral Bilayer Structure . . . 156
6.3.4 Effect on Lipid Rafts . . . 172
6.3.5 Peptide-Induced Fusion . . . 179
6.3.6 Summary and Discussion of the Structural Changes . . . 182
6.4 Permeabilisation . . . 186
6.4.1 Electrical Impedance of Tethered Bilayer Membranes . . . 186
6.4.2 Electrophysiological Studies on Free-standing Membranes . . . 190
6.4.3 Discussion of the Permeabilisation Activity . . . 191

7 Summary and Future Prospects 193
7.1 The Interaction Model . . . 193
7.2 Lipid composition . . . 195
7.3 C-terminal Modifications . . . 196
7.3.1 Peptide Length and Amino Acid Composition . . . 196
7.3.2 Amidation State . . . 197
7.4 Outlook . . . 198

Bibliography 201

List of Figures 224

List of Tables 228

Abbreviations 229

Appendix 233
Acknowledgements . . . 235

1 Introduction

1.1 Aim of the Thesis

One of the most fascinating aspects in nature is the extremely high structural and functional cellular organisation of living organisms. Although the revelation of the processes that enable life have been in the spotlight of research for hundreds of years, even today many of the involved protagonists and their detailed mechanisms remain obscure. However, it has long been known that biological membranes are an essential key to vital cellular interplay. Regardless of whether they define the boundary between inner and outer cell volumes as shown in Fig. 1.1, or subdivide the cytosol into separated compartments of different biochemical function – all membranes share the task of serving as selectively permeable barriers. Membranes enable and control the transport of various substances and thus provide the cells with energy derived from biochemical gradients or facilitate signalling processes. The loss of membrane integrity leads irrevocably to the apoptosis of the entire cell. Various peptides of the innate immune system of multicellular eukaryotic organisms make use of this vulnerability and protect their host by directly perturbing the membranes of microbial invaders. Indeed, exogenous toxic agents have the potential to attack host membranes likewise.

The peptide examined in this thesis is assumed to utilise this kind of membrane disintegration to facilitate the invasion of the human epithelium by its fungal host

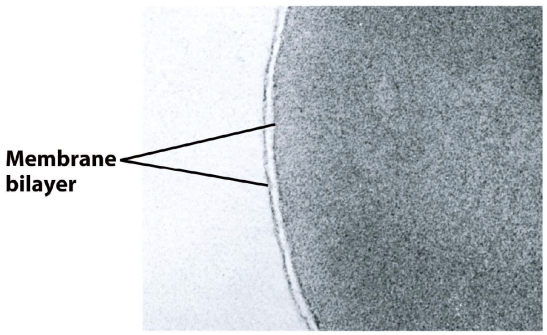

Figure 1.1 – Cross section of a plasma membrane. Biological membranes define the borders of intracellular volumes and the external space. The picture was obtained by electron microscopy after staining with osmium tetroxide. The staining reveals the trilaminar appearance of the lipid bilayer. Reprinted from [2].

organism. This peptide, Ece1-III$_{KR}$, has recently been discovered and it is the first peptide toxin that has been identified in a human pathogenic fungus. Its sequence consists of 32 amino acids and it is processed from its parent protein, Ece1p. The name derives from its coding gene *ECE1* (extent of cell elongation 1), which is exclusively expressed in the invasive hyphal growth of the opportunistic fungus *Candida albicans*. It has been shown that Ece1-III$_{KR}$ triggers the host danger response pathway and activates epithelial immunity at low concentrations; with increasing concentration it exhibits a pronounced cytolytic effect on epithelial cell membranes.

In order to prevent cell damage induced by Ece1-III$_{KR}$, it is essential to understand the peptide-membrane interaction and to find possible inhibiting co-factors. The knowledge of the process may also assist the development of Ece1-III$_{KR}$ modifications with inhibited cytotoxic effects against human cells, but conserved antimicrobial or anticancer activity. These modified versions might then have the potential to be applied for multiple therapeutic purposes [3].

This dissertation aims to characterise the interaction of lipid membranes with Ece1-III$_{KR}$. This is experimentally challenging since the plain peptide properties (e. g. secondary structure) must be elucidated and, at the same time, the peptide's structural effects on the membrane need to be clarified. To this end, a variety of techniques are employed to reveal single features of the interaction, such as binding affinity, peptide orientation with respect to the membrane or the peptide influence on bilayer thickness and acyl chain order. In the first instance, the different aspects are studied with respect to the peptide concentration. In addition to that, the lipid composition is varied to model different types of cell membranes and to unveil possible differences of the interaction behaviour. Modifications of the peptide are examined in order to determine the effect of altered peptide properties, such as decreased charge and increased hydrophobicity. In particular, the peptide Ece1-III$_{K}$, lacking the terminating arginine residue, is studied since it is the peptide variant which predominantly occurs in nature and, additionally, exhibits decreased cationicity. Ece1-III$_{AA}$, where both terminating charged residues are substituted with the apolar amino acid alanine, serves as variant with decreased cationicity and amphiphilicity. As third variant, Ece1-III$_{A}$, a shorter version Ece1-III$_{AA}$ is studied, which lacks one terminating alanine and is therefore a little less hydrophobic.

1.2 Biological Context

1.2.1 *Candida albicans*

The fungus *Candida albicans* is a human pathogen with high clinical relevance, since it is by far the most common species of pathogenic fungi [4–7]. In immunocompromised hosts, infections caused by *C. albicans* often lead to sepsis or even the death of the host [8]. Beyond that, also immunocompetent hosts may suffer from severe superficial epithelia infections by *C. albicans* [9]. Usually, such infections are opportunistic, i. e. the fungus is already a commensal part of the healthy human microbiota and it reveals pathogenicity under certain conditions such as defective immune systems or long-term antibiotic treatments [10]. *C. albicans* is a polymorphic fungus that may grow in yeast, hyphal or pseudo-hyphal form. While it is found as harmless commensal in its yeast or pseudo-hyphal growth, pathogenic evolution is directly attributed to its transition into the invasive hyphal form [11]. During this transition the fungus breeds filamentous hyphae which penetrate epithelial tissues, damage the cells therein and activate a immune response that triggers the release of pro-inflammatory cytokines [1].

1.2.2 Ece1-III

The precise modes of action of *C. albicans* infections are yet unexplained. However, they are supposed to bear a relation to the gene *ECE1*, which is known to be highly expressed by hyphae during mucosal infections [12]. This gene has been predicted to encode Ece1p, a protein secreted by the hyphae and critical for the virulence of *C. albicans* [13, 14]. A *C. albicans* mutant lacking this gene was found to form normal hyphae, which invaded epithelial cell tissues. However, it was neither capable to damage cells nor to induce immune responses [1]. The protein Ece1p is an *in vitro* substrate for Kex2p, a protease located in the Golgi complex, with the task to cleave proteins after lysine-arginine (KR) motifs [15]. Ece1p contains seven of such KR-processing sites suggesting it to be processed into eight peptides. The secretion of these eight peptides terminated by KR motifs was recently confirmed by liquid chromatography-tandem mass spectrometry (LC-MS/MS) in extensive studies by Moyes and co-workers [1]. In their experiment, the researchers also found small amounts of additional peptide fragments with single K or R endings and demonstrated that a less efficient cleavage occurs also after these amino acids. The third of the eight peptides terminated in KR, Ece1-III$_{62-93}$ (SIIGIIMGIL GNIPQVIQII MSIVKAFKGN KR, in the following referred to as Ece1-III$_{\mathrm{KR}}$), has been found to exhibit cytolytic activity and to trigger the immune response. Surprisingly, LC-

MS/MS analyses on the secretome from wild-type *C. albicans* revealed that merely not Ece1-III$_{KR}$, but rather its shorter version Ece1-III$_{K}$ (SIIGIIMGIL GNIPQVIQII MSIVKAFKGN K) is the predominant secreted form [1]. Moyes *et al.* assigned this observation to a further, subsequent cleavage by Kex1p, another protease which is known to remove C-terminal R residues in fungal Golgis [16]. The shorter Ece1-III$_{K}$ variant was also found to damage cells and to induce the danger response. Due to its dominating occurrence, Moyes and co-workers suggested it to be the principle peptide agent responsible for *C. albicans* infections and proposed to name it "Candidalysin". Regardless of its lower natural abundance, the variant primarily studied in this work is Ece1-III$_{KR}$ since it is suggested to exhibit increased toxicity against cell membranes due to its higher C-terminal charge.

1.3 Fundamentals of Membrane Biophysics

This section aims to briefly introduce fundamental aspects of membrane biophysics. In the first instance, the general membrane architecture is presented. Following this, basic membrane dynamics and the variety of membrane lipids are addressed. A basic knowledge of these two aspects is required as both crucially influence the activity of membrane-active peptides. In order to interpret the structural details of the lipid-Ece1-III interaction, theoretic aspects of the phase behaviour of lipids are required. Therefore, relevant lipid phases are also outlined in this section. Finally, the forces acting between adjacent bilayer membranes are introduced. These define the characteristic interbilayer distance of lamellar lipid systems. Changes in the presence of peptides may provide unique insights into involved attractive or repulsive forces.

1.3.1 Membrane Architecture

Biological membranes predominantly consist of phospholipids, sphingolipids and sterols. The two first-mentioned have hydrophilic phosphate headgroups and two acyl chains that are subsumed as hydrophobic tail. Following the hydrophobic effect, these amphiphilic lipids self assemble spontaneously into two-dimensional lipid bilayers in aqueous environments, with the polar headgroups facing towards the aqueous surrounding and their apolar tails shielded from it (cf. Fig. 1.2). In this approximately 5 nm thick lipid matrix, a complex mixture of proteins and other macromolecules is embedded. At the bilayer's surfaces peripheral proteins can be found. These are either loosely associated to it or covalently bound by lipid-anchors. Another class of important constituents of biological membranes are glycolipids and

gylcoproteins which carry polar carbohydrates and expose these exclusively to the external membrane volume, where they serve as markers for cellular recognition.

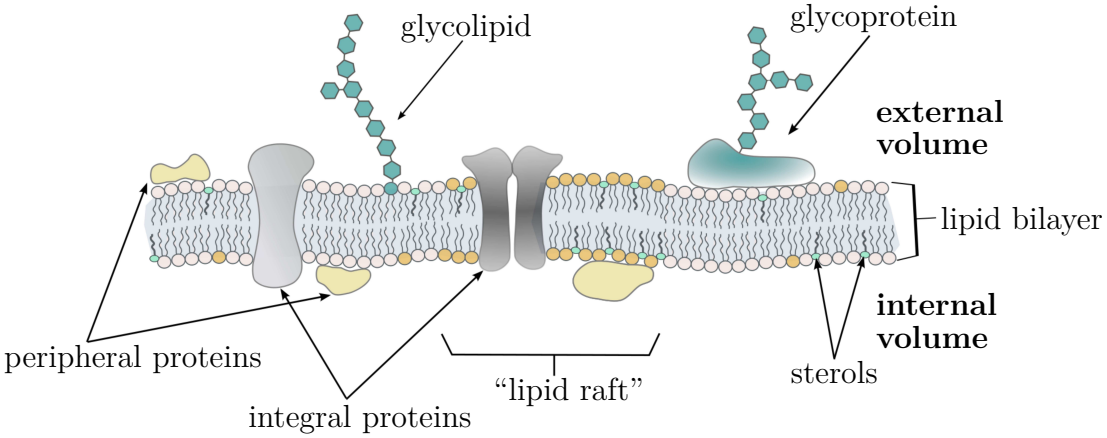

Figure 1.2 – Sketch of a biological membrane. In aqueous surroundings, phospholipids and sterols self-assemble to lipid bilayers with their headgroups exposed to the aqueous phase, shielding their hydrophobic acyl chains from water contact. In a living cell, the resulting membranes host differrent peripheral and integral proteins and carbohydrates as glycoproteins and glycolipids. Lateral segregation of sphingolipids and sterols leads to the formation of stable and transient microdomains ("lipid rafts") which are slightly thicker than the bulk regions and enriched in specific membrane proteins.

The selective membrane permeability which enables the uptake of nutrients and the exclusion of metabolites is determined by both the lipid and the protein constituents. While non-polar substances may diffuse across the lipid matrix easily, specific molecular mechanisms are required to allow the exchange of ions or other hydrophilic substances. To this end, specialised transmembrane protein channels are incorporated into the bilayer, or the cargo is enclosed in lipid vesicles which act as carrier involving several events of membrane fusion. Furthermore, active protein transporters such as the sodium-potassium pump (Na^+/K^+-ATPase) are needed to maintain electrochemical gradients across the membrane [17]. Although the molecule traffic across the membrane is mostly controlled by the involved proteins, the importance of the lipid itself should not be ignored, as the protein association is strongly influenced by the bilayer's composition and state.

1.3.2 Membrane Dynamics

Membrane lipids are held together by noncovalent interactions which provide the individual lipids with some freedom of motion. Hence, membranes are soft and flexible entities that are capable to tolerate mechanical deformations and to recover after minor disruptions. The degree of flexibility of a bilayer depends on lipid composition and temperature as well as on other factors such as the ion concentration of the surrounding buffer.

With increasing temperature, bilayers consisting of a single lipid species show a sharp main phase transition that reflects the change from the gel state L_β to the fluid, liquid-crystalline state L_α. In the L_β-state, the acyl chains are quite well ordered and motions are strongly constrained. In the L_α-state, rotations about the carbon-carbon bonds are allowed, so that the chains are highly flexible and a variety of chain conformations occurs, i. e. the acyl chains are thermally disordered. The liquid-ordered state L_0 reflects an intermediate state in which the acyl chains are less thermally disordered and yet lateral lipid movement across the bilayer can be observed. The particular temperature at which the melting process is induced increases with the acyl chain length and the chains' saturation.

Singer and Nicholson proposed the fluid mosaic model to describe the arrangement of the different membrane components and the dynamics of the entire membrane ensemble in the L_α-phase – the state of primary biological relevance [18]. This model treats the membrane as two-dimensional fluid of lipids with floating proteins scattered across and it is justified by the rapid lateral movement ($\sim \mu\mathrm{m}\cdot\mathrm{s}^{-1}$) that has been observed for the distinct components. Although the fluid mosaic model is commonly accepted, it tends to be too simplistic as many protein functions depend on a lateral membrane organisation. Accordingly, the occurrence of liquid-ordered microdomains cannot be explained in this classic picture. Such "lipid rafts" have a lower fluidity than other regions of the bilayer and serve as functional centres for specific proteins [19]. Just as the rest of the membrane, the composition of the rafts varies widely from domain to domain and from cell to cell. However, most of these rafts contain a notably high amount of sphingolipids and cholesterol which leads to a thickness increase compared to other regions of the membrane.

The transverse diffusion, i. e. the transition of a molecule from one bilayer leaflet to the other, is restricted by the molecule's amphiphilicity and thus, if at all, it occurs very slowly. Typically, the transition times range from a few hours to weeks and as a consequence biological membranes are capable to maintain a high degree of transversal asymmetry [2]. Nonetheless, such a "flip-flop" movement of individual lipids is vital to certain biological processes. In these cases, specialised enzymes, termed flippases, catalyse the transition within a few seconds.

1.3.3 Membrane Lipids

Cell membranes contain a large number of different lipid species which vary in their headgroup structure and chain properties. These lipids can be subdivided into three classes: glycerophospholipids (also called phospholipids), sphingolipids and sterols. Their properties will briefly be introduced below. Fig. 1.5 then summarises lipid

components of high biological relevance and their proportions in the particular cell compartments of mammalian and fungal cells.

Phospholipids: The linkage of two fatty acyl chains to the two free carbons of a glyerol backbone, which is in turn linked to a phosphate group, creates phosphatidic acids. From the additional esterification with alcohol, phospholipids are derived (Fig. 1.3) – the most abundant class of lipids in biomembranes. Prominent examples are phosphatidylcholine (PC), phosphatidylethanolamine (PE), phosphatidylserine (PS), phosphatidylglycerol (PG), or phosphatidylinositol (PI). The phosphate group and the esterified headgroup represent the polar portion of the lipid as they are zwitterionic or negatively charged at physiological pH; the apolar fatty acid chains constitute the hydrophobic part of the complex amphiphilic lipids. Apart from the type of the headgroups, the physicochemical properties of a particular lipid are determined by both the lengths of the fatty acid chains and their degree of saturation.

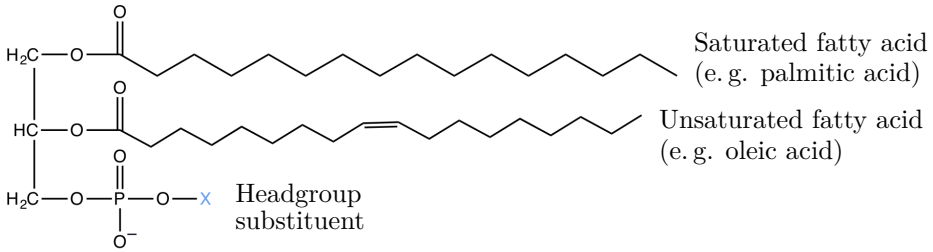

Name of phospholipid	Name of headgroup X	Formula of headgroup X	Net charge (at pH 7.0)
Phosphatidic acid	-	—H	-1
Phosphatidylethanolamine	Ethanolamine	—CH_2—CH_2—$\overset{+}{N}H_3$	0
Phosphatidylcholine	Choline	—CH_2—CH_2—$\overset{+}{N}(CH_3)_3$	0
Phosphatidylserine	Serine	—CH_2—CH($\overset{+}{N}H_3$)—COO^-	-1
Phosphatidylglycerol	Glycerol	—CH_2—CH(OH)—CH_2—OH	-1
Phosphatidylinositol 4,5-biphosphate	*myo*-Inositol-4,5-biphosphate	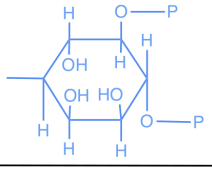	-4

Figure 1.3 – General structure of phospholipids. The parent compound of phopholipids is phosphatidic acid, a phosphomonoester with two fatty acid chains linked to a glycerol scaffold. The additional esterification with a headgroup alcohol (X) yields a phospholipid. Adapted from [2].

In this work, a natural mixture of PS phospholipids from the porcine brain and synthetic dioleoyl-PC (DOPC) were used. DOPC has a zwitterionic headgroup and is ubiquitous in eukaryotic cell membranes. By contrast, PS has an anionic headgroup and is mostly hidden on the inner eukaryotic membrane leaflet. Both fatty acid chains in DOPC are 18:1(Δ9) oleoyl chains, i. e. they consist of 18 carbon atoms and two of them are connected by an unsaturated double bond. Each of these *cis* double bonds corresponds to a kink of 30° in the acyl chain which usually hinders tight chain packing when assembled to a bilayer. Thus, the $L_\beta \rightarrow L_\alpha$ transition of DOPC-bilayers takes place at a relatively low temperature of -17°C.

Sphingolipids: Sphingolipids are similar to phospholipids but consist of a sphingosine backbone instead of a glyerol backbone. To this sphingosine one fatty acid is attached. The most abundant sphigolipids are sphingomyelins (SM) with either phosphoethanolamine or phosphocholine headgroups (Fig. 1.4 A.). In mammalian membranes, the attached fatty acid of SM is usually composed of 16 to 24 carbons that are fully saturated.

Sterols: The structure of sterols is characterised by a rigid steroid backbone which is composed of four fused rings. Three of these rings have six carbons and the remaining one five. Although the biggest proportion of sterols, the steroid backbone, is hydrophobic, most of them also exhibit an amphiphilic behaviour as they contain a small hydrophilic headgroup. Eukaryotic cell membranes contain various of these structural lipids: cholesterol (Chol, Fig. 1.4 B.) is most prominent in animal membranes, while in yeast cells the predominant sterol is ergosterol (Erg, Fig. 1.4 C.), sitosterol and stigmasterol occur mostly in plants. In lipid bilayers, cholesterol imposes an increased conformational order on its neighbouring lipid chains and the larger headgroups of the respective phospholipids cover the cholesterol's top. Due to its close association, cholesterol stabilises the most extended confirmation of the acyl chains. Consequently, cholesterol increases the effective chain length, thickens the bilayer, tightens the lipid packing and decreases the translational mobility of the phospholipids [20]. On the other hand, cholesterol promotes the fluidity of phospholipid bilayers below their melting temperature, so that it stabilises the fluid phase over a broad temperature range. The rigid tetracycle of cholesterol favours the alignment aside from saturated acyl chains. Hence, it rather aligns next to sphingomyelin than to unsaturated phospholipid chains. As a consequence, cholesterol promotes the formation of lipid rafts in ternary mixtures of sphingomyelin and unsaturated phospholipids such as DOPC [19, 21–23].

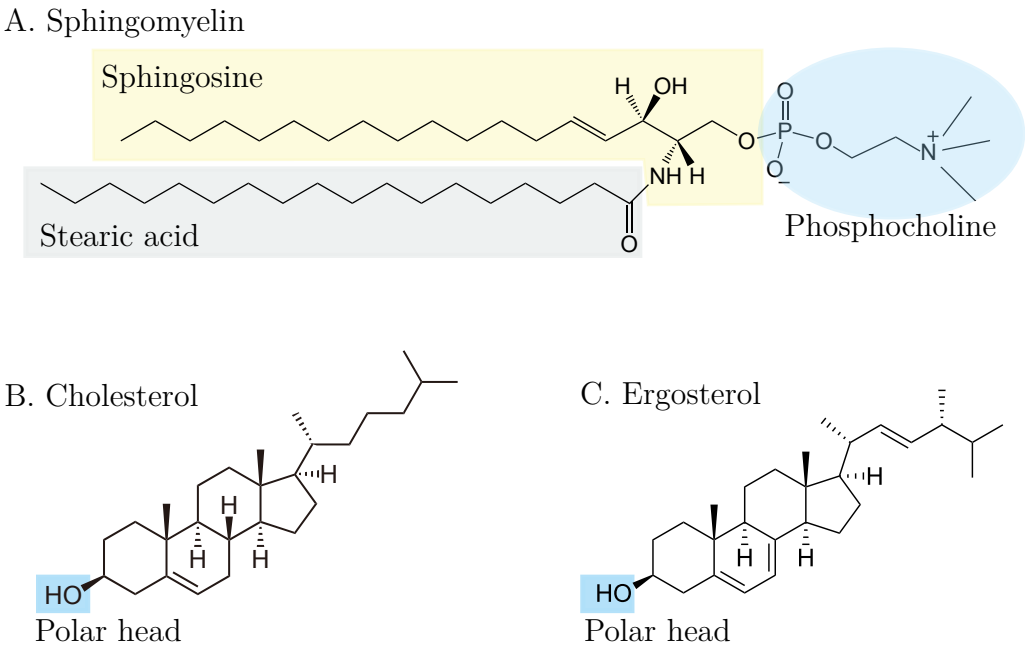

Figure 1.4 – Structures of sphingomyelin, cholesterol and ergosterol. The predominant sphingomyelin species used in this thesis (**A.**) is composed of sphingosine, stearic acid and phosphocholine. The hydroxyl group in both sterols, cholesterol (**B.**) and ergosterol (**C.**), reflects a polar headgroup.

Taking into account the complexity that emerges from combinations of the various headgroups and hydrocarbon chains, biological membranes consist of hundreds of lipid species. The natural distribution of these diverse species varies significantly from cell to cell and even throughout the subcelullar organisation. PCs for instance dominate the plasma membrane of eukaryotic cells but their occurrence in prokaryotic cells is clearly reduced and cholesterol or sphingolipids are completely absent. By contrast, PG is abundant in prokaryotic membranes but in eukaryotic cells, it occurs exclusively in mitochondria where it is synthesised (Fig. 1.5, [24]). Though some of the major phospholipids of eukaryotic cells are synthesised in the mitochondria or the Golgi apparatus, most of them are synthesised in the endoplasmatic reticulum and subsequently trafficked to other cell compartments. Among eukaryotic cells there are distinct differences between mammalian and yeast cells. Certainly, the most striking difference is that yeast cells contain ergosterol instead of cholesterol. Though the lipid compositions throughout the mitochondrial membranes of both organisms are comparable, there are obvious disparities in the plasma membrane: with their high proportions of PS and PI (in total $\sim 50\,\%$), yeast cells contain considerably more anionic phospholipids in their envelope than mammalian cells (in total $\sim 10\,\%$), and the ratio of the total amount of phospholipids to sterol (2:1) is higher than that in mammals (1:1).

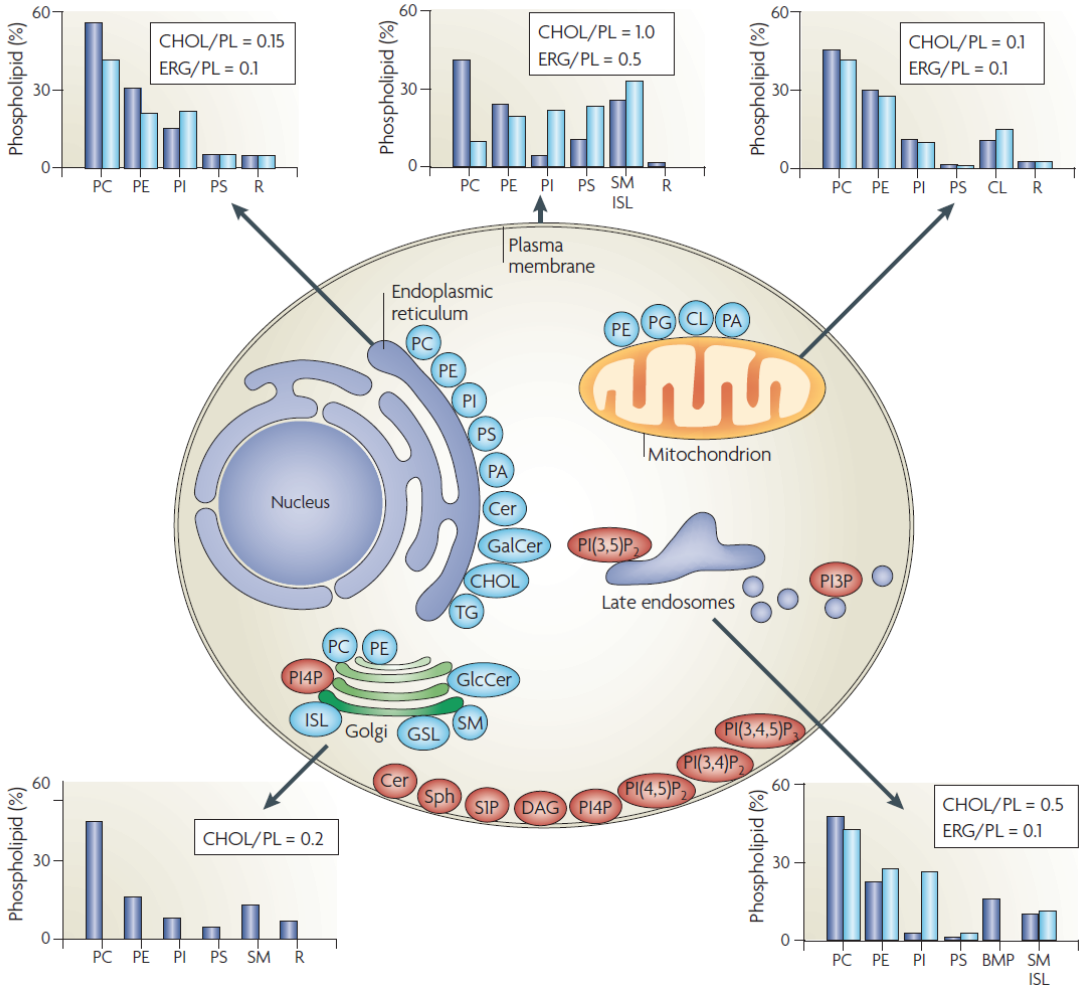

Figure 1.5 – Lipid composition of eukaryotic cells. The outer margin of eukaryotic cells is defined by a specialised plasma membrane and each of the inner cell organelles, the endoplasmic reticulum, Golgi, mitochondria and endosomes is also confined by a membrane of specific composition. The outer graphs give the percentage of the lipid species in mammals (blue) and yeast (light blue) of the respective cell compartment. The molar ratio of cholesterol (CHOL, in mammals) and ergosterol (ERG, in yeast) to the total amount of phospholipid (PL) is also included. The central part of the figure shows the site of synthesis of the major phospholipids (circled in blue) and the lipids involved in signalling and organelle recognition pathways (circled in red). Except for ceramide (Cer) the amounts of the latter lipids are significantly below 1 % of the total phospholipid. The remaining abbreviations used in the illustration denote: phosphatidylcholine (PC), phosphatidylethanolamine (PE), phosphatidylserine (PS), phosphatidylglycerol (PG), phosphatidylinositol (PI), phosphatidic acid (PA), galactosylceramide (GalCer), triacylglycerol (TG), sphingomyelin (SM), glycosphingolipids (GSLs), inositol sphingolipid (ISL, in yeast), diacylglycerol (DAG), cardiolipin (CL), bis(monoacylglycero)phosphate (BMP), phosphatidylinositol-(3,5)-bisphosphate ($PI(3,5)P_2$), phosphatidylinositol-(4,5)-bisphosphate ($PI(4,5)P_2$), phosphatidylinositol-(3,4,5)-trisphosphate ($PI(3,4,5)P_3$), phosphatidylinositol-4-phosphate (PI4P), sphingosine-1-phosphate (S1P), sphingosine (Sph) and remaining lipids (R). Reprinted with permission from [24].

1.3.4 Lipid Polymorphism

Depending on the lipid properties and the water content, the self-assembly of lipid molecules may result in distinct mesoscopic phases that vary drastically from the typical two-dimensional bilayer sheet. Such phases include cubic micellar packings and other cubic or hexagonal superstructures.

Some of the possible lipid phases are found *in vivo*. Therefore, it is proposed that these non-bilayer topologies exert a direct biological function. While PCs, the most abundant phospholipids, prefer the formation of planar bilayers, other lipids such as PE destabilise it and promote the formation of structures of higher three-dimensional complexity. It seems that a balanced mixture of the diverse lipid species is inevitable to diverse structure-function relationships. Accordingly, the formation of local, metastable non-bilayer structures may be the essential key to enable membrane fusion which is relevant to processes like endo- or exocytosis. Another feature that can subtly be tuned with varying lipid compositions is the degree of membrane flexibility which is required to ensure proper membrane protein functions. The latter does, however, not directly relate to the formation of non-planar bilayer structures.

Fig. 1.6 illustrates selected examples of these phases. Therein, the **lamellar phase** is characterised by plane lipid bilayers of thickness d_B alternating with water layers of thickness d_w [25]. The periodicity $d = d_B + d_w$ of these lamellar systems is determined by different interbilayer forces (cf. Sec. 1.3.5) [26].

The **hexagonal phases** H_I and H_{II} consist of hexagonally packed arrays of cylindrical tubes of lipids. Both phases differ in the orientation of the lipids: In the type I aggregates, the tube surface is lined with the hydrophilic heads and the hydrophobic tails point towards the rotational axis of the cylinder. In the aggregates of type II, the lipids align vice versa (= inverted hexagonal phase), yielding cylindrical aqueous pores in their middle. Transitions of the fluid lamellar L_α to the H_{II}-phase are commonly observed upon temperature increases or the dehydration of lipids with small headgroups and relatively long chains [27]. In addition, different membrane-active peptides have the potential to affect lipid phase transformations in different ways (see Sec. 1.4.3) [28].

The **rhombohedral phase** of space group $R\bar{3}m$ represents another phase that emerges under conditions of low water content. This phase has been suggested to reflect the structure of stalk intermediates which occur as intermediate steps in the process of membrane fusion. The phase consists of a dense array of two bilayers interlinked by membrane stalks and residual water reservoirs. The stalks are arranged in a two-dimensional hexagonal lattice and the distinct stalk-linked layers are stacked in ABC periodicity.

Just as the hexagonal phases, **cubic structures** occur in principle also with two different lipid orientations: the normal (type I) and the inverted (type II). However, both the cubic and the hexagonal type I structures do not exist under excess water conditions, which is why they are not considered as biologically relevant [27]. Cubic structures of biological relevance, i. e. the inverted type II structures, are usually bicontinuous, i. e. they consist of two distinct interwoven water reservoirs. Their morphological structure can be described by infinitely periodic minimal surfaces which account for the three-dimensional periodicity and show that the mean curvature of the polar/apolar lipid interface is zero at each point. The biological function

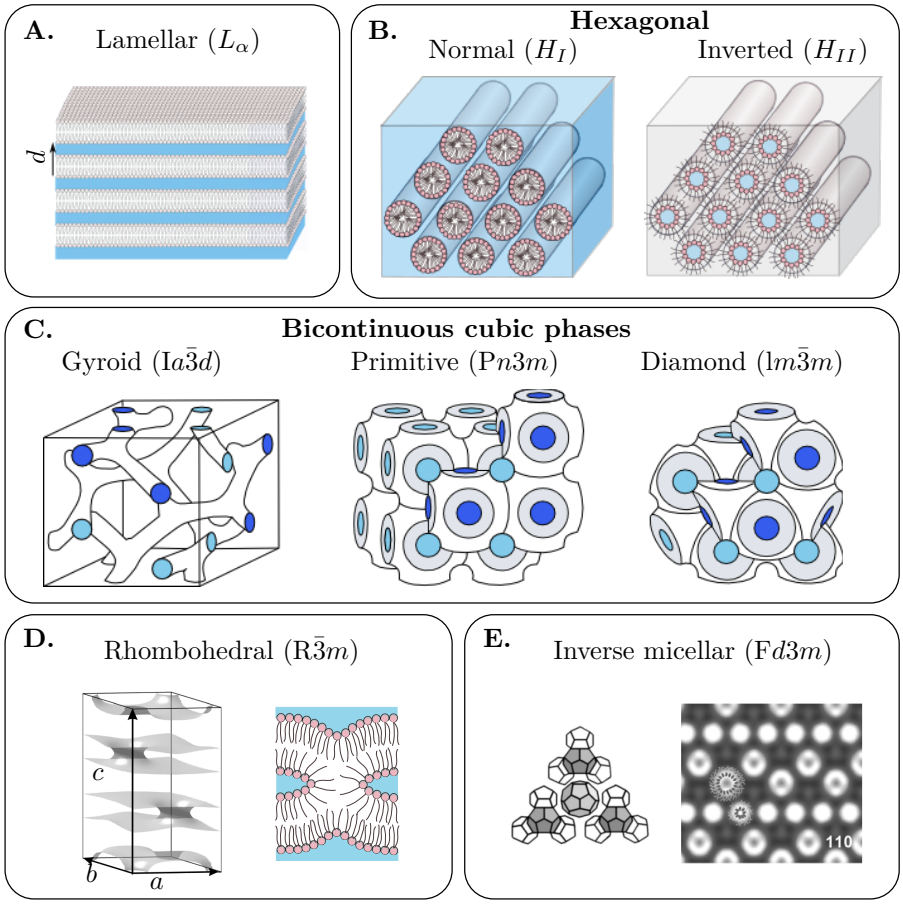

Figure 1.6 – Three-dimensional lipid/water phases. **A.** Sketch of the lamellar L_α-phase including the repeat spacing d. **B.** Fragments of the two different types of hexagonal packings are shown where the lipids assemble in long cylinders. **C.** Unit cells of three different inverted bicontinuous cubic phases are shown. In this phase the lipids form two independent systems of water channels (adapted from [29]). **D.** Unit cell of the rhombohedral R$\bar{3}m$ phase. The definition of the lattice parameters a, b and c is indicated and the two-dimensional sketch next to it resembles the characteristic lipid stalk structure of this phase (both are adapted from [30]). **E.** F$d3m$ packing of the inverse micellar cubic phase. The left side shows a sketch of two adjacent micelle layers as polyhedrons viewed from [111] direction. A two-dimensional representation of the electron density in the (110)-plane is given on the right. The inverted lipid orientation is indicated [27].

of cubic phases is widely unknown. For one thing they are supposed to serve as membranes that efficiently subdivide the cellular space in different compartments [27]. Furthermore, the transition of a lamellar phase into the bicontinuous cubic phase is assumed to mimic the formation of an array of fusion pores [31].

The only **micellar phase** that has yet been observed as stable state under excess of water conditions represents a discontinuous, complex cubic F$d3m$ packing. This phase consists of two different types of quasi-spherical inverse micelles. The unit cell contains 8 micelles of symmetry $\bar{4}3m$ and 16 reverse micelles of smaller diameter and $\bar{3}m$ symmetry [32, 33].

The propensity for the formation of non-lamellar phases can be explained with the thermodynamic packing properties of the involved lipids. Basically, the packing is determined by steric forces due to headgroup-hydration and chain motions which push the lipid molecules apart from each other[1]. The hydrophobic effect on the contrary, exerts a force which pushes the molecules together to minimise hydrocarbon-water contacts at the polar/apolar interface. If this interfacial pressure perfectly counterbalances the lateral repulsive chain and headgroup pressures, the lipids would assemble as plane monolayer leaflet. Usually, these lateral monolayer forces are not balanced and hence the lipids tend to form bent monolayers. The resulting radius of the polar/apolar interface is defined as the intrinsic curvature c_0. By convention, this curvature is expressed with a negative sign if the lipid headgroups line an aqueous compartment and with a positive in the opposite case (Fig. 1.7).

The formation of a bilayer that consists of two similarly curved monolayers is, however, highly unfavourable as it would involve the exposure of the hydrophobic chains to water. Accordingly, fluid bilayers have to withstand their curvature frustration and remain flat. Another way to reach a state of endeavoured curvature, that circumvents the high energetic costs relating to the hydrophobic effect, is the formation of non-lamellar phases. Starting from plane bilayers, the formation of inverse bicontinuous cubic phases represents a first possible step of curvature frustration release. Alternatively, the lipids may pack into the inverted hexagonal phase if even higher curvatures are required. In this case, however, the release of curvature frustration is opposed by a certain extend of packing frustration as the acyl chains have adopted a variety of lengths to occupy the full hexagon avoiding the appearance of any voids [34, 35]. In general, this packing frustration is more efficiently relieved by longer acyl chains than by shorter ones. This relation

[1] Additionally, electrostatic interactions play an important role for the assembly of charged phospholipids.

provides an explanation for frequently observed direct transitions from the L_α to the H_{II}-phase which skip the formation of bicontinuous cubic phases. The highest relief of curvature frustration that can be reached by a lipid/water system relates to a transformation into the micellar phase, the state of maximum mean interfacial curvature.

A simplifying but functional explanation for the tendency of a particular lipid to form non-bilayer structures can be derived from the critical packing parameter P [36]. To define P the lipid's effective molecular shape is described by three geometrical parameters: the mean cross-sectional area a_0 of the headgroup, the length l of the hydrocarbon chains and the occupied chain volume V (Fig. 1.7):

$$P = \frac{V}{l \cdot a_0}.$$

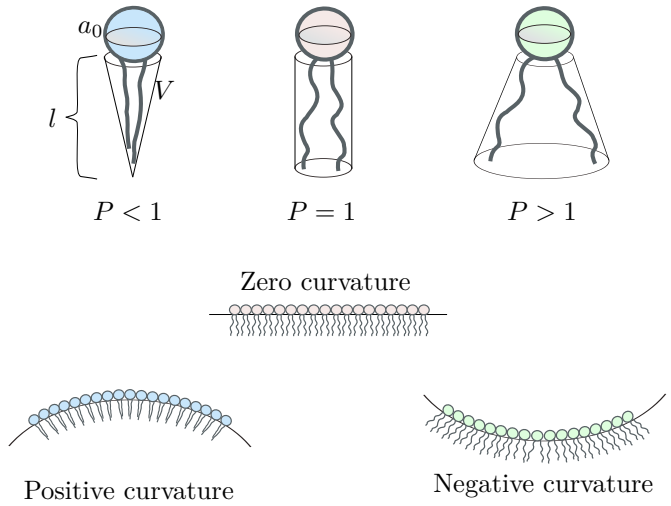

Figure 1.7 – Effective molecular lipid shape and packing parameter P. Cone-shaped lipids with $P < 1$ (typically lipids with a single hydrocarbon chain, e. g. lysolipids) promote positive curvatures, while lipids with cylindrical molecular shape with $P \sim 1$ do not induce any curvature. The chains in wedge-shaped lipids occupy a larger area than the headgroup, so that $P > 1$. These molecules tend to form aggregates with negative curvature.

If the effective molecular shape resembles a cylinder, P approximately equals unity and the lipids tend to pack into lamellar bilayers. Lipid molecules with conical shapes ($P < 1$) will lead to monolayers with positive curvature, i. e. they tend to form micellar structures, while wedge-shaped lipids ($P > 1$) will induce negative curvature and thus, these lipids have a higher propensity to form inverted phases. According to this model, temperature increases, which predominantly induce greater chain disorder, will increase the chain volume relative to the headgroup and consequently promote negative interface curvatures. Likewise, the removal of water

molecules from the lipid/water interface will reduce the effective headgroup size and promote the bending of the headgroup surface towards the water. Following this reasoning, it has been suggested that amphipathic peptides which lower the $L_\alpha \rightarrow H_{II}$ transition temperature induce negative curvature by disrupting the packing in the lipid interface or headgroup region [37] (cf. Sec. 1.4.3).

1.3.5 Interactions between Lipid Bilayers

In lamellar packings, lipid bilayers interact by contributions of attractive and repulsive forces that, in their equilibrium, lead to well-defined interbilayer water spacings. These contributions include attractive long-range van der Waals interactions and repulsions due to steric-hydration forces in unstressed and electrically neutral bilayer systems under excess water conditions (Fig. 1.8). In the presence of charged lipids or osmotic pressures, contributions from electrostatic repulsions appear as well as additional attractive forces due to depletion or hydrophobic interactions. In the following, the different interaction potentials are introduced briefly.

Van der Waals Forces

The van der Waals forces account for the fact that lipid bilayer systems usually do not swell indefinitely with increasing water content. The swelling rather stops once an upper limit of the lamellar repeat distance d is reached. Any additional water will not assemble between the bilayers and instead form a separate phase. At this point, the lipid system is in the state of full hydration [26]. Attractive van der Waals interactions result from mutually induced charge fluctuations of the lipid and water molecules and their different dielectric properties. For a simplified lipid bilayer system, a quantification of this interaction is derived in the framework of Lifshitz theory. Therein, the particular molecular structures are ignored and the interaction is derived for continuous media in terms of its bulk properties as dielectric constants ε or refractive indices n. According to that, the attraction potential for two opposing, plane bilayer sheets with a thin water layer in-between is derived from the Lifshitz-case, which is represented by a planar slab of material that is separated by two semi-infinite media [38–40]:

$$V_{VdW}(d_p) = \frac{k_B T}{8\pi {d_p}^2} \sum_{n=0}^{\infty}{}' \int_{r_n}^{\infty} x \ln\left[1 - \left(\frac{\overline{\Delta}_n(1-\exp(-x\cdot d_c/d_p))}{1-\overline{\Delta}_n \exp(-x\cdot d_c/d_p)}\right)\right] dx. \tag{1.1}$$

For this mathematical description, the polar lipid headgroups and the water layer (with the corresponding thicknesses d_h and d_w) are modelled as one homogeneous slab of thickness d_p and dielectric constant ε_p as indicated in Fig. 1.8. Thus, Eq. 1.1

defines actually not the attraction potential between the two lipid bilayers but between their hydrocarbon layers of thickness d_c and dielectric constant ε_c. k_B denotes the Boltzmann constant, T the temperature. The prime indicates that the $n = 0$ term of the summation has to be multiplied by a factor of 0.5 and the lower limit of the integration is given by $r_n = 2d_p\sqrt{\varepsilon_p}\omega_n/c$, where c denotes the speed of light. $\overline{\Delta}_n$ contains the dielectric permittivities ε of the corresponding slabs at the discrete angular frequencies $\omega_n = 2\pi k_B T n/\hbar$ with $n = (0, 1, 2, 3, ...)$ and the reduced Planck constant $\hbar$. In the non-retarded limit, where the finite velocity of light is neglected (i. e. $r_n \ll 1$, which holds true for small separations d_p), $\overline{\Delta}_n$ can be approximated with

$$\overline{\Delta}_n = \frac{\varepsilon_p(i\omega_n) - \varepsilon_c(i\omega_n)}{\varepsilon_p(i\omega_n) + \varepsilon_c(i\omega_n)}.$$

The additional assumption that $\overline{\Delta}_n^2$ is much smaller than 1 leads to a simplified version of Eq. 1.1:

$$V_{VdW}(d_p) = \frac{H}{12\pi d_p^2} \cdot \left[1 - \frac{2}{(1 + (d_c/d_p))^2} + \frac{1}{(1 + (2d_c/d_p))^2}\right],$$

where $H = 3/2k_BT\,{\sum_{n=0}^{\infty}}'\overline{\Delta}_n^2$ denotes the Hamaker coefficient. This relation is commonly used to estimate the magnitude of van der Waals attractions [41] although the approximations contained lead to inherent shortcomings for $d_p > 0$ as discussed in [39]. Nevertheless, it is known that van der Waals interactions are of long range and their magnitude is reduced with the addition of salt ions which decrease the coefficient H [42].

Entropic Repulsion Forces

The repulsive forces in a lipid bilayer system, which consists of electrically neutral bilayers and water, are of entropic origin. One contribution arises from excluded volumes due to headgroup hydration and the work needed to remove the bound hydrogen atoms. This hydration repulsion has been reported to decay exponentially within a length λ of $\sim$ 2 Å. For average equilibrium water spacings $d_w \gg \lambda$ the approximation

$$V_{Hyd}(d_w) = P_h\lambda e^{-d_w/\lambda} \tag{1.2}$$

applies, where P_h denotes the amplitude of the repulsion [43]. However, the included assumption of well-defined distances between smooth interfaces is to some extent arbitrary and limited in accuracy as thermal motions such as protrusions of lipid molecules vertical to the bilayer plane are entirely neglected in this approach [36, 44].

A second contribution traces back to undulatory waves – the most important mode of thermally excited motion of a bilayer sheet. These long-range undulation modes are restricted if the water spacing shrinks, representing a decrease in entropy and accordingly an increase in the free energy. The mutual restriction of opposing membrane undulations is proportional to the bending rigidity K_c. Following Helfrich [45], the steric free energy per unit area is given by

$$f_U(d_w) = 0.42\frac{(k_BT)^2}{K_c d_w} \tag{1.3}$$

for pure steric interactions caused by collisions of bilayers. The presence of a hydration repulsion, however, softens the membrane confinement which is why a modified version of Eq. 1.3 has been suggested:

$$f_{U2}(d_w) = \frac{\pi k_BT}{16}\sqrt{P_h/(K_c\lambda)}\cdot e^{-d_w/2\lambda}.$$

This approach proposes an exponential decay 2λ which is twice as long as the one of the hydration force. However, studies with imposed external osmotic pressures have shown that the experimentally determined decay length still exceeds this theoretical value [26]. Hence, the exact mechanisms of the repulsive forces within a lipid bilayer system are still a matter of debate and yet remain obscure.

Electrostatic Forces

Another possible cause for repulsive interactions are long-range electrostatic forces from charged lipid headgroups. In lipid/liquid systems such headgroup charges are either obtained from the dissociation of surface groups of anionic lipids, or, from the adsorption of ions from the liquid phase onto the previously uncharged membrane surface in bilayer systems that consist of solely zwitterionic lipids. The latter effect is usually caused by negatively charged ions from electrolyte solutions that adsorb at the amphiphilic membrane interface and provide an anionic surface charge [47, 48]. Yet negligible for chloride ions, this adsorption has been reported to be pronounced for iodide and bromide ions [42]. Hence, even in zwitterionic membrane systems, electrostatic repulsions contribute remarkably to the balance of van der Waals and steric forces if salt ions are present.

The electrostatic repulsion in a membrane system is largely determined by the formation of electrochemical double-layers[2] at the charged bilayer surface, where overlaps of these double-layers repel two opposing membranes due to entropic confinement. Thus, the repulsive contribution is not only influenced by the particular

[2]See Sec. 3.1.2 for a qualitative description of the electrochemical double-layer

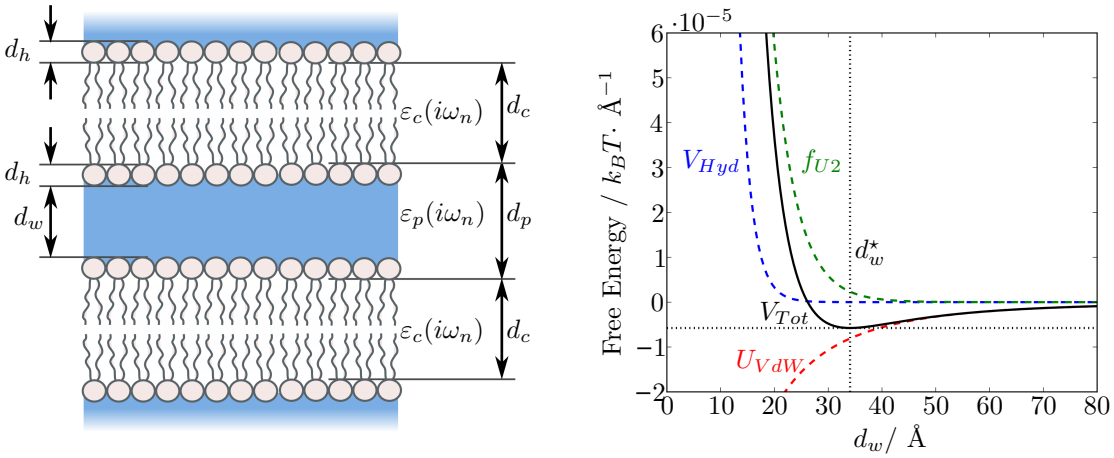

Figure 1.8 – Interaction potentials for two DOPC bilayers at 30°C in excess water. The distance definitions of the bilayer system and the modelled dielectric constants ε_c and ε_p used for the determination of the van der Waals potential are sketched in the left panel. The free energy potentials (right panel) U_{VdW}, V_{Hyd} and f_{U2} are calculated in dependence on the water spacing d_w using the equations given in the text and the parameters given in reference [46]. These are $d_h = 9.0$ Å, $d_c = 26.8$ Å, $H = 5.4 \cdot 10^{-21}$ J, $P_h = 5.5{\cdot}10^7$ J·m^{-3}, $\lambda = 2.2$ Å and $K_c = 8.0\ k_BT$. d_p is correspondingly related by $d_p = d_w + d_h$. V_{Tot} represents the sum of the individual potential contributions. The free energy minimum corresponds to the resulting thickness of the water separation between the bilayers, indicated with $d_w^\star$. Electrostatic interactions are neglected. The bilayer thickness d_B and the bilayer repeat distance d are given by $d_B = 2d_h + d_c$ and $d = d_B + d_w$, respectively.

surface charge (charge density, potential) but also by the properties of the electrolyte solution (type, ionic strength and pH) in which the bilayer system is immersed. Please refer to [36] for a detailed introduction into the electrostatic forces between surfaces in liquids.

Attractive Hydrophobic Forces

With respect to membrane fusion processes, attractive hydrophobic forces play an important role. These interactions are of notably long range, even exceeding the range of van der Waals attractions. In unstressed lipid bilayer systems, the hydrophobic attraction emanating from the hydrocarbon chains is effectively shielded by the hydrophilic headgroups. However, upon global or locally confined tensile stresses, the bilayer expands laterally which is accompanied by an increase in the hydrophobic area exposed to the aqueous space, allowing the hydrophobic attraction to turn up. Fusion between opposing membranes may then occur in consequence of this induced attraction [36].

1.4 Membrane-Peptide Interactions

In this section, the basic properties and membrane mechanisms of membrane-active peptides are introduced by means of the best known class of such peptides, namely host-defence peptides. Aside from their actual host-defending function, their basic characteristic is the direct interaction with lipid membranes. Although Ece1-III is rather a toxin than such a defence peptide, it is assumed to exhibit a similar direct membrane interaction. Hence, an analogy between this well-known class of peptides and Ece1-III is drawn to introduce basic features.

1.4.1 Membrane-Active Peptides

Multicellular eukaryotic organisms produce a wide range of peptides that interact unspecifically with the lipid matrix of cell membranes rather than with dedicated membrane protein receptors. These peptides are essential components of the non-specific innate immune system and it is their principal duty to protect the organism against microbes by directly attacking their cell envelopes. Thus, these agents are referred to as antimicrobial peptides (AMPs) or host-defence peptides (HDPs). Usually, HDPs consist of 12 - 50 amino acids with up to 50 % hydrophobic amino acids and 2 - 11 positively charged arginine or lysine residues, resulting in an overall cationic peptide charge at physiological pH. Thanks to the combination of polar and apolar residues, HDPs fold in secondary structures with amphiphilic character, representing an ideal prerequisite for the binding to lipid bilayers, especially to those carrying negative charges [49, 50]. The variety of HDP structures and their possible mode of action is manifold. Apart from cyclic peptides or peptides with β-sheet or hairpin conformations, a great plenty of the identified HDPs form amphiphilic or hydrophobic α-helices. Hydrophobic helices are usually flanked by hydrophilic amino acids, so that they can span the hydrophobic core of a bilayer and terminate in the region of the bilayer's polar headgroups (transmembrane α-helices). By contrast, amphiphilic helices have alternating patterns of 2 - 3 consecutive polar and apolar residues that facilitate the formation of α-helices with a lateral hydrophobic face and an opposed hydrophilic face. These peptides posses secondary amphiphilicity and in general, the helix formation is triggered upon the intercalation into the amphiphilic lipid membrane interface, so that the hydrophobic face partitions to the bilayer core and the hydrophilic face is accommodated within the polar headgroup region [51].

Most HDPs exhibit a preferential selectivity for Gram-negative bacteria, which is supposed to relate to their general cationicity that mediates the attachment to the negatively charged bacterial cell envelope. This membrane selectivity is reduced when electrostatic effects on the interaction are less pronounced and hydrophobic

effects predominantly influence the disintegration of the lipid bilayer [52]. Thus, electrostatic neutral peptides and peptides with lower cationic net charges or even slight anionic overall charges have been reported to show less selectivity and reduced efficiency towards microbial cells compared with mammalian cells. Prominent examples are the anionic and hydrophobic fungal peptide alamethicin, which exhibits apart from its bacterial activity also cytotoxic activity [53, 54], or, the amphiphilic peptide melittin, an ingredient of the bee venom which perforates cell membranes of bacterial, mammalian and fungal organisms equally [55, 56]. Some HDPs do also exhibit enhanced cytotoxicity towards human-derived tumour cells as opposed to healthy cells. In general, HDPs disturb the integrity of their target cells by the formation of non-specific lesions or specific pores across the lipid bilayer membrane. These destabilise transmembrane voltage potentials and induce leakage which consequently leads to cell death [57]. A similar perturbation of the membrane integrity can be achieved by peptide-mediated cell aggregation as it is observed for the hydrozoan antimicrobial peptide hydramacin-1 [58, 59].

Although it has been shown that the primary target of HDPs is the cell membrane itself, it is assumed that the final killing process results from complex processes that are functionally organised within the membrane environment [60, 61]. Therefore, the antimicrobial action involves additional intracellular targets that can be attacked after internalisation of an HDP [62]. The fungal defensin plectasin and three similar oyster defensin variants (Cg-Defh1, Cg-Defh2, Cg-Defm) for example have been reported to specifically inhibit cell wall biosynthesis in bacteria by binding irreversibly to the bacterial cell wall precursor lipid II [63, 64]. Furthermore, it has been shown that HDPs also act as immune modulators which influence infections and inflammations by activating cytokine and histamine release, enhancing the chemotaxis of immune cells and stimulating wound healing and angiogenesis. All these properties as well as their capabilities to neutralise toxins, such as LPS, and to degrade and prevent biofilm formation have raised the prospect to utilise HDPs as effective therapeutics for multiple treatment goals [3, 50, 65–69].

1.4.2 Mechanisms of Membrane-Disruption by Peptides

A detailed understanding of the interaction mechanisms of membrane-disrupting peptides is crucial with view to potential biotechnological applications including the utilisation of such peptides as antibiotics or the development of agents that protect mammalian cells against disintegration by toxic peptides from venoms of other organisms. Two essential pore models have been evolved that attempt to explain the mode of action of membrane-active peptides: the “barrel-stave” and the “toroidal”

pore model [70]. In addition, several non-pore models have been proposed to describe the formation of lesions in lipid membranes. Among these phenomenological models, the "detergent-like carpet" mechanism is the one most frequently applied [71]. As initial step these models have in common that the peptides accumulate at the lipid headgroup region in parallel orientation to the membrane surface (Fig. 1.9). The attraction of the peptide towards the membrane surface is driven by hydrophobic and by electrostatic interactions. However, it is assumed that the charge-charge interactions between lipids and peptides are not crucial to the process of membrane perturbation itself [72].

Barrel-Stave Pore Formation

The barrel-stave model involves the creation of discrete transmembrane pores which form in consequence of self-association and subsequent realignment of these peptides to an orientation perpendicular to the membrane surface [57, 73]. The resulting pore is constructed by a bundle of amphipathic α-helices with their hydrophobic sides facing the phospholipid acyl chains and their hydrophilic surfaces facing inwards to an aqueous pore (Fig. 1.9 B). The pore acts as ion channel that dissipates transmembrane potential gradients which leads to the loss of the permeability barrier. Leakage of cell content as well as increased water and ion flows finally cause cell swelling, osmolysis and cell death. The apolar character of the fatty acyl chains and the inability to form hydrogen bonds will not facilitate the polar peptide face to get in direct contact with the hydrophobic bilayer core. Therefore, the appearance of a single traversing amphiphatic α-helix is energetically highly unfavourable. The accumulation of peptide monomers at the membrane surface prior to the insertion of the resulting peptide bundle represents a crucial step of this mechanism.

The barrel-stave model is observed for peptides with predominant hydrophobic character. The most popular and well-studied example is alamethicin [74]. Neutron and X-ray scattering studies [75–78] have shown that at high concentration this 20-residue peptide from the fungus *Trichoderma veridae* forms stable water-filled pores which are lined by seven to nine monomer α-helices depending on lipid composition and hydration level [79]. Accordingly, the channel diameter results in 18 - 26 Å. For this kind of membrane pore, the peptides have to be sufficiently long to span the hydrophobic core of the bilayer (typically 32 - 38 Å[80]) which cannot be accommodated by short peptides comprised of less than 20 amino acids residues. Furthermore, in a barrel-stave pore, the peptides get in close contact to each other which is often not favourable due to electrostatic repulsions. Thus, another pore mechanism, the toroidal pore model, has been proposed.

Toroidal Pore Formation

In the toroidal-pore model, the peptide helices remain in close contact with the lipid headgroups such that the lipids bend around the bilayer normal upon the spontaneous realignment of the peptide helices and both, inner and outer leaflet of the bilayer, are connected (Fig. 1.9 A). Thus, the resulting pore is lined by polar lipid head groups and the hydrophilic surfaces of the amphipathic peptide helices [81]. This kind of pore formation is facilitated by a positive curvature strain on the membrane which is induced by the surface embedding of peptide, representing excluded volume for the lipid headgroups and forcing them to pack more closely [72]. Pore formation is then favoured, once this strain overcomes the corresponding line tension of the pore. Since the peptides intercalate preferentially in the headgroup region, the volume of the hydrocarbon region stays constant. Consequently, the hydrocarbon thickness decreases proportional to the areal stretching, i.e. proportional to the peptide-to-lipid ratio (P/L) [82]. The proposed membrane thinning and the fact that toroidal pores involve the perturbation of the lipid orientation itself (so that the peptide does not necessarily need to extend across the entire hydrophobic bilayer core) enable the toroidal pore model to explain the induction of stable pores by short peptides. Furthermore, repulsive interactions of positively charged peptides are reduced if negatively charged phospholipids are present in the pore-lining [83]. By contrast, the interaction of peptides is strongly reduced in membranes consisting of zwitterionic phospholipids or cholesterol. Both lipids are prominent constituents of the outer membrane layers of eukaryotic cells (see Sec. 1.3.3), which would provide an explanation for the reduced lytic activity of highly cationic HDPs against their host cells. The formation of toroidal pores was demonstrated, for example, for melittin [84, 85], magainin-2 [86] (a member of the magainin family first found in amphibians) and the human cathelicidin LL-37 [87, 88].

For both the barrel-stave and the toroidal pore mechanism a two-state model has been proposed, which describes the process of the pore formation by α-helical peptides [82]. Thereby, the peptides initially accumulate parallel to the bilayer surface (S-state) and spontaneously realign into the bilayer core to form a transmembrane pore state (I-state) as soon as a critical threshold concentration $P/L^{\star}$ is reached. The threshold concentration $P/L^{\star}$ is mainly determined by the lipid composition, i. e. chain length, headgroup charge and phospholipid geometry. Therefore, this model explains that differences in cell susceptibilities towards a membrane-active peptide are not directly correlated to the peptide's particular binding affinity to the membrane surface.

The traditional picture of the toroidal pore has been challenged by findings from molecular dynamics simulations with the peptide MG-H2, an analogue of magainin-2 [89]. This study has indicated that only one or two peptide monomers are located near the centre of the pore, while the other peptides from the initial aggregation remained bound at the membrane surface in close vicinity to the pore opening. Thus, there are more peptides with an orientation parallel to the surface as proposed by the two-state model. The authors raised the question of the validity of the conventional toroidal pore model and suggested a modified disordered model.

Detergent-like Carpet Mechanism

The detergent-like carpet model provides a more general approach to describe the bilayer disintegration with increasing peptide concentration, lacking supramolecular pore structures. This model was first proposed by Shai *et al.* to explain the mode of action of the mammalian cecropin P1, which accumulates at the membrane surface like a carpet and permeates it in a detergent-like fashion once the local threshold concentration is reached [90, 91]. In consequence of high peptide concentrations, the membrane is then disintegrated by micellisation (cf. Fig. 1.9 C). Similar to the toroidal pore model, the presence of negatively charged lipids enhances the disintegration process as cationic repulsions are reduced, promoting the formation of a dense peptide carpet. Another similarity to the toroidal pore formation is that the peptides stay in close contact to the lipid headgroups throughout the detergent-like disintegration process. Therefore, toroidal pore lesions can be regarded as an intermediate step prior to micellisation [57].

Which One is the Correct Model for a Certain Peptide?

As reviewed in e. g. reference [93], the particular mechanism of membrane permeabilisation and disintegration does not only depend on the characteristics of the peptide itself but also on several other physicochemical parameters as peptide-to-lipid ratio, lipid composition and individual lipid structures or environmental conditions such as temperature, hydration and buffer constitution. Therefore, it is probably incorrect to assign one of these pore models as general interaction mechanism for one particular peptide. Depending on the detailed conditions, all of them may occur and represent an initial or intermediate step with another one as consequence. Furthermore, the problem of assigning a concrete peptide-induced disintegration to one of the models arises from the experimental difficulty of following transient processes which happen on the order of a few tens of nanoseconds on a molecular level [89]. Due to experimental circumstances, real-time tracking of the permeabilisation

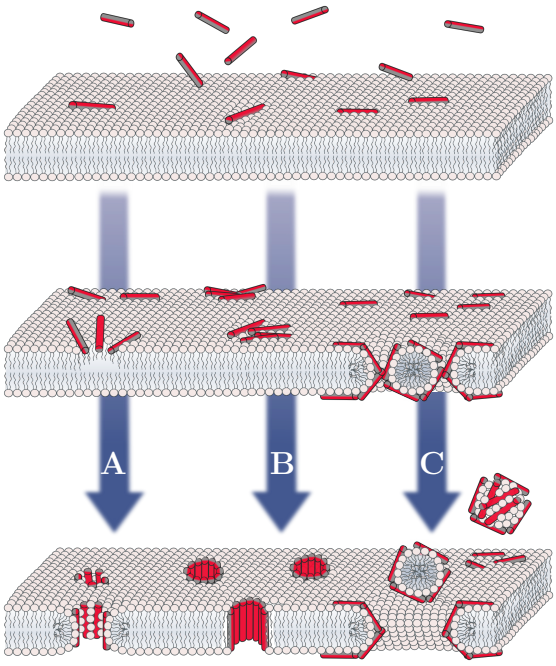

Figure 1.9 – Possible mechanisms of pore formations in lipid bilayers induced by amphipathic peptides. Three different stages of the pore mechanisms are sketched: **A.** the toroidal pore formation, **B.** the formation of barrel-stave pores and **C.** the detergent-like carpet mechanism. All three have in common that the peptide adsorbs parallel to the bilayer surface as initial step. The amphipathic peptides are depicted as two-coloured tubes with the red part representing the hydrophilic face and the grey part the hydrophobic one. The figure is adapted from [92].

is often impossible, so that a wide range of structural experiments are carried out before and after peptide addition [87, 94]. The mode of actions can only be probed indirectly and the results are therefore often ambiguous.

1.4.3 Lipid Polymorphism in the Presence of Peptides

Apart from their disruptive effects various amphipathic peptides crucially affect the phase behaviour of lipid membranes. This includes either a change of the phase transition temperature of the $L_\alpha \rightarrow H_{II}$ transition, or the induction of unpaired or coexisting inverse cubic phases [95]. Similar to the factors that mediate disruptive membrane defects, these interactions are influenced by hydrophobicity, charge, steric confinements, peptide surface accumulation as well as the orientation and depth of the peptides' insertion into the bilayer.

The presence of peptides which induce toroidal-like lipid pores often increases the $L_\alpha \rightarrow H_{II}$ transition temperature. It is assumed that this stabilisation of the lamellar phase is linked to the positive curvature exerted by the pores which opposes the negative membrane curvature of the non-lamellar H_{II} phase. Accordingly, these

kinds of peptides rather promote the formation of regular H_I phases or micellisation of the bilayer [28]. The situation is different with peptides that induce membrane fusion and thus promote negative lipid curvature. These peptides reduce the $L_\alpha \rightarrow H_{II}$ transition temperatures [96, 97].

Peptide-induced cubic lipid phases constitute a porous lipid structure that may lead to membrane destabilisation and a final degradation into micelle-like lipid fragments. For a detailed outline on this topic the reader is referred to an excellent review by Haney and co-workers [28].

1.4.4 Functional Relevance of C-terminal Peptide Amidation

It has been observed that a variety of membrane-active peptides including melittin [98], cecropins [99] and PGLa [100], another member of the magainin family, exhibit C-terminal amidation which is assumed to serve a biological function. However, the effect of this post-translational modification is not understood yet [101]. Some authors have observed that a C-terminal amidation promotes the formation of α-helices. They argued that this is caused by an additional hydrogen bond provided by the carboxamide group which stabilises the α-helical structure [102, 103]. However, it has also been reported that the formation of an α-helix is no essential prerequisite for the formation of lesions [89]. An increased degree of helicity may even reduce the peptide's activity [104]. It has also been suggested that the increased positive charge of C-terminal amidated peptides enhances electrostatic interactions with lipid bilayers. Therefore, it increases their specificity and membrane-lytic activity towards anionic lipid components. Accordingly, investigations on the amphibian peptide maximin H5 [105] and on the synthetic HDP Modelin-5 [106] have shown that the C-terminal protection has the potential to enhance the peptide activity against membranes with anionic lipid components, while the activity against zwitterionic membranes is maintained at comparatively low level. On the contrary, the synthetic amphiphilic peptide MSI-103 [100] has been reported to show reduced haemolytic but preserved antimicrobial activity without the amidation. Nonetheless, for non-amidated isoforms of PGLa and the synthetic MAP peptide, the activity towards both membrane types is reduced [100]. These three scenarios illustrate the difficulty to draw general conclusions on the effects of amidation.

In Ece1-III, a naturally occurring amidation has not been observed. Nevertheless, effects on the activity and selectivity resulting from such a modification shall be addressed within this work to get further insights into the physicochemical parameters that make up peptides with a high activity against microbial cells but only minimal or none activity against the host.

2 Model Systems

The biochemical complexity of natural cell membranes impedes *in vivo* examinations of their structural properties and interactions extraordinarily as observations are often ambiguous and leave vast room for interpretation. To elude the biological complexity, biomimetic model systems of lipid bilayers are employed, allowing the elucidation of physical membrane properties on molecular scale [107]. These artificial membrane models are commonly composed of only a few components. The particular composition and the chemical structure of the membrane's constituents can be varied systematically. As a consequence thereof, essential membrane characteristics, such as the degree of fluidity or curvature, can be tuned. Thus, model membranes provide ideal, yet simplified, platforms for studying diverse fundamental membrane mechanisms as for instance phase changes, transport processes or fusion events. In addition, structure-function relationships of membrane proteins, enzyme kinetics and membrane-peptide interactions can be explored. The latter aspect is of prior interest in this dissertation. Therefore, model membranes are employed and their properties with and without peptide content are investigated. Distinct compositional variations of the synthetic systems are made to study the effect of lipid composition, since such variations may influence the bilayer insertion mechanism of a peptide significantly.

2.1 Diversity of Lipid Model Membranes

In the past decades, various synthetic model systems have been developed, each of them having its own advantages and drawbacks. Not all systems are equally well-suited to give reasonable information on a particular lipid characteristic and the choice of the model system depends on the distinct property that shall be elucidated. Biological membranes are surrounded by the aqueous cytosol to one side and intercellular fluid space to the other. Accordingly, model membranes are required to mimic this basic feature if the dynamics of a membrane shall be studied. Otherwise, distinct modes of movement such as bilayer undulations might be restricted. Access to fluid space, as it is given in free-standing bilayer membranes for example, is also inevitable for examinations on transmembrane traffic behaviours. Solid supported

membranes by contrast, do not readily resemble these dilute conditions but are often easier amenable to many physical characterisation techniques owing to their planar geometry. In the first section of this chapter, relevant model membrane concepts are introduced and their capabilities are discussed briefly. The sample material and the particular preparation procedures used in this dissertation are described in the second section.

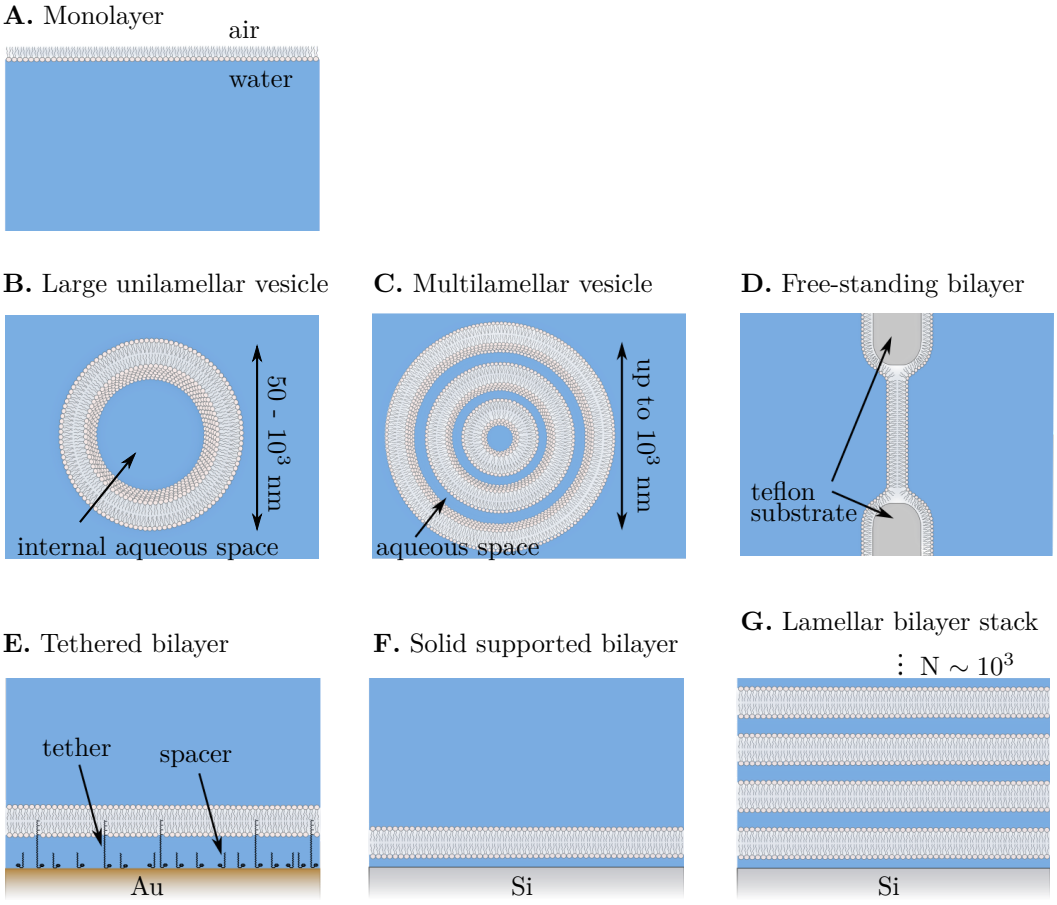

Figure 2.1 – Model Membrane Systems. **A.** Lipid monolayer at the water/air interface. **B.** Large unilamellar vesicle in buffer solution as representative for unilamellar vesicles in general. Small and giant unilamellar vesicles are of a similar appearance but differ in their sizes (see text). **C.** Multilamellar vesicle in solution. **D.** Free-standing bilayer membrane across the aperture of a teflon substrate. **E.** Bilayer membrane tethered to a gold surface. The sketch resembles a sparsely tethered membrane where the substrate surface is also occupied by spacer molecules so that only a few tethers are anchored to the membrane. Hence, the water reservoir between the bilayer membrane and the substrate is maximised. **F.** Bilayer membrane upon a solid silicon support with a thin water layer in between. **G.** Multilamellar stack of bilayers on a solid support.

Monolayer

At polar/non-polar interfaces, such as the water/air interface, lipids usually form a single layer of lateral adjoining lipids [108] (Fig. 2.1 a). This monolayer represents only one moiety of a physical membrane but it can be utilised for many investigations. Using a film balance for instance, the surface area and the corresponding lateral pressure of the monolayer can be controlled to resemble the different planar phase states. At low lateral pressures, the lipids spread over a large area and are considered to be in an gaseous state. Compression of the available area pushes the lipids closer together and increases the lateral pressure. This leads to the formation of liquid-like states at moderate pressures and to gel-like states at higher compression levels. If the compression gets too high, the monolayer collapses which is revealed by discontinuities in pressure-area isotherms [109].

This system also allows studies on how the properties of the aqueous subphase influence the lipid layer. These include pH, ionic strength and the effects of monovalent or multivalent ions. The lateral pressure also provides valuable information on the intercalation behaviour of membrane-active peptides, wherefore film balance experiments are employed in this thesis.

Beyond that, lipid monolayers can be transferred to a smooth solid surface such as silicon or mica [110], where its structural properties may be studied by surface sensitive experimental techniques that require a solid substrate (e. g. atomic force microscopy).

Liposomes

Liposomes are ball-shaped lipid vesicles which emerge from mechanical dispersion of amphiphilic lipids in buffer solution [111]. Although liposomes may be prepared at high concentration, the resulting bilayers are typically under dilute conditions, maintaining the natural membrane flexibility. According to their dimensions, liposomes are subdivided into different groups: small unilamellar vesicles (SUVs, $\leq$ 100 nm), large unilamellar vesicles (LUVs, 100 - 500 nm), giant unilamellar vesicles (GUVs, $\geq$ 1000 nm) and multilamellar vesicles (MLVs, $\geq$ 1000 nm). While all unilamellar vesicles consist of only one lipid bilayer that encapsulate an aqueous compartment, MLVs consists, as their name suggests, of multiple bilayers (Fig. 2.1 b and c).

MLV Dispersions of MLVs are typically quite polydisperse. Possible vesicle diameters range from 0.2 to 10 μm. They comprise up to around 20 lipid bilayers wrapped around each other like the adjacent layers in onion skin, sparing only a small internal vesicle volume. Adjacent bilayers in MLVs are equally separated by water layers and thus comprise a repeat spacing d that is similar

to the one in the lamellar L_α-stack depicted in Fig. 1.6. Depending on the environmental conditions, also non-bilayer phases may readily form in MLVs. Therefore, they are commonly used to study lipid phase behaviour using for instance differential scanning calorimetry (DSC) or Fourier transform infrared spectroscopy (FT-IR). Owing to their comparatively high degree of positional order, MLVs can also be examined by X-ray small angle scattering. However, it has to be noted that it is somewhat unclear to which extent the close vicinity of the different bilayers in MLVs affect each other.

SUV SUVs have diameters between 20 and 50 nm and are typically homogeneous with respect to their size. They are formed by extensive sonication of lipid dispersion in buffer solution and/or by extrusion through polycarbonate filters of defined pore sizes. The vesicles are subjected to repeated freeze/thaw cycles to obtain a high degree of uniform liposome sizes. The drawback of SUVs is that they are small compared to many membrane structures of living organisms. Thus, they often exhibit a stronger curvature which may impede the incorporation of proteins.

LUV LUVs are obtained from preparation procedures similar to those of SUVs. Typical LUV diameters range from 50 nm to 10 μm[1]. Hence, membrane curvature is reduced as compared to that of the smaller SUVs which makes it easier to incorporate proteins. However, their size distribution is usually broader and large vesicles tend to be relatively fragile.

GUV As their name implies, GUVs represent the largest group among unilamellar vesicles. Their diameters may range from 5 to 300 μm. This size allows direct microscopic visualisation provided that the vesicles are immobilised to a support. Appropriate labelling with fluorescent dyes thus enables investigations on lipid rafts or fusion intermediates. Moreover, these vesicles can be manipulated with micropipettes to study their elastic properties and it is possible to insert microelectrodes to measure electrochemical gradients. In contrast to the aforementioned liposomes, GUVs are prepared by electroformation procedures [113].

The preparation of liposomes is usually uncomplicated and can be performed with reproducible quality in a large quantity and at high concentrations. In GUV systems, even asymmetric lipid distributions of both bilayer leaflets can be resembled. Liposome attributes as composition, size or surface charge can be controlled easily

[1] The critical parameter for the final liposome size is commonly the output power of the sonication device [112].

to meet the particular requirements of the experiment. Labelling a certain proportion of the comprised lipids with fluorescent dyes for instance, enables either direct microscopic visualisation or analyses based on the quantity of the fluorescent yield. Beyond that, liposomes represent a suitable system for a variety of other biophysical studies such as size determinations by dynamic light scattering or analyses of their zeta potential by electrophoretic techniques. However, not all liposomes are accessible from both membrane sides, so that liposomes are not perfectly suitable for studies on ion transports across the membrane.

Free-standing Bilayer Membranes

With respect to model membrane systems, the terms free-standing, planar or black lipid membrane (BLM) are commonly referred to membrane designs in which the lipids bilayers are spanned across a hole in a substrate (Fig. 2.1 d). In this free-standing membrane design, the bilayer is exposed to aqueous solution to both sides. This renders it a suitable system for studies on ion flows that are induced upon the interaction with pore-forming substances. The measurements are commonly done in a setup in which the BLM separates two different compartments with buffer solution. The current flow between two electrodes, each placed in one of the buffer compartments, provides an easily amendable measure on the electrical sealing properties of the membrane (cf. Sec. 3.3.2).

Originally, the abbreviation BLM stands for black lipid membranes. The name has emerged from the optical behaviour of the membrane during its formation by a method introduced by Mueller and Rudin [114]. In this preparation, lipids in organic solvent are readily painted across the substrate aperture which is already immersed in buffer. The initial membrane thins out until it consists of only a single bilayer of lipids. This final bilayer causes destructive interference of visible light and appears opaque, i. e. it looks like a black membrane. Another method of preparation has been introduced by Montal and Mueller [115]. In their approach, the bilayer is formed from two monolayers that cover the water surfaces in separated chamber compartments. Gradual elevation of the two water levels will eventually create the bilayer as the water levels pass the substrate opening. This method has two distinct advantages over the earlier painting method: On the one hand, no residual solvents is remained inside the bilayer and, on the other hand, it allows the creation of asymmetric membranes as each bilayer leaflet is determined by its initial monolayer. Finally, neither of the preparation techniques is able to avoid the substantial drawback of the planar model systems: their inherent fragility. Free-standing membranes are very sensitive toward vibration and mechanical shocks; usually, they collapse after several hours at the latest.

Membranes on a Solid Support

Preparations of plane bilayers on solid substrates offer many experimental advantages. Not only do these design strategies drastically increase the membrane stability, they also provide an excellent platform for many surface-sensitive characterisation techniques such as atomic force microscopy, ellipsometry, surface plasmon resonance, and X-ray or neutron reflectivity. Biologically relevant properties as for instance membrane-peptide interactions, lipid phase transitions and microdomains can be studied.

Single Solid Supported Bilayers Among the supported model systems, single bilayers directly supported by a solid substrate (solid supported bilayers, SSBs) represent the most common system [116] (Fig. 2.1 f). They are prepared from Langmuir-Blodgett transfer [117], by vesicle fusion in aqueous solution [118], or by a combination of both. The resulting flat bilayer is separated from the solid substrate by a thin water layer (5 - 20 Å) [119–121]. Thus, SSBs maintain a certain degree of fluidity allowing examinations of their dynamics. Nevertheless, it has been observed that the physical and chemical properties of the substrate still affect the bilayer's properties to some extent: On the one hand, the solid substrate may induce asymmetric molecular distributions between both bilayer leaflets [122] and on the other hand, the support may affect the dynamical bilayer properties as it has been found to reduce the lateral lipid mobility [123] and to suppress thermal bilayer fluctuations normal to the interface [119]. Substrate coupling may furthermore impede the incorporation or the function of membrane proteins.

In this work, SSBs are prepared by fusion from LUVs for all applications. In the fusion method, the substrate is incubated with the vesicle solution. Eventually, the vesicles adhere to the substrate surface where they fuse and rupture to form homogeneous planar bilayers. The stability of the membrane is mediated by a balance of van der Waals, electrostatic, hydration and steric forces [43]. Biological inert, hydrophilic and smooth substrate surfaces are essential prerequisites for the SSB formation from vesicles, since the substrate's hydrophilicity mediates the fusion process and increasing molecular roughness has been suggested to impair the dynamical behaviour of the bilayer [124]. Common substrate materials are fused silica, mica, borosilicate glass, quartz, oxidised silicon, or oxidised titanium.

The clear advantages of SSB models are their planar geometry and their high mechanical stability provided by the underlying substrates. The excess water ensures a physiological bilayer state of full hydration and allows membrane active molecules to access the bilayer directly from the solution. SSBs must be kept in excess water since they strip off from the substrate when exposed to an air/water interface [125].

Solid Supported Multilayers In order to reduce the impact of artefacts due to substrate coupling, model systems consisting of stacks of distinct bilayers upon a solid substrate have been introduced (solid supported multilayers, SSM). Similar to SSBs, these stacks are directly adjoined by the substrate (except for the thin water layer between substrate and lowest bilayer, Fig. 2.1 g). Thus, the lowest bilayer of the stack is still coupled to the substrate which causes similar demands on the surface properties (i. e. hydrophilicity and molecular smoothness). Most commonly, multilamellar membrane stacks are prepared by spreading from solution, where the solvent is allowed to evaporate [126]. Subsequent contact with water vapour rehydrates the deposited lipids which consequently self-assemble to highly oriented stacks of ~ 1000 bilayers within a few hours. This technique is also chosen for the experiments in this work.

Commonly, the stack does not homogeneously cover the entire substrate. Both the total number of bilayers and the number of membrane defects depend on the amount of lipid deposited, but also on the solvent properties. Studies on most bilayer properties will be averaged over hundreds of bilayers, which – at least in some cases – might represent a delicate drawback of these models. In these instances, the introduction of spin-coating preparation schemes may provide a remedy since these allow the total number of bilayers to be precisely limited and controlled [127].

In the state of full-hydration (or almost full-hydration), multilamellar lipid samples usually constitute in the L_α-phase where the lipid packing in the bilayer plane is thermally disordered. Yet, the vertical stacking of bilayers reflects a high periodicity since the distributions of the bilayer normal vectors are usually narrow ($\sim 0.01°$). Hence, these stacks appear as one-dimensional crystals with smectic liquid-crystalline symmetry. With respect to X-ray studies, this periodicity represents an obvious advantage, constituting an enormous increase in the scattering volume compared to single bilayers or multilamellar vesicles in which the bilayer stacks are dispersed over a broad orientation range. Moreover, low mosaicities, i. e. narrow ranges of normal vector orientations, enable the differentiation between two distinct components of the scattering vector: normal and parallel to the bilayer plane [128]. In addition, the osmotic pressure imposed on the membrane can be varied easily by outer stressors, so that the molecular forces between the membranes can be controlled (cf. Sec. 1.3.5). This consequently enables measurements of inter-bilayer interaction potentials and fluctuations of the stack [43, 129]. As mentioned previously, one inherent disadvantage of multilamellar membrane stacks is that their physical properties must be probed as ensemble average and the corresponding results often leave tremendous room for interpretation. Another drawback results from the uncertainty of the concentration of ions and protons present in the

interlamellar water space as the system does not allow precise determinations of the pH value. On the one hand, a certain amount of natural salts will be included in the system which originates from the lyophilisation of the lipids. On the other hand, the rehydration may introduce a superior number of protons as the ultra-pure water used is in general associated with a slightly acidic pH.

Membrane Bilayers Tethered to a Solid Support Tethered bilayer membranes (tBLMs) represent a third kind of single model membranes on a solid support. In contrast to the SSBs described above, tBLMs are immobilised to the support by specially designed anchor molecules (Fig. 2.1 e) which allow the expansion of the aqueous reservoir underneath the bilayer. This kind of tethering prolongs the membrane's stability drastically compared to free-standing BLMs while its two-dimensional fluidity is almost entirely maintained and, in addition, both bilayer leaflets can be widely exposed to aqueous reservoirs. Thanks to these features, tBLMs represent remarkably good hosts for transmembrane proteins and its electrical properties can be accessed. The latter is of particular importance to studies on transmembrane ion transports. In this thesis, electrical impedance spectroscopy is used to quantify peptide-induced permeabilisation of different lipid membranes attached to conducting gold surfaces (see section 3.3.1).

In the past years, various anchor designs have been developed, gradually improving the properties of the model bilayer. First tBLM preparations were hybrid bilayers consisting of only one leaflet of phospholipids and one leaflet of alkanethiols chemisorbed to a thin gold surface [130]. This preparation strategy takes advantage of the strong affinity of metals for sulfur atoms [131] so that the alkanethiols self-assemble as monolayer on the gold surface. The assembly of apolar alkane chains in turn exposes a highly hydrophobic surface which provides an excellent adsorption site for lipid vesicles. The essential disadvantage of this hybrid bilayer design is the lack of an aqueous reservoir between bilayer and substrate which is necessary for the incorporation of membrane proteins. Other design approaches employ macromolecular spacers on top of the solid substrate. These act as soft cushion for the bilayer, lifting it up for a few nanometers. Such tBLM architectures already enable the association of small transmembrane protein fractions but lead to a decrease in the membrane's sturdiness because the membrane is not tethered itself [132].

Lang *et al.* [133] combined the advantageous features of thiol groups (to fixate to metal surfaces) and spacer molecules (to maintain a water reservoir) by synthesising a special class of lipidic anchor molecules, termed thiolipids. These thiolipid tethers comprise short hydrophilic chains in their midsection and are terminated by sulfur groups to the proximal side. The distal side is terminated by hydrophobic chains

which incorporate into subsequent formed bilayers [134]. In this way the hydrophilic tethering chains function as linkers which allow the constitution of a liquid reservoir. Resulting bilayers from such preparations are often referred to as densely tethered bilayer membranes (dtBLMs), since the proximal bilayer leaflet usually consists entirely of tether molecules with only minimal amounts of phospholipids. By contrast, a reduced surface density of tethers leads to the formation of sparsely tethered bilayer lipid membranes (stBLMs). This can be achieved by utilising co-adsorbing anchor molecules which function as hydrophilic backfiller (spacer). Consequently, free phospholipid proportions assemble in the proximal layer [135], both leaflets become more symmetric and the lateral lipid mobility is substantially increased [136]. Furthermore, spacer molecules can stabilise longer tether molecules allowing the increase of the reservoir space between membrane and solid support [137]. Therefore, stBLMs represent a superior platform for the reconstitution of membrane proteins [138]. To which extent protein fractions may span the membrane is directly determined by the design of the tethering unit since the choice of particular molecules or the ratio of tether to spacer molecules strongly influence the structural and electrical properties of a tBLM [139]. Variations of the architecture therefore allow the control of several membrane parameters as for example stability, flexibility or electrical capacitance.

Tethered bilayers are typically formed in two steps: First, the self-assembled monolayer is formed on the substrate surface. The second step can be carried out in two different ways. In the classical procedure small unilamellar vesicles are exposed to the hydrophobic monolayer surface, fuse upon it and form the distal bilayer leaflet. This procedure is rather applicable to the formation dtBLMs and does not allow the formation of stBLMs because the resulting surface of sparsely distributed tethers is too rough. In this work, an alternative strategy, namely a solvent-exchange, was utilised. Within this preparation proposed by Cornell [107], the monolayer is incubated in an organic solution of lipids and the solvent phase is subsequently exchanged by buffer solution, leading to spontaneous bilayer formation. Usually, these bilayers have lower defect densities and higher electrical resistance compared to bilayers from vesicle fusion [134]. The stability of the tethered membrane allows aqueous rinsing to effectively eliminate solvent residues, which may be retained inside the bilayer. This represents an advantage compared to free-standing membranes.

2.2 Sample Preparation

2.2.1 Lipids

Lipids used for reconstituted membrane systems throughout this thesis are listed in table 2.1. DOPC and DOPC/Chol (9:1, n/n) membranes were chosen to model the outer leaflet of eucaryotic human cell membranes. The inner leaflet as well as apoptotic and tumour cells were modelled using DOPC/PS (9:1, n/n) mixtures. While the phosphatidylcholine DOPC has an overall neutral charge due to its zwitterionic headgroup, PS exhibits an anionic headgroup charge due to one amine and one carboxylic group. Thus, PS promotes electrostatic surface interactions. A composition of DOPC/Erg (9:1, n/n) was chosen to mimic fungal cell membranes.

To measure the Förster resonance energy transfer (FRET) between two fluorescent dyes, proportions of 1,2-dihexadecanoyl-sn-glycero-3-phosphoethanolamine (DHPE) attached with one of the fluorescent dyes, (N-(7-nitrobenz-2-oxa-1,3-diazol-4-yl) (NBD) or Lissamine^{TM} Rhodamine B (Rho), were employed. For investigations on the behaviour of lipid rafts upon peptide addition, sphingomyeline was added to DOPC/Chol and DOPC/Chol/PS mixtures for atomic force microscopy (AFM) and X-ray reflectivity (XRR) experiments, because it is well known to form stable liquid-ordered domains in combination with cholesterol [19, 21–23]. DOPC/SM/Chol mixtures were prepared at lipid-to-lipid ratios of 2:2:1 or 9:9:2 (n/n/n) and DOPC/SM/Chol/PS mixtures at 2:2:1:1 or 9:9:2:2 (n/n/n).

Acronym	Substance	Origin
DOPC	1,2-dioleoyl-sn-glycero-3-phosphocholine	synthetic
PS	phosphatidylserine	brain, porcine
SM	sphingomyelin	brain, porcine
Chol	cholesterol	ovine wool
Erg	ergosterol	synthetic
NBD-DHPE	(N-(7-nitrobenz-2-oxa-1,3-diazol-4-yl)-1,2-dihexadecanoyl-sn-glycero-3-phosphoethanolamine	synthetic
Rho-DHPE	Lissamine^{TM} Rhodamine B 1,2-dihexadecanoyl-sn-glycero-3-phosphoethanolamine	synthetic

Table 2.1 – Lipids used in this thesis. NBD-PE and Rho-DHPE were purchased from Life Technologies (Carlsbad, CA, USA), ergosterol was purchased from Sigma-Aldrich (St. Louis, MO, USA). All others were purchased from Avanti Polar Lipids (Alabaster, AL, USA).

For the preparation of stock solutions, lipid components were separately dissolved in organic solvent and mixed in the desired molar ratios. All stock solution were prepared in glass vials with chloroform resistant closures and stored at −20°C.

2.2.2 Buffer

Reconstituted membrane systems in aqueous surroundings were prepared in buffer solutions which mimic different biologically relevant situations. The principal buffer used in this thesis represents a physiological salt concentration that is present in the intracellular space. It contains 100 mM KCl (AppliChem GmbH, Darmstadt, Germany) and 5 mM HEPES (4-(2-hydroxyethyl)-1-piperazine-ethanesulfonic acid; Merck KGaA, Darmstadt, Germany) at a pH of 7.0. Salts, concentrations and pH values varied in some experiments for reasons of stability or to decrease artefacts. All buffers were prepared in ultrapure water (0.055 μS·cm^{-1} at 25 °C; Milli-Q Advantage A10, Millipore, Billerica, MA, USA) and adjusted to pH 7.0 using 1 M KOH solution (Merck). Before use it was sterile filtrated with a 0.22 μm filter (Express^{TM} PLUS, Millipore). For measurements with the Montal-Mueller setup or the film balance, the buffers were exclusively stored in thoroughly rinsed glass bottles to avoid possible contamination from plastic containers.

For the haemolysis assay, a PBS buffer (phosphate buffered saline, Biochrome, Berlin, Germany) was employed. It is comprised of 137 mM sodium chloride, 2.7 mM potassium chloride and 12 mM total-phosphate (HPO_4^{-2} and $H_2PO_e^-$), ensuring a constant pH of 7.4 and resembling physiologic saline solution.

2.2.3 Lipid Membrane Systems

Monolayer

Monolayers were only used for film balance experiments. The lipid films were prepared by spreading 7 μl of a 1 mg·ml^{-1} lipid stock solution in chloroform (Merck) onto the surface of 65 ml buffer solution carried in a Langmuir trough (cf. Sec. 3.4.1). The volatile solvent was allowed to evaporate for 5 min, leaving only lipid molecules at the water/air interface. These were then compressed to a lateral pressure of 20 mN·m^{-1} at which the lateral distribution of lipids resembles a biological membrane leaflet.

Bilayer Membranes

Bilayer membranes (BLMs) were prepared according to the Montal and Mueller technique (cf. Sec. 2.1 and [115]) using the planar bilayer setup described in Sec. 3.3.2.

Each Teflon compartment was filled with 1.5 ml of the standard KCl buffer. 10 μl lipid solution of a 1 mg·ml^{-1} stock solved in chloroform (Merck) were spread onto the buffer surfaces in both compartments. The solvent evaporated, leaving two distinct monolayers at the separated buffer/air interfaces. The buffer levels were raised carefully and subsequently above the aperture which links both chamber compartments. At this juncture, the two monolayers fold up against each other and a bilayer membrane is formed.

Large Unilamellar Vesicles

Liposomes were either directly used (FRET, DLS, CD experiments) or utilised to prepare solid-supported bilayers (see below).

The vesicle solutions were prepared from stock solutions of 10 mg·ml^{-1} lipid in chloroform (Merck). The solvent was evaporated under a gentle stream of nitrogen gas and the remaining lipids were resuspended in buffer solution. The total lipid concentration used for a particular experiment is given in respective experimental sections. LUVs were obtained by sonicating the lipid solutions with a tip sonicator (HTU-SONI 130, G. Heinemann, Schwäbisch Gmünd, Germany) for two minutes per 200 - 250 μl sample volume at a constant output amplitude of 30 %. To obtain (almost) uniform vesicle sizes, the LUV solutions were equilibrated by subsequent cooling to 4 °C (for 30 min) and heating to 60 °C (for 30 min). This temperature sequence was repeated three times in total, before samples were stored at 4 °C for at least 24 h.

Solid-Supported Bilayer

Solid-supported bilayer membranes were examined by X-ray reflectivity and by AFM. For both applications, the bilayers were prepared from the LUV solutions described above.

For X-ray reflectivity measurements, silicon-(111)-wafers with a thickness of 500 μm (Silchem, Freiberg, Germany) cut to rectangular chips with lateral dimensions of 10 $\times$ 15 mm^2 served as substrates. The chips were cleaned by subsequent and repeated sonication in methanol and ultrapure water (three times, each step for 10 min) and finally dried with a stream of nitrogen gas. Shortly before the sample deposition, the thin native oxide surface of the silicon substrate was rendered hydrophilic by exposing it to an air plasma (generated by the plasma cleaner PDC-002 from Harrick Plasma, Ithaca, NY, USA) for 2.5 min where the formation of silanol groups is promoted [140]. The substrate was assembled to the sample chamber (for a description of the sample chamber see Sec. 3.5.4), where the bilayer was prepared

by spreading 200 μl vesicle solution (1 mg·ml^{-1}) onto the wafer. After an incubation period of 20 min, 2 ml buffer solution was added. The aqueous volume was rinsed for at least five times with each 1 ml buffer to remove remaining lipids from the solution.

For the AFM experiments on the domain behaviour, LUV solutions of molar mixtures of either DOPC/SM/Chol (2:2:1) or DOPC/SM/Chol/PS (2:2:1:1) at 1 mg·ml^{-1} were prepared 24 h prior to the bilayer preparation. Rectangular Mica platelets of about 20 × 30 mm^2 glued onto the bottom of a petri dish served as substrates. Prior to the bilayer preparation, these were thoroughly rinsed with ethanol and the uppermost mica layer was cleaved using customary cellotape. 2850 μl buffer solution and 150 μl vesicle solution were added onto the substrate. The dish was sealed to prevent evaporation and incubated for at least 12 hours with gentle shaking. Finally, the solution was thoroughly rinsed (at least 15 times with 1 ml buffer) to remove lipids which are not immobilised on the mica surface.

Solid-Supported Multilayers

Solid-supported multilayer samples were employed for the X-ray diffraction and the OCD measurements. The samples were prepared similar to a protocol first described by Seul and Sammon [126]: 10 mg·ml^{-1}-stocks of lipid or lipid/peptide in organic solvent were spread onto a flat substrate. Evaporation of the solvent and rehydration of the lipids then yields bilayers stacked on top of one another.

For X-ray diffraction experiments, these stocks were prepared using a 1:1 (v/v) mixture of chloroform and 2,2,2-trifluoroethanol (TFE, Carl Roth, Karlsruhe, Germany) since this mixture has been found to generate lipid films with only a small number of defects [141]. An aliquot of 80 μl was then spread onto the cleaned, hydrophilic silicon substrate described in the previous subsection. The solvent was allowed to evaporate slowly ($\sim$ 20 min) to prevent film rupture. Subsequently, it was kept under medium vacuum for at least 12 h to ensure complete solvent removal. Prior to the measurements, the sample was assembled with the teflon chamber described in the X-ray instrumentation section 3.5.4. Inside the chamber, the sample was rehydrated at room temperature for a few hours ($\simeq$ 3 h and $\simeq$ 8 h for experiments at I07 and P08, respectively) in a saturated water atmosphere generating partial hydration. During this equilibration process, the lipids spontaneously assemble as stack of typically $\sim 10^3$ bilayers aligned parallel to the silicon surface. For OCD measurements, the lipid and lipid/peptide stocks were solved in a 1:1 (v/v)

mixture of chloroform and methanol (Merck, Uvasol®-quality[2]). The amount of peptide and lipid was limited to 4.5 - 6.5 μg and 25 - 200 μg, respectively, ensuring a detectable CD signal range while keeping the sample thickness as small as possible to avoid artefacts caused by absorption or linear dichroism [142]. 5 and 1 mg·ml^{-1} stock dilutions were used to deposit respective aliquots of $\sim$ 30 - 40 μl onto a quartz glass plate (Suprasil QS, Hellma Optik GmBH, Müllheim, Germany). Beforehand, the quartz glass windows were cleaned in concentrated nitric acid, extensively rinsed with ultrapure water and finally rinsed with ethanol, before they were dried in an oven at 50°C. In the spreading process it is of extremely high importance to achieve an equal distribution of the sample material within a circular spot size of $\sim$ 12 mm in diameter. To this end, a solvent mixture of chloroform/methanol was chosen since its spreading behaviour is better controllable than that of the chloroform/TFE mixture which tends to transport a high portion of sample material to the outer rims. After the samples appeared dry, they were stored under vacuum (2 mbar) for not less than two hours to remove possible solvent residues. Full hydration of a sample was reached by assembling it into the OCD cell where it was kept for at least eight hours at 25°C and 97 % relative humidity, generated by saturated K_2SO_4 solution.

Tethered Bilayer Membranes

The stBLM design used for the impedance spectroscopy was first described by Cranfield and co-workers [143]. The tethering unit applied comprised 10 % tether and 90 % spacer molecules, so that sparsely tethered membranes formed upon it allow reconstitutions of membrane-embedded protein fractions with molecular masses up to 40 kDa. The membranes themselves have been found to be stable for up to three months [143]. Benzyl-disulfide-octo-ethylene-glycol-phytanyl was utilised as tether molecule. Its terminating hydrophobic phytanyl chain incorporates into the inner leaflet of the bilayer assembly. The spacing between these tethers was obtained by benzyl-disulfide-tetra-ethylene-glycol with a hydrophilic hydroxy-termination. Both molecule species have benzyl disulfide groups which accomplished the attachment to the gold surface of the substrate used. This combination of molecules extends the available space in the reservoir between the bilayer and the substrate since the spacer molecules are only half as long as the tether molecules. For that reason, the mobility of ions within the reservoir is increased and steric interferences, which might arise from extramembraneous parts of membrane proteins, are relieved.

[2]For OCD measurements it is of high importance to avoid any kind of contamination that could influence the spectroscopic properties of the sample. For that reason, these high quality solvents were used here.

Tether:

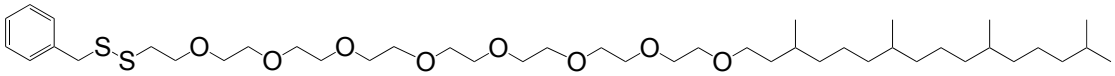

Spacer:

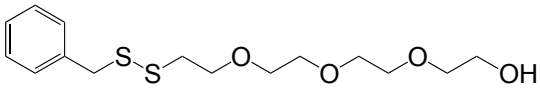

Figure 2.2 – Molecular structure of the tether and spacer molecules. Benzyl-disulfide-octo-ethylene-glycol-phytanyl was used to anchor the membrane to a gold surface and benzyl-disulfide-tetra-ethylene-glycol with a hydrophilic hydroxyl head was utilised as spacer. The ratio of tethers to spacers used in the present thesis is 1:9.

The preparation procedure of stBLMs followed the one described in reference [143]. Bilayers were formed on slides upon which the described tethering unit is already pre-prepared, occupying an area of 2.1 mm^2 (SDx T-10 tethaPlate^{TM}, SDx Tethered Membranes Pty Ltd., Sydney, Australia). Beforehand, these slides were assembled to the tethaPlate^{TM} cartridge which provides six 1 μl flow-cell chambers, each connected to a liquid storage chamber of 500 μl. After the plate assembly, aliquots of 8 μl from 3 mM lipid stocks dissolved in ethanol (ethanol abs., Merck) were pipetted onto each flow-chamber and incubated for two minutes at 37°C. 93.4 μl buffer solution (100 mM KCl, 5 mM HEPES, pH 7.0) were added before the flow-chamber was rinsed three times with 100 μl buffer to eliminate ethanol residues. The resulting distance between gold substrate and lower bilayer leaflet is 2 - 2.5 nm [144].

2.3 Peptides

Altogether, seven different peptide variants were used throughout the present work. While Ece1-$III_{KR(N)}$ with an amidated C-terminus was studied with all techniques described in the following, its non-amidated isoform Ece1-$III_{KR(C)}$ was only used at some points for comparison. Likewise, the amidated Ece1-$III_{AA(N)}$ and non-amidated Ece1-$III_{AA(C)}$, the shorter non-amidated peptide variants Ece1-$III_{K(C)}$ and Ece1-$III_{A(C)}$ were employed to elucidate the influence of varying C-termini critical to the peptide function. A rhodamine-labelled version of Ece1-III_{KR} (Rho-Ece1-$III_{KR(N)}$) was used in a FRET assay (see Sec. 3.2.3) to study the binding of Ece1-$III_{KR(N)}$ to liposomes.

2.3.1 Synthesis

Peptides with an amidated C-terminus and Rho-Ece1-III_{KR} were synthesised by Rainer Bartels (Research Center Borstel, Germany) using standard solid-phase Fmoc

protocols [145]. The material was purified by reversed-phase high performance liquid chromatography. Peptides without C-terminal amidation were synthesised similarly. These were kindly provided by Bernhard Hube (Hans Knöll Institute, Jena, Germany) and Julian Naglik (King's College London, UK).

Peptide	C-terminal motif	Number of amino acids	Molecular mass [g · mol^{-1}]	Net charge at pH 7.0
Ece1-III$_{KR(C)}$	KR-COOH	32	3466.4	+4
Ece1-III$_{KR(N)}$	KR-CONH$_2$	32	3465.4	+5
Rho-Ece1-III$_{KR(N)}$	KR-CONH$_2$	32	3877.8	+5
Ece1-III$_{K(C)}$	K-COOH	31	3292.2	+3
Ece1-III$_{AA(C)}$	AA-COOH	32	3324.2	+2
Ece1-III$_{AA(N)}$	AA-CONH$_2$	32	3323.2	+3
Ece1-III$_{A(C)}$	A-COOH	31	3235.1	+2

Table 2.2 – Peptides used in this thesis. The table summarises the relevant features and differences of the employed peptide variants.

2.3.2 Peptide Stock Solutions

The peptides were dissolved in ultrapure water at a concentration of 1 mg·ml^{-1} for FRET assays. For the preparation of solid-supported multimembrane systems (section 2.2.3), purified and lyophilised peptides were dissolved in a chloroform/TFE (1:1, v/v) mixture at a concentration of 10 mg·ml^{-1}. For some impedance spectroscopic experiments, the non-amidated peptide isoforms were dissolved in H_2O with a proportion of 40 % DMSO (dimethyl sulfoxide, v/v) since these isoforms show improved solubility in this system. All other peptide stocks were prepared in 0.01 % (v/v) trifluoroacetic acid (TFA, Riedel-de Haën, Seelze, Germany) at concentrations of 1 mg·ml^{-1} or 1 mM, respectively.

2.3.3 Solubility

Ece1-III$_{K(C)}$, Ece1-III$_{AA(C)}$ and Ece1-III$_{A(C)}$ did not readily solve in one of these solutions. To support the solvation processes, the respective stocks were thoroughly vortexed until the solutions mostly cleared up. A successful solvation was confirmed by inspection with the eye. Some results suggest that the peptide monomers tend to cluster in solution. This is for example the case for the CD spectra presented in Section 5.2.1. The results given there indicate that the peptide solubility is impaired by the salt concentration of the buffer applied.

3 Applied Biophysical Methods

Despite the usage of model membranes, the characterisation of lipid-peptide interactions remains a complex obstacle. There is a wide range of techniques combining biological, chemical and biophysical principles that have been established to study the fundamental mechanisms, dynamics and structural consequences. Depending on the particular principle, each of these methods can provide distinctly different insights into the molecular interaction processes. To highlight the capabilities of the biophysical methods applied throughout this thesis, this section briefly summarises them and describes their experimental implementation. Additional information on a particular method can be obtained from the referred literature.

3.1 Techniques based on Light Scattering

3.1.1 Dynamic Light Scattering

The technique of dynamic light scattering (DLS) is used to obtain size distributions of small particles in aqueous solution, based on the relation between Brownian motion and particle size. With this method the size of hydrodynamic liposomes up to 6 μm can be determined.

Relating Brownian Motion to Particle Size Distributions

Light rays that impinge on small particles will be scattered by the particles. Due to the random positions of the scattering centres in a liquid, the light scattered from a particle ensemble in solution will cause a speckled interference pattern on a detector placed at the scattering angle 2θ. This pattern fluctuates as a consequence of Brownian motion and the fluctuation rate provides information on the particle's size as both can be related by the Einstein-Smoluchowski equation:

$$D = \mu k_B T.$$

D denotes the diffusion coefficient, k_B Boltzmann's constant, T the absolute temperature and μ describes the particle's mobility. For fluids with low Reynold numbers,

i. e. in laminar flow situations, the mobility equals the inverse drag coefficient γ. Stoke's law gives

$$\gamma = 6\pi\eta r \tag{3.1}$$

for spherical particles of radius r in a fluid of viscosity η. Finally, the Stokes-Einstein equation

$$D = \frac{k_B T}{6\pi\eta r} \tag{3.2}$$

can be derived, providing the relation between diffusion and particle radius. Information on the particle diffusion in a dispersant with refractive index n_L is experimentally obtained from the intensity fluctuations of light scattered with wavelength λ at a particular scattering angle 2θ, i. e. with the momentum transfer $q = (4\pi n_L/\lambda)\sin\theta$. With the intensities I at certain time points t and delayed time points $t + \delta t$, the second-order autocorrelation function $g^{(2)}(q, \delta t)$ is generated by multiplying and arithmetically averaging these intensities:

$$g^{(2)}(q, \delta t) = \frac{\langle I(q,t) I(q, t+\delta t)\rangle}{\langle I(q,t)\rangle^2}.$$

After a very short time period t from the initial state, the correlation is maximal because the particles were only able to move a short distance. The correlation decays exponentially for longer time periods because the particles move further away from their initial positions and the intensity patterns lose their correlation. In addition, the decay time scale depends on the particle size: small particles show a fast relaxation, whereas for large particles correlation is maintained for a longer time. In the limit of small scattering angles and monodisperse sample solutions the decay consists of one exponential term:

$$g^{(2)}(q, \delta t) = B + \beta[g^{(1)}(q, \delta t)]^2 = 1 + \beta e^{-2Dq^2\delta t},$$

whereby the Siegert relation gives the connection between second-order $g^{(2)}(q, \delta t)$ and first-order autocorrelation $g^{(1)}(q, \delta t)$ [146]. β denotes a constant term which depends on the experimental geometry. The absolute factor B is the baseline or long-term value of $g^{(2)}(q, \delta t)$. Theoretically, it should be unity but due to instrumental noise its value usually deviates slightly. The factor Dq^2 corresponds to the mean relaxation rate τ^{-1} $(= \Gamma(q))$ of the intensity fluctuations. In polydisperse solutions and for larger scattering angles $g^{(1)}(q, \delta t)$, the correlation decay gets more complex

and $g^{(1)}(q, \delta t)$ can be described as superposition of different exponential relaxation times τ, or a distribution of different relaxation rates $G(\Gamma(q))$

$$g^{(1)}(q, \delta t) = \int G(\Gamma(q)) e^{-\Gamma(q)\delta t} \, \mathrm{d}\Gamma(q),$$

where $G(\Gamma(q))$ is normalised so that

$$\int_0^\infty G(\Gamma(q)) \, \mathrm{d}\Gamma(q) = 1.$$

Eventually, $G(\Gamma(q))$ has to be extracted from the experimental data of $g^{(2)}(q, \delta t)$ or $g^{(1)}(q, \delta t)$, respectively, in order to extract information on the diffusion processes and thus on the size populations. This is an ill-posed problem but different approaches have been developed to solve this issue [147, 148]. One of the simplest ways to characterise sufficiently narrow distributions $G(\Gamma(q))$ properly, is the method of cumulants first proposed by Koppel [149]. Basically, this approach expands the logarithm of $g^1(q, \delta t)$ in terms of the cumulants of the distribution to obtain a polynomial in the delay time that allows least-square fitting. With the basic assumption of a baseline value of 1, the cumulant series leads to:

$$\ln[g^{(2)}(q, \delta t) - 1] = \ln \frac{\beta}{2} - \frac{\kappa_1(q)}{1!}\delta t + \frac{\kappa_2(q)}{2!}\delta t^2 - \frac{\kappa_3(q)}{3!}\delta t^3 + ...$$

Herein, the first cumulant $\kappa_1(q)$ describes the average decay rate of the distribution $\bar{\Gamma}$

$$\kappa_1(q) = \int_0^\infty G(\Gamma(q))(\Gamma(q) - \bar{\Gamma}(q)) \, \mathrm{d}\Gamma(q) \equiv \bar{\Gamma}(q).$$

The averaged particle size can then be derived from $\bar{\Gamma}(q)$ with Eq. 3.2. $\kappa_2(q)$ gives the variance of the distribution $G(\Gamma)(q)$ and $\kappa_3(q)$ is a measure of its asymmetry [150]. Note that the particle radius obtained by DLS measurements is always the size of a sphere that moves like the scatterer. For vesicle in solution, this is a hydrodynamic radius that includes molecules electrostatically adhered to the vesicle surface (cf. section 3.1.2).

Experimental Implementation

The avoidance of any contamination through dust particles is of high importance for DLS measurements. Therefore, all aqueous solutions were sterile filtrated prior to use. SUV stocks at a total concentration of 2 mM were prepared in 100 mM KCl and 5 mM HEPES at pH 7.0. A set of 1 ml samples with 50 μM lipids, 10 mM KCl and 0.5 mM HEPES was diluted from the stock using appropriate amounts of buffer solution and ultrapure water. This dilution had to be carried out for the subsequent

measurements of the zeta potential described in the following section (Sec. 3.1.2). Folded capillary sample cells (DTS1070, Malvern Instruments Ltd, Worcestershire, UK) were used and thoroughly rinsed with ethanol and pure water. Diluted lipid suspensions were then filled into the sample cell and reused afterwards for peptide-titration measurements. Therefore, the sample solution was taken out of the cell and an according peptide aliquot from a 150 μM stock in 0.01 % TFA (v/v) solution was added before the sample cell was refilled again. DLS measurements were performed using Malvern's Zeta Sizer Nano ZS (Malvern Instruments Ltd.) equipped with a laser which emits monochromatic light at a wavelength of 532 nm. The instrument has the capability to detect particle sizes in a range of 0.6 nm - 6 μm. The scattered intensity was analysed at a backscatter angle of $2\theta = 173°$, the results presented are averages from three subsequent acquisition cycles of 13 acquisitions with 10 s each. The refractive index n and the viscosity η of the dispersant were approximated by known values for 40 mM HEPES solution ($n_S = 1.331$, $\eta = 0.8417$ mPa·s), the refractive index of the suspended material was approximated with the one of polystyrene latex ($n_M = 1.59$).

The internal software of the zeta sizer instrument determined the averaged particle diameter of the sample population by least-square fittings to the logarithmic correlation function according to the cumulant method. Cumulant orders higher than second-order were neglected to avoid over-determination of the data which would result in less precise determinations of all fitting parameters. The polydispersity index (PDI) defined as $2\kappa_2\bar{\Gamma}(q)^{-2}$ was given as measure of the width of the size distribution. Note that this analysis procedure did not give reliable particle sizes for highly polydisperse samples with polydispersity indices exceeding a value of 0.5. All measurements were performed at a temperature of 25°C.

3.1.2 Zeta Potential

The zeta potential is commonly used to characterise the surface potential of charged particles in solution relative to the surrounding solvent phase. It can be deduced from the particles' velocity in an electric field.

The Electrochemical Double-Layer

In aqueous solution, particles with non-zero surface potential Φ_0 attract counter ions or dipoles from the solvent phase that compensate the charge. As consequence, a characteristic electrochemical double-layer is formed, consisting of one layer with counter ions tightly adsorbed to the particle surface (Stern layer) and a moveable, diffuse ion layer which loosely encases the Stern layer (Gouy-Chapman layer). The

electrically neutral bulk solvent is adjoined once the potential Φ dropped to zero. The characteristic thickness of the double-layer is given by the Debye length κ^{-1} which solely depends on the properties of the solution and notably not on any property of the charged surface. For solutions containing different types of ions i, κ^{-1} is described by

$$\kappa = \sqrt{\sum_i \frac{\rho_{\infty,i} e^2 z_i^2}{\varepsilon k_B T}} \tag{3.3}$$

where z_i gives the valency of the respective ion type, k_B denotes Boltzmann's constant, e the elementary charge and T the temperature. $\varepsilon = \varepsilon_r \varepsilon_0$ is the product of the dielectric constant of the dispersion medium and the permittivity of free space. The parameter $\rho_{\infty,i}$ defines the ionic concentration in the bulk, i. e. where $\Phi = 0$, as number density (molecules per cubic metre).

Upon the particle's movement, the diffuse layer is partly cast off due to friction and another boundary plane is exposed: the hydrodynamic shear or slipping plane. The potential ζ at this plane is called zeta potential.

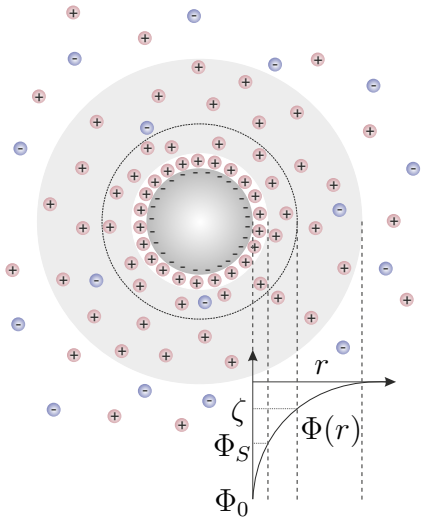

Figure 3.1 – Schematic illustration of the potential $\Phi(r)$ in the vicinity of a spherical particle with negative surface charge in solution. Counter ions from the saline medium adhere tightly to the particle's surface and form the Stern layer. At the edge of the Stern layer, the surface potential Φ_0 has dropped to Φ_S. With increasing distance r, the surface charge is further screened by weak attractions of ions until the potential drops to zero at the edge of the Gouy-Chapman layer. Upon motion this diffuse layer is partly lost and the potential at the resulting shear plane is defined as zeta potential ζ.

Although the zeta potential does neither equal the potential at the actual particle surface nor the potential at the Stern layer, it is often the only experimentally accessible quantity which provides information on the double-layer. Using Henry's

equation, the zeta potential can be obtained from the electrophoretic mobility μ_e of the particle or its drift velocity ν in an electric field of strength E:

$$\zeta = \frac{3\mu_e\eta}{2\varepsilon f(ka)} = \frac{3\nu\eta}{2\varepsilon E f(ka)}, \tag{3.4}$$

with η denoting the dynamic viscosity coefficient. $f(ka)$ is Henry's function, which is usually approximated by two values: either 1.0 or 1.5. The first value is used in Hückel approximation for small particles in media with low dielectric constant, whereas the value of 1.5 refers to the Smoluchowski approximation for electrophoretic determinations in aqueous solution at moderate electrolyte concentrations ($> 10^{-3}$ M salt). The Smoluchowski approximation results in

$$\zeta \approx \frac{\mu_e\eta}{\varepsilon} = \frac{\nu\eta}{\varepsilon E} \tag{3.5}$$

and is only valid in the limit of particle sizes that are much larger than the thickness of the double-layer [151]. The drift velocity is detected by laser Doppler velocimetry where the Doppler shift in a beam scattered from moving particles is compared to a reference beam.

Experimental Implementation

Measurements of the zeta potential were carried out subsequent to DLS measurements with the same instrumentation and samples as described in the respective section. The relatively high ionic strength of the standard buffer (conductivity $\simeq$ 12 mS/cm) would cause Joule heating. Therefore, it would affect the mobility and integrity of the dispersed particles [152] and induce degradation of the sample electrodes. Thus, the standard buffer was diluted at a ratio of 1:10 resulting in a salt concentration of 10 mM KCl and 0.5 mM HEPES at pH 7.0. The dielectric constant of the dispersant was also approximated with the known constant for 40 mM HEPES solution ($\varepsilon = 78.5$). The zeta potential was averaged from six acquisition cycles of 20 measurements at 3 s acquisition time each. The potential applied within the acquisition procedure was set to 15 V. With an ionic concentration of 10 mM KCl, i. e. $\rho_{\infty,\mathrm{KCl}} = 0.01\ \mathrm{mol}\cdot\mathrm{l}^{-1} = 10\ \mathrm{mol}\cdot\mathrm{m}^{-3} = 10\cdot 6.022\cdot 10^{23}\ \mathrm{m}^{-3}$, the Debye length κ^{-1} (Eq. 3.3) results in approximately 3 nm at 25°C, which is considerably smaller than the lipid vesicles ($\sim$ 100 nm). Correspondingly, Smoluchowski approximation (Eq. 3.5) was used to determine a mean value of the zeta potential.

3.2 Spectroscopic Techniques

3.2.1 (O)CD Spectropolarimetry

Circular dichroism (CD) spectropolarimetry is a special variant of absorption spectroscopy. For this technique, the absorption difference of left- and right-handed circularly polarised light of optically active molecules is used to investigate the conformation and structure-related changes of biomolecules [153–156]. Furthermore, the effect of circular dichroism can be used to probe the alignment of secondary structure elements in lipid arrays.

Circular Dichroism

Absorption processes in the UV/VIS spectral range are primarily given by electronical transitions from the ground state to an energetically higher, excited state. Such an excitation represents a charge displacement inside the molecule which usually involves a change in the electric dipole moment $\vec{\mu}_0$. Considering the dipole moments of both, ground 0 and excited j state, quantum mechanical perturbation theory allows the calculation of the electric transition dipole moment $\vec{\mu}_{0,j}$ to quantify the interaction between molecule and electrical component of an electromagnetic wave. Another quantity used to describe the possibility of electronic transitions is given by the integral over the wavelength-dependent extinction signal ε_λ, known as oscillator strength. Carbonyl groups have an intense absorption band around 190 nm, expressing a high oscillator strength for the electronic transition from the occupied, bonding π orbital to the unoccupied, antibonding π^* orbital (cf. Fig. 3.2). The absorption band associated to the transition of the nonbonding n oribital to π^* around

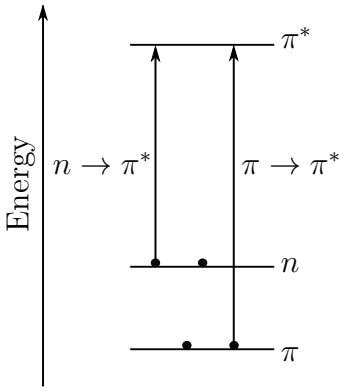

Figure 3.2 – Energy levels of the molecular orbitals of a carbonyl group and possible electronic transitions from the occupied π and n orbitals (ground state). The relations between wavelength and frequency is given in Sec. 3.5.1.

222 nm is less intense, since the overlap of the wave functions of both orbitals is significantly reduced and therefore oscillator strength and $\vec{\mu}_{0,j}$ shrink.

The charge displacement induced by the interaction of a valence electron and light can be understood as oscillatory dipole which also induces a magnetic dipole moment $\vec{m}_{0,j}$. While the electric dipole $\vec{\mu}_{0,j}$ describes a linear displacement, $\vec{m}_{0,j}$ characterises a charge circulation. The combination of both leads to a light-induced current loop. If $\vec{m}_{0,j}$ has a component parallel to the electric dipoles, this loop involves a helical charge displacement that in turn results in different extinction coefficients ε_λ for light with different polarisation. The special case of the difference $\Delta\varepsilon_\lambda$ between left- and right-handed circularly polarised light describes the phenomenon of circular dichroism.

$$\Delta\varepsilon_\lambda = \varepsilon_{\lambda,L} - \varepsilon_{\lambda,R} \tag{3.6}$$

Analogous to the oscillator strength of ordinary absorption, the integral over $\Delta\varepsilon_\lambda$ of a particular transition is then referred to as rotational strength. This optical activity is inherently exhibited by all molecules that are not equipped with a centre or plane of symmetry. Among them are all amino acids (except for glycine) due to their asymmetric α-carbon to which four different substituents are attached. However, optical activity of chromophores can also be induced by asymmetric environments. In peptides, this can be achieved through the formation of a secondary structure which fosters the coupling of carbonyl groups of neighbouring peptide bonds. Thus, α-helices or β-sheet motifs additionally contribute to the peptide's intrinsic optical activity owing to their amino acids and give rise to characteristic CD spectra in the far-UV region (180 - 250 nm). As shown in Fig. 3.3, an α-helical peptide backbone causes two distinct minima around 208 and 222 nm and a maximum at

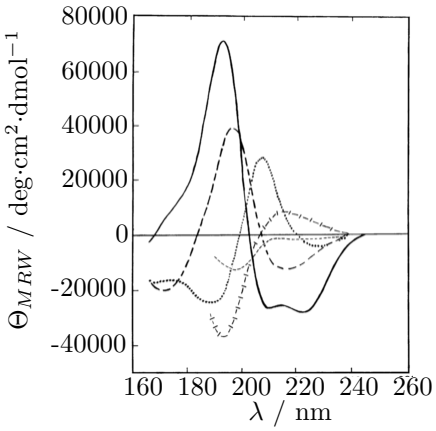

Figure 3.3 – Far-UV CD spectra of various types of secondary structure. Shown are line shapes of the following elements: α-helix (solid line), anti-parallel β-sheet (long dashed line), type I h-turn (dotted line), extended 3_1-helix or poly-(Pro)-II helix (cross dashed line) and random coil (short dashed line). Taken from [157] with permission.

195 nm, whereas β-sheet confirmations lead to a positive peak at 198 nm and one single minimum around 216 nm. Peptides without a specifically structured peptide backbone result in a minimum around 199 nm [157, 158].

Oriented Circular Dichroism

Moffitt's theory predicts that the transition dipole moments $\vec{\mu}_{\pi,\pi^*}$ of amide chromophores in a helix are polarised either parallel or perpendicular to the longitudinal helix axis [159, 160]. Hence, the absorption bands of α-helical peptides depend on the angle between helix axis and the direction of incident light causing distinct orientation-dependent CD spectra. For peptides embedded in arrays like lipid matrices, this effect can be utilised to explore the peptide's orientation with respect to the array reference frame. The method that arose from this principle is called oriented circular dichroism (OCD) [161, 162]. Olah and Huang have shown that the CD band around 208 nm is associated to a polarisation parallel to the α-helical axis [163]. Accordingly, the interaction of the transition dipole moments and the electric field $\vec{E}$ of the polarised light gets maximal if both are in parallel, and so does the CD band at 208 nm if $\vec{\mu}_{\pi,\pi^*}$ lies in the plane of rotation of $\vec{E}$. On the contrary, the band diminishes if the helix is oriented perpendicular to $\vec{E}$, showing no optical activity for this transition. In other words, if the light incidences perpendicular onto the surface of a lipid membrane, the presence of the negative CD band around 208 nm shows that the peptide is aligned parallel to the lipid surface (S-state). The absence of the band would thus point out that the peptide is aligned along the membrane normal (inserted I-state). Any other orientation would cause OCD spectra that reflect linear combinations of these extreme spectra [164].

Quantification of the Circular Dichroism

As circularly polarised light will have elliptical polarisation after its passage through an optically active sample, circular dichroism is usually expressed as ellipticity Θ which is defined by

$$\tan(\Theta(\lambda)) \;=\; \frac{I_R(\lambda) \;-\; I_L(\lambda)}{I_R(\lambda) \;+\; I_L(\lambda)},$$

where $I_R(\lambda)$ and $I_L(\lambda)$ denote the attenuated intensities of right- and left-handed circularly polarised light. The intensities are connected to the extinction coefficients via Lambert-Beer's law, which describes the exponential intensity decay along the travel path d:

$$I(d) = I_0 \; e^{-\mu \cdot d} = I_0 \cdot 10^{-\varepsilon_\lambda \cdot c \cdot d}. \tag{3.7}$$

Herein, I_0 represents the initial intensity, c the speed of light and μ the absorption coefficient which relates to the extinction coefficient according to $\mu = 2.303 \cdot \varepsilon_\lambda \cdot c$. Using Lambert-Beer's law and a taylor series, the ellipticity derives to

$$\Theta(\lambda) \;=\; \ln(10) \cdot \frac{180^\circ}{4\pi} \cdot (\varepsilon_{\lambda,L} \;-\; \varepsilon_{\lambda,R}) \cdot c \cdot d \;\approx\; 32.98\ \Delta A$$

for small values of Θ with ΔA representing the differential absorbance. To decouple the ellipticity signal (given in degrees) of CD signals of solutions from its dependence on the sample's molar concentration c and the path length d, the molar ellipticity Θ_{mol}

$$\Theta_{mol}(\lambda) \;=\; \frac{\Theta(\lambda)}{c \cdot d}$$

is defined which scales to both. The CD data can also be normalised by scaling it to the peptide's repeating unit represented by the peptide bond. This step is required if absolute values of CD spectra shall be compared, regardless of the distinct peptide sequence. The ellipticity relating to the mean residue weight ($MRW = (M/(N-1))$ of the peptide bonds is thus calculated from

$$\Theta_{MRW}(\lambda) \;=\; \frac{\theta(\lambda) \cdot M}{c_m \cdot d \cdot (N-1)}, \tag{3.8}$$

where M is the molecular mass of the polypeptide chain, N is the number of amino acids in the chain and c_m the mass concentration of the peptide in solution (in $\mathrm{g{\cdot}l^{-1}}$). The typical unit in which mean residue ellipticity and molar ellipticity are given is $\mathrm{deg{\cdot}cm^2{\cdot}dmol^{-1}}$. A peptide with a perfectly ordered α-helix would result in a minimum of approximately $\Theta_{MRW} = -30\,000\ \mathrm{deg{\cdot}cm^2{\cdot}dmol^{-1}}$ at 222 nm [158]. However, in reality only a certain proportion of the amino acids constitute as α-helix or β-sheet and CD spectra always reflect the overall conformation of the peptide structure. The relative content of each standard structure type can be calculated by a number of algorithms [165–168]. To obtain reliable results, an accurately determined protein concentration is an inevitable prerequisite.

In conclusion, it shall be emphasised that (O)CD spectropolarimetry represents a low-resolution method which does not provide detailed information on microenvironments such as the interaction of individual amino acids but can be used as a powerful tool to investigate secondary structures (and their orientations) of soluble or membrane bound peptides. It reflects the averaged signal arising from the overall peptide conformation with relatively low effort, small necessary sample amounts and short acquisition times compared to high-resolution methods such as nuclear magnetic resonance experiments or X-ray crystallography [157, 164, 169, 170].

Experimental Implementation

Circular Dichroism of Peptides in Solution Isotropic CD data of peptides in solution were acquired with a Jasco J-720 CD spectropolarimeter (Jasco, Easton, MD, USA) using a quartz glass cuvette with 1 mm path length (Hellma Optik GmBH, Müllheim, Germany). The instrument was calibrated using a standard solution of camphorsulphonic acid (CSA). The spectra were measured from 250 to 190 nm in steps of 1 nm at a scanning speed of 20 nm·s^{-1} with 8 s response time. The bandwidth was confined to 2 nm. For each spectrum, at least four spectra of Θ were accumulated and averaged to improve the signal-to-noise ratio. Spectra were collected for pure peptide solution (200 μl 0.1 mg·ml^{-1} in 0.01 % (v/v) TFA) and a mixture of peptide/lipid solution (200 μl peptide solution + 80 μl 1 mg·ml^{-1} in 100 mM KCl, 5 mM HEPES, pH 7.0). Reference spectra of 0.01% TFA (v/v) or 0.01% TFA:buffer (2.5:1, v/v) solution were subtracted subsequently. Afterwards, the mean residue ellipticity Θ_{MRW} was calculated using Eq. 3.8 and the data was smoothed using the Savitzky-Golay algorithm [171] provided by the `scipy.signal` library for Python (Python Software Foundation. Python Language Reference, version 2.7. Available at http://www.python.org). For this processing, a filter window of 15 and a quadratic polynom were applied. Estimates of the secondary structure were obtained using the K2D program [172] with a fit algorithm premised on neuronal networks and provided by the Dichroweb server [173–175]. This program provides a data base of weights. Based on these weights, it determines α-helical and β-sheet structure elements with input data from 240 to 200 nm. The advantage of K2D is that it gives good estimates even though only CD data with a limited wavelength range are available [154]. However, due to the appearance of different artefacts, which are discussed in the respective result sections, peptide conformation and structural changes were predominantly evaluated qualitatively.

Circular Dichroism on Oriented Peptides Multilamellar lipid and lipid/peptide samples on a quartz glass window were prepared according to the protocol described in section 2.2.3. Together with a second window, it was assembled into an OCD cell that enabled controlled settings for temperature and humidity. Partial hydration of 97 % relative humidity (rH) of the lipid samples was achieved by a saturated K_2SO_4 atmosphere. The optical path of the cell is along its vertical (rotationally symmetric) axis. Hence, once adapted to a spectropolarimeter, the polarised beam incidences perpendicularly onto the quartz glass and bilayer surfaces. Detailed information on the cell design is given in [170].

The OCD measurements presented in this work were partly carried out using a J-810 benchtop spectropolarimeter (Jasco) and partly using UV-CD12 beamline

at the synchrotron source ANKA (Karlsruhe Institute of Technology, Germany). Compared to the benchtop spectropolarimeter, which is equipped with laser light, the synchrotron-based OCD (SR-OCD) instrumentation provided a tremendously higher photon flux. This high flux enhanced the signal-to-noise ratio especially for wavelengths smaller than 200 nm, thereby allowing a threefold decrease in acquisition time [176]. Another advantage of the UV-CD12 end station was the 4.3-fold smaller beam size (h×v: 2.5 mm × 4.8 mm) compared to the conventional spectropolarimeter (h×v: 4 mm × 13 mm). Thus, the synchrotron beam only hits the more homogeneous central area of the sample, whereas measurements with J-810 also include the rather inhomogeneous outer rims of the sample. A detailed description of the UV-CD12 beamline is presented in Bürck *et al.* [176]. In the present work, a P/L series of Ece1-III$_{\mathrm{KR(N)}}$ in DOPC membranes was measured at the synchrotron station. Measurements with the peptide and lipid variants were carried out at the benchtop instrument with the same sample cell.

The SR-OCD spectra were collected in the range of 270 - 180 nm with a stepwidth of 0.5 nm. The spectral bandwidth was kept constant to 1 nm. Lock-in and dwell time were set to 300 ms and 1.5 s, respectively, resulting in a scan rate of 15 nm·min^{-1}. One spectrum is averaged from spectra acquired at different rotation angles of the sample cell, starting from 0° in steps of 45° to 315°. This procedure is necessary to eliminate spectral artefacts caused by linear dichroism and birefringence from imperfections of the sample or the quartz glass plate [162, 177]. The collected eight spectra were averaged and a pure lipid spectrum obtained similarly, but with 0.5 s dwell time and a scan rate of 34 nm·min^{-1}, was subtracted to get the peptide spectrum. Finally, a Savitzky-Golay filter was applied as described above for solution-CD data. The high voltage $HT_{S,R}$ applied to the photomultiplier tube (PMT) and the synchrotron beam current $I_{S,R}$ of sample (index S) and reference (index R) measurements were used to calculate the sample absorbance A for each measurement, following a procedure suggested by Sutherland [178]. Accordingly, the absorbance can be calculated by

$$A = \lg\left(\frac{I_S}{I_R}\right) + \alpha \cdot \lg\left(\frac{HT_S}{HT_R}\right). \tag{3.9}$$

Herein, the factor α accounts for the gain of the PMT. At UV-CD12, it was determined by a neutral density filter method, resulting in $\alpha = 9.5498$.

With the J-810 spectropolarimeter, OCD spectra ranging from 260 to 180 nm in 0.1 nm-steps were collected with similar acquisition parameters. The scanning speed was 10 nm·min^{-1} with 8 s response time and 1 nm bandwidth. Depending on the measurement, two or three consecutive repetition scans were averaged for each

of the eight rotational angles. As for the SR-OCD data, the rotational spectra were averaged and corrected for the respective lipid spectrum. The ellipticity of both, the UV-CD12 beamline and the J-810 spectropolarimeter, were calibrated with standard CSA-solution. All measurements were performed at a temperature of 25°C. At 40°C and full-hydration, the Ece1-III/DOPC system got so liquified that a homogeneous distribution of the sample material during the rotations could not be guaranteed as the samples even tended to slide off the vertically positioned quartz window. For that reason, no realiable OCD spectra could be obtained for 40°C.

3.2.2 Fourier Transformation Infrared Spectroscopy

In contrast to CD spectropolarimetry, spectroscopic studies utilising infrared wavelengths do not probe the dipole moments of electronic transitions but the energetically lower dipole moments of vibrational transitions of different molecular groups. Just as it is the case for CD spectra, different molecules cause characteristic infrared-absorption spectra which can be considered as their unique fingerprint. Conformational changes of the molecules can be examined by monitoring particular spectral features, such as those caused by the fundamental stretching vibrations of the methylene groups in lipid molecules. Infrared-spectroscopy, thus, is a well-suited technique to observe the acyl chain melting in transitions from the lamellar gel phase L_β to the liquid-crystalline L_α-phase, where the rates and amplitudes of intra- and intermolecular chain motion notably increase [179]. Accordingly, the accompanying infrared bands broaden and their amplitudes decrease.

Fourier transformation infrared spectroscopy (FT-IR) differs from conventional infrared spectroscopy in that the acquisition is carried out by means of an interferogram which traverses the sample. This unique signal contains every frequency emitted by the light source. A Fourier transformation of the corresponding transmitted signal delivers the sample's entire absorption spectra without probing each single frequency individually.

Experimental Implementation

In this work, the impact of Ece1-III$_{\mathrm{KR(N)}}$ on the thermotropic transition of DOPC/SM/Chol (9:9:2, n/n/n) and DOPC/SM/Chol/PS (9:9:2:2, n/n/n/n) was examined. Therefore, only the position of the widely unperturbed absorption maxima of the symmetric stretching vibration of the CH_2 groups around 2850 cm^{-1} was monitored over a range from 7 to 70°C[1]. Note that possible contributions of CH_2 groups in the peptide will not notably affect the transition itself, since their popu-

[1]The relations between wavelength, wavenumber and frequency are given in Sec. 3.5.1.

lation is small and, in addition, conformational changes in the peptide do usually not occur within the same temperature range. For the experiments, 20 μl aliquots of pure LUVs or LUV/peptide mixtures (from LUV solutions of 10 mM in 20 mM HEPES buffer, stored at 4°C for at least 12 h prior to measurement) were deposited between two calcium fluoride windows separated by a 12.5 μm thick Teflon spacer. The spectra were recorded on an IFS-55 spectrometer (Bruker, Billerica, MA, USA) with a heating rate of $0.6°\text{C}\cdot\text{min}^{-1}$.

3.2.3 Förster Resonance Energy Transfer Assays

Experiments based on the fluorescent or Förster resonance energy transfer (FRET) provide a simple spectroscopic tool to probe the spatial separations of different molecules on molecular scale.

Förster Resonance Energy Transfer

The excess energy a molecules gains by absorbing a photon is usually released again within 10^{-5} s. The pathways for this release are, however, complex. One possibility is for instance that the energy is internally transferred by setting the molecule in motion. Another one, is that the molecule is deactivated by fluorescence, i. e. by directly emitting another photon. The latter effect is utilised in different spectroscopic techniques. A special form of such a fluorescence analysis is to probe the Förster resonance energy transfer (FRET) between two different fluorescent molecules (fluorophores), which serve as donor and acceptor, respectively [180]. The FRET effect describes the radiation-free transfer of the excess energy from an excited donor to a weakly coupled acceptor molecule, which in turn emits a photon of longer wavelength. Accordingly, it does only occur if the emission spectrum of the donor and the excitation spectrum of the acceptor overlap. The energy transfer itself is mediated by dipole-dipole interactions. From a quantum mechanical calculation, it can be derived that the interaction energy E_{DD} between both fluorophores is described by

$$E_{\text{DD}} = \frac{1}{R^3 n_L^2} \cdot \left[\vec{\mu}_D \vec{\mu}_A - \frac{3}{R^2} \left(\vec{\mu}_D \vec{R} \right) \left(\vec{\mu}_A \vec{R} \right) \right] \tag{3.10}$$

for optical frequencies. Herein, $\vec{\mu}_D$ denotes the transition dipole moment ($\vec{\mu}_{0,j}$) of the donor and $\vec{\mu}_A$ the corresponding acceptor moment. $\vec{R}$ is the distance between both and n_L is the index of refraction of the surrounding solvent. In view of the fact that E_{DD} decreases with R^3 (and its transfer rate $k_T \propto E_{\text{DD}}^2$ even with R^6), the FRET effect is highly distance-dependent and it only occurs if both fluorophores are in close proximity to each other, which is typically a distance shorter than ~ 8 nm.

Hence, the effect can be utilised experimentally as a molecular ruler. In this work, it was used to probe the peptide binding to liposomes and the subsequent integration into the bilayers. In addition, the peptides' ability to trigger liposome fusion was examined. The corresponding assay designs are described in the following.

For each experiment, a volume of 1950 μl LUVs at a concentration of 10 μg·ml^{-1} (in 100 mM KCl, 5 mM HEPES at pH 7.0) was measured in rectangular Suprasil quartz cuvettes (Type-101-QS, Hellma Optik GmbH, Müllheim, Germany) under continuous stirring. Fluorescence excitation and emission detection were performed on Fluorolog-3 or Spex Fluorolog 1681 spectrofluorometer (HORIBA Ltd., Kyoto, Japan). Both use 450 W xenon lamps (UXL-450S-O, Ushio, Steinhöring, Germany) as light source. Single grating monochromators are employed to select excitation and detection wavelengths. PMTs serve as intensity detectors. The spectrofluorometers have T-shaped sample compartments which allow for dual-wavelength detection, i. e. both the donor and the acceptor emission intensity are detected simultaneously in opposite compartments. NBD and Rho dyes (attached to the lipids) served as donor/acceptor pairs. The donor was excited with a wavelength of 470 nm and the corresponding fluorescence intensities of donor and acceptor were detected at 531 nm and 593 nm, respectively. Due to the utilisation of pairs of acceptor and donor dyes, peptide-induced changes of the FRET signals may be discriminated from intensity changes due to self-quenching. For all assays, 50 μl of peptide (1 mg·ml^{-1} in H_2O) were added in five successive steps and thereby, the concentration was gradually increased from 0.74 μM (P/L = 1:13.5) to 3.65 μM (P/L = 1:2.7).

FRET Binding Assay

In the binding assay, properly labelled liposomes serve as donor while the peptide is labelled with a corresponding acceptor dye. As initial situation in such an assay only the liposome solution is present. Consequently, the donor dye fluoresces as response to its excitation. The addition of the labelled peptide will not cause any difference if no lipid-peptide interactions occur. However, as soon as the peptide binds to the liposome, both dyes get in close proximity to each other and an energy transfer will be observed by an increased FRET efficiency, i. e. an increase in the acceptor fluorescence and a corresponding decrease in the donor signal as sketched in Fig. 3.4.

Starting from pure LUV-solution with a proportion of 2 % NBD-DHPE, 5 μl of Rho-labelled Ece1-III$_{\mathrm{KR(N)}}$ (1 mg·ml^{-1} in H_2O) were added every 100 s. The measurement was stopped 100 s after the fifth peptide addition. A similar titration of pure water served as negative control. To adjust the analyser slit openings, the final lipid/peptide samples served as reference sample prior to the actual measurement.

With this sample, the fluorescence emissions of NBD-PE and Rho-Ece1-III$_{KR(N)}$ were adjusted to yield identical intensities.

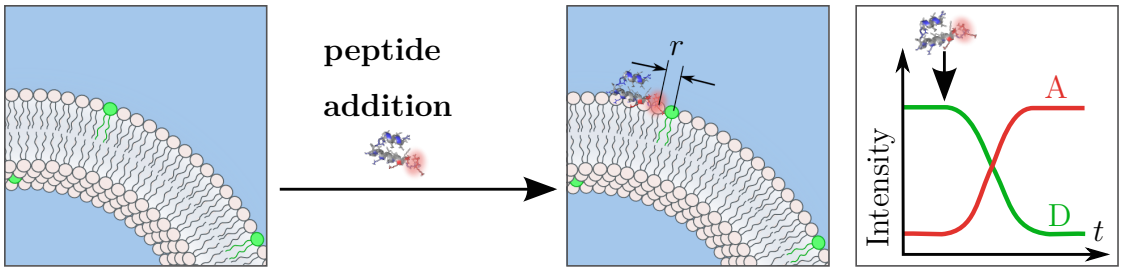

Figure 3.4 – Principle of a FRET binding assay. In this assay, the peptides labelled with an acceptor dye are added to LUV solutions with a donor label (green). If the peptide binds tightly to the bilayer, the donor will transfer its energy to the acceptor fluorophore. Corresponding intensity changes of the donor (D) and acceptor (A) emission are detected as function of time t (right panel).

FRET Intercalation Assay

In lipid solutions that are equally labelled with donor and acceptor dyes, the FRET effect will always be observed due to the random distribution of both dyes which warrants that some donor/acceptor pairs neighbour one another within a range $r_1 < 8$ nm (cf. Fig. 3.5). If the averaged distance between them is enlarged to $r_2 > 8$ nm, a decreased acceptor intensity and, in turn, an increased donor intensity will result. Thus, the FRET signal can be used to monitor changes in the averaged lateral lipid-to-lipid distance. Accordingly, it may be probed whether a peptide added to the liposome solution integrates into the bilayer membrane as such an intercalation would dilute the lipids [181], i. e. it would push lipid donor/acceptor pairs apart from each other as sketched in Fig. 3.5.

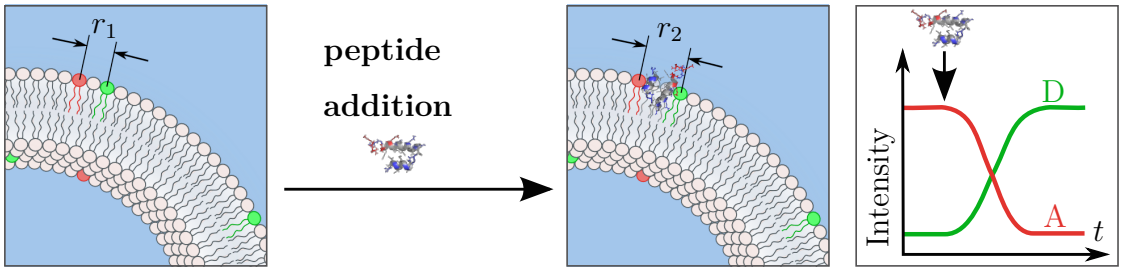

Figure 3.5 – Principle of a FRET intercalation assay. This assay is utilised to determine the peptide intercalation into liposomes. To this end, the peptides are added to LUV solutions containing both the donor (green) and the acceptor dye (red). If the peptide is integrated into the bilayer, the spatial separation between the donor/acceptor pair will increase (central panel), resulting in a loss of the acceptor (A) but an increase in the donor (D) fluorescence (right panel).

For this experiment, the LUV solution was prepared with equal proportions of NBD-DHPE and Rho-DHPE at a molar ratio of 100:1:1 (lipid:NBD-DHPE:Rho-DHPE). The fluorescence emissions of both dyes were adjusted to yield identical intensities and recorded for 50 s to determine the baseline. In five subsequent steps 5 μl of Ece1-III$_{\mathrm{KR(N)}}$ (1 mg·ml^{-1} in H_2O) were titrated, each after an interval of 100 s. A similar titration of pure water served as negative control.

FRET Fusion Assay

In a fusion assay, stable mixtures of two differently labelled liposome populations are utilised. Since interactions between both vesicle species can be neglected, no FRET effect will be observed and only the donor fluorescence is detected. An increased acceptor signal will, however, be detected if both lipid populations mix, i. e. if they fuse. Due to the angular dependence of the FRET effect, it can be excluded that the acceptor intensity is caused by mere vesicle approaches or agglomerations. In this case, the transition dipole moments of the donor and acceptor fluorophores would be oriented primarily antiparallel towards each other. Under this condition the energy transfer is vanishingly small (cf. Eq. 3.10).

For the fusion assay, two different LUV solution were prepared in the standard buffer: one containing 2 % NBD-DHPE and another one with 2 % Rho-DHPE, each at a total lipid concentration of 10 μg·ml^{-1}. Both were mixed and filled into the sampling cuvette where the analyser slits were adjusted to obtain equal emission yields of both dyes. A baseline was recorded for 50 s. In five subsequent steps 5 μl of Ece1-III$_{\mathrm{KR(N)}}$ (1 mg·ml^{-1} in H_2O) were added, each after an interval of 100 s. Again, a similar titration of pure water served as negative control.

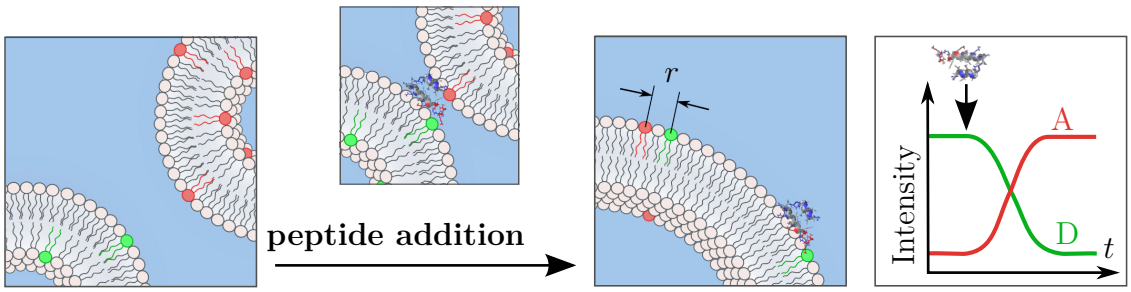

Figure 3.6 – Principle of a FRET fusion assay. A mixture of two independently labelled liposomes populations is used in this assay. As initial condition, both the donor (green) and the acceptor (red) dye are not within the FRET distance. If both liposome populations fuse due to a peptide-mediated interaction, this is observed as increase in the acceptor intensity and a corresponding decrease in the donor intensity (right panel).

3.2.4 Haemolysis Assay

The cytotoxic activity of the peptides is tested utilising an haemolysis assay which reflects the peptides' ability to lyse erythrocytes. This test is listed in this spectroscopic section since the final concentration of intact red blood cells is measured spectrophotometrically.

The erythrocytes for the haemolysis were extracted from fresh whole blood samples from healthy human donors as follows: First, haematocrit and blood plasma were separated by density centrifugation and the plasmic supernatant was discarded. The remaining haematocrit was washed three times in PBS buffer. For this washing procedure, 1 ml haematocrit was diluted in 7 ml PBS buffer and centrifuged for 10 min at 500·g (Biofuge 17RS, Heraeus Sepatech, Osterode, Germany). The supernatant was aspirated and the remaining erythrocytes were diluted again. After the last washing step, the haematocrit was diluted in 5 ml of PBS buffer. The absorption of this solution was measured in terms of the optical density at a wavelength of 412 nm ($\mathrm{OD}_{412} = \mu(412\ \mathrm{nm}) = -\lg(I/I_0)/d$, cf. Eq. 3.7) using a Uvikon 942 spectrophotometer (Kontron Instruments, Rossdorf, Germany). The sample was further diluted with PBS until $\mathrm{OD}_{412} = 1.4$ was reached, which corresponds to an approximate cell density of $5 \cdot 10^8$ cells per millilitre.

The peptides were diluted from 2 mg·ml^{-1} stocks in 0.01 % TFA to an initial concentration of 200 mg·ml^{-1} using PBS buffer. Round-bottom 96-well plates were prepared with a total volume of 80 μl PBS and peptide solution in a serial 1:2 (v/v) dilution. Each peptide concentration was measured at least in duplicate. To achieve maximal lysis of the erythrocytes, desalted sterile water was filled in as positive control. Pure PBS wells served as negative control. 20 μl of the prepared erythrocyte solution were added to each well and the plates were incubated at 37°C with gentle shaking. After an incubation period of 30 min, the plates were transferred to ice to immediately stop the reaction. The plates were then centrifuged for 10 min at 500·g at 4°C using a Varifuge K centrifuge (Heraeus-Christ, Osterode, Germany) with a corresponding plate holder. 10 μl of the cell-free supernatant were diluted at a ratio of 1:10 (v/v) by transferring it to a well of a flat-bottom 96-well plate primed with 90 μl PBS or water, respectively. The optical density values were analysed at 405 nm using an ELISA reader (Rainbow Tecan, Crailsheim, Germany) and the corresponding haemolytic activity was expressed as percentage according to

$$\mathrm{HL}(\%) = 100\% \frac{\mathrm{OD}_{405}(\text{sample}) - \mathrm{OD}_{405}(\text{neg. control})}{\mathrm{OD}_{405}(\text{pos. control}) - \mathrm{OD}_{405}(\text{neg. control})}.$$

3.3 Electrochemical Techniques

3.3.1 Electrochemical Impedance Spectroscopy of tBLMs

Electrochemical impedance spectroscopy is a method that probes frequency-dependent system responses to alternating voltage signals. Applied to tethered bilayer membranes this method allows monitoring changes of the bilayer properties such as bilayer thickness, homogeneity or ion permeability in real time. However, a detailed determination of these physical parameters is not straightforward and proper equivalent electrical circuit modelling of the particular system under investigation is needed [182].

Experimental Setup – the tethaPod™

In the present work, AC impedance spectroscopy was performed using an SDx-R1 tethaPod™ reader in combination with stBLMs prepared on SDx-T10 tethaPlates™ (SDx Tethered Membranes Pty Ltd., Syndney, Australia). One tethaPlate™ provides six measurement chambers, each containing one pair of gold electrodes. The lower gold electrodes serve as reconstitution sites for stBLM preparations (tether electrodes), the other ones are located $\sim$ 100 μm overhead and serve as counter electrodes. The results provided by the system base on simple model assumptions that are depicted in Fig. 3.7.

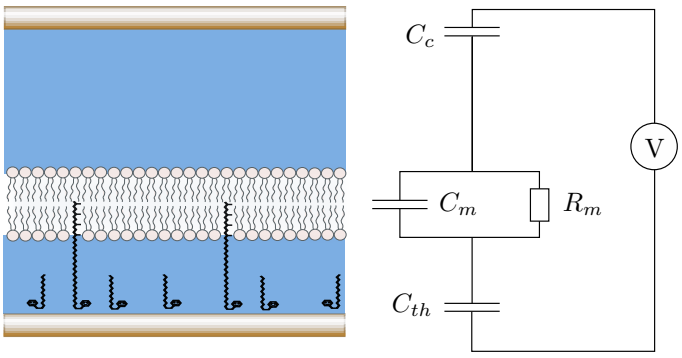

Figure 3.7 – Equivalent circuit of the tBLM system. The bilayer capacity C_m is parallel connected to its resistance R_m and the bilayer element is serial connected with the capacitances of the tethering gold surface C_{th} and the counter electrode C_c, respectively. Adapted from [143].

In this equivalent circuit, the bilayer membranes is modelled as a capacitor (C_m) in parallel with a resistor (R_m), both are in series with the capacitances of the tethering gold surface C_{th} and the counter electrode C_c, respectively. Ideal dielectric membranes are perfect insulators, which means they would not allow any charge transport across the bilayer. Or, in other words, they would have infinite resistance

and assemble charges to both sides. In reality however, membrane imperfections enable ion transports quantified by finite values of R_m or its inverse value, describing the conductance G_m. The tethaPod™ employs a ratiometric measurement strategy which utilises a reference element of known values that are comparable to the ones expected (C_{ref} = 100 nF·cm^{-2}, $G_{ref} = R_{ref}^{-1}$ = 0.2 μS). The reference element is added in series to the equivalent circuit described (cf. Fig. 3.8 A). From measured values of the potential difference across the membrane setup (load network, V_{load}) and the total applied voltage (V_{tot} = 20 mV), a frequency-dependent attenuation factor is calculated:

$$f(\omega) = \frac{V_{load}(\omega)}{V_{tot}(\omega)} = \frac{I(\omega) \cdot Z_{load}(\omega)}{I(\omega) \cdot Z_{tot}(\omega)}.$$

Therein, ω is the the excitation frequency and $I(\omega)$ the current through the network; the impedance values of the unknown load impedance $Z_{load}(\omega)$ and the whole network $Z_{tot}(\omega)$ contain the parameters of interest (R_m, C_m, C_{th}, and C_c). They derive from the fundamental behaviour of capacitors and ohmic resistors in AC circuits. A microprocessor (ADuC70/24, Analog Instruments, Nordwood, MA, USA) contained in the setup fits the model function to the experimental values of $f(\omega)$ obtained at frequencies ranging from 0.125 Hz to 1 kHz and yields respective values for R_m, C_m, C_{th}, and C_c in real time. The goodness of fit (GOF), calculated as root mean square, tests the ability of the idealised model to describe the membrane systems. Significant deviations (GOF > 0.1) indicate that the contributions to G_m and C_m are inhomogeneously distributed over the membrane plane. Accordingly, the system is capable to give insights into membrane-peptide interactions since it allows to roughly estimate spatial distributions of membrane penetration processes and, additionally, it allows the monitoring of peptide-induced thickness changes as the capacity C_m is inversely proportional to the bilayer thickness. Due to its simplistic model assumptions, its validity fails for systems of higher complexity, involving ion channels or heterogeneous peptide insertions [182, 183]. However, tethaPod™ experiments are readily useful to screen the permeabilisation activity of various peptides or the influence of different lipid components. The description of the experimental setup and the ratiometric method employed is given in [143] in greater detail.

Experimental Implementation

The tBLMs were prepared on tethaPlates™ as described in the sample preparation section 2.2.3. The plates were assembled to the SDx-R1 tethaPod™ reader. In order to guarantee stable ground signals, the membranes were measured for 20 min before aliquots of peptide stocks in 0.01 % TFA or H_2O with 40 % DMSO (v/v) were carefully added to the channel reservoir. Several time-dependent additions of pep-

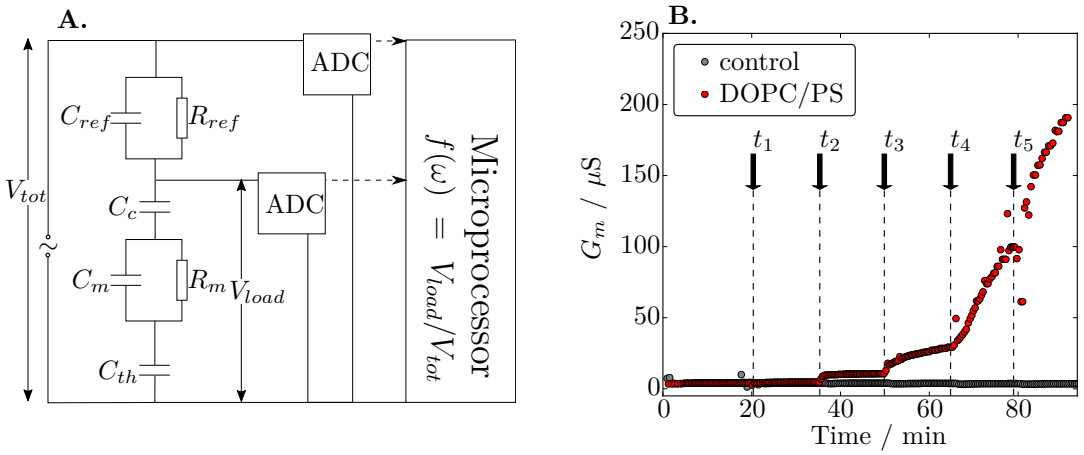

Figure 3.8 – Measurement principle of the tethaPod™ system. A. Equivalent circuit sketch of the ratiometric impedance spectroscopy measurement. V_{tot} is the potential applied across the total network impedance and V_{load} the resultant potential across the unknown load impedance. ADC depicts an analog-to-digital converter. In a microprocessor the idealised function of the the attenuation factor $f(\omega)$ is fitted to experimental values in real time. Adapted from [143]. **B.** Exemplary raw data of the time-dependent increase in membrane conductance G_m (red data points) upon subesequent additions of Ece1-III$_{\mathrm{KR(N)}}$ (see text). By contrast, an equivalent addition of 0.01 % TFA (gray data point, negative control) did not induce any significant changes in conductance. The time points t_i of the repsective additions are indicated by arrows.

tide ensued with intermediate periods of about 30 min (cf. Fig. 3.8 B). As negative controls, respective aliquots of 0.01% TFA or H_2O/40 % DMSO without peptides were measured, but none of these induced detectable changes of the analysed parameters. All measurements were performed in an incubation chamber at 37°C. The final increases in membrane conductance prior to the next peptide addition were then extracted and averaged for at least two independent measurements.

3.3.2 Electrophysiological Characterisation of BLMs

Concept of the Montal Mueller Setup

In this setup a free-standing bilayer membrane is spanned over a vertical hole as described in Sec. 2.2.3. Thus, the membrane separates two distinct buffer-filled compartments. Using two electrodes placed to each side of the membrane, electric signals across the bilayer can be measured to probe electrical membrane properties such as conductance or capacity. This system is particularly suitable to examine inductions of membrane defects or the formation of transmembrane channels since lipid membranes are almost perfect insulators, so that the conductance signal is readily amplified [115, 184]. In this work, the peptide-induced, time-dependent current flow across the BLM was monitored to examine the induction of lesions by Ece1-III$_{\mathrm{KR}}$ qualitatively.

To this end, the BLM was prepared as described in Sec. 2.2.3 in a custom-made Teflon chamber. This chamber basically consists of a metal ring which is assembled with two separated, half-conical compartments that sandwich a 12.5 μm thick Teflon foil with a small aperture ($\sim$ 80 μm in diameter) in its center. To apply a voltage and measure corresponding current traces, an electrode is added to each compartment. A more lengthy description of the experimental setup is given below.

Experimental Implementation

Septum foils with a diameter of $\simeq$ 2.5 cm were prepared by die cutting. In each of these foils an aperture was punched by a high-voltage discharge BD10A (Electro-Technic Products, Chicago, IL, USA) which melts the edges of the Teflon foil and creates holes with diameters of about 40 - 100 μm. The septum was shortly treated with a mixture of hexane/hexadecane (10:1, v/v) to increase its hydrophobicity required for an excellent BLM formation. The Teflon components were thoroughly cleaned in five subsequent washing steps, each taking one hour: first in ethanol, then in nitric acid and afterwards in sodium hydroxide (all three at 60°C), followed by an immersion in ultra pure water and a final one in choloroform/methanol (2:1, v/v), both at room temperature. After the washing, the compartments were dried overnight in a hot-air cabinet at 100°C.

The compartments and the septum were then fastened together using silicone grease (Baysilone, Bayer, Leverkusen, Germany) and the encompassing metal ring, before the chamber was mounted in the measurement setup. Here, a pair of Ag/AgCl wire electrodes (Science Products GmbH, Hofheim, Germany) with a surface area of 21.11 mm^2 was assembled to the Teflon compartments. The voltage signals were amplified and filtered with 10 kHz using a patch-clamp amplifier (L/M-PCA, List-Medical, Darmstadt, Germany). The data was transferred to a PC via an input/output card (PCI-6036E, National Instruments Germany GmbH, Munich, Germany). At the PC, the data was controlled and processed in a customised LabVIEW 7.1 environment (National Instruments Germany GmbH, Munich, Germany). The signals were sampled with 50 kHz and re-sampled to a remaining time-resolution of 300 Hz to reduce the large amounts of data. Additionally, a floating average including 20 data points was applied to smoothen the data.

Each chamber side was filled with 1.5 ml of the standard buffer (100 mM KCl and 5 mM HEPES at pH 7.0) which has a specific conductivity of 17.2 mS$\cdot$cm^{-1}. The vertical planar membrane was prepared as described in Sec. 2.2.3. Hereto, the buffer levels were controlled by two syringes, each connected to one chamber side. For all measurements, a voltage of +50 mV, corresponding to the biological relevant voltage of $-$50 mV (with respect to the interior of a cell), was applied

and the temperature was set to 37°C. After a BLM was prepared, its capacity and conductivity were measured for about ten minutes to equilibrate the BLM itself and to ensure stability, before the peptide (solved in 0.01 % TFA) was added.

3.4 Techniques Based on Force Interactions

3.4.1 Film Balance Experiments

Wilhelmy Method

The lateral pressure Π_s of a monomolecular layer upon water is determined by the difference of the surface tension of the pure subphase σ_0 and the one covered with a surface-active substance σ:

$$\Pi_s = \sigma_0 - \sigma.$$

This force varies with the molecular area available and it can be measured by means of the Wilhelmy method. Hereto, a rectangular plate is partially immersed in the liquid. Alterations of the surface tensions cause distinct displacements of the plate governed by opposing force components: While surface tension and gravitation exerted by the liquid's meniscus drag the plate towards the bulk phase, the buoyancy arising from the displaced subphase volume acts contrary to these forces. Provided that the plate's thickness is negligible, its mass is constant, and it is fully wetted (the contact angle between plate and film interface is zero), these force changes ΔF directly relate to changes in the surface tension $\Delta\sigma$ according to

$$\Delta\sigma = \frac{\Delta F}{2d_P}.$$

with d_p denoting the width of the Wilhelmy plate at the level of the bulk liquid surface. Thus, the connection of this plate to an electronic linear-displacement sensor (electrobalance) allows measurements of Π_s. By measuring Π_s at varying surface area and constant temperature (pressure-area isotherms), the area required per molecule at biological relevant Π_s can be determined and changes can be monitored easily. In this work, the film balance is used to study two different aspects: Firstly, it is employed to evaluate the peptides' amphiphilicity and the averaged interface area required per peptide molecule. Secondly, it is utilised to probe the integration of Ece1-III$_{\mathrm{KR(N)}}$ into lipid monolayers of different composition [185]. Not only does the latter aspect give information on the extent of lipid-peptide interactions with respect to the particular lipid species, it further provides insight into the location of interaction [186]. Exclusive interactions with the phospholipid headgroups will

hardly impact the lateral pressure, while insertion into the hydrophobic region acyl chain region will increase the area required per molecule at constant lateral pressure significantly.

Experimental Implementation

The measurements were performed on a small KSV Nima Langmuir-Blodgett trough (Biolin Scientific Inc., Stockholm, Sweden). The balance consists of a Teflon trough, two Teflon barriers and the Wilhelmy plate attached to an electrobalance (see Fig. 3.9). The hydrophobic trough allows the water height to exceed the trough height. The barriers isolate the interface carrying the monolayer from the pure water/air and allow the symmetric compression of the effective film area. A connection to a feedback system enables the barrier positions to be accommodated according to a particular target lateral pressure. The Wilhelmy plate used was a piece of filter paper with $2d_P = 20$ mm. It was fully soaked with water to ensure constant mass. The film balance is enclosed in a acrylic glass box to reduce outer disturbances and contamination. The temperature of the buffer subphase was controlled by water circulation (Haake, Karlsruhe, Germany) and set to 24°C.

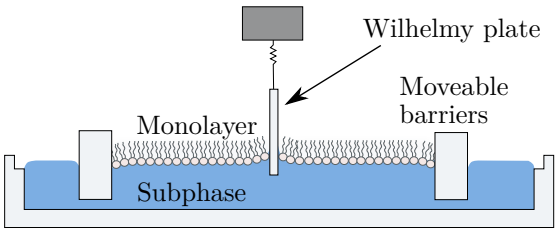

Figure 3.9 – Basic layout of a film balance. The sketch shows a film balance consisting of a hydrophobic flat trough with two barriers and a Wilhelmy plate connected to an electrobalance. The barriers isolate the area carrying an interfacial film (here lipid monolayer) from the pure subphase/air interface. By varying the barrier positions, the area available for the film can be compressed or expanded.

To avoid the presence of contaminative substances, the trough was thoroughly cleaned with pure ethanol prior to each measurement, and either a new Wilhelmy plate was attached to the balance or one that had been incubating in a glass beaker with 250 ml pure water for at least 12 hours. The trough was then filled with 65 ml buffer solution and the lateral pressure of the soaked plate ($\sigma_0 = 72$ mN·m^{-1}) was set to zero on the electrobalance. A contamination-free buffer/air interface was verified with lateral pressure changes below $\Pi_s \simeq 0.5$ mN·m^{-1} after closing the barriers up to a position where the buffer menisci of the barriers and the Wilhelmy plate did not affect one another.

Pure peptide solution (solved in 0.01 %) was spread onto the surface of the buffer subphase to evaluate the peptides' amphiphilicity by determining their ability to form stable monolayers. After an equilibration time of 5 min, a pressure-area-isotherm $\Pi_s(A_m)$ (where A_m is the averaged area per molecule) was recorded by compressing the film area (closing the barriers) with a constant compression rate of 10 mm·min^{-1}.

In order to study the peptide integration into lipid monolayers, firstly monolayers were prepared by dropwise spreading lipid solution (7 μl lipids dissolved at 1 mg·ml^{-1} in chloroform) onto the buffer surface. After an equilibration time of 5 min, the film was compressed with a barrier speed of 10 mm·min^{-1} until a lateral pressure of Π_s = 20 mN·m^{-1} was reached. This target lateral pressure was kept constant during the whole measurement. In an equilibration time of at least 20 min, the monolayer area had to stay constant at Π_s = 20 mN·m^{-1} to reflect a stable monolayer preparation. 15 μl of 0.1 mM Ece1-III$_{\mathrm{KR(N)}}$ in 0.01 % TFA were injected into the subphase through a careful syringe puncture through the monolayer. The lipid/peptide interaction accompanied by areal increases was then monitored at constant Π_s as function of time for 50 min.

Both, pure peptide and lipid/peptide measurements, were repeated three to five times. All lipid or peptide samples were handled with gastight microsyringes (Hamilton Co., Reno, NV, USA) to ensure high volumetric precision.

3.4.2 Atomic Force Microscopy

Basic Principle

Atomic force microscopy (AFM) is a technique which enables recording of images of surface topologies with nanometre resolution. The method is based on the interactions between the sample surface and a tiny tip of a cantilever. This cantilever acts like a spring which is, in close proximity to a sample surface, deflected by the forces between the surface and the tip (i. a. forces from van der Waals or electrostatic potentials) [187, 188]. Thus, the sample can be rastered with the tip and the cantilever displacements at each position can be transformed into a corresponding height image.

The precise movements needed for such raster scans are facilitated by piezoelectric elements and the cantilever displacement is commonly measured optically. To that end, a laser beam is focused on the cantilever where it is differently reflected depending on the particular deflection of the cantilever. The reflected beam is detected by a quadrinomial photodiode in which voltage signals are induced as function of the spot position. These electric signals are either directly transformed into a height

image, or forwarded to a feedback mechanism which controls the vertical position of the cantilever so that a constant interaction between tip and surface (and therefore a constant cantilever deflection) is maintained.

Atomic force microscopes provide two fundamental imaging modes: contact-mode and non-contact (tapping) mode. In the first one, the tip is moved across the sample surface and the contours of the surface corresponding to a constant probe-sample interaction are transferred into a height image. The other mode works, as its name suggests, (almost) without direct contact to the sample surface. In this mode, the cantilever spring is oscillated with its resonant frequency ω_0 (frequency modulation) or a slightly shifted frequency (amplitude modulation) a few nanometres above the surface. If the tip approaches a surface, the respective van der Waals potential (or any other long-range potential which extends above the surface) superposes the tip potential which results in a reduction of the resonance frequency $\delta\omega = \omega - \omega_0$ and an accompanied decrease in the oscillation amplitude. Hence, the amplitude is a measure of the surface forces and provides topographical information. In this mode even very soft samples can be imaged without inducing destructions. Please refer to the dedicated literature (e. g. [189, 190]) for more detailed descriptions on AFM instrumentation and the basic imaging modes.

Experimental Implementation

AFM measurements were performed on a MFP-3D microscope (Asylum Research Santa Barbara, CA, USA). The image processing (flattening, plane fitting, extraction of height histograms) was performed using the associated software package under IGOR Pro (Lake Oswego, OR, USA). The surfaces of erythrocytes, solid-supported multilayers and single bilayers were studied.

To image the appearance of erythrocytes prior to and after their interaction with the peptide, the samples from the haemolysis assay (see Sec. 3.2.4) were used. Particularly, the controls and the aliquots containing 10 μg·ml^{-1} Ece1-III$_{\mathrm{KR(N)}}$ served as specimen. To prepare these samples for the imaging, they were transferred into reaction tubes (Eppendorf, Hamburg, Germany) and centrifuged for 3 min at 400·g. The supernatant was discarded and the remaining precipitate was solved in 100 μl of a fixing solution of 3 % formaldehyde (v/v) and 0.1 % glutaraldehyde (v/v) in PBS buffer solution. The samples were incubated for 4 h at room temperature before they were again centrifuged for 3 min at 400·g. The resulting pellet was washed in and mixed with 100 μl PBS buffer solution (samples without a visible pellet were only mixed with 50 μl of the PBS buffer solution). For each sample, a droplet of 20 μl was applied on a glass slide where the buffer solution was allowed to evaporate. When the samples appeared dry, they were washed carefully by threefold

dipping into a beaker filled with ultrapure water. The samples were again dried and afterwards imaged in contact mode using CSG11 cantilevers (NT-MDT, Moscow, Russia). These have a typical spring constant of $k \sim 0.03$ - 0.2 N·m^{-1} and a resonant frequency of $\omega_0 \sim 16$ kHz.

The solid-supported multilayer samples were used for XRR and GID measurements before the topographical imaging was carried out. The respective preparation procedure is described in Sec. 2.2.3. The silicon wafers carrying the multilayers were fixed in a petri dish using silicone grease (Baysilone, Bayer, Leverkusen, Germany). This dish was installed in a heatable petri dish holder which allowed the control of the sample temperature. The sample stacks were examined under dry[2] and under partially hydrated conditions. The latter was obtained by adding 300 μl of pure water to the petri dish without direct contact to the sample chips. A silicone capping was mounted to the cantilever holder of the AFM to seal the dish. The multilayer topography was predominantly imaged in non-contact mode (with a frequency detuning of 5 - 10 %) using high stiffness NSG11 or NSG10 cantilevers (NT-MDT) with gold coating for increased reflectance. NSG11 cantilevers provided two different tips. For the measurements in this work, the shorter ones (tip A), with a length of about 100 μm and a typical spring constant of $k \sim 11.5$ N·m^{-1}, were used. Both, their spring constant and their resonant frequency of $\omega_0 \sim 255$ kHz, were similar to the tip properties of the newer NSG10 cantilevers. Some measurements were also carried out with the softer CSG11 cantilevers (see above).

Single bilayers were prepared by spreading vesicle solutions of 1 mg·ml^{-1} lipid in 100 mM KCl, 5 mM HEPES (pH 7.0) as described in Sec. 2.2.3. The bilayers were imaged in non-contact mode by the use of gold-coated silicone nitride RC800PSA cantilevers (Olympus, Tokyo, Japan). These cantilevers have a typical spring constant of $k \sim 0.76$ N·m^{-1}. Hence, they are softer than the ones employed for multilayers. In buffer, the typical resonant frequency of $\omega_0 \sim 71$ kHz of these cantilevers is reduced to about $\omega_0 \sim 20$ - 30 kHz. To study the influence of Ece1-III$_{\mathrm{KR(N)}}$ on the topography of the bilayer, 10 μl peptide solution (1 mg·ml^{-1} in 0.01 % TFA) were carefully added to the petri dish. In a separate experiment, the same amount of 0.01 % TFA without peptide was added as negative control.

[2]Note that these samples are not completely dehydrated since the imaging was carried out at the atmospheric conditions present in the lab. Here, the humidity was typically about 60 % rH which also led to a partial sample hydration. However, throughout this work these samples are referred to as dry samples to distinguish them from the partially hydrated samples which were examined in an atmosphere of increased water vapour saturation.

3.5 X-Ray Diffraction

Methods based on X-ray diffraction are powerful tools to characterise biomembrane model systems on molecular length scale – they are mostly non-destructive and allow the exploration of the structural membrane organisation with Ångström resolution. In this work, X-ray reflectivity (XRR) and grazing incidence diffraction (GID) on solid-supported membrane systems were performed to examine distinct structural changes which accompany lipid-peptide interactions. In particular, XRR was used to study features along the bilayer normal, while GID was applied to reveal lipid phase and acyl chain order. The following section briefly introduces X-ray diffraction phenomena, explains the particular techniques employed in this work and describes the experimental implementation. To avoid confusion, it shall be noted that the term *scattering* usually considers the general result of the interaction between radiation and matter whereas the term *diffraction* rather relates to the interaction with well-determined repeating structures such as crystal structures that give rise to unique scattering patterns. Although this section is headlined with the latter, special case, contributions from diffuse scattering are also addressed and although correlations from acyl chain groups are of less-defined order, their reflections are treated as diffraction events. Rigorous descriptions of the different interaction phenomena touched here can be found in several textbooks as for example in [191–195].

3.5.1 Fundamental Aspects of X-ray Diffraction

Classification of X-rays

Electromagnetic radiation with photon energies in the range of $\sim$ 1 - 10^2 keV is subsumed as X-radiation. Traditionally, X-rays are considered as plane waves, each having a wavelength λ which is defined by its propagation velocity in vacuum c (speed of light) and its frequency ν

$$\lambda = \frac{c}{\nu}.$$

As viewed from a quantum mechanical perspective, X-rays are quantised into photons with an energy of $E = h\nu$ with Planck's constant h. Accordingly, the relation between photon energy and wavelength is given by

$$E = h\nu = \frac{hc}{\lambda} \longrightarrow \lambda\ [\text{Å}] \approx \frac{12.3984}{E\ [\text{keV}]}$$

and the corresponding X-ray wavelengths range from a few fractions of an Ångström up to ~ 10 Å (1 Å $= 10^{-10}$ m). A mathematical expression for the complex amplitude $A(\vec{k})$ of a plane X-ray wave is given by

$$A(\vec{k}) \propto \exp(i\vec{k} \cdot \vec{r}),$$

where $\vec{k}$ describes the wave vector. This wave vector points along the direction of propagation and its modulus $k = |\vec{k}| = 2\pi/\lambda$ defines the wave number.

The Scattering Process

The primary interaction partners for X-rays in media are electrons and the interaction proceeds in two possible ways: either an X-ray photon is scattered by an electron, or it is absorbed. Analyses of the corresponding interaction results, thus, provide insight into the electron distribution in the media probed. For now, absorption processes shall be neglected and only elastic scattering, i. e. processes without any energy loss or gain, will be considered. The scattering event may then be described as follows: An incident X-ray wave which illuminates an electron, excites an oscillatory movement of this electron, which consequently radiates with a spherical wave of the same wavelength as the incident wave, but with altered phase. In a distance much larger than the electron, the curvature of this spherical wave is negligible and the wave may be approximated by a plane wave (far-field approximation). In the kinematical or (first-order) Born approximation, where multiple scattering of one single photon is neglected, the scattering of an ensemble of electrons is calculated by a coherent sum of all corresponding waves. From this sum, it can be derived that the scattering amplitude of a continuous medium corresponds to the Fourier transform of its electron density distribution $\rho_e(\vec{r})$:

$$A(\vec{q}) \propto \int \rho_e(\vec{r}) \exp(i\vec{q} \cdot \vec{r}) d^3r. \tag{3.11}$$

This integration involves the illuminated sample volume and the scattering vector $\vec{q} = \vec{k}_f - \vec{k}_i$. The latter describes the momentum transfer between incident and scattered wave, both characterised by their wave vectors $\vec{k}_i$ and $\vec{k}_f$, respectively. With the boundary condition of elastic scattering, the relation

$$k = |\vec{k}_i| = |\vec{k}_f| = \frac{2\pi}{\lambda}$$

holds and thus, the modulus of the momentum transfer equates to

$$q = |\vec{q}| = 2k \sin\frac{2\theta}{2}, \tag{3.12}$$

where 2θ is the angle between incident and scattered wave (cf. Fig. 3.10). The aforementioned phase difference between both waves results from their varying path lengths with respect to a certain point of reference $\vec{r}$. This phase shift is equal to

$$\Delta\varphi = \vec{k}_f \cdot \vec{r} - \vec{k}_i \cdot \vec{r} = (\vec{k}_f - \vec{k}_i) \cdot \vec{r} = \vec{q} \cdot \vec{r}.$$

As the scattered amplitude is usually a complex-valued quantity it may be written as product of the amplitude's modulus and an exponential term which contains the phase information:

$$A(\vec{q}) = |A(\vec{q})| \cdot \exp[i\varphi(\vec{q})].$$

In a scattering experiment, the scattered amplitude itself is not the actual measur-

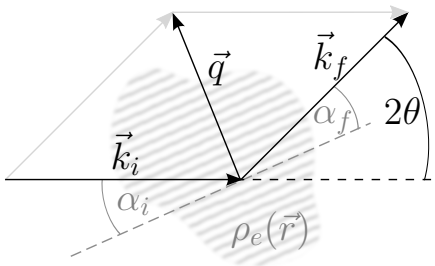

Figure 3.10 – Illustration of a scattering experiment at a sample with electron density $\rho_e(\vec{r})$. The figure depicts the wave vectors of the incoming ($\vec{k}_i$) and scattered wave ($\vec{k}_f$), the wave vector transfer $\vec{q}$ and the corresponding scattering angle 2θ are also indicated. In addition, the sketch contains the corresponding angles α_i and α_f with respect to a certain preferential direction defined by $\rho_e(\vec{r})$ (e. g. its surface).

able parameter – only its absolute square, the intensity $I \propto |A(q)|^2$ is detectable. As a consequence, the phase information $\varphi(\vec{q})$ cancels out and the measured signal does not allow an unambiguous extraction of the electron density distribution. Thus, scattering experiments in the framework of the kinematical approach require additional treatments to solve this phase problem.

Diffraction From Ideal Crystals

As indicated in the introductory part of this section, X-ray diffraction relates to the scattering of crystals. All scattering entities in ideal crystals are identical and arranged in periodic order. Such a structural entity, or unit cell, may consist of a single atom or a particular ensemble of a multitude of atoms. Its periodic three-dimensional alignment along a point lattice provides a simple mathematical description of the entire crystal. The point lattice is spanned by certain base vectors $\vec{a}$, $\vec{b}$ and $\vec{c}$ whose

moduli define the lattice parameters. The translational symmetry of the lattice is described by the lattice vector $\vec{R}$

$$\vec{R} = n_1\vec{a} + n_2\vec{b} + n_3\vec{c} \tag{3.13}$$

with integer values for n_1, n_2 and n_3. In accordance with this description, the electron density distribution $\rho_e(\vec{r})$ of a crystal may be expressed as convolution of the electron density within the unit cell $\rho_{e,u}(\vec{r})$ and the point lattice

$$\rho_e(\vec{r}) = \sum_{\vec{R}} \delta(\vec{r} - \vec{R}) \otimes \rho_{e,u}(\vec{r}),$$

where δ represents Dirac's delta function. Using the unique properties of this function and the convolution theorem, the scattering amplitude in Eq. 3.11 can be rewritten as

$$A(\vec{q}) \propto \underbrace{\sum_{\vec{R}} \exp(i\vec{q}\cdot\vec{R})}_{S(\vec{q})} \cdot \underbrace{\int_{V_u} \rho_{e,u}(\vec{r}) \exp(i\vec{q}\cdot\vec{r}) d^3r}_{F(\vec{q})},$$

whereby the integration is performed over the volume of only the unit cell. The first term, $S(\vec{q})$, is a sum over the lattice, known as structure factor. It represents the Fourier transform of the crystal lattice which in turn also resembles a periodic arrangement of points, the reciprocal lattice. The second term, $F(\vec{q})$, is the Fourier transform of the electron density distribution inside the unit cell, known as form factor. For perfect crystals, it may be described as sum over the scattering amplitudes of the particular atoms inside the unit cell using atomic form factors. These contain the scattering ability of one single, isolated electron quantified by the Thomson scattering length r_0. This elementary unit is also referred to as the classical electron radius. It is obtained by a quantum-mechanical consideration which equates the rest-mass energy mc^2 of the electron with its electrostatic energy at radius r_0:

$$r_0 = \frac{e^2}{4\pi\varepsilon_0 mc^2} \approx 2.818 \cdot 10^{-5}\text{Å},$$

where ε_0 denotes the permittivity of free space.

Usually, the lattice sum $S(\vec{q})$ contains a huge number of unit cells and each term is a complex number $e^{i\varphi}$, located on the unit circle. Only if all phases are 2π or multiples thereof, all terms will become $e^{i\varphi} = 1$ and thus, the sum will equal the huge number of terms. This is the case, as soon as the scattering vector fulfils the

condition $\vec{q} \cdot \vec{R} = 2\pi n$ (with $n \in \mathbb{Z}$). Following this condition, the reciprocal vectors $\vec{a}^\star$, $\vec{b}^\star$ and $\vec{c}^\star$ are defined as

$$\vec{a}^\star = \frac{2\pi}{V_u}(\vec{b} \times \vec{c}), \quad \vec{b}^\star = \frac{2\pi}{V_u}(\vec{c} \times \vec{a}), \quad \vec{c}^\star = \frac{2\pi}{V_u}(\vec{a} \times \vec{b}), \tag{3.14}$$

each scaled to the unit cell volume $V_u = \vec{a} \cdot (\vec{b} \times \vec{c})$. An arbitrary linear combination of these vectors then describes the crystal lattice in reciprocal space $\vec{Q}_{hkl} = h\vec{a}^\star + k\vec{b}^\star + l\vec{c}^\star$, with the integers $h, k, l \in \mathbb{Z}$ giving the Miller indices. The reciprocal lattice vector $\vec{Q}_{hkl}$ is parallel to the real space vector $\vec{R}$ and, just as $\vec{R}$, perpendicular to a set of lattice planes with the indices (hkl). Consequently, the spacing between these lattice planes d_{hkl} may be described by either of them: $d_{hkl} = |\vec{R}| = 2\pi/|\vec{Q}_{hkl}|$. Using Eq. 3.13 it can easily be verified that the premised condition is fulfilled:

$$\vec{q} \cdot \vec{R} = \vec{Q}_{hkl} \cdot \vec{R} = 2\pi(hn_1 + kn_2 + ln_3) = 2\pi n.$$

To put it straight, the scattered amplitude will only be non-vanishing if the scattering vector $\vec{q}$ coincides with the reciprocal lattice vector $\vec{G}_{hkl}$. This reasoning is also known as Laue condition, which is equivalent to the well-known Bragg's law for constructive interference. The corresponding relation can be derived using Eq. 3.12:

$$2k \sin\theta_{hkl} = \frac{2\pi}{d_{hkl}} \longrightarrow 2d_{hkl} \sin\theta_{hkl} = n\lambda.$$

Diffraction From Model Membranes

Compared to ideal crystals, the structural order in systems of biological model membranes is greatly reduced. However, there is still a certain degree of long-range order left. MLVs of the L_α phase for instance show a distinct lamellar repetition of their bilayer sheets. Due to their spherical character, these lamellae adopt all possible orientations in space and, hence, MLV systems resemble powder samples of small crystallites with random orientation.

In membranes stabilised by solid supports, where the lamellae align parallel to the substrate surface, the orientational order is even higher. The alignment quality is reflected by the distribution of the bilayer normal vectors – i. e. the lower this mosaicity, the higher is the orientational order of the system. Similar to the smectic phase of a liquid crystal, oriented lipid samples exhibit one-dimensional crystallinity along the surface normal but lack distinct long-range order in the membrane plane as sketched in Fig. 3.11. Consequently, the scattering vector $\vec{q}$ can be split into two distinct components: one that provides the information perpendicular to the membrane planes, $\vec{q}_\perp = \vec{q}_z$ (out-of-plane), and another one which describes the

structural properties within the plane, $\vec{q}_r = \sqrt{\vec{q}_x^2 + \vec{q}_y^2}$ (in-plane). Neglecting any in-plane order, the unit cell may be thought of as one-dimensional repetition unit of the electron density profile $\rho_{e,z}$ with the lattice constant d. According to this, Bragg peaks will occur if $\vec{q} = \vec{q}_z = 2\pi/d$, what immediately reveals another advantage over unoriented samples: The steady repetition of scattering entities of identical orientation amplifies the scattering signal enormously compared to the low scattering contributions from randomly oriented crystallites.

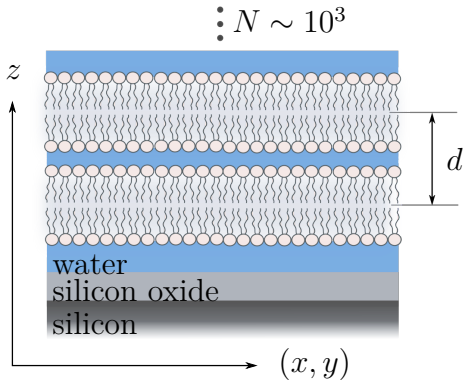

Figure 3.11 – Two-dimensional character of oriented lipid multilayers. The sketch illustrates the one-dimensional crystallinity of the lamellar alignment along the substrate normal z with the lattice constant d. These bilayers exhibit no distinct order in the plane parallel to the substrate (x, y) although this schematic drawing might imply a certain lateral lipid ordering. Under physical conditions the disorder of both headgroups and chains is higher as it is sketched here.

Bilayer stacks with non-lamellar lipid phases usually consist of a multitude of crystallites with random orientation around the surface normal of the substrate but preserved alignment parallel to the surface plane (cf. Fig. 3.12). Hence, these systems may be considered as two-dimensional powders which cause characteristic in-plane scattering contributions. In reciprocal space, these reflections can be illustrated as concentric rings around the $\vec{q}_z$-axis as sketched in Fig. 3.12. At this point, it is useful to introduce the concept of the Ewald sphere which visualises possible reflections for the incoming X-ray beam in reciprocal space. The sphere's center is fixed by the starting point of the wave vector $\vec{k}_i$ of the incident beam and its radius is defined by the corresponding modulus k_i. In case of elastic scattering, Bragg reflections will appear if and only if the sphere's shell coincides with the reciprocal lattice points since this represents the case $\vec{q} = \vec{Q}_{hkl}$ (see Sec. 3.5.1). Due to their continuous extent, the in-plane rings will intersect the Ewald sphere twice (provided that it is large enough, i. e. for large k_i or small λ, respectively). Hence, it is possible to excite more than one reflection without changing the angle of incidence of k_i and therefore the position of the Ewald sphere. By contrast, the lattice points which correspond to the lamellar spacing are highly localised in reciprocal space. To detect different

reflections, it is required to stepwise change the angle of incidence. However, these reflections are in general much stronger than in-plane reflections since the amount of crystallites with an orientation that matches the Ewald sphere is considerably increased.

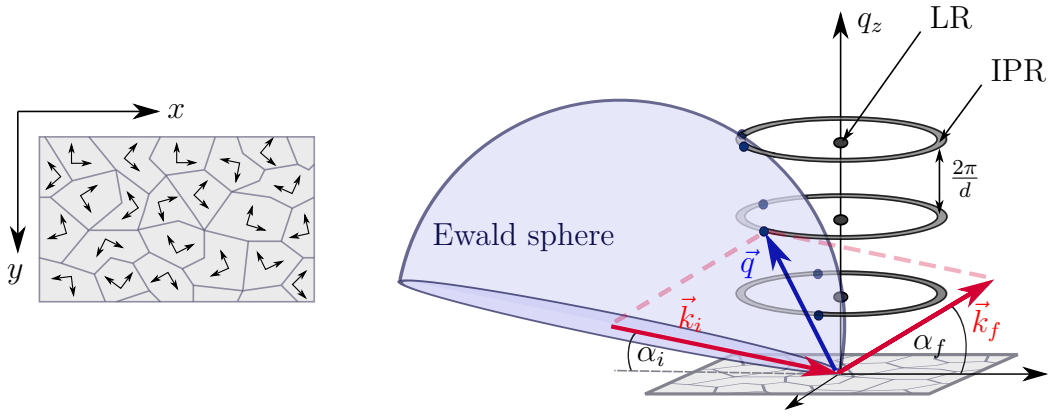

Figure 3.12 – Diffraction from oriented lipid model membranes. A sketch of the orientation of non-lamellar phase structures upon a planar substrate is shown on the left. They align parallel to the substrate surface but have random orientation in the x-y-plane, i. e. perpendicular to the surface normal (adapted from [196]). The right side illustrates the diffraction geometry of such a two-dimensional powder sample in reciprocal space. The properties of the incoming X-ray $\vec{k}_i$ define both radius ($|\vec{k}_i|$) and orientation (α_i) of the Ewald sphere. Due to their random orientation in x-y, in-plane reflections (IPR) from solid-supported membrane sample extend circularly in reciprocal space and therefore intersect the Ewald sphere twice. By contrast, reflections from lamellar spacings d are localised on the q_z-axis (LR), the position of the Ewald sphere has to be varied to detect all these reflections. This sketch of the Ewald sphere is adapted from [197].

Complex Index of Refraction and Fresnel Equations

The theoretical aspects introduced so far correspond to the framework of the kinematical or (first-order) Born approximation. Scattering events may be applied within this limit if multiple scattering effects of a single photon can be neglected. This holds true for objects with low scattering cross-sections. However, for low angles close to the incident beam and in the vicinity of Bragg reflections the kinematical approximation becomes invalid and diverges from observed phenomena, so that the corresponding diffraction results have to be treated within the more general formalism of the dynamical scattering theory.

In the framework of this theory, a complex refraction index n is introduced which strongly depends on the properties of the particular material. It is expressed by

$$n = 1 - \delta + i\beta. \tag{3.15}$$

Therein, the parameter δ contains the material's most important scattering property, which is its electron density ρ_e, and the classical electron radius:

$$\delta = \frac{2\pi\rho_e r_0}{k^2}. \tag{3.16}$$

The imaginary part of Eq. 3.15 accounts for absorption processes and relates to the absorption coefficient μ according to

$$\beta = \frac{\mu}{2k}. \tag{3.17}$$

The refraction of X-ray beams at smooth, planar interfaces is governed by Snell's law:

$$n_1 \cos\alpha_i = n_2 \cos\alpha_t. \tag{3.18}$$

It defines the refracted angle α_t as function of the angle of incidence α_i using their refractive indices n_1 (superphase) and n_2 (subphase). The refractive indices of X-rays are usually a little smaller than unity. Thus, Snell's law implies that X-rays experience total external reflection for incident angles smaller than a certain critical angle α_c. Applying the approximations $\alpha_i = \alpha_c$, $\alpha_t = 0$ and $\beta = 0$, the expansion of the cosine then allows the estimation of the critical angle for total reflection in vacuum ($n_1 = 0$) by relating Eq. 3.15 and Eq. 3.18: $\alpha_c \approx \sqrt{2\delta}$. For angles $\alpha_i > \alpha_c$, the X-rays start to penetrate the medium and only certain parts will be reflected (Fig. 3.13). The amplitude proportions of these both wave parts can be described by the Fresnel equations for reflectivity r and transmittivity $t = 1 - r$. Above the critical angle, they are given by

$$r = \frac{A_R}{A_I} \approx \frac{\alpha_i - \alpha_t}{\alpha_i + \alpha_t} \quad \text{and} \quad t = \frac{A_T}{A_I} \approx \frac{2\alpha_i}{\alpha_i + \alpha_t}, \tag{3.19}$$

where the coefficients A give the amplitudes of the incoming (A_I), reflected (A_R) and transmitted (A_T) waves; α_t is the transmitted angle. Up to the critical angle, both α_t and α_i are complex numbers and due to absorption effects they may also be complex-valued for even higher angles of incidence. The Fresnel equations base on the boundary conditions that the involved normal components of the X-ray waves and their derivatives must be continuous across the interface, and on the law of reflection which states that the reflected angle equals the incident angle. For increasing angles α_i, the quantities of r and t change subtly, depending on the polarisation of the X-ray electric field relative to the reflecting interface. Again, the absolute square of the amplitude corresponds to the respective intensity.

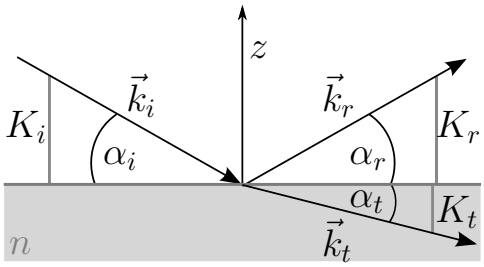

$$|\vec{k}_i| = |\vec{k}_r| = k = \tfrac{2\pi}{\lambda}$$
$$|\vec{k}_t| = nk$$
$$|\vec{k}_t|^2 + |\vec{k}_r|^2 \cos^2 \alpha_i = K_t^2$$

Figure 3.13 – Refraction and reflection at an ideal smooth interface. An X-ray with wave vector $\vec{k}_i$, which impinges on a material with refractive index n, is partially reflected $\vec{k}_r$ and transmitted $\vec{k}_t$. The corresponding angles are defined by Snell's law and illustrated with $\alpha_i = \alpha_r$ for the reflected and α_t for the refracted (transmitted) beam. The Fresnel equations can be expressed by relations of the segments K_i, K_t and K_r.

The reflected intensity of a single surface R_F is known as Fresnel reflectivity. Well above the critical angle it can be approximated with

$$R_F \simeq \frac{\delta^2}{4\alpha_i^2} = \left(\frac{\alpha_c}{2\alpha_i}\right)^4 \propto q^{-4}.$$

As δ is proportional to ρ_e, the Fresnel reflectivity is proportional to the square of the electron density of the surface, and with increasing incident angle (or q) it falls off with its inverse fourth power. This relation for the intensity decay is, however, only valid for smooth surfaces. As soon as the surface has a roughness on a scale comparable to the X-ray wavelength, the reflectivity drops even stronger. To account for this vertical root-mean-square roughness σ, an additional factor is introduced. This factor, $\exp[-(2k\alpha_i\sigma)^2]$, is known as Névot-Croce factor and it is multiplied to R_F for $\alpha_i \gg \alpha_c$. In order to describe X-ray interaction phenomena in terms of diffraction, it may be of advantage to handle the exact expressions with reciprocal wave numbers rather than the approximated angular expression. Therefore, the approximations in Eq. 3.19 may be re-written using the segments shown in Fig. 3.13:

$$r = \frac{K_i - K_t}{K_i + K_t} \quad \text{and} \quad t = \frac{2K_i}{K_i + K_t}.$$

Based on the assumption that $\vec{k}_i$ and $\vec{k}_r$ are in vacuum, their wave number is $k_i = k_r = k = 2\pi/\lambda$; the wave number of the transmitted beam is $k_T = nk$. Accordingly, the definitions $K_i = k \sin \alpha_i$ and $K_t = k\sqrt{n^2 - \cos^2 \alpha_i}$ apply.

In combination with Snell's law, it is possible to describe the specular reflection of multilayered systems with consecutive considerations of r and t of each single interface. However, such an analysis may become challenging for systems consisting of more than one thin slab upon a substrate. Parratt's recursive algorithm [198] provides a convenient solution to this complexity. It calculates the reflectivity of

each slab with thickness d_j and refractive index n_j within a stack of N layers, starting from an infinitely thick substrate from which reflections can be neglected, i. e. $r_{N+1} = 0$. Using the equations for reflected and transmitted amplitudes, the reflectivity of the jth layer is then given by

$$R_{j-1,j} = \frac{A_R}{A_T} = \left[\exp\left(\frac{-iKK_jd_j}{2}\right)\right]^4 \cdot \left(\frac{R_{j,j+1} + r_{j-1,j}}{1 + R_{j,j+1} \cdot r_{j-1,j}}\right)$$

with

$$r_{j-1,j} = \frac{K_{j-1} - K_j}{K_{j-1} + K_j} \cdot \exp\left(-2\sigma_{j+1}^2 K_j K_{j+1}\right).$$

The last recursion, i. e. $R_{1,2}$, will then yield the reflected amplitude of the uppermost layer and the total intensity reflected from the sample is $R = |R_{1,2}|^2$. The transmission of this first layer is by definition normalised to unity.

With this algorithm, the reflectivity of an arbitrary electron profile $\rho_e(z)$ can be modelled as function of the incident angle. This is of crucial experimental relevance, as it enables the remodelling of recordings of reflectivity profiles $R(\alpha_i)$ and delivers the corresponding $\rho_e(z)$ straightforwardly. The electron density of a multilayered system is mathematically expressed as step profile of the consecutive layers and the root-mean-square roughness σ_j of the jth interface is incorporated as error function:

$$\rho_e(z) = \sum_{j=0}^{N} \Delta\rho_{e,j} \frac{1}{2}\left(1 - \operatorname{erf}\left[\frac{z - z_j}{\sqrt{2}\sigma_j}\right]\right) \quad \text{with} \quad \Delta\rho_{e,j} = \rho_{e,j+1} - \rho_{e,j}. \tag{3.20}$$

As a result, sharp steps in $\rho_e(z)$ are blurred. It should be noted that this formalism is only valid for specular reflections, i. e. incident and reflected angle must be equal and in the same plane. In addition, it is required that the roughnesses are smaller than the layer thicknesses as otherwise discontinuities would appear in the reconstruction. However, if the jumps in the electron density between adjacent layers are comparatively small, as it is the case for lipid systems, the roughnesses may even be as large as the thicknesses.

Another possibility to describe the reflectivity profiles for $\alpha_i \gg \alpha_c$ can be found within the kinematical approximation. In this approach, the reflectivity is given by the so-called master formula for reflectivity,

$$R(q) = R_F(q)\left|\frac{1}{\Delta\rho_e}\int_{-\infty}^{\infty}\frac{\mathrm{d}\rho_e(z)}{\mathrm{d}z}\exp(-iq_z z)\mathrm{d}z\right|^2, \tag{3.21}$$

where $R_F(q)$ denotes the Fresnel reflectivity of an ideal interface between two media with density contrast $\Delta\rho_e = \rho_e(\infty) - \rho(-\infty)$; the second term is the Fourier transform of the derivative of ρ_e. With this formula, the reflectivity of a known electron

density distribution can be calculated easily. On the contrary, the inverse calculation is an ill-posed problem due to the missing phase information of the complex valued transformation. Thus, additional information is required to elucidate $\rho_e(z)$ from a measured reflectivity.

3.5.2 X-Ray Reflectivity of Oriented Lipid Model Membranes

Scattering Geometry

With specular X-ray reflectivity experiments it is possible to examine the structure perpendicular to the surfaces of aligned membranes while the lateral structure is averaged. Therefore, the momentum transfer probed is given by

$$q = \begin{pmatrix} q_x \\ q_y \\ q_z \end{pmatrix} = \begin{pmatrix} 0 \\ 0 \\ q_z \end{pmatrix} = \frac{4\pi}{\lambda} \sin \alpha_i. \tag{3.22}$$

To record the intensity profiles, the lipid film and a detector, placed behind the sample, are aligned parallel to the incident X-ray beam. This alignment represents the condition $q_z = 0$. Starting from this position, the angle of incidence α_i is gradually increased by a rotation of the sample (due to experimental circumstances the position of the X-ray beam is usually fixed, especially at synchrotron radiation sources). The detector is simultaneously rotated by $2\alpha_i$ to measure the reflected signal (at $\alpha_f = \alpha_i$ with respect to the sample surface). This geometry is shown in Fig. 3.14 A.

In this thesis, both single lipid bilayers and stacks of multiple bilayers have been measured using XRR. As elucidated in the previous section, each layer of a multilamellar sample provides contrast for an X-ray which will be partially reflected in correspondence. Interferences between all reflected beams will then give rise to a distinct reflectivity pattern which relates to all included layer thicknesses. For a single lipid bilayer on a solid support, these interferences appear as “Kiessig fringes”. As already stated, the reflectivity is drastically amplified in a multilamellar stack due to multiple interferences, so that narrow Bragg peaks of high intensity result (Fig. 3.14 B).

Apart from the specular reflectivity, lipid samples always cause scattering contributions along the directions q_x and q_y owing to lateral inhomogeneities on mesoscopic length scale (nanometres to a few micrometres) like spatially fluctuating interfaces. These diffuse scattering contributions broaden the Bragg peaks laterally (“Bragg sheets”) and reflectivities along q_z must be corrected for this background in order to apply Parratt’s reconstruction analysis. To this end, the diffuse scattering is de-

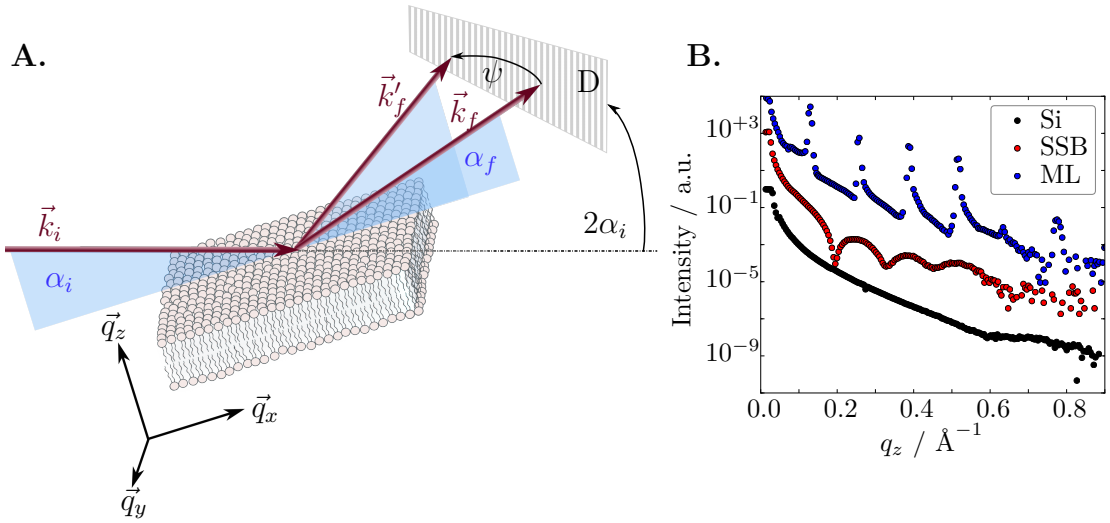

Figure 3.14 – X-ray reflectivity of aligned lipid membranes. A Geometry of XRR-measurements. The angle of incidence α_i is gradually increased by rotating the sample. The intensity of the reflected beam, i. e. $\alpha_f = \alpha_i$ and $\psi = 0$, is detected with the detector (D) at the angle $2\alpha_i$ with respect to the fixed position of the incident beam. Using multidimensional detectors, intensity contributions from diffuse scattering ($\psi \neq 0$) can be measured simultaneously. Panel **B** depicts typical reflectivity profiles of a lipid single bilayer (SSB, red) and a multilayer stack (ML, blue) upon silicon support. The pure wafer reflectivity is also shown (Si, black). The profiles are shifted vertically for clarity.

termined by separate offset-scans which are slightly detuned by a small angle $\Delta\alpha$. Using one- or two-dimensional detectors, the background can also be determined simultaneously with the recording of the specular XRR (cf. Fig. 3.14). In this work, the latter option is performed. Details on the experimental setup and data processing are presented in Sec. 3.5.4.

3.5.3 Grazing Incidence X-Ray Diffraction on Lipid Multilayers

Scattering Geometry

For X-ray diffraction in grazing incidence, the sample surface is oriented almost parallel to the X-ray beam with an incident angle α_i around the critical angle. The diffraction pattern, known as reciprocal space map, is recorded using an area detector placed in a distance D behind the sample (cf. Fig. 3.15). Hence, different scattering angles 2θ (and therefore also different scattering vectors $\vec{q}$) are measured simultaneously, each represented by a distinct pair of angles (α_f, ψ) within the detector image. The data obtained in this geometry provides information on the averaged lateral structure of multimembrane stacks[3] and is therefore complementary

[3]The solid supported bilayer system does not allow effective GID studies due to the pronounced scattering of the aqueous subphase and the comparatively low intensity contributions from the bilayer.

to the XRR data. In accordance with Fig. 3.15, the wave vectors of the incident $\vec{k}_i$ and scattered beam $\vec{k}_f$ are described by

$$\vec{k}_i = k \begin{pmatrix} \cos\alpha_i \\ 0 \\ -\sin\alpha_i \end{pmatrix} \quad \text{and} \quad \vec{k}_f = k \begin{pmatrix} \cos\alpha_f \cos\psi \\ \cos\alpha_f \sin\psi \\ \sin\alpha_f \end{pmatrix}$$

with $k = 2\pi/\lambda$. Due to the two-dimensional character of the lipid system, the in-plane components (q_x, q_y) of the scattering vector $\vec{q} = \vec{k}_f - \vec{k}_i$ are averaged, so that $\vec{q}$ may be decomposed into two components (q_r, q_z), parallel and perpendicular to the substrate surface. Thus, their GID patterns exhibit mirror symmetry with respect to the axis $q_r = 0$. The individual components are given by

$$q_r = \sqrt{q_x^2 + q_y^2} = k\sqrt{\cos^2\alpha_i + \cos^2\alpha_f - 2\cos\alpha_i \cos\alpha_f \cos\psi} \tag{3.23}$$

$$q_z = k(\sin\alpha_i + \sin\alpha_f). \tag{3.24}$$

The total scattering angle 2θ then equates to

$$\cos(2\theta) = \cos\alpha_i \cos\alpha_f \cos\psi - \sin\alpha_i \sin\alpha_f.$$

In conventional GID experiments, α_i is usually chosen to be smaller than the critical angle α_c of the sample to limit the penetration depth. Hence, with the samples used in this work, α_i should be smaller than the critical angle for silicon which is 0.07° at an energy of 25 keV. However, with a beam height of $\simeq 150$ μm, the condition $\alpha_i < \alpha_c$ would reduce the scattering efficiency since only a fraction of photons would impinge on the sample[4]. Since the penetration depth is no issue in this work, the angle of incidence was increased to obtain information on the entire sample stack (i. e. GID was not used in its conventional sense). Additionally, α_i had to be small enough to ensure that no detectable diffraction peaks are shaded by the sample horizon. Here, the incident angle was fixed to $\alpha_i = 0.2°$, which represents a good compromise between these considerations.

Lattice reflections from randomly ordered non-lamellar lipid phases are detected in the small-angle region of the diffraction image since these arise from the lipids' long-range order. As thermal disorder and other surface defects broaden the reflections from the lamellar lattice [199], these diffuse contributions also appear in the small-angle region. Reflections from short-range orders, on the contrary, appear in the wide-angle region. For lipid membranes, such short-range orders arise from cor-

[4]With a sample length of 10 mm in the beam direction, the angle at which the entire sample covers the X-ray beam is $\alpha_G \simeq 0.6°$ (see discussion on the illumination correction factor in Sec. 3.5.2).

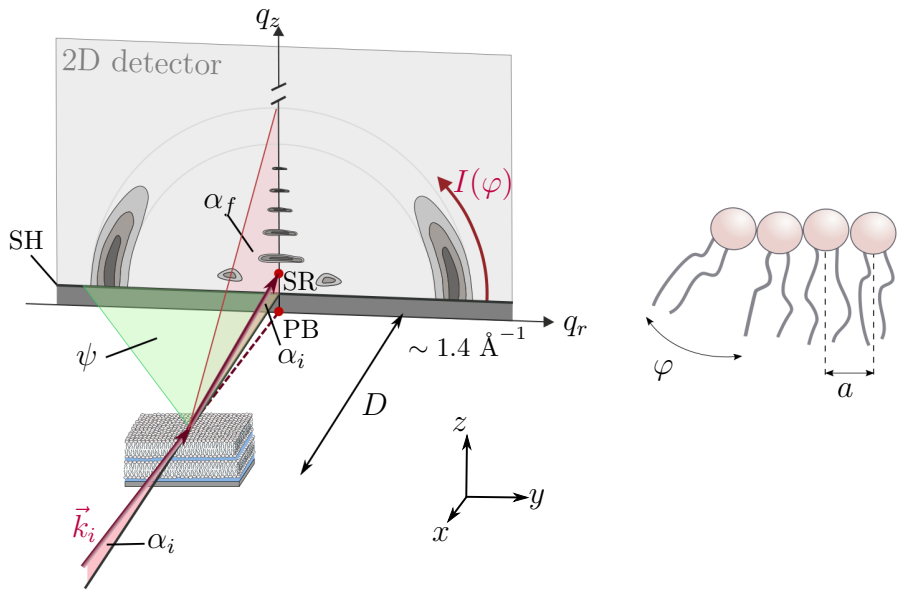

Figure 3.15 – Scattering geometry of GID experiments. The multilamellar lipid sample is tilted by the angle α_i with respect to the incident beam given by $\vec{k}_i$. The positions of the primary beam (PB) and the specular reflection (SR) as they appear on a two-dimensional detector, placed at distance D behind the sample, are indicated in the sketch. Along the q_z-axis, reflections from diffuse Bragg sheets are detected at equidistant angles α_f. Reflections from in-plane correlations appear for distinct pairs of angles (α_f, ψ) with $\psi \neq 0$. The arc-shaped reflection around 1.4 Å^{-1} represents the chain correlation peak. Its azimuthal intensity distribution $I(\varphi)$ reflects the chain tilt with respect to the membrane normal and its position is related to the averaged chain-chain distance a (both are indicated on the left). For small values of q_z, the projection of the sample horizon (SH) shades the reciprocal space map.

relations of their acyl chains. Their typical nearest-neighbour distance is about 4.5 Å and, thus, corresponds to a lateral momentum transfer of $q_r \simeq 1.4$ Å^{-1} [200]. Since the acyl chains are usually subjected to pronounced fluctuations in fluid phases, their characteristic reflection extends azimuthally with regard to $(q_r, q_z) = (0, 0)$. Hence, the chain correlation reflection provides information on the acyl chain's angular distribution φ relative to the membrane normal and the corresponding lateral chain packing $a(\varphi)$ [201].

3.5.4 Experimental Setups

The X-ray diffraction experiments presented in the following were carried out using synchrotron radiation at two different facilities: at the I07 beamline at the Diamond Light Source (Oxfordshire, UK) and at the high-resolution diffraction beamline P08 at the synchrotron light source PETRA III at DESY (Hamburg, Germany). Compared to X-radiation emitted from conventional sealed tubes, synchrotron radiation is the superior probe to examine lipid systems as it maintains a tremendously high

brilliance for monochromatic beams, i. e. it provides a vast photon flux at small angular divergence. According to this, weak scattering features from biological samples can be probed with higher sensitivity in remarkably shortened acquisition times.

At both beamlines, a photon energy of 25 keV was selected. Admittedly, the scattering cross sections for the lipid molecules increase with subsiding energies, however, the substrate-supported samples are also highly sensitive to radiation damage at lower photon energy. An energy of 25 keV provides a good compromise. With a few exceptions, all samples were measured at 25°C and 40°C, whereby the XRR at lower temperature was measured first. After one XRR acquisition, the lateral position of the sample was varied in order to prevent radiatio-induced sample damage. To ensure a correct sample positioning, the alignment procedure had to be repeated after this lateral movement. The GID measurements were performed subsequent to the XRR acquisition. Again, the lateral sample position was changed by ~ 1 mm to reduce effects of radiation damage. In the following, details on the particular sample environment and both beamline setups are presented.

Sample Environment

A custom-built Teflon cell with silicone seals and bolt-on Kapton windows glued to a steel frame was used for all diffraction-based experiments. This chamber has a dimension of 10 mm along the beam path, a height of 32 mm and a width of 42 mm; its inside has a volume of $\simeq 2.5$ ml. The silicon substrate (10×15 mm) can be assembled in three optional positions with respect to the windows. The uppermost position, in which the substrate is detached from the chamber bottom, is used for multilamellar lipid samples to avoid contact with bulk water which is needed to achieve a saturated pressure atmosphere (see below). The lowest possible position is defined by the bottom of the chamber. It is used for single bilayers to prevent that the bilayer slips from the substrate surface. Regardless of the particular position, the substrate wafer is fixed with a thin Teflon buckle. Prior to a measurement, the cell's accessories were cleaned in an ultrasonic bath for 10 min. The Teflon body and the screws were washed in acetone, while the Kapton windows and the silicone seals were immersed in methanol.

To ensure a saturated vapour atmosphere close to 100 % rH in which the lipid system is equivalent to the condition of excess water, two 30 μl droplets of ultrapure water were added to lateral water reservoirs. It should be noted, that the chamber properties are of fundamental importance with respect to the maximal bilayer hydration that can be achieved in it. Many investigators observed lamellar repeat distances which were significantly smaller than those in bulk water. This was commonly known as "vapor pressure paradox". In 1998, however, Katsaras demonstrated

that this effect is an artefact caused by temperature gradients and corresponding condensation effects within the chamber [202]. The Teflon chamber used in this work is covered with massive stainless steel sleeves which thermally isolate the inner cell volume and minimize temperature gradients. The inner side of these sleeves is lined with resistive heating pads out of silicone (Freek Ltd., Menden, Germany). The temperature inside the chamber is measured by a Pt100 sensor and the temperature control is performed by a heating unit, which regulates the current output for the resistive heating sleeves in response to the temperature input. As temperature control, a Lake Shore 335 unit (Lake Shore Cryotronics Inc., Westerville, OH, USA) was employed at P08 and a 340 model at I07. The relative humidity was measured independently using a DKRF400 probe with analog output (Driesen+Kern Ltd., Bad Bramstedt, Germany). With this design, a nominal humidity of 98 % rH was achieved in the sample cell. As a consequence, the membranes could not swell to their full extent. Leaving enough space for only a few water molecules in the interlamellar space ($\sim$ 1 nm), thermal undulations can be neglected. However, even at these partial hydration levels the interaction with HDPs may cause substantial disorder and fluctuations as it has for example been observed for Magainin in anionic membranes [203].

Experiments at the Surface and Interface Diffraction Beamline I07 at the Diamond Light Source

At I07 the white beam from the cryo-cooled undulator device was monochromatised to a photon energy of 25.00 keV using a Si(111) double crystal monochromator. The beam size at the sample position was adjusted to 250 μm $\times$ 300 μm (v $\times$ h) by a terminating set of horizontal and vertical slits ($\sim$ 40 cm before the sample) as well as a pair of Kirkpatrick Baez focusing mirrors which focus both the vertical and the horizontal beam dimensions independently and additionally suppress higher harmonic radiation. The energy resolution had a bandwidth of about $\Delta E/E \simeq 10^{-4}$ and the flux at the sample position was roughly 10^{10} photons/s.

The sample chamber was mounted in horizontal scattering geometry upon a hexapod on the (2+3)-circle diffractometer in the first experimental hutch of I07. A Pilatus 100k area detector (Dectris, Baden, Switzerland) with a resolution of 195 $\times$ 487 pixels and a pixel size of 172 $\times$ 172 μm^2 was mounted horizontally (i. e. with its long axis parallel to the plane of the storage ring) on a diffractometer circle at a detector-to-sample distance of 900 mm. This detector was used to record XRR profiles and the chain correlation peak in GID geometry. The latter was obtained by azimuthal detector scans from $\varphi = 0°$ to $\varphi = 90°$ in angular steps of $\Delta\varphi = 10°$, each with an acquisition time of 10 s. A full XRR scan was obtained from overlapping

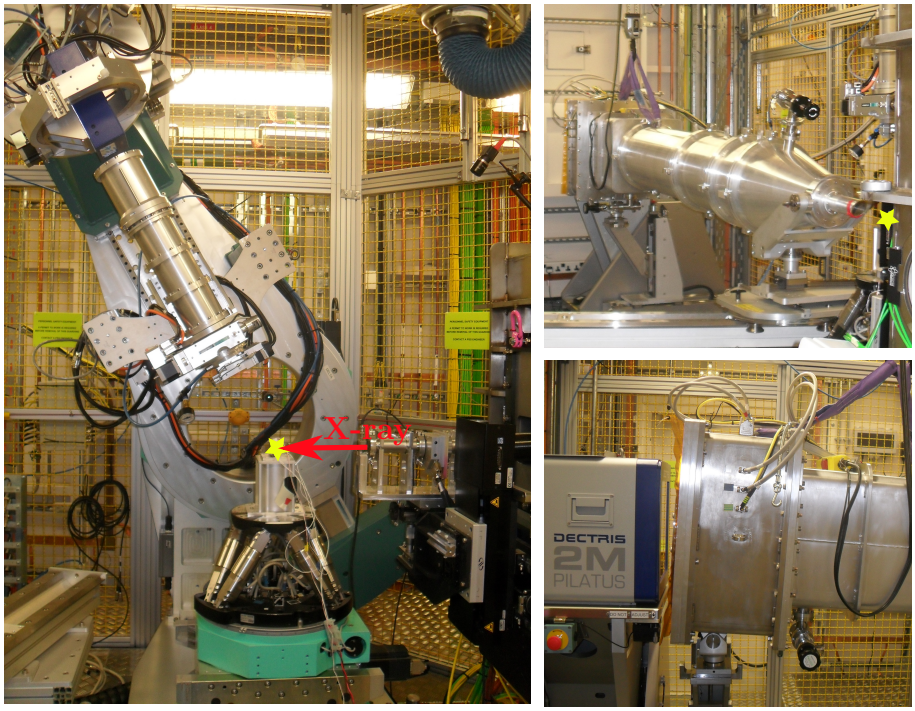

Figure 3.16 – Experimental setup at beamline I07. The position of the sample chamber in the center of the (2+3)-circle diffractometer is marked by a star. The left panel shows the Pilatus 100k detector mounted on the (2+3)-circle diffractometer (with the corresponding flight tube). The position of the incoming X-ray beam is indicated by a red arrow. On the left hand side, the $\simeq$ 2.8 m long flight tube between sample and Pilatus 2M detector is depicted.

scan snippets, each with appropriate attenuator settings to prevent oversaturation of the detector. The acquisition time for one data point was 1 s. To detect the small angle signals in GID experiments a Pilatus 2M area detector (Dectris), with 1475 pixels in the horizontal and 1679 pixels in the vertical direction (each having a size of 172 $\times$ 172 μm^2), was placed 2.96 m behind the sample. The primary beam was blocked using a beamstop (3 mm in diameter) at a distance of $\simeq$ 10 cm before the detector. One image was obtained from illuminations of 60 s. In order to increase the signal-to-noise ratio by reducing background scattering, helium-flushed flight tubes were installed between detector and sample as shown in Fig. 3.16.

Experiments at the High-Resolution Diffraction Beamline P08 at PETRA III

At P08 the photon energy of 25.00 keV was isolated from the polychromatic undulator beam using two double-crystal monochromators, the first equipped with Si(111) crystals and the second with Si(511) crystals [204]. The beam was collimated with compound refractive lenses between both monochromators, resulting in a divergence (FWHM) of 2 μrad vertically and 10 μrad horizontally. The corresponding flux of the primary beam was on the order of 10^{10} photons/s. Special about this setup is

that it provides a final energy resolution of $\Delta E/E \simeq 10^{-5}$ which is about one order of magnitude higher than than the bandwidth provided at I07 beamline. In addition, higher harmonics are effectively suppressed by the Si(511) double-crystal monochromator. The sample chamber was mounted in horizontal scattering geometry upon a x, y, z stage at P08's six-circle diffractometer (Kohzu Precision, Kawasaki, Japan) with Eulerian cradle. The X-ray beam was collimated to a size of 150 × 500 μm^2 (v × h) using a slit system at a distance of approximately 1 m in front of the sample.

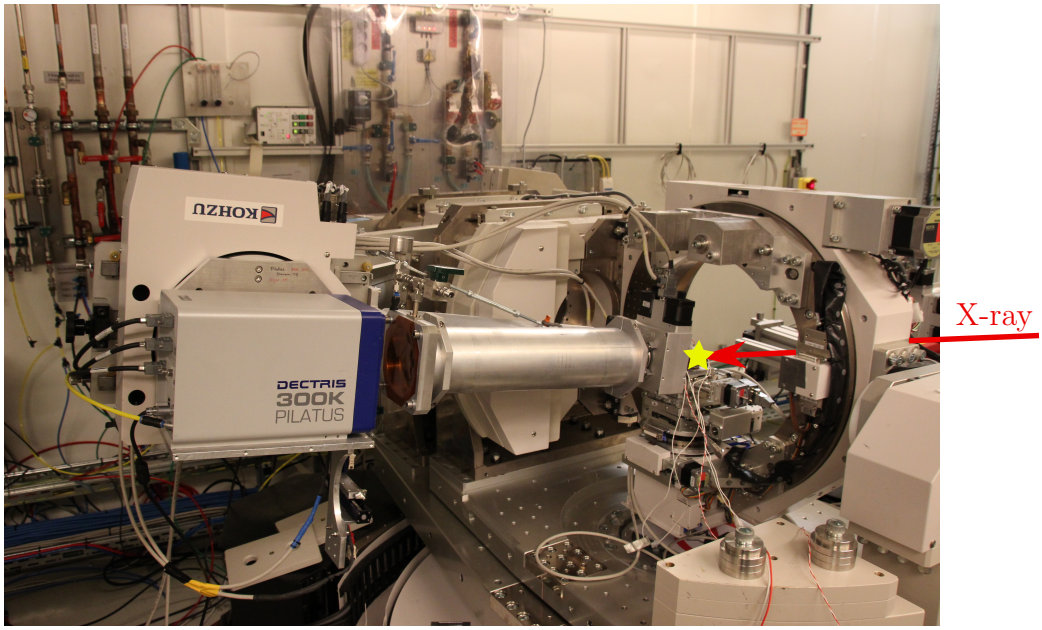

Figure 3.17 – Experimental setup at beamline P08. The star marks the position of the sample chamber in the center of the 6-circle diffractometer. The setup shown was used for measurements on multilamellar lipid samples, featuring the slit system behind the sample, the evacuated flight tube and the Pilatus 300k detector. For measurements on solid supported bilayer membranes, the Pilatus 300k detector was exchanged by a Mythen 1k detector. The position of the incoming X-ray beam is indicated by the red arrow.

XRR and GID measurements of multilamellar lipid samples were recorded by a Pilatus 300k area detector (Dectris) with a resolution of 619 × 487 pixels and a pixel size of 172 × 172 μm^2. It was mounted to the diffractometer at a sample-to-detector distance of 729.2 mm in horizontal orientation, i. e. with its short axis parallel to the plane of the storage ring[5]. The beam path was evacuated to a remaining pressure of 10^{-3} Pa using flight tubes sealed by Kapton exit windows up to ∼ 50 cm before the sample. The space between sample and detector position was evacuated, too, using a 50 cm long vacuum tube of 10 cm diameter equipped with a slit system. It

[5]Note that with this setup, it was not possible to acquire both the small-angle and the wide-angle diffraction simultaneously as the solid angle covered by the detector is too small. Thus, the detector position was varied and the complete diffraction pattern is an assembly of four independent acquisitions.

was also mounted on the diffractometer arm as shown in Fig. 3.17. The essential advantage of this tube is a significant increase in the signal-to-noise ratio in the GID images since air scattering is reduced effectively. However, as its diameter is comparable to the field of view of the Pilatus 300k detector (8.38×10.65 cm^2), it also implicates scattering contributions from the exit window edges. These contributions vary strongly with the detector position as the corresponding tube movement involves a positional change relative to the primary beam. This practical disadvantage impedes to merge GID images from different detector positions in a proper way.

Reflectivity profiles were acquired with an angular resolution of 0.01° and an acquisition time of 1 s for each position. An automated attenuation system was employed to prevent oversaturation of the detector. In case of GID measurements, a funnel-shaped beamstop of 1 mm diameter was positioned at the detector window to attenuate the primary beam intensity. Due to the detector dimensions and the fixed sample-to-detector distance, a complete recording of the GID pattern, including both small and wide-angle regions, required four different detector positions: two horizontal positions and two which are shifted vertically to cover the full angular extent of the chain correlation peak and to prevent information loss due to the horizontal gaps of the detector's active area. Due to the sample's mirror symmetry it was sufficient to acquire only one moiety of the reciprocal space pattern. For each detector position, the acquisition time was set to 60 s. Note that only the GID data obtained at P08 is presented in this work. Corresponding data sets obtained at I07 were used to verify the findings.

XRR recordings of single supported bilayers were acquired similar to those of the multilamellar samples. However, instead of the area detector a Mythen 1k line detector (Dectris) with 1280 pixels and a pixel size of 8000×50 μm^2 (h $\times$ v) was employed. It was mounted to the diffractometer in vertical orientation (i. e. with the pixels along the plane of reflection).

3.5.5 XRR Data Analysis

Data Processing

For each α_i, a single Pilatus 300k detector image was recorded. From each of these images, three horizontal detector lines across the specular reflection were extracted and integrated vertically. This processing created a two-dimensional intensity distribution $I(\alpha_i, \Delta\text{px})$, where Δpx denotes the respective pixel numbers. An exemplary horizontal line of $I(\alpha_i, \Delta\text{px})$ is shown in Fig. 3.18. The data from the Mythen 1k detector in vertical alignment was processed similarly, but resulted in a one-

dimensional data set $I(\alpha_i)$. The vertical angular dependency of the reflectivity, θ, was transformed into q-space using the relation given in Eq. 3.24[6].

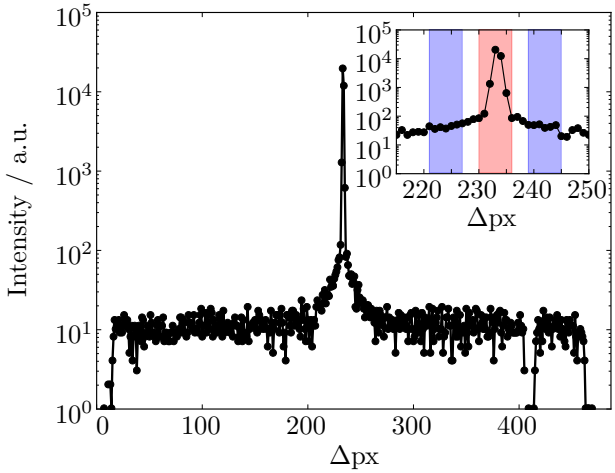

Figure 3.18 – Horizontal intensity profile of an XRR scan at the position of a Bragg peak. To obtain the specular reflectivity, the specular intensity $I(q_z, \Delta\text{px}_{spec})$ was integrated (red box in the inset) and the average of the diffuse background $I(q_z, \Delta\text{px}_{back})$ (blue boxes) was subtracted. This exemplary profile was obtained from a lipid multilayer sample containing Ece1-III$_{\text{KR}}$.

Thereafter, $I(q_z, \Delta\text{px})$ is corrected for the beam's footprint using a correction factor C_I which can be determined from the following geometric consideration: For small incident angles α_i, a certain fraction of incoming photons from the X-ray beam miss the sample as the incident beam is of height h. Thus, not all photons can be reflected. Assuming that the beam's cross section is rectangular and the sample length in beam direction is l, the entire sample is illuminated once the angle $\alpha_G = \arcsin(h/l)$ is reached (cf. Fig. 3.19). Hence, the correction

$$C_I = \begin{cases} \frac{l \sin \alpha_i}{h} = \frac{\lambda l q_z}{4\pi h} & \text{for} \quad q_z < q_G = \frac{4\pi}{\lambda} \sin \alpha_G \\ 1 & \text{for} \quad q_z \geq q_G \end{cases} \tag{3.25}$$

can be applied.

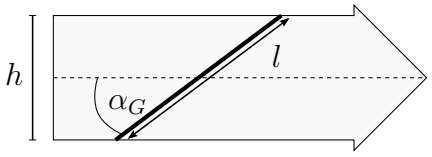

Figure 3.19 – Geometrical illustration of the illumination correction. For angles of incidence α_i smaller than α_G, the sample of length l does not reflect the entire beam height h. Hence, the illumination correction must be considered.

[6] A horizontal transformation according to Eq. 3.23 is not necessarily required and therefore omitted here.

To finally obtain the specular reflectivity $R(q_z)$, the central intensity profile $I(q_z, \Delta\mathrm{px}_{spec})$ is corrected for the diffuse scattering by subtracting an offset $I(q_z, \Delta\mathrm{px}_{back})$, which is determined as equally-sized average of two symmetric regions to both sides of the specular beam as shown in Fig. 3.18. The situation is different for the one-dimensional data sets obtained from the Mythen 1k detector, where the background is determined from a single region beneath the specular intensity.

Determination of the Electron Density Profiles From Lipid Multilayers

Since the kinematical approximation fails in general for XRR data at α_i close to the critical angle, the analysis of most of the reflectivities was not be elaborated within the framework of this approximation. Instead, the concept of the complex refractive was taken into account since it provides the appropriate approach to describe the observed phenomena. The specular reflectivity was fitted with Parratt's formalism (see Sec. 3.5.1). This procedure assumes ideal bilayer stacking, which includes constant bilayer thickness throughout the entire stack and a complete substrate coverage[7]. However, membrane imperfections due to partial dewetting and static defects from the preparation procedure lead to thickness variations and inhomogeneous coverage (cf. AFM images in Sec. 6.3.1 and [205]). Accordingly, Parratt's algorithm also comprises some drawbacks as it disregards these defects and artefacts caused by disorder and fluctuation. Since the influence of such defects rose sharply with increasing peptide content, the fitting quality was drastically impaired. Still, the corresponding simulations matched the experimental data with surprisingly good precision.

Alternatively, X-ray reflectivities may also be analysed with semi-kinematical approaches like the one derived in [141] and references therein or by the help of a Fourier synthesis as explained in [206]. The latter option was used to analyse reflectivities of phase separated multilayer samples. Due to the distinct height differences of the two lipid domains, the reflectivities of these samples exhibit two different families of Bragg reflections. As this would almost double the number of fit parameters, the application of the Parratt is not reasonable for such lipid systems. In brief, a Fourier synthesis utilises only the integrated diffraction intensities of the Bragg peaks to evaluate the coefficients of a Fourier series which represents the relative electron density within the unit cell. For this analysis, additional phase information ν_n is required. Due to the bilayer's mirror symmetry, ν_n of the Fourier coefficients reduces to a set of positive or negative values of unity. For the Fourier analysis, the

[7] In principle, a linear approximation for the substrate coverage can be included in the fit. However, this is not implemented in the MOTOFIT software used in this work.

XRR profiles were Lorentz corrected by multiplying the intensity with q^{-2} [141]. To obtain the set of Fourier coefficients, the peak intensities were modelled with Gaussian profiles and multiplied with ν_n using the phase combination -1, -1, $+1$, -1 which applies for DOPC samples [196]. A set of electron densities (without and with high peptide content) obtained from the dynamical Parratt recursion was compared to the one obtained from such a semi-kinematical Fourier synthesis. The profiles obtained from the two different analyses agreed well. The spatial uncertainties were less than $\pm$ 0.5 Å, demonstrating the validity of both the Parratt approach and the six-slab model applied (see below).

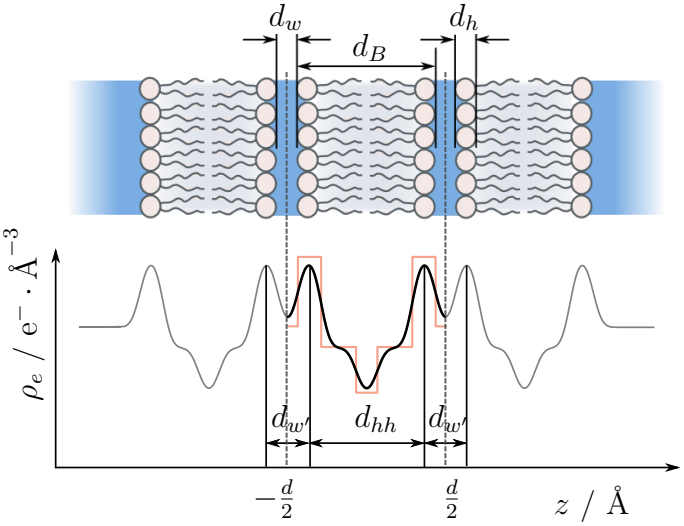

Figure 3.20 – Electron density distribution of a lipid bilayer including distance definitions. The upper part of the figure sketches a cross section of three stacked bilayers and the lower part shows the corresponding electron density $\rho_e(z)$. The maxima in $\rho_e(z)$ relate to the lipid headgroups and the minima to the interface between the opposing monolayer sheets. The step-profile (coloured in red) sketches the assumed six-slab-model (in this illustration the water layer is divided by two and attached to both sides of the headgroup slabs). In this work, the bilayer thickness d_B is approximated as headgroup-to-headgroup distance d_{hh}. Its difference to the lamellar spacing d defines $d_{w'}$.

The fitting of the experimentally obtained data $\log[R(q_z)]$ was carried out with a non-linear least-square method using the MOTOFIT software package [207]. The program provides either genetic optimisation or Levenberg-Marquardt algorithm to optimise the different parameters and calculates the reflectivity profile utilising the Abeles matrix formalism [208]. In MOTOFIT, an arbitrary number of sample layers j can be modelled, each having a thickness d_j, a complex X-ray scattering length SLD_j and a roughness σ_j. Whereby the connections between the X-ray scattering lengths and the corresponding refractive indices n_j are given by

$$\delta_j = \frac{\lambda^2}{2\pi}\,\mathrm{Re}(\mathrm{SLD}_j) \quad \text{and} \quad \beta_j = \frac{\lambda^2}{2\pi}\,\mathrm{Im}(\mathrm{SLD}_j).$$

Thus, the electron density ρ_{ej} of each slab can be calculated by dividing the real part of SLD_j by the classical electron radius r_0 (cf. Eq. 3.5.1):

$$\rho_{ej} = \frac{\mathrm{Re}(\mathrm{SLD}_j)}{r_0}.$$

The total electron density profile of the entire model system is then represented by a summation according to Eq. 3.20. The box model applied to describe the multilamellar lipid stack was comprised of a water layer on top of the bilayer stack and a silicon dioxide slab underneath it, which is the native oxide layer of the infinitely thick silicon substrate (cf. Fig. 3.11). These substrate parameters were fitted independently using the reflectivity of a pure silicon wafer. Their approximate quantities are summarised in Table 3.1. One lipid bilayer was modelled as multilayer of six different slabs: two headgroup layers (H1, H2), two acyl chain layers (C1, C2), a central slab for the interfacial region between both monolayer sheets (F) and a water spacing (W). Starting from the top, the succession of these layers is H1-C1-F-C2-H2-W. This multilayer was repeated for about $N \sim 200$ times[8]. For the fit, the profile had to fulfil the boundary condition of mirror symmetry. Hence, the following demands applied:

$$\begin{aligned} d_{H1} &= d_{H2} & d_{C1} &= d_{C2} & \\ \mathrm{SLD}_{H1} &= \mathrm{SLD}_{H2} & \mathrm{SLD}_{C1} &= \mathrm{SLD}_{C2} & \\ \sigma_{H1} &= \sigma_{C2} & \sigma_{C1} &= \sigma_F & \sigma_{H2} &= \sigma_W \end{aligned}$$

In addition, a minimum slab thickness of $d_j = 5$ Å was required and the SLD real part values were kept within reasonable limits, i. e. $11 \cdot 10^{-6}\text{Å}^{-2} \leq \mathrm{Re}(\mathrm{SLD}_{H1,H2}) \leq 15 \cdot 10^{-6}\text{Å}^{-2}$ and $4 \cdot 10^{-6}\text{Å}^{-2} \leq \mathrm{Re}(\mathrm{SLD}_F) \leq 7 \cdot 10^{-6}\text{Å}^{-2}$ (empirical limits). To account for absorption effects, it was attempted to fit the imaginary SLD parts of the substrate using Levenberg-Marquardt algorithm. Although these fits led to substantial reductions in data misfit for the XRR profile between Bragg peaks, the resulting values for β were non-physical since their values were about two orders of magnitude larger than the actual material values (which are roughly $\beta \sim 10^{-3}\delta$). Inserting the actual absorption values, however, did not notably affect the fit quality compared to values with imaginary parts of zero. Thus, absorption was neglected for simplicity and $\mathrm{Im}(\mathrm{SLD}_j)$ was set to zero for all slabs. Finally, the modelled parameters were collected to calculate the electron density profile of a bilayer and

[8]The real lipid system consists of much more bilayers ($N \sim 1000$). However, the effect of $N >$ 200 repetitions on the reflectivity profile is marginal. Only the calculation time is increased dramatically.

	d [Å]	$\mathrm{Re}(\mathrm{SLD}_j)$ [10^{-6}Å^{-2}]	σ_j [Å]
silicon	∞	21.2	1.4
silicon dioxide	6.9	18.5	3.0

Table 3.1 – Box model parameters of the silicon wafer. The parameters were obtained in an independent fit of the pure wafer reflectivity using Motofit.

the water spacing. From this profile, the distances d, d_{hh} and $d_{w'} = d - d_{hh}$ were determined as shown in Fig. 3.20.

Determination of the Electron Density Profiles From Single Bilayers

As a first step, $R(q_z)$ was normalised to the Fresnel reflectivity $R_F(q_z)$ of the silicon substrate which was fitted to $R(q_z)$ using data points up to $q_z \simeq 0.12$ Å^{-1} (cf. Eq. 3.19) and a least-square algorithm (cf. Figure 3.21). The normalised profile was then fitted using the iterative regularisation method presented in [209]. To this end, a corresponding MATLAB [210] routine REFREG.M provided in the supplementary information to this article was employed (cf. Fig. 3.22). The iterative regularisation method bases on a kinematic approach using the master formula of reflectivity in-

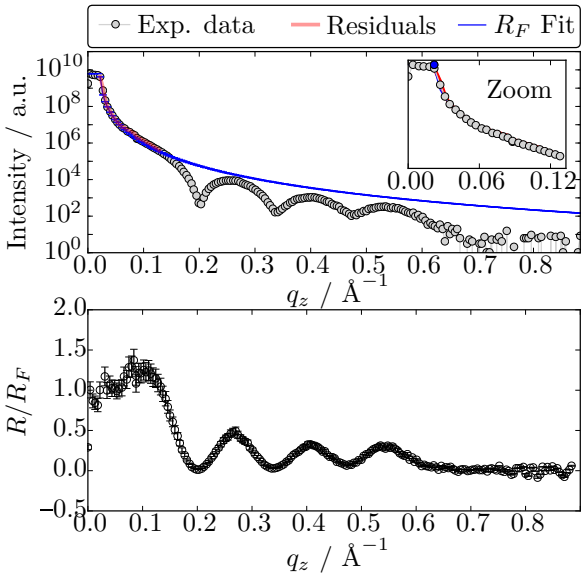

Figure 3.21 – Normalisation of the experimental reflectivity to Fresnel reflectivity of silicon. The upper panel shows an exemplary reflectivity profile $R(q_z)$ of a solid supported bilayer. The Fresnel reflectivity of an ideally smooth substrate (blue) is simulated using least-square fitting within the interval $q_z \in (0, 0.12$ Å$^{-1})$. The determined critical q_c-value for total external reflection is indicated as blue data point in the inset. The lower panel shows the final normalisation of $R(q_z)$ to $R_F(q_z)$. The errorbars represent an uncertainty of 10 %.

troduced in Eq. 3.21. The authors proved that the missing phase may be uniquely reconstructed if the sample contains one strong contrast, i. e. one interface with a sharp electron density jump, which is known and larger than the sum of all other jumps. With this at hand, their numerical method is capable to solve the inverse problem using an initial guess of a general non-parametric electron density profile model and Newton conjugated-gradient (CG) iterations. However, the formalism neglects absorption processes and certain *a priori* information is required. This includes a section a_z, in which the electron density distribution is known, and, at the same time, certain bounds which restrict the XRR reconstruction. The latter may be provided by experimental errors. In this thesis, it was found that approximated

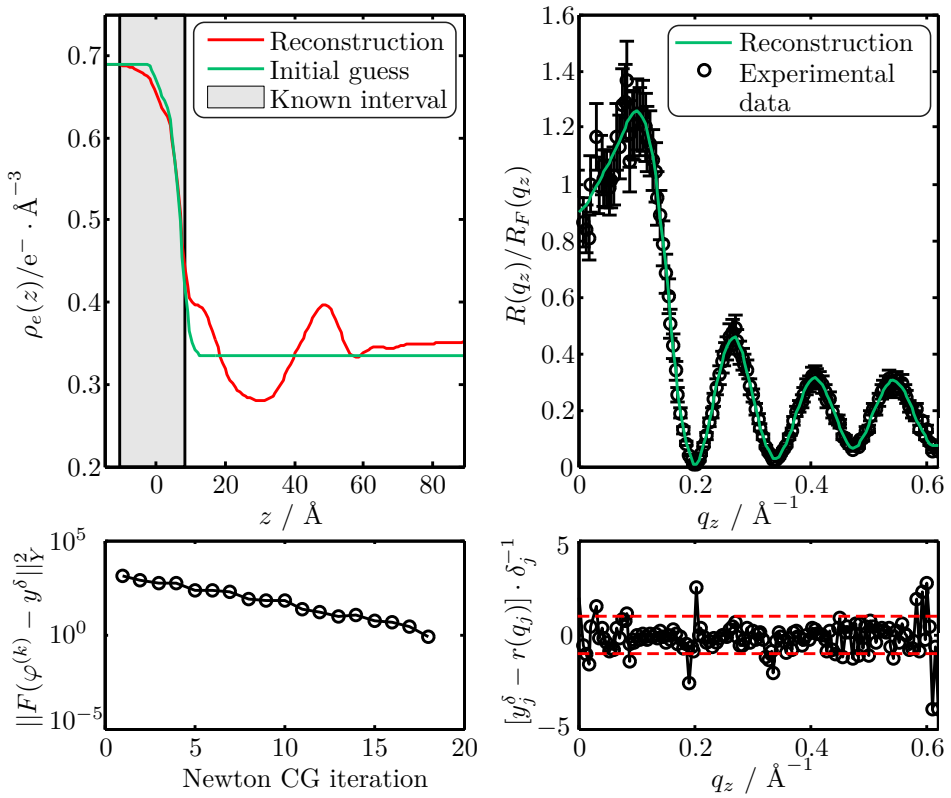

Figure 3.22 – Electron density reconstruction of a single bilayer using iterative regularisation. The figure shows the graphical output of the MATLAB routine REFREG.M [209]. The upper left panel contains the initial guess for the electron density reconstruction (green) and the final reconstruction of the single bilayer (red). The shaded area marks the interval a_z, in which the substrate profile was assumed to be a correct representation of the true one. The simulation of the corresponding experimental reflectivity (normalised to $R_F(q)$, solid green-line) is given in the upper right panel. The corresponding residuals, normalised to the expectation value of the simulated errors, are shown underneath. Most of them lie within the errorbars defined by the red-dashed lines. In the lower left panel, the data misfit is shown as function of Newton-CG-iterations. In this exemplary analysis, the algorithm stopped according to the discrepancy principle after 18 iterations, leading to a data misfit of about 0.87, representing a good fit to the experimental data.

errors of 10 % led to reasonable reconstruction results; the risk of over-fitting [209] was very high with smaller bounds. The known part of the electron density in solid supported bilayer systems was defined by the silicon substrate and its native oxide layer. Hence, the parameters given in Tab. 3.1 were used to model $\rho_e(a_z)$, the section in which the algorithm is forced to predominantly follow the initial profile. The regularisation approach was chosen over the dynamical approach using box models since no assumptions on the bilayer itself are required. Regardless of the exact procedure chosen, the resulting bilayer thicknesses are similar [209], which was, at least in this work, the result of primary interest.

3.5.6 GID Data Analysis

Data Processing

Dead or hot pixels of the raw images obtained with Pilatus 300k detector were masked, before the diffraction images were assembled to obtain one single diffraction image. To that end, the images were cut at distinct angles α_f or ψ in such a way that both the small-angle reflections and the chain correlation peak are largely displayed in the center of their original image. This was necessary because the images acquired at different detector positions were inhomogeneously affected by background scattering and, therefore, it was not possible to merge the images properly (e. g. using pixel binning) without obtaining immense artefacts. The assembled diffraction image $I(\Delta\mathrm{px}_z, \Delta\mathrm{px}_x)$ was then transformed into angular coordinates (α_f, q_ψ) using the relations

$$\tan\alpha_f = \frac{(\mathrm{pb}_z - \Delta\mathrm{px}_z)\, l_{px}}{D} - \alpha_i \quad \text{and} \quad \tan\psi = \frac{(\mathrm{pb}_x - \Delta\mathrm{px}_x)\, l_{px}}{D}.$$

for the vertical and the horizontal pixel dimension $\Delta\mathrm{px}_z$ and $\Delta\mathrm{px}_x$, respectively. In these relations, pb gives the pixel position of the primary beam, l_{px} the length of one pixel and D the distance between sample and detector. As a next step, the images were corrected for the horizontal polarisation of the synchrotron beam with $C_p = (\cos^2\psi)^{-1}$, before the transformation into reciprocal coordinates (q_z, q_r) was done (see Eq. 3.24 and 3.23). In principle, the polarisation correction was not mandatory for this particular setup since its influence is negligible – it results in intensity corrections smaller than 1 % even for scattering angles as large as 10°. The data obtained at I07 with Pilatus 2M and 100k detectors was processed similarly. Only slight modifications had to be applied to adapt the respective experimental situation (detector size and number of merged images).

Analysis of Small-Angle Reflections

The coordinates of reflections from non-lamellar lipid phases were extracted to determine the reciprocal point lattice corresponding to $|S_{hkl}(\vec{q})|$ which readily revealed the lipid phase in real space. In order to correctly extract the absolute two-dimensional electron density distribution it is further required to obtain the form factor amplitudes $|F_{hkl}(\vec{q})|$ of all observed reflections. To this end, additional measurements in other scattering geometries are necessitated due to the two-dimensional character of the samples [211]. The lacking information can be obtained from diffraction on powder samples, where it is also allowed to precisely measure in the vicinity of the direct beam, which is shaded by the sample horizon in GID measurements. Such powder samples can be prepared by using a substrate with a rough surface instead of smooth silicon wafers. On these rough supports the lipids will not orient with a preferential direction with respect to the substrate normal and thus, on a two-dimensional detector all reflections will appear as concentric circles. Such an analysis is, however, elaborate and not trivial. Since it was not mandatory to evaluate the effect of the peptide it was not part of this work.

Analysis of Chain-Correlation Peak

For the analysis of the chain correlation peak, radial intensity profiles $I(q)$ were extracted from the two-dimensional reciprocal space matrix for $q(\varphi) = \sqrt{q_z^2 + q_r^2}$. To avoid intensity artefacts on these profiles only the two horizontally shifted detector images were merged to one for this particular analysis. Thus, it was necessary to eliminate matrix values belonging to modular gaps of the detector area (white horizontal voids in Fig. 3.23) and only profiles up to an angle of $\varphi = 62.5°$ were accessible. Profiles corresponding to angles smaller than 2.5° were ignored because of the shadow from the sample horizon. Adjacent profiles with $\varphi = 0.1°$ were averaged over an opening angle of 5°. The cross sections of the chain correlation peaks show Lorentzian lineshapes. Thus, they may be evaluated as a function of φ using least-square fits of Lorentzian profiles with appropriate background approximation $f_{back}(q)$ [212]:

$$f_L(q) = \frac{L_0 \cdot \omega^2}{(q - q_0)^2 + \omega^2} + f_{back}(q),$$

where L_0 is the maximum peak intensity, q_0 the peak center and ω the half width at half maximum (HWHM). It was found, that the superposition of a linear function and a second Lorentzian profile, with its maximum at $q = 0$ Å^{-1}, modelled the background best. This background assumption is, however, only valid over the range of the peak. Close to specular beam and non-lamellar lattice reflections, the back-

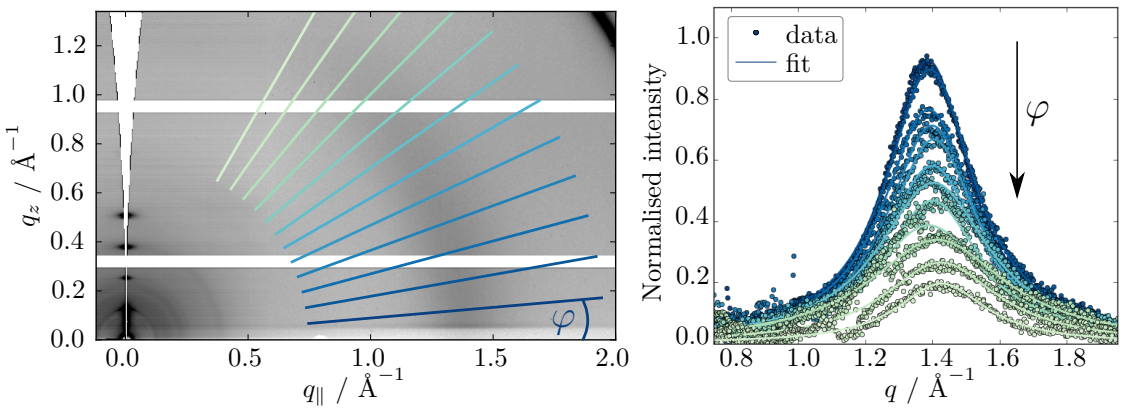

Figure 3.23 – Analysis of the chain correlation peak. The left figure shows the reciprocal space matrix and the radial cuts across the chain correlation peak, which appears around $q = 1.4$ Å^{-1}. The angular distance between the cuts is $\varphi = 5°$ and for each azimuthal angle the intensity within $\varphi \pm 2.5°$ is averaged. The resulting intensity profiles and Lorentzian fits are shown on the right; both are corrected for the background and normalised to the peak maximum of the 5°-profile: $[f_L(q) - f_{back}(q)]/[L_0(5°)]$.

ground is afflicted with strong non-linearities. Hence, the fitting was performed for $q \in [0.75, 1.95]$ Å^{-1}. Assuming a Lorentzian structure factor and a small peak width compared to the center position ($\omega q_0 \ll 1$), the acyl chains' correlation length ξ and the averaged lateral chain distance a can be derived from their radial distribution function [200]. Both parameters are given by

$$\xi = \omega^{-1} \qquad \text{and} \qquad a \simeq \frac{9\pi}{4q_0} - \frac{3\omega}{2q_0^2}. \tag{3.26}$$

In the framework of bulk smectic elasticity theory, a detailed analysis of the diffuse scattering signals would be capable to yield distinct elastic bilayer properties [201]. However, such an analysis was not carried out in this work as the elastic properties are not of primary interest for the aim of this thesis. Furthermore, the validity of the results is still questioned as the obtained values differ from atomistic simulations [213].

4 Biological Peptide Activity

This chapter briefly evaluates the biological activity of the Ece1-III peptides with respect to human red blood cells by means of two experimental approaches. Firstly, the cytoxicity of the individual peptide variants is screened in a haemolysis assay. Secondly, microscopic imaging (phase contrast, AFM) is utilised to illustrate the outward experience of the erythrocytes prior to and after their destruction by Ece1-III_{KR}.

4.1 Cytotoxic Activity

The cytotoxicity of the different Ece1-III peptide variants against human red blood cells was probed using a haemolysis assay as described in Sec. 3.2.4. Fig. 4.1 shows the resulting relative amount of lysed cells as function of the respective peptide concentration. Each of the values was obtained from at least two independent measurements.

Both, the amidated and non-amidated versions of Ece1-III_{KR} (i. e. Ece1-$III_{KR(N)}$ and Ece1-$III_{KR(C)}$), exhibit a strong cytotoxic activity even at concentrations $\leq 10\ \mu g{\cdot}ml^{-1}$. Although the amount of lysed cells at $2.5\ \mu g{\cdot}ml^{-1}$ is lower with Ece1-$III_{KR(C)}$ ($(15.1 \pm 5.2)\,\%$) than with Ece1-$III_{KR(N)}$ ($(51.2 \pm 5.9)\,\%$), both variants lead to $\simeq 60\,\%$ cell lysis at a concentration of $10\ \mu g{\cdot}ml^{-1}$. Upon further concentration increases to maximal $160\ \mu g{\cdot}ml^{-1}$, the relative effect becomes less intense and the haemolysis approaches the limit of full lysis hyperbolically. With this concentration-dependent progress, the cytotoxicities of both isoforms are comparable to the cytotoxic effect observed for the antimicrobial peptide Melittin, which is tested for comparison. The rhodamine-labelled Rho-Ece1-$III_{KR(N)}$ is also capable to induce haemolysis, albeit with an overall reduced efficiency. Indeed, with an amount of $(15.3 \pm 3.5)\,\%$ lysed cells at a concentration of $2.5\ \mu g{\cdot}ml^{-1}$, its lysis is comparable to the one obtained with Ece1-$III_{KR(C)}$. However, at $10\ \mu g{\cdot}ml^{-1}$ the cytotoxicity of Rho-Ece1-$III_{KR(N)}$ is already significantly reduced to an amount of $(20.3 \pm 2.7)\,\%$. Even at the highest concentration probed, only a maximum level of $(56.1 \pm 6.8)\,\%$ haemolysis is reached. Again, the concentration dependence shows a hyperbolic approach to this saturation level. Though reduced in its extent, this

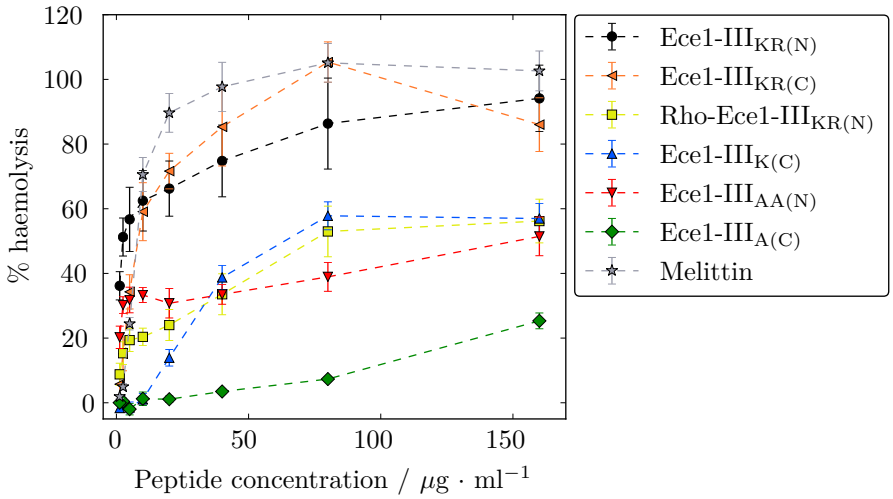

Figure 4.1 – Cytotoxic activity of different peptide variants. The relative amount of lysed erythrocytes is shown as function of the peptide concentration. Both the cytotoxic activity of the amidated Ece1-III$_{KR(N)}$ (●) and non-amidated Ece1-III$_{KR(C)}$ (◀) isoforms are comparable to that of Melittin (★), whereas the variants Ece1-III$_{K(C)}$ (▲), Rho-Ece1-III$_{KR(N)}$ (■) and Ece1-III$_{AA(N)}$ (▼) exhibit a notably reduced activity. The lowest toxicity is observed for Ece1-III$_{A(C)}$ (◆). The data was obtained from at least two measurements. The values represent the calculated mean and the errorbars the respective standard deviation.

observation verifies that the toxic activity of Ece1-III$_{KR(N)}$ is preserved despite the synthetic addition of the rhodamine label. A similar cytolytic behaviour is also observed for Ece1-III$_{K(C)}$ whose C-terminal charge is reduced to +3 compared to Rho-Ece1-III$_{KR(N)}$ or Ece1-III$_{KR(N)}$, which have a cationic charge of +5. Unlike Rho-Ece1-III$_{KR(N)}$, however, the lysis does not set in until a minimum concentration of 10 μg·ml^{-1} is reached. On the contrary, Ece1-III$_{AA(N)}$, which has also a C-terminal charge of +3, leads to a pronounced lysis of $(20.2 \pm 3.5)\,\%$ even for the lowest concentration probed (1.2 μg·ml^{-1}). However, its cytotoxicity does then only slightly but linearly increase with increasing peptide concentration. The relative amount of lysed cells at a concentration of 160 μg·ml^{-1} is $(51.4 \pm 6.0)\,\%$. Since its concentration dependence proceeds rather linearly than hyperbolically, it is possible that the cytoloytic effect of Ece1-III$_{AA(N)}$ may further increase with even higher peptide concentration. Similar to Ece1-III$_{K(C)}$, Ece1-III$_{A(C)}$ does not induce lysis at concentrations lower than 10 μg·ml^{-1}. With increasing concentration the observed haemolysis proceeded linearly up to $(25.3 \pm 2.4)\,\%$. This progression is comparable to the one observed for Ece1-III$_{AA(N)}$, although offset by $\sim 25\,\%$. Compared to Ece1-III$_{AA(N)}$, it has one terminating hydrophobic arginine less and due to the missing amidation its C-terminal charge is also reduced to +2.

In summary, the results of this assay suggest the following conclusions: (i) The amidation state of Ece1-III$_{KR}$ does not notably affect its cytotoxic effect. (ii) The N-terminal rhodamine label reduces the cytolytic activity by a factor of ~ 0.5. (iii)

The reduced C-terminal charge of Ece1-III$_{\mathrm{AA(N)}}$ and Ece1-III$_{\mathrm{K(C)}}$ impedes the cytotoxicity in a similar way and for Ece1-III$_{\mathrm{K(C)}}$ a certain minimal concentration is required to obtain lysis. (iv) The shorter and less cationic variant Ece1-III$_{\mathrm{A(C)}}$ exhibits its cytolytic potential only at high concentration. Due to the diversity of the observed effects, no general rule can be derived for the impact of the varying C-terminal properties on the cytolytic peptide activity. The missing amidation in peptides with less polar C-terminus, however, seems to impede the overall cytotoxicity, while the amidation has no obvious effect on the variant terminated by the additional polar residue arginine (R).

4.2 Microscopically Visible Effects on Erythrocytes

To get a deeper understanding of the underlying mechanisms of the evidenced killing, the outward appearance of the erythrocytes before and after their interaction with the peptide was studied using phase contrast and atomic force imaging. Representative images are shown in Fig. 4.2. The phase contrast images visualise two distinct

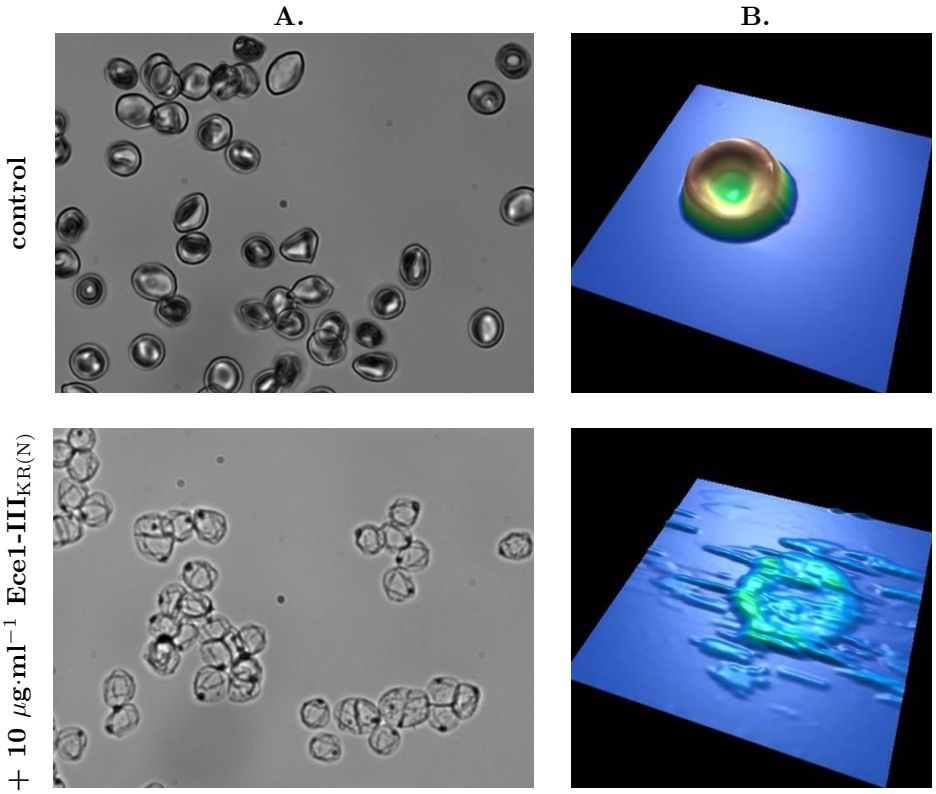

Figure 4.2 – Microscopic changes in erythrocytes induced by Ece1-III$_{\mathrm{KR(N)}}$. **A.** Phase contrast and **B.** AFM height images of erythrocytes prior to (upper panels) and after the addition of 10 μg·ml^{-1} Ece1-III$_{\mathrm{KR(N)}}$ (lower panels). The samples were prepared as described in Sec. 3.4.2 and studied at room temperature. The phase contrast images were obtained with an Olympus IX81 microscope (Tokyo, Japan). The AFM images depict an area of 15 × 15 μm^2 in a in a three-dimensional perspective.

outcomes: First, an increased cell translucency which indicates the leakage of cell content. Second, the loss of the cells' typical biconcave shape which implies that Ece1-III$_{\mathrm{KR(N)}}$ alters the membrane curvature. The images obtained by AFM imply similar effects as the biconcave erythrocytes become flat and appear squashier after their incubation with Ece1-III$_{\mathrm{KR(N)}}$. Accordingly, it is assumed that the peptide dramatically affects the bilayer structure which consequently disturbs the integrity of the plasma membrane and leads to the cell's death.

In order to understand the varying activities of the different peptide variants, it is necessary to elucidate their distinct properties on a structural level. This aspect is addressed in the following chapter. Thereafter, the properties of the peptides' interactions with lipid model membranes are studied. This is required to explain the detailed mode of action of the direct damage of the cell envelope.

5 Peptide Characteristics

The following chapter focusses on structural characteristics of Ece1-III$_{KR}$ and examines its differences to the variants Ece1-III$_{K}$ and Ece1-III$_{AA}$. Possible secondary structure formations and corresponding amino acids positions are assessed by model calculations and experimentally evidenced. Thereby, information on the peptides' secondary structure and possible changes in presence of lipid vesicles are obtained by CD measurements in solution. Finally, the amphipathic character of the peptides is demonstrated by film balance experiments.

5.1 Theoretical Analysis of the Peptide Sequence

5.1.1 Net Charge

As mentioned in Sec. 1.4, the net charge of membrane-active peptides is one of the key factors for the interaction with lipid membranes and it is assumed to predominantly determine the peptide's membrane selectivity. The net charge of Ece1-III$_{KR(N)}$ at pH 7.0 is made up of the protonated N-terminal amino group NH_3^+, and the four amino groups belonging to the basic amino acid residues arginine and lysine. The natural peptide (Ece1-III$_{KR(C)}$) contains a negative charge from the deprotonated carboxyl group COO^- at the C-terminus, which compensates one of these positive charges. The amidated peptide version, with a terminating carboxamide $CONH_2$, on the contrary has no such compensation. Thus, the natural and the amidated Ece1-III$_{KR}$ result in a net charge of +4 and +5, respectively. The net charge of the shorter, non-amidated Ece1-III$_{K(C)}$ is reduced by −1 since the arginine residue is cleaved. Through the substitution of the terminating lysine and arginine residues, Ece1-III$_{AA}$ results in a net charge of +2 for the non-amidated and +3 for the amidated variant. The net charge of Ece1-III$_{A(C)}$ is also +2.

With a net charge of +4, Ece1-III$_{KR(C)}$ compares well with the charge average of +4 of all cationic antimicrobial peptides listed in the Antimicrobial Peptide Database [214–216]. Due to their moderate cationic net charges, it is assumed that the peptides have no pronounced selectivity for bacterial cell envelopes and that hydrophobically driven interactions play an important role. However, due to electrostatic

attractions, its binding to acidic lipids might still be pronounced compared to zwitterionic lipids.

5.1.2 Secondary Structure Prediction

Function and mode of action of peptides or proteins are closely related to their structure. Hence, structural analyses and the identification of possible interaction sites are inevitable to gain insights into peptide-peptide or peptide-membrane interaction processes. However, detailed structural information can only be resolved by X-ray crystallography or NMR studies. Both usually involve extremely high experimental expenditures since the samples have to be crystallised or labelled with different isotopes. For peptides, several theoretical approaches have been introduced which attempt to predict secondary structure conformations by analysing the primary structure information, i. e. the amino acid sequence.

Helical Wheel Analysis

The amino acid sequence of a peptide already allows tentative conclusions on possible functional properties. Membrane-active peptides for instance are usually featured by a spatial segregation of hydrophobic and hydrophilic amino acid residues. Periodic occurrences of doublets or triplets of apolar residues, alternating with similar successions of polar residues usually lead to the formation of amphiphilic α-helices. On the contrary, cysteine-rich hydrophobic clusters in the central section of a sequence with terminating hydrophilic residue successions rather tend to form folded β-sheets. Therefore, graphical analyses can readily be employed to estimate a peptide's amphiphilicity by a visualisation of the periodicity of hydrophobic and hydrophilic residues. One commonly used method is the helical wheel projection introduced by Schiffer and Edmunson [217], where amino acid residues are plotted on a circle and consecutive residues are separated by an angle of 100° with respect to the centre of the circle. This procedure results in 18 possible positions for consecutive residues.

Fig. 5.1 shows the helical wheel projection of the full amino acid sequence of Ece1-III$_{\mathrm{KR}}$. Its sequence contains alternating patterns of apolar residues which are shown in black and polar residues which are coloured in blue – except for the basic residues arginine and lysine, both have a positive net charge of +1 at physiological pH and are depicted in red.

The helical wheel implies that the hydrophobic residues tend to cluster on one side and the polar residues form a hydrophilic face on the opposite side of the α-helix. However, it is unlikely that all residues participate in forming one linear α-helix as some polar residues close to the C-terminus also plot on the rather hydrophobic

face. In order to simplify this illustration, the number of amino acids is reduced and the helical wheel projection of two separated is depicted in Fig. 5.2. The proline residue P^{14} was chosen as break point for both partial projections since proline is commonly known to interrupt helix formations as it lacks a hydrogen-bonding donor group itself and hydrogen bonding to the preceding residue is impeded by steric clashes [218]. The partial projections shown in Fig. 5.2 clearly illustrate that an α-helical structure formation of the first section of Ece1-III's sequence would result in a wide assembly of hyrdophobic residues and an opposing narrow region with hydrophilic residues. The same applies for the second section of the sequence. With this kind of macroscopic amphiphilicity the peptide would be able to align at the amphiphilic interface of a bilayer – between the hydrophobic acyl chain core and the polar headgroups. The three terminating amino acid residues N^{30}, K^{31} and

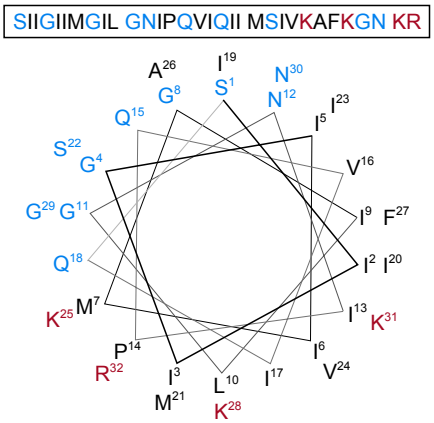

Figure 5.1 – Helical wheel projection of Ece1-III$_{KR}$. Alkaline residues are coloured in red and the remaining polar residues in blue. All apolar amino acid residues are shown in black.

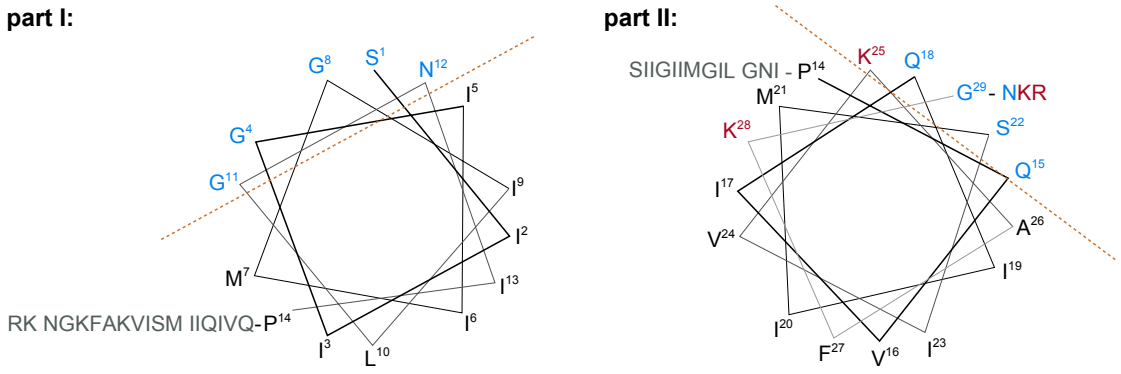

Figure 5.2 – Helical wheel projections of Ece1-III$_{KR}$ separated in two parts. Left: First part of the peptide sequence. Right: Second sequence part. Alkaline residues are coloured in red and the remaining polar residues in blue. All apolar amino acid residues are shown in black. The dashed line indicates the interface between hydrophobic and hydrophilic helix faces.

R^{32} in Ece1-III_{KR} are excluded from the helical wheel since the projection would suggest a location inside the hydrophobic region which is not likely due to their high polarity. The free energy cost of partitioning this polar carboxyl terminus into the hydrophobic bilayer core is highly unfavourable [102]. However, it can also argued that these residues reside inside the hydrophobic region and stretch their long ($\sim$ 6 Å) side chains, carrying the positive charge at their ends, out to the more preferable polar headgroup environment. Such a 'snorkelling mechanism' of arginine and lysine has previously been evidenced for the membrane-partitioning of amphipathic α-helical model peptides [219, 220]. According to this, it has been proposed that the snorkelling leads to an increase of the hydrophobic part of the α-helix at low energetic cost, which in turn allows a deeper position in the membrane and consequently a stronger binding [221].

3D Modelling

In order to get a more detailed idea on the conformational properties of the Ece1-III variants, structural models were generated using two different peptide structure prediction web servers, Robetta[1] and PEP-FOLD[2]. The latter provides a *de-novo* modelling approach which predicts the folding of short peptides with high accuracy. Currently, it is capable to handle amino acid sequences starting from 9 residues up to 36 residues. Its algorithm bases on the concept of a structural alphabet, i. e. the starting point of the computation is an ensemble of structural prototype elements which are able to describe the diversity of possible protein conformations. Subsequent to the assembly of the structural alphabet, coarse-grained force field simulations are performed which obtain different possible solutions. These predicted results are clustered in groups of similar models which will be ranked by the lowest sOPEP energy value (which is the optimised potential for efficient structure prediction). This sorting procedure of the clusters usually results in the proposal of native or near native conformations in the top 5 ranks [222]. Please refer to the literature for a detailed description of the model calculations and the sorting algorithm of PEP-FOLD [222–226]. The results presented here correspond to 100 simulation runs for each structure predicted. As observed previously [225] and verified in the present work, this number is sufficient to give reproducible results which are invariant to 200 simulations.

Fig. 5.3 A shows the local structure prediction profile which depicts the probabilities of each structural alphabet letter against the corresponding residue positions. The best ranked model for the sequence of Ece1-III_{KR} is shown in Fig. 5.3 B. Illus-

[1]Robetta is available at `http://robetta.bakerlab.org`.
[2]Available at `http://bioserv.rpbs.univ-paris-diderot.fr/services/PEP-FOLD/`.

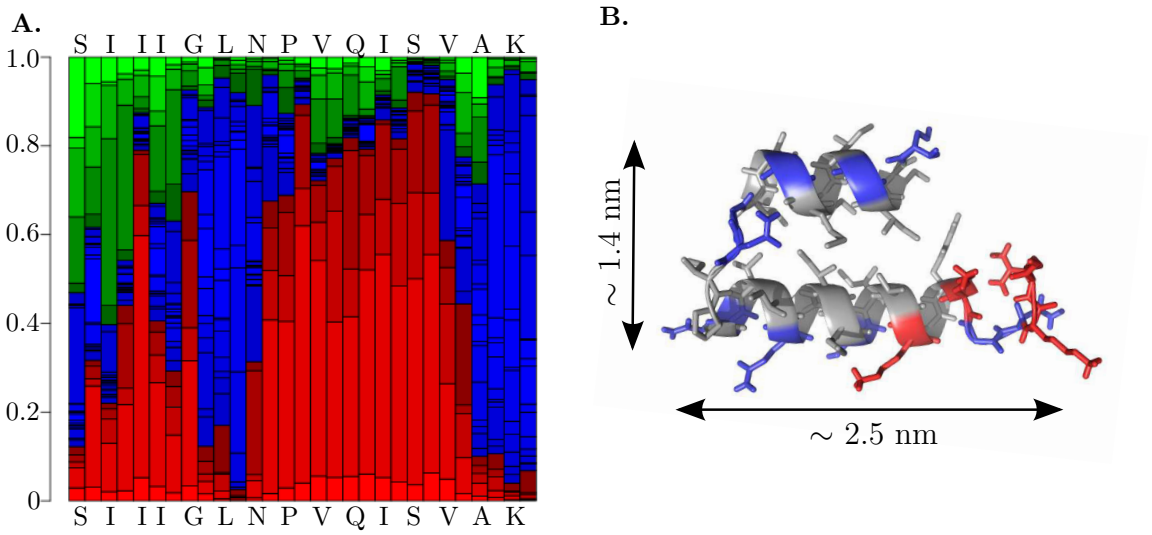

Figure 5.3 – Secondary structure prediction of Ece1-III$_{KR}$ using PEP-FOLD. A. Local structure prediction profile of Ece1-III$_{KR}$ representing the probabilities of structural alphabet letters for each residue from S^{1} to R^{32}. Helical (red), extended (green) and coil (blue) structure elements are illustrated. **B.** Three dimensional cartoon illustration of the amino acid backbone and respective side chains of the best ranked Ece1-III$_{KR}$ model. Apolar residues are shown in grey, basic residues are coloured in red and the remaining polar residues in blue. The 3D structure was rendered using PyMOL (Schrödinger LLC, New York, NY, USA), approximated length scales are indicated.

trations of the remaining 4 best ranked models, the predictions for Ece1-III$_{AA}$ and Ece1-III$_{K}$ are not shown here since all these structures are highly similar to each other. The structure presented in Fig. 5.3 B is thus considered as adequate representative for all peptide variants. All secondary structures predicted by PEP-FOLD have a predominant α-helical content. The analysis with STRIDE [227] revealed that $\sim$ 66 % of the amino acids participate in the formation of α-helices; the remaining residues are randomly structured. From Fig. 5.3 B it can be seen that the hydrophilic residues align at one face of the α-helix, whereas the major amount of the helix surface has a hydrophobic character. This is similar to the prediction of the helical wheel above. The model structure further demonstrates that the terminating amino acid residues N^{30}, K^{31} and R^{32} belong to the random coil structure. In consequence, it is assumed that Ece1-III$_{KR}$ aligns its amphiphilic interface parallel to the headgroup/chain interface of a lipid bilayer – burying its hydrophobic face deeply into the membrane interior while keeping its hydrophilic face in close contact to the polar headgroups. The polar C-terminal tail structure may seek its preferred location in this orientation in a flexible manner. The same holds true for the shorter variant Ece1-III$_{K}$. The main difference to the Ece1-III$_{AA}$ peptide is that the coiled tail structure is composed of the two hydrophobic residues alanine. The peptide will have to anchor these residues inside the hydrophobic lipid core which presumably leads to a tighter peptide-lipid binding. Another feature that all predicted struc-

tures have in common, is that their helices are not consistent throughout the entire peptide length as a strong kink occurs coincident with the position of the proline residue. For the amphibian defence peptide gaegurin, it has been shown that this kind of flexible hinge is pivotal for the membrane penetration. A linear alanine derivative of this peptide exhibited preserved binding affinity for anionic bilayers but resulted in reduced antimicrobial activity but [228]. Likewise, Dathe and co-workers [53] reported that the proline-induced kink in alamethicin is essential to its cytotoxicity. The resulting bent-rod structure of the Ece1-III variants are therefore also assumed to strongly influence the membrane disruption.

The Robetta web server used a template-based approach to model the three-dimensional structure of the different Ece1-III variants. Prior to the actual structure prediction Robetta uses Ginzu domain parsing to identify similar amino acid domains which are already deposited in the protein data bank (PDB) [229, 230]. Similar to the prediction by PEP-FOLD, Robetta also presents five possible models which are ranked according to the probability of their alignment clusters.

For Ece1-III$_{\mathrm{KR}}$, the predicted homolog entry in the PDB is 2V6L [231]. The comparative modelling of Robetta then yielded structures similar to the ones predicted by the *de-novo* approach of PEP-FOLD, i. e. discontinuous α-helices with C-terminal random coil structures. However, the extent of the kink between both α-helical parts varied. As already indicated in the corresponding analysis of the PEP-FOLD structures, this observation can be explained with the high flexibility of the hinge, lacking particular bonds between the helices. In contrast to the PEP-FOLD prediction, Robetta also suggests two α-helical conformations without a discontinuity on the fourth and fifth place of the probability ranking. Taking all predicted model structures into account, it is however most likely that each Ece1-III variant partially forms a highly flexible α-helix with randomly ordered anchor chains at the C-terminus.

5.1.3 Classification of Amphipathic Helix

Hydrophobicity and amphiphilicity of a secondary structure are closely related to the peptide's membrane activity as these properties define possible orientations within the amphipathic lipid environment. Considering that the particular secondary structure is often not certainly known, it tapers to a highly complex problem to derive detailed predictions on the amphiphilic behaviour. An easy and commonly used approach to overcome this problem has been proposed by Eisenberg *et al.* [232]. Therein, the three-dimensional amphiphilicity of an α-helical peptide backbone is reduced to a single quantity, the hydrophobic moment μ_H of an amino acid sequence.

This dipole moment provides information on the structural alignment of hydrophilic and hydrophobic residues in a regular repeat structure. For consecutive residues i it is estimated by

$$\mu_H = \sqrt{\left(\sum_i H_i \cos(i\delta)\right)^2 + \left(\sum_i H_i \sin(i\delta)\right)^2}.$$

The basic assumption of this equation is that each residue can be represented by a single vector of length H_i, which is proportional to its hydrophobicity and points perpendicular to the axis of an α-helix or the strand of a β-sheet. Hydrophobic residues are indicated by positive values of H_i, while negative values indicate hydrophilic residues. δ describes the angle separation of two consecutive backbone residues and analogue to the helical wheel projection, it can be approximated by 100° for an α-helix. By introducing the hydrophobic moment plot methodology, Eisenberg and co-workers then attempted to assign the behaviour of putative amphiphilic α-helices in the presence of lipid bilayers according to three possible scenarios: an accumulation parallel to the bilayer surfaces, a transmembrane alignment or the formation globular aggregates [233]. In this approach the most amphiphilic part of a putative α-helix is determined and plotted against its corresponding hydrophobicity. The researchers found that different types of peptides cluster in separated areas of this plot and thus they defined areas which classify different membrane-interaction types empirically (cf. Fig. 5.4 B). Harris and co-workers extended these proposed areas by introducing a region for helices which adopt oblique orientation with respect to the bilayer surface [234].

To determine data points for the hydrophobic moment plot, mean hydrophobicities $\langle H_{11} \rangle$ and the corresponding mean hydrophobic moments $\langle \mu_H \rangle$ of 11-residue long windows, equivalent to three turns of an α-helix, are calculated for the peptide sequence according to

$$\langle \mu_H \rangle = \frac{1}{11} \sum_i^{i+10} \langle \mu_{H,i} \rangle \quad \text{and} \quad \langle H_{11} \rangle = \frac{1}{11} \sum_i^{i+10} \langle H_i \rangle$$

using the hydrophobicity consensus scale introduced by Eisenberg [232]. The window with the highest value of $\langle \mu_H \rangle$ and its corresponding $\langle H_{11} \rangle$ value are then chosen for the graphical analysis. Fig. 5.4 A illustrates the calculated gradients for Ece1-III_{KR} (quantified according to the consensus hydrophobicity scale [232]). The most amphiphilic, helical 11-residue long segment centres around I^{23} and has a mean hydrophobic moment of $\langle \mu_H \rangle = 0.65$ and a mean hydrophobicity of $\langle H_{11} \rangle = 0.33$. This segment is invariant to the C-terminal modifications in Ece1-III_K, Ece1-III_{AA}

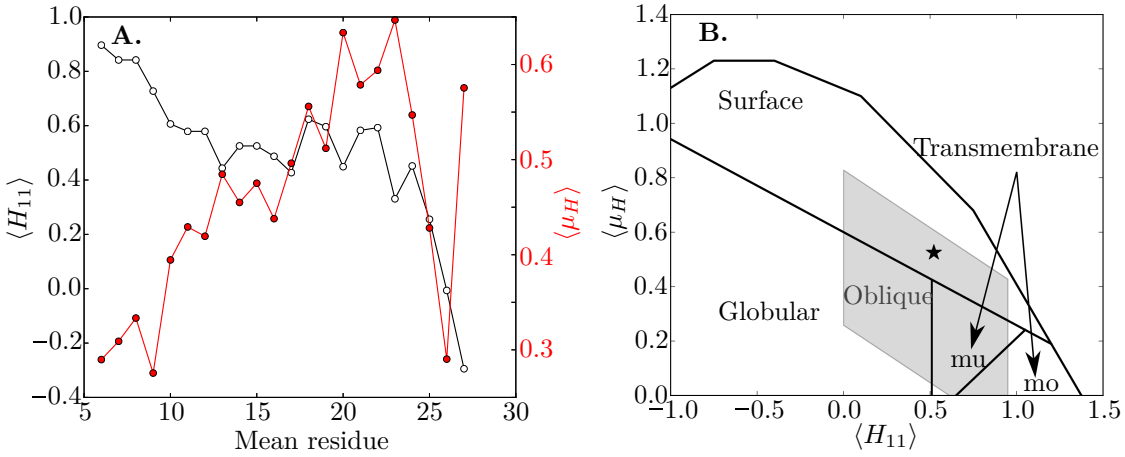

Figure 5.4 – Hydrophobicity analysis of Ece1-III$_{KR}$. A. Mean hydrophobicity $\langle H_{11} \rangle$ (○) and mean hydrophobic moment $\langle \mu_H \rangle$ (●) of a 11-residue window along the amino acid sequence. The calculations are based on the hydrophobicity consensus scale [232]. **B.** Extended hydrophobic moment plot analysis. The location of the most amphiphilic 11-residue window (⋆) is indicated in the figure. It is the same for Ece1-III$_{KR}$ and its three variants Ece1-III$_K$, Ece1-III$_{AA}$ and Ece1-III$_A$. The lines separate the empirical locations of candidates for globular, surface and multimeric (mu) or monomeric (mo) transmembrane helices according to the conventional hydrophobic moment plot diagram introduced by Eisenberg *et al.* [233]. Harris *et al.* proposed that α-helices with oblique orientation with respect to the bilayer surface can be identified inside the grey-shaded area [234].

and Ece1-III$_A$ where it is also identified as the most amphiphilic part. From the location of the resulting data point indicated in Fig. 5.4 B, an oblique orientation for the α-helices of Ece1-III is proposed.

Although this method has often been shown to predict the right scenarios, it also failed for some cases in which the hydrophobic moment for a sequence is highly affected by a few extreme amino acids. Their spatial arrangement can mask the overall nature of a helix and thus impair the predictive power of the hydrophobic moment plot [235]. Wallace *et al.* suggested that the assumption of a separation angle of 100° represents a second possible error source as the separation in naturally occurring α-helices varies between 95° and 105° [236]. However, both error sources can be excluded for the Ece1-III variants since the amino acid sequences do not contain such extreme singularities. Further, the variation of the separation angles affected the value of the mean hydrophobic moment only marginally ($\langle \mu_H(95°) \rangle$ = 0.57, $\langle \mu_H(105°) \rangle$ = 0.66); the most amphiphilic segment stayed the same for all variations.

Another indication which supports the putative oblique membrane orientation of the different Ece1-III variants is the hydrophobic gradient along the amino acid sequence (cf. Fig 5.4 A): The asymmetric hydrophobicity distribution along the α-helical axis enables shallow bilayer penetration which perturbs the regular packing of

the lipid acyl chains. Thus, it contributes to the destabilisation of the lipid structure and promotes vesicle fusion [234, 237, 238].

5.1.4 Effect C-terminal Amidation

Dennison *et al.* investigated the toxicity of a series of amidated and non-amidated membrane-active peptides. They correlated the efficiency of membrane permeabilisation against the peptides' amidation state and hydrophobic properties. As a result, they found that amidation tended to decrease toxicity in peptides with larger hydrophobicity gradients. In the absence of pronounced hydrophobicity gradients, amidation appeared more likely to increase the efficiency [101]. To explain these effects the authors speculated that deep bilayer penetration, which is facilitated by large gradients, could be perturbed by amidation leading to a decreased efficiency. In contrast, the additional charge of amidation might enhance bilayer binding and therefore increase the peptide's disruption activity.

In Ece1-III$_{\mathrm{KR}}$, the hydrophobic gradient per residue is approximately -0.19 which represents an intermediate gradient value compared to those examined in reference [101]. Thus, the particular effect of an amidation on Ece1-III$_{\mathrm{KR}}$ cannot be estimated easily. However, the hydrophobic gradients per residue in Ece1-III$_{\mathrm{K}}$ (-0.15), Ece1-III$_{\mathrm{AA}}$ (-0.06) and Ece1-III$_{\mathrm{A}}$ (-0.07) are clearly reduced and therefore it is assumed that the amidated variants of these peptides exhibit increased efficiencies.

5.2 Experimental Analysis of the Secondary Structure

5.2.1 Isotropic Circular Dichroism

Soluble Peptide Spectra in 0.01 % TFA

Spectra of three Ece1-III peptides (Ece1-III$_{\mathrm{KR(N)}}$, Ece1-III$_{\mathrm{K(C)}}$, Ece1-III$_{\mathrm{AA(N)}}$) at 25°C and 40°C in 0.01 % acidic acid solution (TFA) are shown in Fig. 5.5 A. None of these peptide spectra shows significant temperature effects, indicating that the peptide conformations are stable within the temperature range used for the experiments throughout the present work.

The spectra of Ece1-III$_{\mathrm{KR(N)}}$ show the characteristic line shape of a peptide with significant α-helical content, having two negative minima around 208 and 223 nm and a positive maximum at wavelengths < 200 nm. The determination of the secondary elements with K2D program obtained that the Ece1-III$_{\mathrm{KR(N)}}$ spectrum at 25°C contains around (28 ± 4) % α-helix, (13 ± 3) % β-sheet and (59 ± 2) % random coil conformations. The calculation was performed with varying concen-

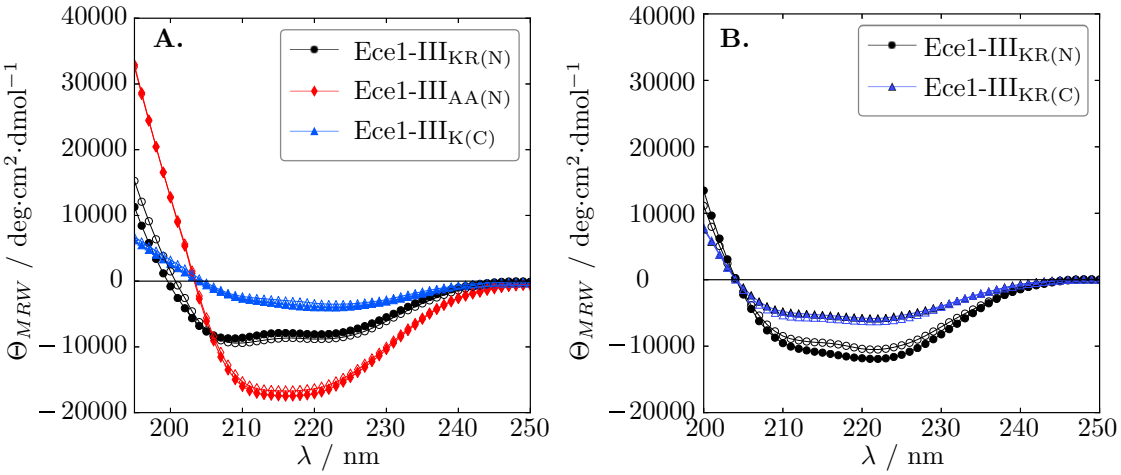

Figure 5.5 – Soluble peptide CD spectra of (**A.**) Ece1-III$_{K(C)}$ (▲), Ece1-III$_{KR(N)}$ (●) and Ece1-III$_{AA(N)}$ (♦) in 0.01 % TFA (v/v) solution at 25°C (filled markers) and 40°C (open markers), and of (**B.**) the amidated Ece1-III$_{KR(N)}$ (●) and non-amidated Ece1-III$_{KR(C)}$ (▲) isoforms in the standard buffer of 100 mM KCl, 5mM HEPES at pH 7.0 at 25°C (filled markers) and 40°C (open markers).

trations, allowing mass deviations of up to 20 %. In all results the normalised root-mean-square deviations (NRMSD) were < 0.1, representing good fit results [174]. Another goodness-of-fit parameter for K2D analysis is the maximum error, which represents the mean error of each of the three predicted element percentage (α-helix, β-sheet, random coil) obtained. This value should not exceed 0.22. In the analysis of the Ece1-III$_{KR(N)}$ spectrum, this maximum error reached a value of 0.08. Consequently, the secondary structure analysis for Ece1-III$_{KR(N)}$ can be considered as good estimate. It demonstrates that a significant amount of amino acids constitute as α-helix in the peptide's soluble state. An identical analysis for the Ece1-III$_{AA(N)}$ peptide indicates an α-helical content of (63 ± 6) %, which is higher than that of Ece1-III$_{KR(N)}$. However, the resulting maximum error exceeds 0.22 and thus does not allow sufficient conclusions about the real secondary structure content. A similar problem occurs for the Ece1-III$_{K(N)}$ spectrum. For this variant, the α-helical content was predicted to be only (9 ± 1) %, but here both indicators, NRMSD and maximum error, exceeded tolerable values. Neither the spectrum of Ece1-III$_{AA(N)}$ nor the spectrum of Ece1-III$_{K(C)}$ show well marked CD bands for the $\pi \rightarrow \pi^*$ transition around 208 nm. This might either be caused by real structural effects or by absorption flattening – an experimental artefact which occurs when chromophores are closely packed and shadow each other with respect to impinging photons, resulting in a decreased effective cross section. Correspondingly, the absorption is reduced and distortions of CD spectra appear [239, 240]. Due to the high magnitude of the negative CD bands in the Ece1-III$_{AA(N)}$ spectra, it is possible

that the physical concentration was higher than expected. On the contrary, the negative bands of the Ece1-III$_{K(C)}$ spectra are poorly marked, implying that the effective cross section is reduced due to the formation of peptide clusters. In fact, Ece1-III$_{K(C)}$ is hardly soluble and its aggregation preference was also indicated in film balance measurements (Sec. 5.2.2). Probably, this clustering effect would be reduced for an amidated variant of the peptide, as it is also the case for Ece1-III$_{KR}$ (see below).

Soluble Peptide Spectra in Buffer

Figure 5.5 B shows the CD spectra of the amidated Ece1-III$_{KR(N)}$ and non-amidated Ece1-III$_{KR(C)}$ isoforms of Ece1-III$_{KR}$ in the standard buffer of 100 mM KCl, 5mM HEPES at pH 7.0. The line shapes of both spectra are similar to one another, indicating that the overall secondary structure is almost independent on the amidation state. Only the extent of the CD signal is enhanced for the amidated variant implying a slight increase in α-helical content.

However, the line shape of Ece1-III$_{KR(N)}$ in buffer slightly differs to the spectra of Ece1-III$_{KR(N)}$ in 0.01 % TFA (Fig. 5.5 A.) as the ratio of both minima is changed: The minimum around 208 nm is increased relative to the one at 222 nm. Ratios similar to this one have also been observed for structural coiled-coil motifs where two or more α-helical monomers are coiled into one another [241, 242]. This observation suggests that the increased concentration of salt ions in the buffer promotes a clustering to oligomers, whereas the increased proton concentration of the acidic TFA-solvent rather promotes the formation of α-helical monomers.

Membrane-associated Peptide Spectra

Figure 5.6 shows the spectra of Ece1-III$_{KR(N)}$ in presence of lipid vesicles of different composition at 25°C. For these experiments, the peptide was solved in 0.01 % TFA and the lipids were suspended in buffer solution (100 mM KCl and 5 mM HEPES at pH 7.0). In this system, spectra could not be measured reliably up to a wavelength of 195 nm. The reason for that is found in the absorbance of lipid/peptide samples which exceeds reasonable limits and thus strongly impairs the signal-to-noise ratio. In the Jasco J-710 spectropolarimeter, the absorbance is basically monitored by the high voltage (HT) applied to the photomultiplier which amplifies the modulated measuring signal. As a rule of thumb, this voltage should not exceed a value of 650 V to give trustworthy CD signals.

In the detectable wavelength range, the CD spectra conserve a pronounced α-helical appearance, indicating that the exposure to lipid membranes does not sig-

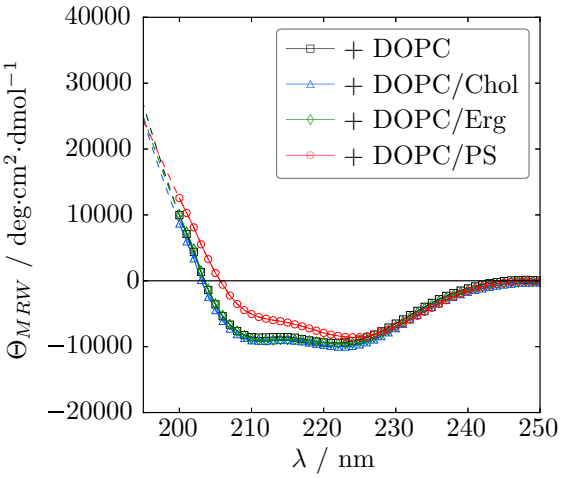

Figure 5.6 – Membrane-associated CD spectra of Ece1-III$_{KR(N)}$ in 0.01 % TFA (v/v) solution in the presence of lipid vesicles at 25°C. Peptide spectra with DOPC (□), DOPC/Chol (△) or DOPC/Erg (◇) content are identically, only the line shape of the DOPC/PS (○) spectrum differs. Due to experimental circumstances (see text) Θ_{MRW} of membrane-bound spectra is not fully reliable between 195 nm and 200 nm (dashed lines). Peptides were solved in 0.01% TFA and lipid vesicles were suspended in buffer solution of 100 mM KCl and 5 mM HEPES at pH 7.0. Lipid-lipid ratio was 9:1 (n/n) and lipid-peptide ratio was 18:1 (n/n).

nificantly affect the peptide's secondary structure. However, two distinct changes occur in comparison to the pure peptide spectrum: the CD spectra are red-shifted by around 1 nm and the minimum around 208 nm is less pronounced. With the addition of the lipid vesicles, also salt ions from the buffer solution were added to the peptide system. These might cause the formation of coiled-coils and therefore explain the latter effect. It is also likely that this effect represents experimental artefacts caused by the presence of the lipid vesicles and a non-uniformly distribution of the peptide chromophores, namely absorption flattening or differential light scattering. The absorption flattening might affect the spectra as this effect is not only a function of the concentration of chromophores but also of the particle size [240]. The latter artefacts are a consequence of the inherent differences of the indices of refraction for left and right circularly polarized light [239]. It occurs for particle dimensions that are comparable to or greater than the wavelength λ and it is particularly pronounced for shorter wavelengths since the scattering cross section is proportional to λ^{-4}. Correspondingly, a pronounced differential scattering at 208 nm may lead to an abnormally small CD peak.

While both effects are negligible with SUVs, they appear to be a general problem in CD spectra of membrane proteins embedded in LUVs [239]. Even though the liposomes utilised here are of comparatively small size ($\sim$ 100 nm, see Sec. 6.2.2), these artefacts exhibited a strong influence. This observation indicates that the

lipid vesicles form large aggregates in the presence of Ece1-III$_{\mathrm{KR(N)}}$ – especially for DOPC/PS vesicles, for which the spectral distortion was found to be remarkably strong. For that reason, it is assumed that the physical appearance of the DOPC/PS aggregates in contact with Ece1-III$_{\mathrm{KR(N)}}$ is different compared to the one of pure DOPC or DOPC/Chol and DOPC/Erg. This assumption is evidenced by DLS measurements (Sec. 6.2.2), where the interaction with Ece1-III$_{\mathrm{KR(N)}}$ resulted in vesicle sizes of about 250 nm for pure and sterol-containing DOPC liposomes, and a by far larger size of ~ 1.2 μm for DOPC/PS liposomes.

The observed red-shift might also be assigned to differential light scattering artefacts or trace back to polarity changes of the peptide's local environment. Consistent with previously observed solvent dielectric-related shifts [243–245], this effect might reflect the intercalation of the peptide into the hydrophobic core layer of the lipid vesicle. However, this conclusion is vague due to the pronounced spectral artefacts.

In order to draw confident conclusions on the secondary structure content and possible environmental changes, it is required to eliminate the occurrence of absorption and differential light scattering artefacts. As Mao and Wallace [239] have suggested, this can be accomplished by reducing the P/L ratio to decrease peptide-induced aggregation effects. However, for this particular system investigated here, this strategy is not promising because the DLS data (Sec. 6.2.2) shows that lipid vesicles aggregate already at comparatively low P/L values of 1:150. Another possibility to circumvent the occurrence of size-related artefacts might be to sonicate the sample solution prior to each acquisition scan to dissipate the aggregates.

5.2.2 Evidence for the Amphiphilicity of Ece1-III

The presumed amphiphilic nature of the Ece1-III conformations is evidenced by the peptides' preference to assemble at water/air interfaces. This is easily proven using a film balance. Additionally, these experiments can provide information on the interfacial area required per peptide molecule $A_{P,m}$. To this end, the peptides were injected onto the buffer surface and the barriers were closed until an increase in lateral pressure was detected. For the peptides Ece1-III$_{\mathrm{KR(N)}}$, Ece1-III$_{\mathrm{AA(N)}}$ and Ece1-III$_{\mathrm{K(C)}}$, representative curves of such an isothermal compression at 20°C are shown in Fig. 5.7.

All these peptides form interfacial monolayers, demonstrating their structural amphiphilicity. The same is true for Ece1-III$_{\mathrm{A(C)}}$. However, monolayers formed by this peptide variant were non-reproducible, indicating that the peptide is subjected to pronounced aggregation processes which is also supported by the turbid appearance of this peptide sample. For the reproducible films of Ece1-III$_{\mathrm{KR(N)}}$, Ece1-III$_{\mathrm{AA(N)}}$

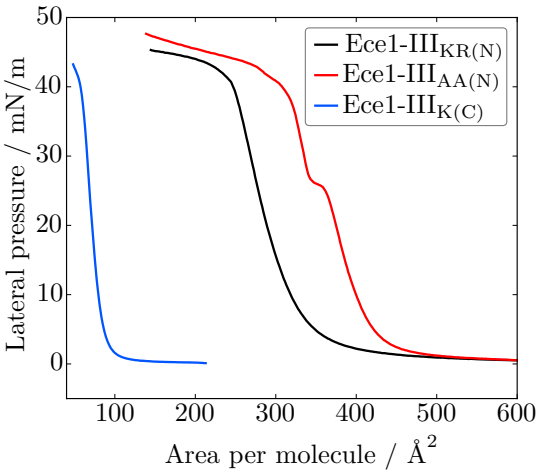

Figure 5.7 – Compression isotherms of peptide monolayers. Shown are representative measurements of monolayers formed by Ece1-III$_{KR(N)}$ (black), Ece1-III$_{AA(N)}$ (red) and Ece1-III$_{K(C)}$ (blue) at 20°C. Peptides were solved at a concentration of 0.1 mg·ml^{-1} in 0.01% TFA. Either 50 μl or 70 μl of the peptide solution were injected into the subphase composed of 100 mM KCl and 5 mM HEPES at pH 7.0.

and Ece1-III$_{K(C)}$, distinct differences in the resulting molecular areas were found. At a lateral pressure of $\Pi_s = 20$ mN·m^{-1} present in physiological fluid bilayers, Ece1-III$_{AA(N)}$ requires the largest molecular area with $A_{P,m}$ =(379.1 ± 23.1) Å^2. The area required per Ece1-III$_{KR(N)}$ molecule, $A_{P,m} = (290.2 \pm 7.0)$ Å^2, is a little smaller. The smallest area, $A_{P,m} = (64.8 \pm 6.6)$ Å^2, is obtained for Ece1-III$_{K(C)}$. Note that for the determination of these values, the presence of peptide in the liquid bulk phase was neglected, i. e. it was assumed that all injected peptide monomers assembled at the interface. Taking into account the previously indicated tendency of Ece1-III$_{K(C)}$ to form aggregates (cf. Sec. 5.2.1) and its remarkable small $A_{P,m}$ in comparison to the other variants, this assumption thus appears to be too simplistic for poorly solving peptides.

For Ece1-III$_{KR(N)}$ and Ece1-III$_{AA(N)}$, the interfacial area per molecule was additionally studied as function of temperature. To this end, isothermal compression curves were recorded at different subphase temperatures ranging from 15°C to 40°C. The $A_{P,m}$ at $\Pi_s = 20$ mN·m^{-1} is plotted in Fig. 5.8 A. It can be seen that the area per molecule decreases linearly with increasing temperature. As obtained by least-square fitting, slope and intercept of this behaviour were determined to be (-5.1 ± 0.2) Å^2/°C and (392.0 ± 5.7) Å^2 for Ece1-III$_{KR(N)}$, and (-8.3 ± 0.7) Å^2/°C and (544.4 ± 19.0) Å^2 for Ece1-III$_{AA(N)}$. Consequently, the molecular areas required are almost halved from lower to higher temperature within the probed temperature range. This observation is attributed to a temperature-dependent reduction of the peptide cross section, arising from minor reorganisations of particular amino acids.

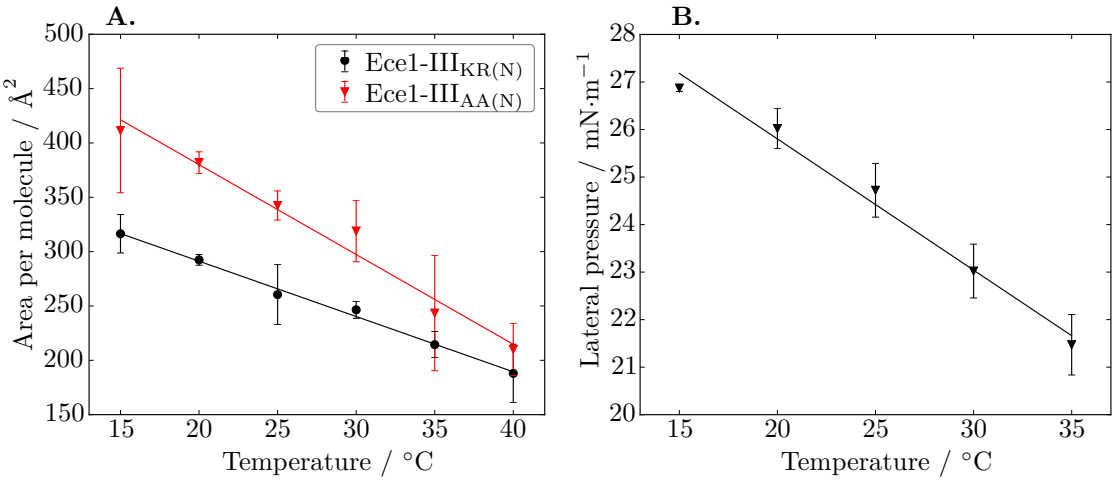

Figure 5.8 – Temperature-dependent characteristics of peptide monolayers. **A.** Molecular areas of Ece1-III$_{KR(N)}$ (●) and Ece1-III$_{AA(N)}$ (▼) at a lateral pressure of 20 mN·m^{-1}. **B.** Lateral pressure at which the monolayer formed by Ece1-III$_{AA(N)}$ is reorganised, i. e. the pressure at which the kink in the compression isotherm occurs (cf. Fig. 5.7). Each data point is plotted as mean of two independent measurements, the errorbars illustrate the respective standard deviation. The solid lines represent linear least-square fits to the data.

However, it cannot be excluded that this finding relates to a decreasing amount of peptide at the water/air interface.

Another characteristic peptide reshaping is displayed in the area-pressure-isotherms of Ece1-III$_{AA(N)}$, where a narrow section exists in which the area compression is accompanied by only a negligible change in lateral pressure (cf. Fig. 5.7). It covers an areal change of $(23 \pm 5)\,\text{Å}^2$ at 20°C but decreases with increasing temperature until it is completely vanished at 40°C. The lateral pressure, at which this conformational transition occurs, also shifts linearly to lower values as shown in Fig. 5.8 B. The origin of this observation can not be explained yet. Its revelation will require extensive structural studies of the peptide conformation.

6 The Lipid-Peptide Interaction

In this chapter, the results of the different measurements on the lipid-peptide interaction are presented. This interaction is subdivided into four stages: First, the binding of the peptide is addressed. Second, the peptide's intercalation into bilayer membranes and the associated alignment of the peptide helix are discussed. In the third stage, peptide-induced alterations of the bilayer structure are examined. The fourth and final stage concentrates on the peptides' permeabilisation activity. The strategy to examine each of these stages is briefly introduced at the beginning of the corresponding sections. The results are then summarised and discussed at the end of each section.

6.1 Peptide Binding to Lipid Membranes

In this first section on the lipid-peptide interaction, the binding of Ece1-III$_{\mathrm{KR(N)}}$ to different liposome mixtures is addressed using a FRET binding assay. Measurements of the zeta potential of liposomes are employed to complement the data. In addition, the zeta potential experiments are also used to examine the influence of the peptide variants Ece1-III$_{\mathrm{K(C)}}$ and Ece1-III$_{\mathrm{AA(N)}}$.

6.1.1 FRET Binding Assay

To study the binding preference of Ece1-III$_{\mathrm{KR(N)}}$ to lipid bilayers of different composition, FRET binding assays were carried out. The resulting fluorescence intensities, I_A and I_D, of both acceptor and donor dyes as well as their ratio are shown in Fig. 6.1. While the negative control measurements did not lead to any signal difference, I_D drops significantly upon the addition of Rho-Ece1-III$_{\mathrm{KR(N)}}$ for all liposome compositions. Corresponding to this steep decrease, I_A increases for the DOPC, DOPC/Chol and DOPC/Erg samples, demonstrating the onset of the FRET effect based on the binding of Rho-Ece1-III$_{\mathrm{KR(N)}}$ to the liposomes. Upon further peptide additions, also I_A starts to decrease but still, the ratio of I_A to I_D displays a positive slope. One possible explanation for this effect is the formation of peptide aggregates in which the acceptor fluorescence is commonly known to be subjected to self-quenching. An alternative explanation is the spectral overlap of the fluorescence

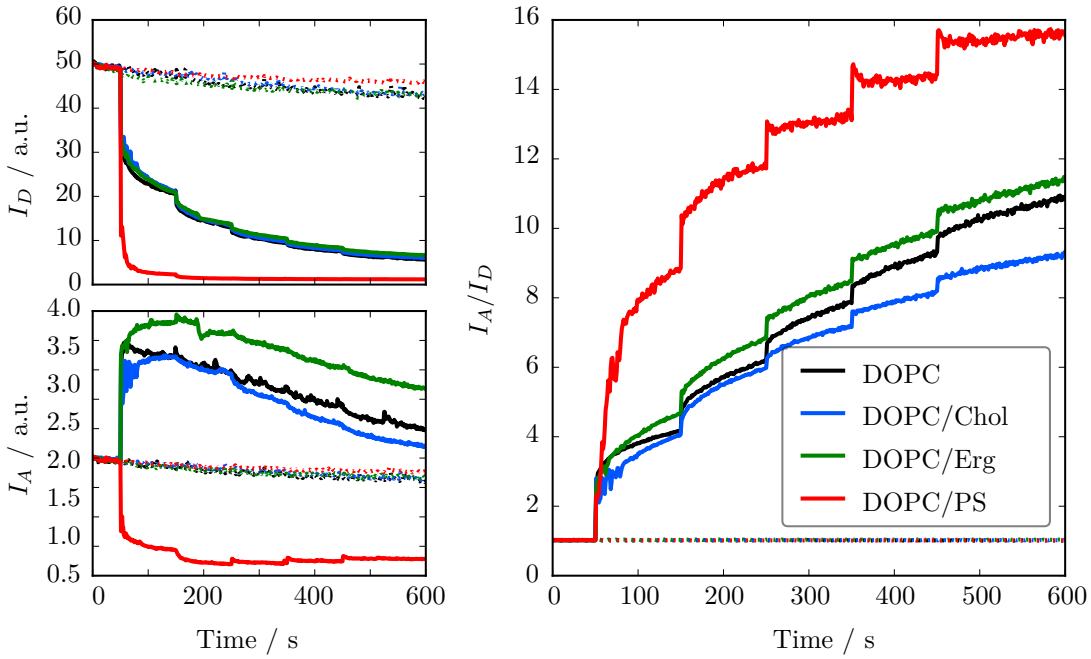

Figure 6.1 – Time dependence of a FRET binding assay of Rho-Ece1-III$_{KR(N)}$. The figure shows the resulting FRET signals of the interaction of NBD-labelled liposomes (donor) and Rho-Ece1-III$_{KR(N)}$ (acceptor) as function of time and concentration. Starting from 50 s, 50 μl peptide (1 mg·ml^{-1} in H_2O) were titrated every 100 s. Accordingly, the peptide concentration was gradually increased from 0.74 μM (P/L = 1:13.5 $\approx$ 0.074) after the first injection to 3.65 μM (P/L = 1:2.7 $\approx$ 0.37) after the final injection. The upper left panel contains the raw donor signals, I_D, and the lower right panel the corresponding acceptor signals, I_A. Their ratios I_A/I_D, normalised to the starting point, are shown in the right panel. While the ratios of the FRET signals demonstrate the strongest binding affinity for DOPC/PS liposomes (red), the binding affinities of DOPC/Erg (green), DOPC/Chol (blue) and pure DOPC liposomes (black) are comparable. Lipid-lipid ratio was 9:1 (n/n). Corresponding H_2O-controls are shown with dotted lines. The assay was performed at 37°C.

spectra of both dyes: if the donor intensity falls off, the intensity detected at the acceptor wavelength also drops to a certain extent.

For the DOPC/PS vesicles, the binding is not that straightforwardly evidenced. Here, both the donor and the acceptor fluorescence show a considerable decrease immediately after the addition of Rho-Ece1-III$_{KR(N)}$. Still, the ratio of I_D to I_A preserves a positive progression and thus indicates the onset of the FRET effect. The direct decrease in I_A observed in this case, can only be explained by a combination of self-quenching of the acceptor dye and its spectral overlap with I_D: Basically, there should be no acceptor signal at all before the acceptor, i. e. the peptide, is added to the system. The initial counts of I_A in the experiment are thus only determined by the donor fluorescence. According to that, a simple reduction of I_D (without the occurrence of the FRET effect), would essentially entail a steady value

for I_A/I_D. The same applies if the energy transfer takes place but I_A would be quenched entirely. The measured positive progression of I_A/I_D, thus, proves that Rho-Ece1-III$_{\mathrm{KR(N)}}$ binds to the liposomes, where the energy gained by the FRET effect is only partly released by the emittance of light, which in turn indicates self-quenching. The increase in I_A/I_D is about two times stronger for DOPC/PS than for the DOPC, DOPC/Chol and DOPC/Erg samples. Assuming a uniform self-quenching in all sample systems, this result suggests that the amount of Rho-Ece1-III$_{\mathrm{KR(N)}}$ bound to one liposome is increased in the presence of PS.

6.1.2 Zeta Potential

Lipid Composition

The binding of Ece1-III$_{\mathrm{KR}}$ was also demonstrated by measurements of the zeta potential of differently composed liposome solutions. With increasing P/L, the zeta potentials of the lipid/peptide mixtures increase as illustrated in Fig. 6.2. The progress is similar for DOPC, DOPC/Chol and DOPC/Erg vesicles, where ζ increases from a slightly negative value of about -4 mV for the pure liposomes to a positive value of $\approx +39$ mV at P/L = 1:18. Also, the highly negative potential of $\zeta = (-56.1 \pm 7.9)$ mV of DOPC/PS vesicles alters by $\approx +77.5$ mV to a positive value of $\zeta = (21.4 \pm 2.3)$ mV at P/L = 1:18. In these samples, the resulting potential change $\Delta\zeta$ is about two times larger than in DOPC, DOPC/Chol and DOPC/Erg samples. Samples containing only Ece1-III$_{\mathrm{KR(N)}}$ and no liposomes were below the detection limit of the Zeta Sizer for peptide concentrations lower than 1.56 μM (equivalent to P/L = 1:32 $\approx$ 0.031). For higher concentrations, a constant potential of $\zeta \approx 27.5$ mV was detected. The ζ-increase in peptide/liposomes solutions for P/L values below 1:32, thus, demonstrates a progressive accumulation of the cationic peptide on the liposome shell. The binding proceeds as sigmoidal function of P/L until a saturation level is reached at $\zeta \approx +39$ mV, a potential value above the one of the unbound peptide in solution. The independence between the zeta potentials of the pure peptide and the peptide/liposome systems again evidences the peptide binding, as ζ is proportional to the particles' surface charge density [246]. Consequently, the amount of peptide bound to the outer liposome surface is also saturated at this limit. Hence, the results imply that DOPC vesicles with 10 % PS are capable to bind more Ece1-III$_{\mathrm{KR(N)}}$ molecules than pure DOPC or DOPC with an equal proportion of sterols.

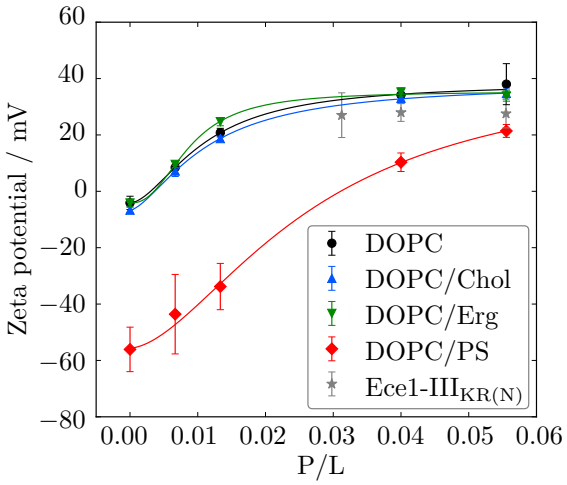

Figure 6.2 – Zeta potential of different liposomes as function of Ece1-III$_{KR(N)}$ content. While the increase in the zeta potential upon the addition of Ece1-III$_{KR(N)}$ is similar in DOPC/Erg (▼), DOPC/Chol (▲) and pure DOPC liposomes (●), it is significantly pronounced in DOPC/PS vesicles (♦). The solid lines represent least-square fits of a Hill function to the experimental data. The zeta potential of equivalent solutions of only Ece1-III$_{KR(N)}$ (★) measured at three different peptide concentrations (1.56, 2.0 and 2.78 μM) are plotted additionally (without fit). For lower concentrations, the count rate was too low to obtain reliable results of ζ. Lipid-lipid ratio was 9:1 (n/n) and the measurements were performed at 25°C.

Peptide Variants

The effects of Ece1-III$_{K(C)}$ and Ece1-III$_{AA(N)}$ on the zeta potentials of vesicles formed from either pure DOPC or DOPC with 10 % PS are shown in Fig. 6.3. Again, the zeta potential increases as function of P/L. The corresponding potential differences $\Delta\zeta$ from P/L = 0:1 to P/L = 1:18 are: $\Delta\zeta \approx +33$ mV for both variants in DOPC/PS samples, $\Delta\zeta = +(18.8 \pm 1.9)$ mV for Ece1-III$_{AA(N)}$ in DOPC and only $\Delta\zeta = +(10.2 \pm 5.1)$ mV for Ece1-III$_{K(C)}$ in the same lipid system. In accordance with this, the binding of Ece1-III$_{AA(N)}$ to DOPC vesicles is slightly enhanced compared to Ece1-III$_{K(C)}$, but both variants bind equally well to the DOPC/PS vesicles. Although the binding is again pronounced in DOPC/PS samples, it is significantly smaller than that observed for Ece1-III$_{KR(N)}$. Likewise, the binding to DOPC is also weaker. The zeta potentials of the corresponding pure peptide solutions at a concentration of 2.78 μM (equivalent to P/L = 1:18 $\approx$ 0.056) are found to be $\zeta = +(18.7 \pm 0.8)$ mV for Ece1-III$_{K(C)}$ and $\zeta = +(22.5 \pm 2.0)$ mV for Ece1-III$_{AA(N)}$. Note that due to the low number of data points, it can not be evaluated whether the increase proceeds in a hyberbolic or a sigmoidal manner.

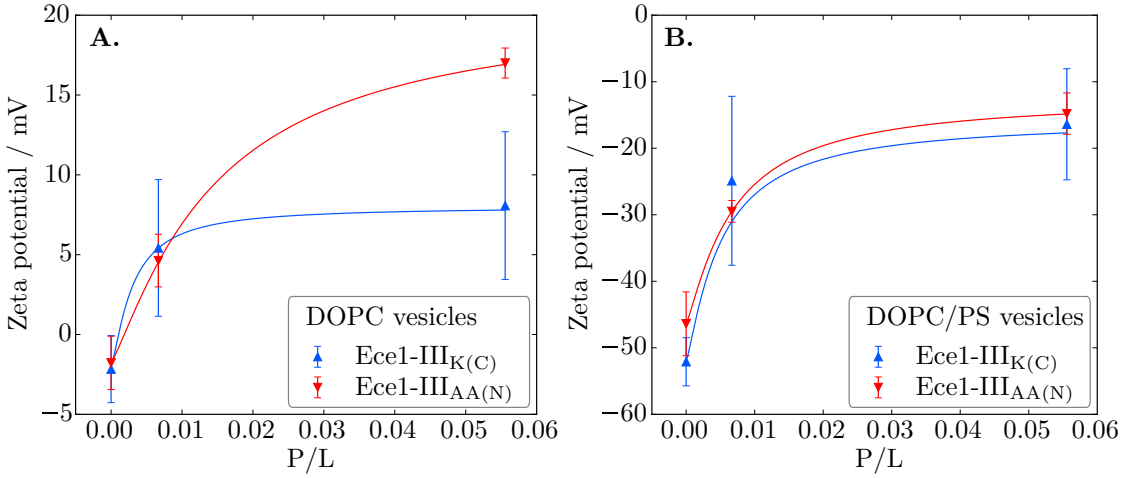

Figure 6.3 – Zeta potential of liposomes as function of increasing P/L. The hydrodynamic surface potential increases in DOPC (**A.**) and DOPC/PS (9:1, n/n, **B.**) with increasing content of either Ece1-III$_{AA(N)}$ (▼) or Ece1-III$_{K(C)}$ (▲). In DOPC vesicles, the increase observed for Ece1-III$_{AA(N)}$ is slightly pronounced compared to the one observed for Ece1-III$_{K(C)}$. The solid lines only indicate a possible Hill function which would match the data. They do not represent actual fits as the number of data points is not representative. The measurements were performed at 25°C.

6.1.3 Discussion of the Binding Data

The observation that the zeta potentials show sigmoidal dependencies on the Ece1-III$_{KR(N)}$-concentration indicates a cooperative interaction with the lipid membranes. Such a sigmoidal concentration dependence was not apparent in the FRET assay which probably relates to the comparatively high initial P/L of 1:13.5 ($\approx$ 0.074). As a consequence, the inflection point, which occurred at values lower than P/L $\approx$ 1:100 (= 0.001) in the zeta potential data, might be missed. There is a discrepancy between the results of membrane-specific binding capacities observed from the two experimental approaches. Despite their similarity concerning the increased affinity for DOPC/PS membranes, the saturation levels occurred at different P/L values. While it already reached its limit at P/L $\sim$ 1:50 (= 0.02) in the zeta potential measurements, the binding proceeded to P/L $\sim$ 1:2.7 ($\approx$ 0.37) in the FRET assay. This effect may either be caused by a higher affinity of the rhodamine-labelled peptide version or, it may represent a misleading observation due to self-quenching artefacts.

The peptide variants Ece1-III$_{K(C)}$ and Ece1-III$_{AA(N)}$ demonstrated a notably decreased binding affinity to both, DOPC liposomes with and without PS. This observation is in accordance with the studies of Kim *et al.* [246] and Mosior *et al.* [247], who found that either the deletion of basic residues or the addition of alanine

residues to the end of a peptide sequence reduces the peptide's binding affinity to (anionic) membrane surfaces.

6.2 Peptide Intercalation into Lipid Membranes

In this section, the peptides' intercalation into bilayer membranes is addressed. Firstly, the intercalation is studied on the basis of the expansion of lipid monolayer films. Subsequently, the size enlargement of liposomes, detected by DLS and the decreasing FRET efficiency in liposomes, is utilised to discuss the integration behaviour. Following this, additional information on the peptides' orientation in lipid multilayers is obtained by OCD experiments.

6.2.1 Peptide Integration into Lipid Monolayers

First, lipid monolayers were used to probe whether Ece1-III$_{\mathrm{KR(N)}}$ not only binds to lipid surfaces, but also penetrates the lipid matrix. Starting with the injection of Ece1-III$_{\mathrm{KR(N)}}$ to the subphase (P/L $\simeq 1:6 \approx 0.167$), Fig. 6.4 displays the time-dependent expansion ΔA of monolayers formed of DOPC, DOPC/Chol, DOPC/Erg and DOPC/PS as measured by a film balance at constant lateral pressure of $\Pi_s = 20\ \mathrm{mN{\cdot}m^{-1}}$. These expansions clearly demonstrate the peptide inclusion. For all monolayers, the area increases hyperbolically within $\sim$ 20 min and then slowly converges a saturation level. This saturation level is reached when the film area has expanded by $\Delta A = (8.9 \pm 0.1)\,\mathrm{cm}^2$ in case of DOPC. For DOPC/PS monolayers, the maximal expansion level, $\Delta A = (11.7 \pm 1.3)\,\mathrm{cm}^2$, is only marginally higher, whereas the area expansion in the sterol-containing monolayers is about one third smaller than that of DOPC, i. e. $\Delta A = (5.4 \pm 1.2)\,\mathrm{cm}^2$ and $\Delta A = (6.5 \pm 1.0)\,\mathrm{cm}^2$ for DOPC/Chol and DOPC/Erg, respectively. Consequently, the data suggest that the presence of sterols hampers the intercalation of Ece1-III$_{\mathrm{KR(N)}}$.

The mean molecular space requirement of Ece1-III$_{\mathrm{KR(N)}}$ in the pure peptide monolayer was determined to be $A_{P,m} = (2.70 \pm 0.08)\,\mathrm{nm}^2$ at 24°C (see Sec. 5.2.2). Assuming the required peptide area in the lipid monolayer to be identical to its cross section in the pure peptide layer, a complete incorporation of Ece1-III$_{\mathrm{KR(N)}}$ into the DOPC monolayer would lead to an area expansion of 24.4 cm^2, corresponding to a relative expansion of 63 % with respect to the initial lipid film area. According to this rough estimation, little less than half of the injected amount of peptide is assumed to intercalate into the lipid monolayer. The maximal area expansion observed for the peptide incorporation into the DOPC monolayer would thus correspond to a peptide-to-lipid ratio of roughly $\sim$ 1:15 (≈ 0.067). Note that this estimation bases

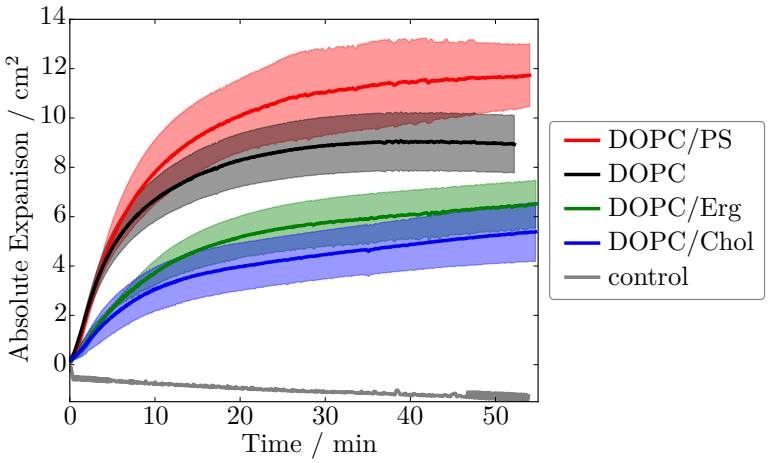

Figure 6.4 – Absolute area expansion of lipid monolayers in response to their interaction with Ece1-III$_{KR(N)}$. The monolayers were composed of DOPC/Erg (green), DOPC/Chol (blue), DOPC/PS (red) and pure DOPC (black). The figure plots the means from triplicate measurements at 24°C; the shaded area reflects the estimated uncertainties. The gray line illustrates the control measurement of a DOPC monolayer with a corresponding addition of 0.01 % TFA without peptide. The lipid-lipid ratio was 9:1 (n/n).

on the assumption of a theoretical lipid monolayer area of $A_L = 38.9$ cm^2 which follows from $A_L = nN_A A_{L,p}$ – the applied amount of DOPC n, Avogadro's constant N_A and the area required per DOPC molecule in the fluid phase $A_{L,m}$ which has been found to be $A_{L,m} = 0.725$ nm^2 [248]. However, the experimental films only covered an area of about $A_L = 28$ cm^2.

The deviation from the estimated theoretical monolayer area of the lipid/peptide systems may have different reasons. On the one hand, these may be of experimental origin – small inaccuracies such as $\Delta V = 0.5$ μl of the added volume and $\Delta c = 0.1$ mg·ml^{-1} of the respective concentration for instance, lead quickly to deviations of $\pm$ 7 cm^2. On the other hand, the deviations may be explained by the simplicity of the model assumed. It neglects the presence of lipids or peptides in solution and assumes that the molecular area required per peptide is identical to its monolayer cross section in the absence of lipids. However, the peptide orientation in the lipid monolayer is probably different than it is in the peptide monolayer.

6.2.2 Dynamic Light Scattering

Lipid Composition

The integration of Ece1-III$_{KR(N)}$ into lipid bilayers was demonstrated in DLS experiments, in which the hydrodynamic size of differently composed liposomes was monitored as function of the peptide-to-lipid ratio (P/L). For each liposome solution, the experimental results, plotted in Fig. 6.5 A, suggest a linear enlargement of

the vesicle diameter and therefore support the previous finding that Ece1-III$_{KR(N)}$ intercalates into the lipid matrices. While the expansion's slope is similar in DOPC, DOPC/Chol and DOPC/Erg vesicles (cf. table in Fig. 6.5 B), it is increased by a factor of almost five in vesicles composed of DOPC/PS. At a P/L of 1:18 (≈ 0.056), the increases correspond to a relative surface expansion of $\sim 60\,\%$ for DOPC, $\sim 78\,\%$ for DOPC/Chol and $\sim 95\,\%$ for DOPC/Erg vesicles. The increase observed for DOPC/PS vesicles amounts to $\sim 1075\,\%$.

To give a rough estimate on the maximal surface extension that can be obtained by the integration of Ece1-III$_{KR(N)}$, all molecules are for simplicity assumed to assemble as flat bilayers and monomolecular peptide layers, respectively. Accordingly, the relative areal increase $A_{P/L}$ may be approximated by $A_{P/L} \approx A_P/A_L$ – the ratio of the area obtained after the peptide integration A_P to the initial lipid area A_L. The latter is given by $A_L = \frac{1}{2} N_L A_{L,m}$, where N_L defines the number of lipid molecules,

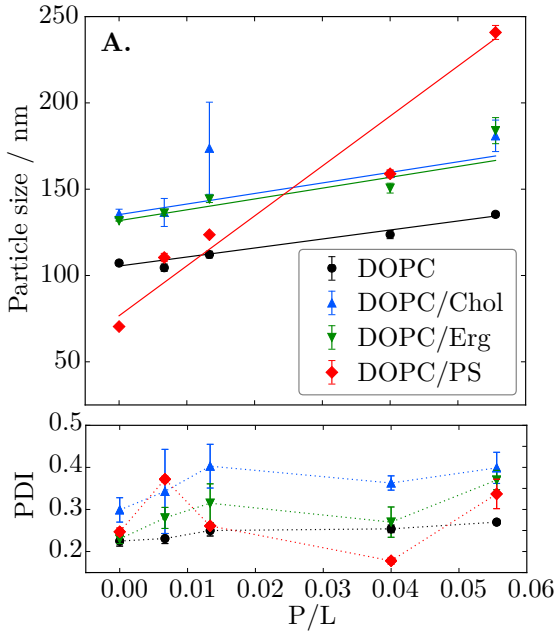

B.

Liposomes	slope(P/L) [nm]
DOPC	521.5 ± 52.0
DOPC/Chol	611.6 ± 78.7
DOPC/Erg	627.6 ± 126.0
DOPC/PS	2891.7 ± 549.8

Figure 6.5 – Liposome diameter as function of Ece1-III$_{KR(N)}$ content. A. The upper panel depicts the measured vesicle diameters of different lipid and lipid/Ece1-III$_{KR(N)}$ mixtures as function of P/L. For each liposome mixture, the P/L-dependence is approximated with linear fits, which are illustrated by solid lines. DOPC/Chol (▲) and DOPC/Erg (▼) vesicles are ~ 30 μm larger than pure DOPC liposomes (●), but their enlargements as function of the peptide concentration are comparable. Without peptide content, DOPC/PS (♦) vesicles are the smallest. However, their size is significantly enlarged upon the addition of Ece1-III$_{KR(N)}$. The lower left panel depicts the corresponding PDIs. Except for DOPC/PS, these values increase slightly with increasing P/L indicative for a broadened distribution of liposome sizes. However, the PDIs do not exceed a value of 0.5 for which no reliable size determination could be made. Lipid-lipid ratio was 9:1 (n/n) and the measurements were performed at 25°C. **B.** The table gives the slope values obtained from the fits given in **A**.

$A_{L,m}$ the space requirement per molecule and the factor $\frac{1}{2}$ is due to the lipids' assembly into a bilayer. By analogy, the peptide area is expressed by $A_P = N_P A_{P,m}$. The area per DOPC molecule has been determined to be 0.725 nm^2 [248]. The area per PS molecule is even smaller [248], which is why the presence of PS may be neglected in this approximation. With a mean molecular space requirement of 2.6 nm^2 at 25°C (see Sec. 5.2.2), the area per Ece1-III$_{\mathrm{KR(N)}}$ molecule is then $A_{P,m} \approx 3.6 A_{L,m}$. For this particular example, $N_L = 18 N_P$ applies and therefore, the maximum relative area increase is estimated to be

$$A_{P/L}A \approx \frac{A_P}{A_L} \approx \frac{N_P \cdot 3.6 A_{L,p}}{0.5 \cdot 18 N_P \cdot A_{L,p}} = 0.4.$$

The relative surface expansions entailed by the intercalation of the peptide is therefore limited to approximately 40 %[1]. Although this estimation is utterly simplistic since liposome curvature and also the increasing inhomogeneity of the size distribution are neglected, it predicts that size expansions on the order of 1000 %, as observed for DOPC/PS liposomes at small PDI, can not solely be explained by peptide intercalation into the bilayers. Effects such as peptide-induced vesicle aggregation or fusion must play a distinct role. This hypothesis is consistent with the results obtained from the FRET assay presented in Sec. 6.3.5. Herein, fusion of DOPC/PS liposomes was observed upon the addition Ece1-III$_{\mathrm{KR(N)}}$.

Peptide Variants

A similar analysis on the intercalation of Ece1-III$_{\mathrm{K(C)}}$ and Ece1-III$_{\mathrm{AA(N)}}$ was carried out using DOPC and DOPC/PS (9:1, n/n) liposomes. The corresponding results are given in Fig. 6.6 A for DOPC and in Fig. 6.6 B for DOPC/PS samples.

With a slope of (759.8 ± 379.4) nm for increasing P/L and a relative area expansion of ∼ 90 % at P/L = 1:18 (≈ 0.056), the magnitude of the enlargement of DOPC vesicles upon the interaction with Ece1-III$_{\mathrm{K(C)}}$ is roughly comparable to the one observed for DOPC and Ece1-III$_{\mathrm{KR(N)}}$ (cf. previous section). Also, the expansion is pronounced with DOPC/PS vesicles. Compared to Ece1-III$_{\mathrm{KR(N)}}$, however, the magnitude of this effect is notably reduced with Ece1-III$_{\mathrm{K(C)}}$, where the area increase and the slope are found to be ∼ 350 % and (1394.4 ± 210.0) nm, respectively. It is concluded that Ece1-III$_{\mathrm{K(C)}}$ intercalates into vesicles of solely DOPC, but triggers an additional vesicle-vesicle interaction in liposomes containing anionic PS.

[1] Note that the difference between the experimentally obtained hydrodynamic liposome size (particle size) and the physically smaller liposome size is neglected in this consideration. This approximation is justified since the system is treated within the Smoluchowski regime (cf. Sec. 3.1.2).

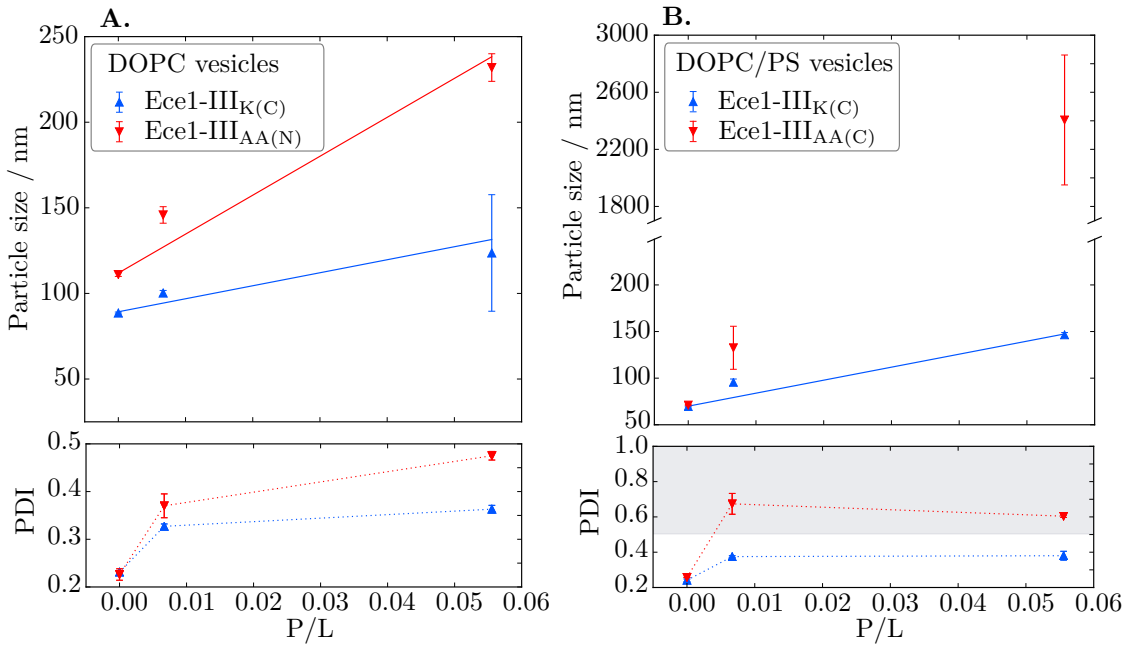

Figure 6.6 – Liposome diameter as function of increasing P/L. DOPC (**A.**) and DOPC/PS (9:1, n/n, **B.**) vesicles enlarge with increasing content of either Ece1-III$_{AA(N)}$ (▼) or Ece1-III$_{K(C)}$ (▲). The upper panels depict the measured vesicle diameters (markers) and corresponding linear fits (solid lines, except for DOPC/PS/Ece1-III$_{AA(N)}$ mixtures). The lower panels depict the corresponding PDIs which increase with increasing P/L. In both liposome species, the enlargement observed for Ece1-III$_{AA(N)}$ was more pronounced than that observed for Ece1-III$_{K(C)}$. However, the PDI of the DOPC/PS solution with Ece1-III$_{AA(N)}$ was larger than 0.5 and the corresponding size determination is thus imprecise. The measurements were performed at 25°C.

The interaction of DOPC and DOPC/PS liposomes with Ece1-III$_{AA(N)}$ is also found to enlarge the vesicle sizes. In the DOPC sample, the surface is increased by $\sim 336\,\%$ at P/L = 1:18 (≈ 0.056) with a corresponding slope of (2273.9 ± 584.2) nm. Thus, the possible peptide intercalation is assumed to be accompanied by liposome aggregation or fusion. A similar conclusion is also made from the interaction of Ece1-III$_{AA(N)}$ and DOPC/PS. Although the expansion in this case is evident in the data, distinct statements on the corresponding magnitude are rather vague since the PDIs of these samples exceeded a value of 0.5 and thus indicate a broad distribution of particle sizes. This observation may be explained by non-uniform liposome aggregations or fusions.

For both peptide variants Ece1-III$_{K(C)}$ and Ece1-III$_{AA(N)}$, the vesicle-vesicle interactions indicated by the DLS data are also consistent with the FRET fusion assays discussed in Sec. 6.3.5.

6.2.3 FRET Intercalation Assay

Amidated Peptide Variants

FRET intercalation assays were employed as a second technique to study the integration of Ece1-III$_{KR(N)}$ into bilayers. The results obtained from experiments with the amidated peptides Ece1-III$_{KR(N)}$ and Ece1-III$_{AA(N)}$ are shown in Fig. 6.7. Ece1-III$_{KR(N)}$ was tested with pure DOPC liposomes, but also with liposomes with Chol, Erg and PS content, while Ece1-III$_{AA(N)}$ was only tested with DOPC and DOPC/PS liposomes. For all samples, the detected donor intensity increases and the acceptor intensity decreases upon successive peptide additions. This relation is reflected by an increase in their ratio I_D/I_A, plotted in the figure, and it demonstrates the reduction of the FRET effect due to the dilution of the lipids. Consequently, the increasing I_D/I_A ratio confirms that the peptides integrate into the bilayers.

For Ece1-III$_{KR(N)}$, the increase in I_D relative to I_A, after its first addition (P/L = 1:13.5 ≈ 0.074), is similar in all lipid samples. Further increases of the P/L lead to obvious differences in I_D/I_A, which manifests to be one third greater in samples of pure DOPC and DOPC/PS than in the sterol-containing DOPC samples. Hence,

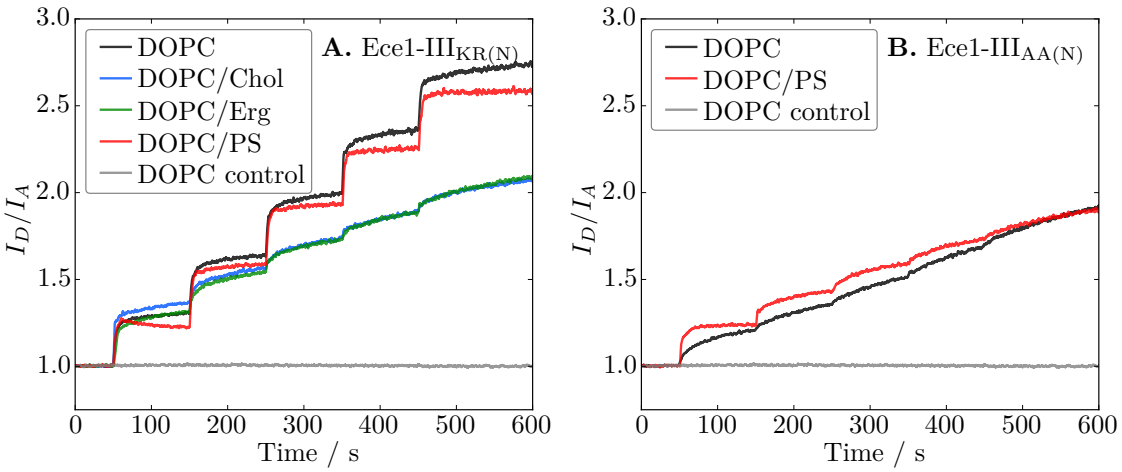

Figure 6.7 – FRET intercalation assays of amidated Ece1-III variants. The ratio of the fluorescence yields of donor to acceptor I_D/I_A (NBD-DHPE and Rho-DHPE) are shown for **A.** Ece1-III$_{KR(N)}$ and **B.** Ece1-III$_{AA(N)}$ as function of time and peptide concentration. Starting from 50 s, 50 μl peptide (1 mg·ml^{-1} in H_2O) were titrated every 100 s. Accordingly, the peptide concentration was gradually increased from 0.74 μM (P/L = 1:13.5 ≈ 0.074) after the first injection to 3.65 μM (P/L = 1:2.7 ≈ 0.37) after the final injection. The strongest increase in I_D/I_A is observed for the interaction of Ece1-III$_{KR(N)}$ with DOPC (black) and DOPC/PS (red) liposomes. It is reduced for DOPC/Erg (green) and DOPC/Chol (blue) samples and also for the interaction of Ece1-III$_{KR(N)}$ with DOPC and DOPC/PS. No intensity changes were observed in any of the control measurements. As exemplary data sets only the negative DOPC controls (gray) are shown. A moving average with a window of 15 points was applied to smoothen the data. Lipid-lipid ratio was 9:1 (n/n) and the measurements were carried out at 37°C.

beyond this boundary at P/L = 1:13.5, the reduction of the FRET efficiency is less pronounced in the sterol systems. This observation immediately suggests a favoured incorporation of Ece1-III$_{\mathrm{KR(N)}}$ in the absence of sterols, consistent with the film balance data (cf. Sec. 6.2.1). However, it should be noted that this effect may also be the result of a non-uniform distribution of intercalation sites across the liposome. In other words, a reduced I_D/I_A may on average also arise from Ece1-III$_{\mathrm{KR(N)}}$ aggregates inside the membrane. Thus, it is also possible that the formation of peptide clusters is enhanced in membranes containing Erg or Chol.

For each concentration increment, I_D/I_A shows a distinct hyperbolic progression with time. With its steep positive slope shortly after the peptide addition, it suggests a rapid initial intercalation. The efficiency of this process slows as I_D/I_A and the corresponding amount of integrated peptide approaches a certain saturation level. As evidenced by the equidistant increments of $\Delta(I_D/I_A) \approx 0.25$, the particular saturation levels increase linearly with increasing P/L in the DOPC and DOPC/PS samples. The situation is different in the sterol-containing samples. Here, the progressions of I_D/I_A exhibit kinetics similar to that of DOPC and DOPC/PS as response to the first peptide injection, but have reduced overall velocity for concentration increases beyond the boundary P/L = 1:13.5 (≈ 0.074).

Ece1-III$_{\mathrm{AA(N)}}$ also intercalates into the lipid matrix of DOPC and DOPC/PS liposomes as the increases in I_D/I_A demonstrate. Compared to the corresponding experiments with Ece1-III$_{\mathrm{KR(N)}}$, however, the concentration-dependent slopes are reduced. These signals rather compare with those obtained for the interaction of Ece1-III$_{\mathrm{KR(N)}}$ with DOPC/Chol or DOPC/Erg vesicles. The kinetics of the interaction of Ece1-III$_{\mathrm{AA(N)}}$ and DOPC/PS are also very similar to these results since the hyperbolic progression flattens with increasing peptide concentration. For the interaction with pure DOPC vesicles, by contrast, the process is already slowed for the lowest peptide concentration.

Non-amidated Peptide Variants

The FRET signals accompanied by the intercalation of the non-amidated variants Ece1-III$_{\mathrm{KR(C)}}$, Ece1-III$_{\mathrm{K(C)}}$, Ece1-III$_{\mathrm{AA(C)}}$ and Ece1-III$_{\mathrm{A(C)}}$ into liposomes of different composition are shown in Fig. 6.8.

The increases of I_D/I_A obtained by the interaction of Ece1-III$_{\mathrm{KR(C)}}$ and Ece1-III$_{\mathrm{K(C)}}$ are of moderate extent, similar to those observed for the addition of the amidated Ece1-III$_{\mathrm{KR(N)}}$ to DOPC/Chol or DOPC/Erg liposomes. A distinct difference between the pure DOPC and the sterol-containing lipids is not detected. In the presence of PS, the extent and the dynamics of the increasing I_D/I_A signal are slightly enhanced.

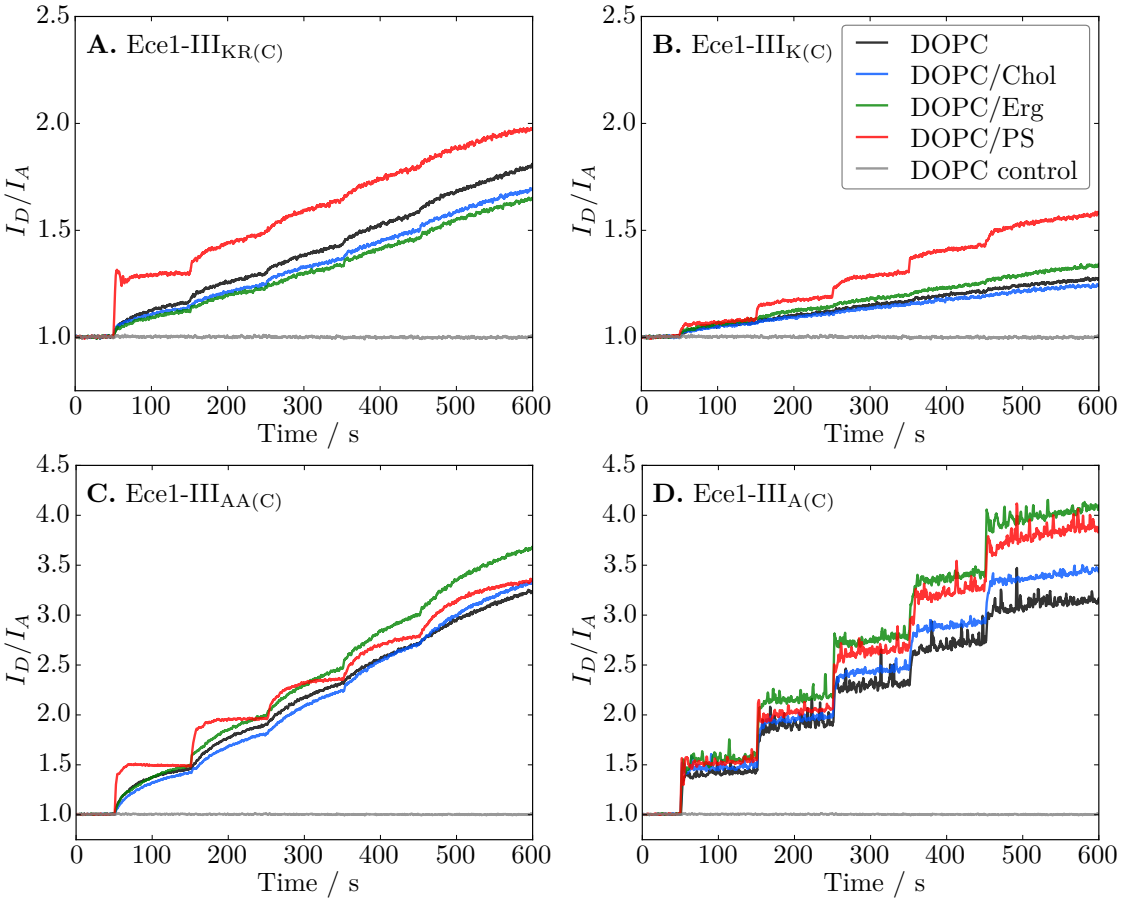

Figure 6.8 – FRET intercalation assays of non-amidated Ece1-III variants. The ratio of the fluorescence yields of donor to acceptor I_D/I_A (NBD-DHPE and Rho-DHPE) are shown for **A.** Ece1-III$_{KR(C)}$, **B.** Ece1-III$_{K(C)}$, **C.** Ece1-III$_{AA(C)}$ and **D.** Ece1-III$_{A(C)}$ as function of time and peptide concentration. Each peptide variant was tested with DOPC (black), DOPC/Chol (blue), DOPC/Erg (green) and DOPC/PS (red) liposomes. Starting from 50 s, 50 μl peptide (1 mg·ml^{-1} in H_2O) were titrated to the liposome solutions every 100 s. Accordingly, the peptide concentration was gradually increased from 0.74 μM (P/L = 1:13.5 $\approx$ 0.074) after the first injection to 3.65 μM (P/L = 1:2.7 $\approx$ 0.37) after the final injection. No intensity changes were observed in any of the control measurements. As exemplary data set only the negative DOPC controls (gray) are shown. A moving average with a window of 15 points was applied to smoothen the data. Lipid-lipid ratio was 9:1 (n/n) and the measurements were carried out at 37°C.

Both variants with the terminating alanine substitutes, Ece1-III$_{AA(C)}$ and Ece1-III$_{A(C)}$, show I_D/I_A increases that are similar in all lipid systems and also similar to each other. This increase is more than doubled compared to that observed for the variants with cationic C-terminus, i. e. Ece1-III$_{KR(C)}$ and Ece1-III$_{K(C)}$, and the amidated isoform Ece1-III$_{AA(N)}$. While the intercalation of Ece1-III$_{AA(C)}$ proceeds comparatively slow in DOPC, DOPC/Chol and DOPC/Erg liposomes, it is slightly accelerated in the presence of PS. With Ece1-III$_{A(C)}$, the concentration-dependent saturation level is reached very rapidly for all stages and lipid compositions.

6.2.4 Peptide Orientation in Aligned Lipid Bilayers (OCD)

P/L Dependence

To study the orientation of the bound and intercalated peptide, oriented circular dichroism spectra were obtained as function of the peptide-to-lipid ratio. Normalised SR-OCD spectra of Ece1-III$_{\mathrm{KR(N)}}$ in fully hydrated and oriented DOPC multilayer samples at a temperature of 25°C are shown in Fig. 6.9. The figure also includes the absorbance spectra and the progressions of the high voltage (HT) applied to the photomultiplier tube during the corresponding peptide/lipide sample acquisitions. Absorption and scattering of DOPC's unsaturated fatty acid chains is strong for wavelengths $\lambda < 200$ nm which becomes evident in the amplifying voltage applied. It exceeds the approximate upper limit of 400 V and, thus, reflects that the intensity reaching the PMT is too low to obtain reliable results. Consequently, the OCD values corresponding to HT values greater than 400 V (depicted with dotted lines) exhibit erroneous extents of the positive CD band around 195 nm: It gradually decreases with increasing lipid content, although it is expected to stay constant for all normalised spectra. The absorbance spectra shown in the lower part of Fig. 6.9 exhibit some inconsistency as the positions of the absorption maxima are shifted for varying lipid content. In peptide/lipid samples usually two major effects contribute to the samples' absorbance. These are (1) the inherent contribution of the peptide chromophore absorption around the respective electronic transitions (195, 208 and 223 nm) and (2) the high absorption of the unsaturated double bonds of the alkene chains between $\sim$ 200 - 230 nm (cf. Fig 6.10) leading to maximal absorbance between $\sim$ 190 and 210 nm. However, the calculated absorbance of the sample at P/L = 1:100 (= 0.01) has values even smaller than zero in this wavelength range. This observation makes no physical sense. It indicates that the probed volume of the lipid reference sample did not match the one of the peptide/lipid sample. These deviations are probably caused by inaccuracies of the sample preparation such as thickness mismatches due to varying sample spot diameters on the quartz glass plate. To reduce the influence of these variances, samples obtained from vesicle spreading [161, 164] may be of advantage since it is easier to control the spot size for lipids solved in aqueous buffer than it is for lipid stocks in organic solvent. In general, absorption mismatches might also be caused by radiation induced peptide denaturation. These can occur if the density flux exceeds a threshold limit of $0.4{\cdot}10^{11}$ photons$\cdot$s$^{-1}\cdot$mm^{-2}, as it has been indicated by Miles and co-workers [249]. Although the exerted density flux of about $0.8{\cdot}10^{11}$ photons$\cdot$s$^{-1}\cdot$mm^{-2} was in the magnitude of this limit, such artefacts are not expected with the experimental conditions applied here [176].

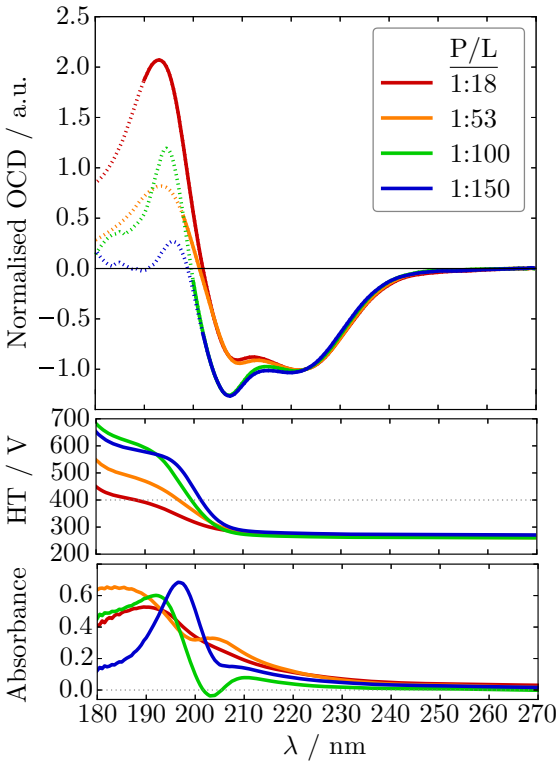

Figure 6.9 – SR-OCD and calculated absorption spectra of Ece1-III$_{KR(N)}$ in aligned and fully-hydrated DOPC membranes at different P/L. The spectra with low peptide concentration (P/L = 1:150 ≈ 0.007, blue, and P/L = 1:100 = 0.01, green) show intense negative CD bands around 208 nm which are identical to each other. In spectra of higher peptide concentration (P/L = 1:53 ≈ 0.019, orange, and P/L = 1:18 ≈ 0.056, red), this CD band is less pronounced. The CD spectra shown here are corrected for the corresponding lipid spectra and normalised to 223 nm. The HT applied during the acquisition of the peptide/lipid spectra is shown in the middle, a dashed line indicates the HT tolerance limit at 400 V. SR-OCD values acquired with higher HT values are not reliable and plotted with dotted lines. The lower part depicts the absorption spectra calculated according to Eq. 3.9. The acquisition was carried out at 25°C at the UV-CD12 beamline.

Just as the isotropic CD spectra, the line shapes of the OCD spectra of Ece1-III$_{KR(N)}$ exhibit a substantial α-helical content. At P/L = 1:150 and P/L = 1:100, the CD band around 208 nm is more intense than the band around 224 nm, indicating that the peptide aligns parallel to the membrane surface. With higher peptide content (P/L = 1:53 and 1:18), the orientation alters which is reflected by the intensity decrease of this band. Correspondingly, the α-helix is rotated to a certain extent with respect to the bilayer surface. This state is referred to as tilted T-state [170]. Note that from the OCD experiments it cannot be distinguished whether the T-state is a stable state itself, an orientational average of more extreme S- and I-state spectra or a respective time average. To discriminate between these three scenarios, NMR techniques have to be employed. A T-state spectrum similar to that of Ece1-III$_{KR(N)}$ has been found by Bürck *et al.* for the peptide PGLa [170]. To explain

this spectrum, the authors discussed two previous NMR observations. While the first one has evidenced the existence of dynamic interconversions between a T- and the S-state on ms-timescale [250], the second one has clearly demonstrated that the tilted orientation reflects a stable state [251]. Eventually, Bürck and co-workers inferred the OCD spectrum of PGLa to be caused by the latter case, namely a stable T-state population. Albeit corresponding solid-NMR studies on Ece1-III$_{\mathrm{KR(N)}}$ have not been carried out yet, it is rather unlikely that the obtained T-state spectra represent dynamical averages of S- and I-state conversions (please refer to the discussion in Sec. 6.2.5 for a justification of this conclusion). However, with regard to the GID data, which indicate peptide-mediated formations of non-lamellar lipid super structures, it can not be excluded that the spectra arise from averages of different peptide orientations within the lipid scaffold. Regardless of the detailed reason which causes the spectral changes, the SR-OCD data confirms that Ece1-III$_{\mathrm{KR(N)}}$ and the bilayer interact in a concentration-dependent manner as the line shapes clearly differ for high and low P/L.

Lipid Composition

To examine the influence of different lipid components on the alignment of Ece1-III$_{\mathrm{KR(N)}}$ inside the DOPC membrane, DOPC multilayers with proportions of 10 % PS, cholesterol or ergosterol were utilised. OCD spectra at two different P/L values were acquired with the J-810 spectropolarimeter: one at low P/L (P/L = 1:200 = 0.005), where the S-state orientation was expected, and another one with increased peptide concentration (P/L = 1:18 $\approx$ 0.056), at which a T-state orientation was expected. The resulting spectra, normalised to 223 nm, are shown in Fig. 6.10. For the samples at P/L = 1:18, it was sufficient to acquire and average two consecutive scans due to their high peptide but low lipid content. For the P/L = 1:200 samples, the signal-to-noise ratio of the acquisitions with the J-810 spectropolarimeter was drastically decreased compared to the synchrotron setup. Hence, the averages of at least three scans were required to give reliable OCD spectra. The spectra are presented up to 200 nm – for smaller wavelengths, the absorption was again too high which is evident in distorted appearances of the positive CD band around 195 nm. However, the HT did not exceed a critical limit of 400 V. This inconsistency is presumably explained by an automated slit mode of the J-810 instrument that enlarges the exit slit size behind the prism monochromator if the detected intensity becomes too low. This broadens the spectral bandwidth and, thus, distorts the positive band [176].

The OCD spectra at P/L = 1:200 (= 0.005) show similar line shapes for all lipid compositions. In each case, the negative band around 208 nm is more pronounced

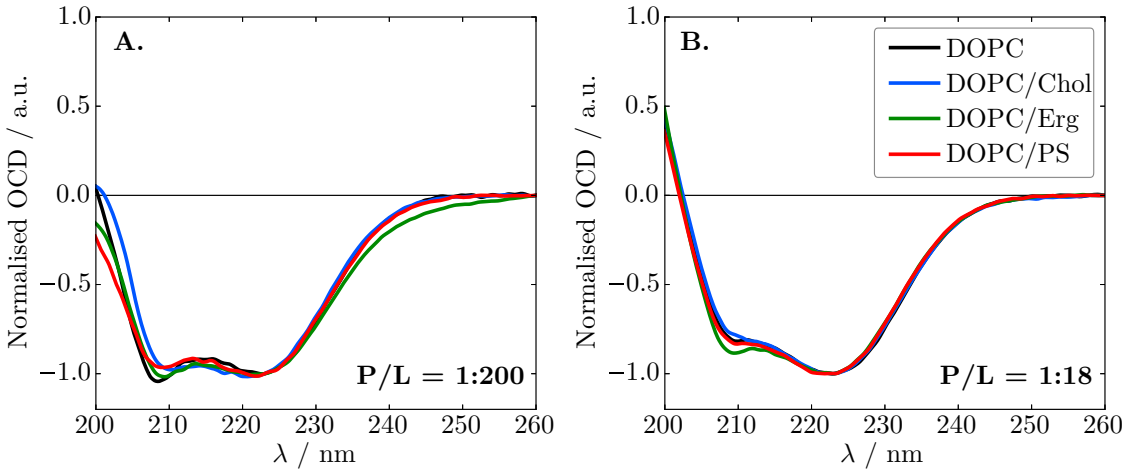

Figure 6.10 – OCD spectra of Ece1-III$_{KR(N)}$ in aligned and fully hydrated membranes of different lipid composition at P/L = 1:200 = 0.005 (**A.**) and P/L = 1:18 ≈ 0.056 (**B.**). The spectra associated to DOPC (black) and DOPC/Erg (green) at P/L = 1:200 show a marginally stronger CD band around 208 nm, but beyond that they do not show distinct differences to DOPC/Chol (blue) and DOPC/PS (red) associated spectra. The spectra at P/L = 1:18 have similar line shapes, albeit the CD band around 208 nm is slightly more intense in the DOPC/Erg associated spectrum (green). Lipid-lipid ratio was 9:1 (n/n). Two consecutive scans were averaged for the P/L = 1:18 spectra, whereas the P/L = 1:200 spectra represent the average of three scans. All spectra are corrected for the corresponding lipid spectra and normalised to 223 nm. The acquisition was carried out at 25°C at a J-810 benchtop spectropolarimeter.

than the band around 223 nm, indicating that Ece1-III$_{KR(N)}$ aligns predominantly parallel to the membrane surface. In DOPC membranes with 10 % PS or cholesterol content, the ratio of both bands is slightly reduced. This might represent a minor peptide tilt into the bilayer. However, due to the low signal-to-noise ratio, such slight profile deviations only allow speculating. Thus, it is concluded that the peptide orientation at low concentration is independent on the particular lipid content. Likewise, Ece1-III$_{KR(N)}$ adapts a T-state in all membranes at P/L = 1:18, which is represented by an intensity reduction of the band around 208 nm. The tilt extent of Ece1-III$_{KR(N)}$ is the same in DOPC/Chol, DOPC/PS and pure DOPC stacks, as indicated by their almost identical line shapes. In DOPC/Erg membranes, however, the minimum at 208 nm is slightly more intense suggesting that the peptide tends to adapt a shallower tilt with respect to the bilayer surface. This goes well with the assumption that ergosterol might have a stabilising influence on the membrane integrity as it impedes deep penetration. Nevertheless, it is indisputable that Ece1-III$_{KR(N)}$ is capable to intercalate into DOPC/Erg membranes, too. For this reason, it is concluded that also at high peptide concentration, none of the probed lipid components is capable to significantly mediate the orientation of Ece1-III$_{KR(N)}$.

Peptide Variants

To study the influence of the terminating amino acids on the peptide orientation at high concentration (P/L = 1:18 ≈ 0.056), additional OCD spectra of Ece1-III variants, namely Ece1-III$_{K(C)}$ and Ece1-III$_{AA(N)}$, embedded in fully hydrated DOPC stacks were acquired. The resulting spectra, normalised to 223 nm, are depicted in Fig. 6.11. A corresponding spectrum of Ece1-III$_{KR(N)}$ is additionally shown for comparison. Again, the data is only shown within a range of 200 - 260 nm as absorption effects were severe for wavelengths lower than 200 nm (see above).

Both peptides cause spectra with similar line shapes. The comparatively weak CD bands around 208 nm indicate that both peptide variants also adapt a T-state alignment in the bilayer at high concentration. Compared to Ece1-III$_{KR(N)}$ and Ece1-III$_{AA(N)}$, this band is least intense for Ece1-III$_{K(C)}$. However, the band is still far apart from vanishing completely, so that Ece1-III$_{K(C)}$ does not adapt an I-state but tilts more deeply into the membrane than the other variants. Since the latter ones comprise one additional terminating amino acid and two additional positive charges due to their amidation, it is suggested that these extensions represent steric obstacles which hinder the peptide to tilt deeply into the membrane.

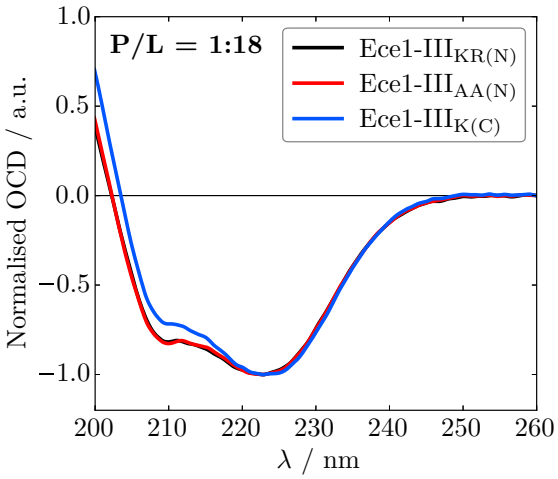

Figure 6.11 – OCD spectra of the Ece1-III variants Ece1-III$_{KR(N)}$, Ece1-III$_{K(C)}$ and Ece1-III$_{AA(N)}$ in aligned and fully hydrated DOPC membranes at P/L = 1:18 (≈ 0.056). The spectra of Ece1-III$_{KR(N)}$ (black) and Ece1-III$_{AA(N)}$ (red) have identical line shapes and the intensity of the CD band around 208 nm is stronger than that of the Ece1-III$_{K(C)}$ spectrum (blue). The OCD spectra are averages from two consecutive scans, corrected for the corresponding lipid spectra and normalised to 223 nm. The acquisition was carried out at 25°C at a J-810 benchtop spectropolarimeter.

6.2.5 Discussion of the Integration Data

Effect of P/L and Lipid Composition

The FRET intercalation assay indicated that the integration of Ece1-III$_{KR(N)}$ is independent on the particular lipid composition at peptide-to-lipid ratios smaller than P/L $\leq$ 1:13.5 ($\approx$ 0.074). This result is consistent with the DLS experiments, where the DOPC, DOPC/Chol and DOPC/Erg vesicles are found to swell equally up to P/L = 1:18 ($\approx$ 0.056), the highest P/L probed with this technique.

For P/L values greater than 1:13.5 ($\approx$ 0.074), the FRET intercalation assay implies that the penetration of Ece1-III$_{KR(N)}$ into sterol-containing membranes is either impeded by the sterols or dominated by the integration of whole peptide clusters. The film balance data provides support for the first explanation, since the area expansion is greater in DOPC and DOPC/PS monolayers than it is in monolayers with Chol or Erg content. The assembly of an identical amount of peptide would entail a film expansion that is independent on the peptide's monomeric or clustered appearance, assuming the cross section per peptide to be identical. Additional support for the conclusion that the aggregation behaviour of Ece1-III$_{KR(N)}$ is not enhanced by sterols can be inferred from the FRET binding assay (cf. Sec. 6.1.1). Its results suggested a similar aggregation tendency in DOPC, DOPC/Chol and DOPC/Erg vesicles since the self-quenching was similar in all three samples. Although cholesterol is well-known to rigidify most phospholipid membranes, it does not stiffen DOPC membranes [252]. The absence of this stiffening effect is also assumed for ergosterol, since its properties are similar to those of cholesterol. Thus, the raised barrier for a high number of peptide to penetrate the bilayer is rather determined by steric hindrances such as the tight lipid packing than by the elastic properties of the bilayer.

The results obtained from the film balance indicate a slightly enhanced assembly of Ece1-III$_{KR(N)}$ in DOPC/PS monolayers as compared to monolayers of pure DOPC. Such a distinct difference is not indicated by the FRET intercalation assay. Therefore, it is concluded that, although the binding is facilitated in the presence of PS, the intercalation is not notably enhanced compared to that of pure DOPC. Further, the DLS data suggests additional interaction effects for liposomes formed of DOPC and PS, as the observed surface expansion of $\sim$ 1075 % exceeds the proposed magnitude of the expansion by one order. This effect is discussed in more detail in Sec. 6.3.5.

Eventually, the data suggests that the area required per Ece1-III$_{KR(N)}$ molecule in the presence of a lipidic interface is smaller than in the pure peptide monolayer at the same lateral pressure. This conclusion is inferred by combining the observations

from the FRET intercalation, which evidence an ongoing intercalation even for P/Ls higher than 1:13.5 (≈ 0.074), and the film balance experiments, where the area expansion in DOPC was notably smaller than it was expected to be at P/L $\simeq$ 1:6 (≈ 0.167). However, given the disparity in the experimental methods and model systems, this conclusion is tentative. Nevertheless, it achieves support by similar findings for other peptides as for instance alamethicin [94]. Huang and his co-workers have attempted to explain the reduced area expansion with the release of water molecules from the lipid headgroup region, which they have speculated to accompany the peptide binding [94, 253]. Moreover, an altered peptide orientation with a smaller effective cross section is also a likely of this difference.

Effect of the C-terminal Amino Acids

The strongest intercalation preference is observed for Ece1-III$_{\mathrm{KR(N)}}$ which exhibits both highest cationicity and highest hydrophobic gradient at the C-terminus. In the FRET intercalation assay, the effect of its non-amidated isoform is found to be reduced. However, it cannot be excluded that the higher FRET efficiency persisting in case of Ece1-III$_{\mathrm{KR(C)}}$ arises from an augmented incorporation of peptide clusters since this peptide was already found to strongly aggregate in buffer. As explained above, these aggregates may cause a lower signal I_D/I_A at the same amount of incorporated peptide monomers. The shorter peptide variant, Ece1-III$_{\mathrm{K(C)}}$, which also tends to aggregate in buffer, intercalates into the liposomes with a halved efficiency compared to Ece1-III$_{\mathrm{KR(C)}}$. With regard to the assumption that the arginine and lysine residues reside inside the hydrophobic part of the bilayer and snorkel their charged side chains to the lipid headgroups, this observation may be attributed to the lack of the terminating R and a corresponding reduced potential to snorkel.

The less pronounced intercalation of the amidated Ece1-III$_{\mathrm{AA(N)}}$ compared to its non-amidated isoform Ece1-III$_{\mathrm{AA(C)}}$ is also consistent with this intercalation hypothesis. The additional hydrophilic NH_2-group attached to the terminating alanine evidently increases the free energy barrier for the partition into the hydrophobic core and hinders the intercalation. A pronounced incorporation is also observed for Ece1-III$_{\mathrm{A(C)}}$ in DOPC liposomes. Again, this is consistent with its energetic need to insert its hydrophobic C-terminus into the lipid core in order to hide it from the aqueous surrounding.

The Relation of Intercalation and Orientation of Ece1-III

The OCD spectra evidence that the peptide's initial parallel orientation to the lipid bilayer alters with increasing lipid-to-peptide ratio. A similar behaviour was also

observed for various antimicrobial peptides, which led to the development of the two-step model (cf. Sec. 1.4.2). These peptides typically show a sigmoidal (all-or-none) orientation dependence and insert with perpendicular orientation at high peptide concentrations (or full membrane hydration). This represents a unique mechanism of penetrating and destabilising the lipid membrane [177, 253, 254]. For the four increasing Ece1-III$_{\mathrm{KR(N)}}$ concentrations probed, only two clearly differing states were observed. This might indicate that Ece1-III$_{\mathrm{KR(N)}}$ also exhibits a similar sigmoidal concentration dependence, particularly, because the binding was also found to proceed in a cooperative fashion (cf. Sec. 6.1.3). However, a subtle conversion between both states cannot be excluded, as the number of concentrations probed is very small and the range, in which according transition spectra would occur, might be missed. Neglecting the occurrence of dynamic interconversions, the orientation observed for Ece1-III$_{\mathrm{KR(N)}}$ at high P/L is considered as stable T-state. Hence, an analogue two-step disintegration mechanism for Ece1-III$_{\mathrm{KR(N)}}$ would involve the S-state and this characteristic oblique orientation.

Dennison and co-workers analysed the properties of numerous α-helical host-defence peptides and concluded that many of them insert only shallow into the membrane interior, demonstrating that a perpendicular penetration is not an indispensable requirement to induce membrane disruptions [51]. These peptides with oblique helix orientation have asymmetric hydrophobicity distributions along their long axis, just like the Ece1-III variants examined in this work (see Sec. 5.1.3). This reasoning also supports the assumption that the OCD spectra at high peptide concentration are caused by a stable T-state. The particular trigger which eventually evokes the bilayer disintegration by oblique-oriented peptides is still under speculation. However, this process is assumed to involve the induction of defects of the lipid packing. This is supported by studies of Bhargava and Feix, who examined the orientation of CM15, a cecropin-melittin hybrid, in LUVs composed of inner membrane lipids of *E. coli* at a high P/L [255]. They found it to intercalate into the bilayer with an alignment parallel to the surface and reported its central helical axis to be buried at a depth of 5 Å. With this positioning, the peptide may snorkel its lysine residues to the hydrophilic phosphates of the lipid, while hiding its hydrophobic residues among the acyl chains. In turn, the lipids have to accommodate the entire peptide volume. The authors argued that this may be an important factor which promotes the destabilisation of the bilayer, eventually leading to its collapse. Such a deep oblique intercalation of the peptide would thus relate to remarkable expansion of the lipid area as it was observed for Ece1-III$_{\mathrm{KR(N)}}$.

6.3 Peptide-induced Structural Changes in Bilayers

This section focuses on alterations of the lipid bilayer structure owing to the interaction with the peptides Ece1-III$_{\mathrm{KR(N)}}$, Ece1-III$_{\mathrm{K(C)}}$ and Ece1-III$_{\mathrm{AA(N)}}$. In the first instance, atomic force microscopy is utilised to illustrate the outward appearance of solid-supported multilayer membranes in both the absence and presence of Ece1-III$_{\mathrm{KR(N)}}$. Secondly, the vertical structure is studied in greater detail on the basis of the X-ray reflectivity of solid-supported single and multiple bilayer samples. Thirdly, the lateral bilayer structure is addressed by evaluating the diffuse scattering as well as the samples' diffraction in grazing incidence. From the latter, both small- and wide-angle information are analysed. Fourthly, the effect of Ece1-III$_{\mathrm{KR(N)}}$ on membranes with coexisting liquid-ordered and liquid-disordered domains is examined, using real-time AFM studies, XRR analyses and Fourier-transform infra-red measurements. In a fifth step, the peptides' capability to trigger liposome fusion is investigated. Finally, the findings are summarised and discussed.

6.3.1 Microscopically Visible Impact on Multilayer Membranes

The structural impact of Ece1-III$_{\mathrm{KR(N)}}$ on lipid model membranes was investigated visually by probing the surface topography of solid-supported multilayer samples with atomic force microscopy. First, dry samples of DOPC with increasing amount of Ece1-III$_{\mathrm{KR(N)}}$ content were imaged (Fig. 6.12).

The pure DOPC sample exhibits a mostly flat surface with a root-mean-square roughness of $\sigma = 2.2$ nm. The height profiles are characterised by defined steps of 43.7 Å, corresponding to single bilayers which do not extend over the entire sample width. With increasing P/L, more and more holes (which do not necessarily span the entire sample stack) emerge in the sample stack. While there are only a few holes with diameters of $D \simeq 7$ μm observed at P/L = 1:62, the defect density at P/L = 1:40 is significantly increased which leads to a spongy appearance. At a P/L of 1:18, the multilamellar character of the sample is apparently lost as the surface does not have any flat membrane patches. Here, the surface exhibits a roughness of $\sigma = 9.4$ nm and it is not featured with a distinct pattern.

Surface topographies of dry multilayer samples of DOPC/Chol, DOPC/Erg and DOPC/PS in absence and presence of Ece1-III$_{\mathrm{KR(N)}}$ at a P/L of 1:18 are shown in Fig. 6.13. Each of the pure lipid samples exhibits a flat surface without detectable defects and the step heights of $d \sim 43$ Å correspond to the thickness of a bilayer. The samples containing Ece1-III$_{\mathrm{KR(N)}}$ are again featured with rough surfaces of $\sigma = 17$ nm in case of the DOPC/Chol stack, $\sigma = 23$ nm for DOPC/Erg and $\sigma = 22$ nm for the DOPC/PS sample. While there are no distinct patterns recognisable

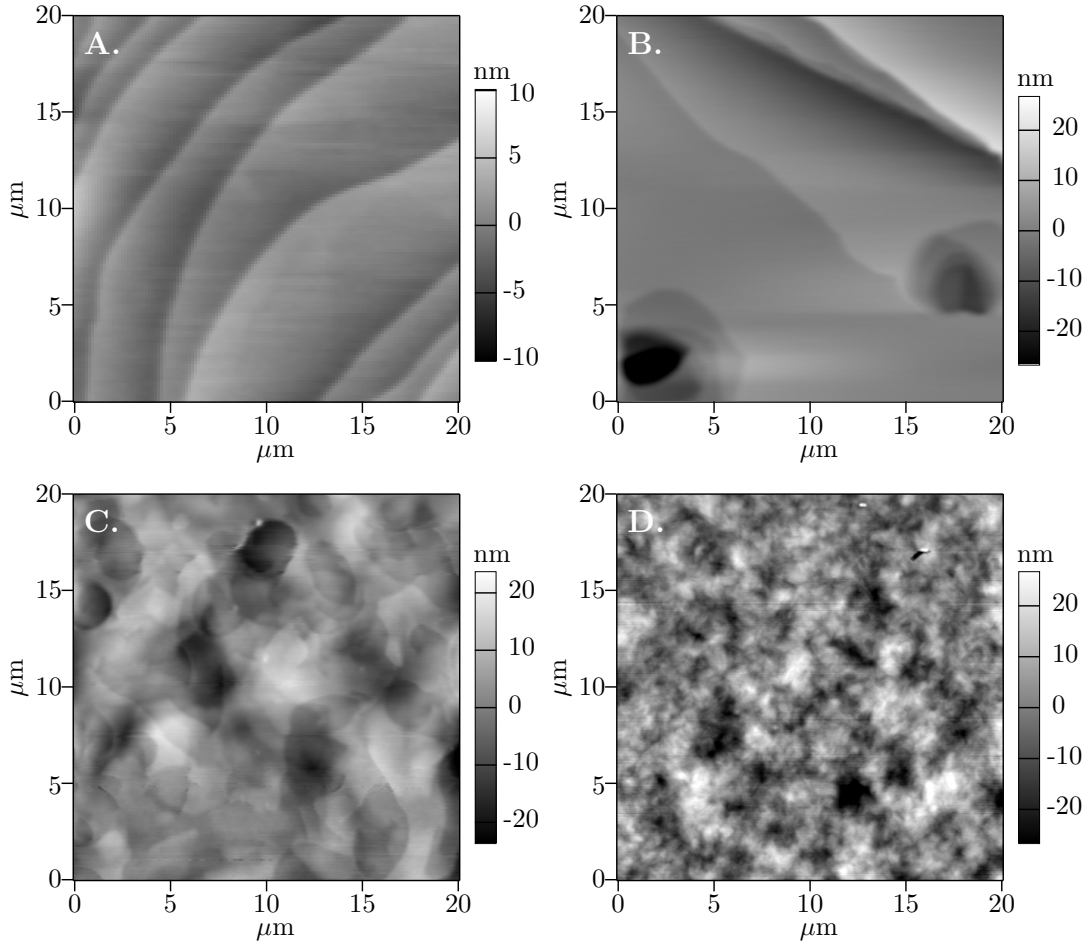

Figure 6.12 – AFM height images of dry Ece1$_{KR(N)}$/DOPC multilayers in dependence on the peptide concentration. The P/L increases from panels A to D: **A.** P/L = 0:1, **B.** P/L = 1:62 ($\approx$ 0.016), **C.** P/L = 1:40 (= 0.025) and **D.** P/L = 1:18 ($\approx$ 0.056). These representative height images demonstrate that the defect density of the sample surface increases with increasing peptide content. The samples were measured at room temperature and the images were obtained with NSG10 (A and B) and NSG11 (C and D) cantilevers in tapping mode at a scanning rate of 0.5 Hz/line.

in the DOPC/Erg/Ece1-III$_{KR(N)}$ and DOPC/PS/Ece1-III$_{KR(N)}$ samples, the surface of the DOPC/Chol/Ece1-III$_{KR(N)}$ sample seems to be arranged with some kind of regularity.

All examinations on these dry multilayer samples clearly demonstrated that Ece1-III$_{KR(N)}$ dramatically alters the bilayer structure on nano- to micrometre scale. Since the lipids themselves tend to form non-lamellar structures in partially dehydrated condition, this observation merely implies that the presence of the peptide promotes such formations. To advance the measurements towards the physiological condition of full hydration, the samples were partially hydrated. Fig. 6.14 depicts two representative examples of these experiments: First, a pure DOPC stack in the absence of Ece1-III$_{KR(N)}$ and in its presence at P/L = 1:50. Second, DOPC/PS with and without Ece1-III$_{KR(N)}$ at P/L = 1:62. In the partially hydrated DOPC/PS sample,

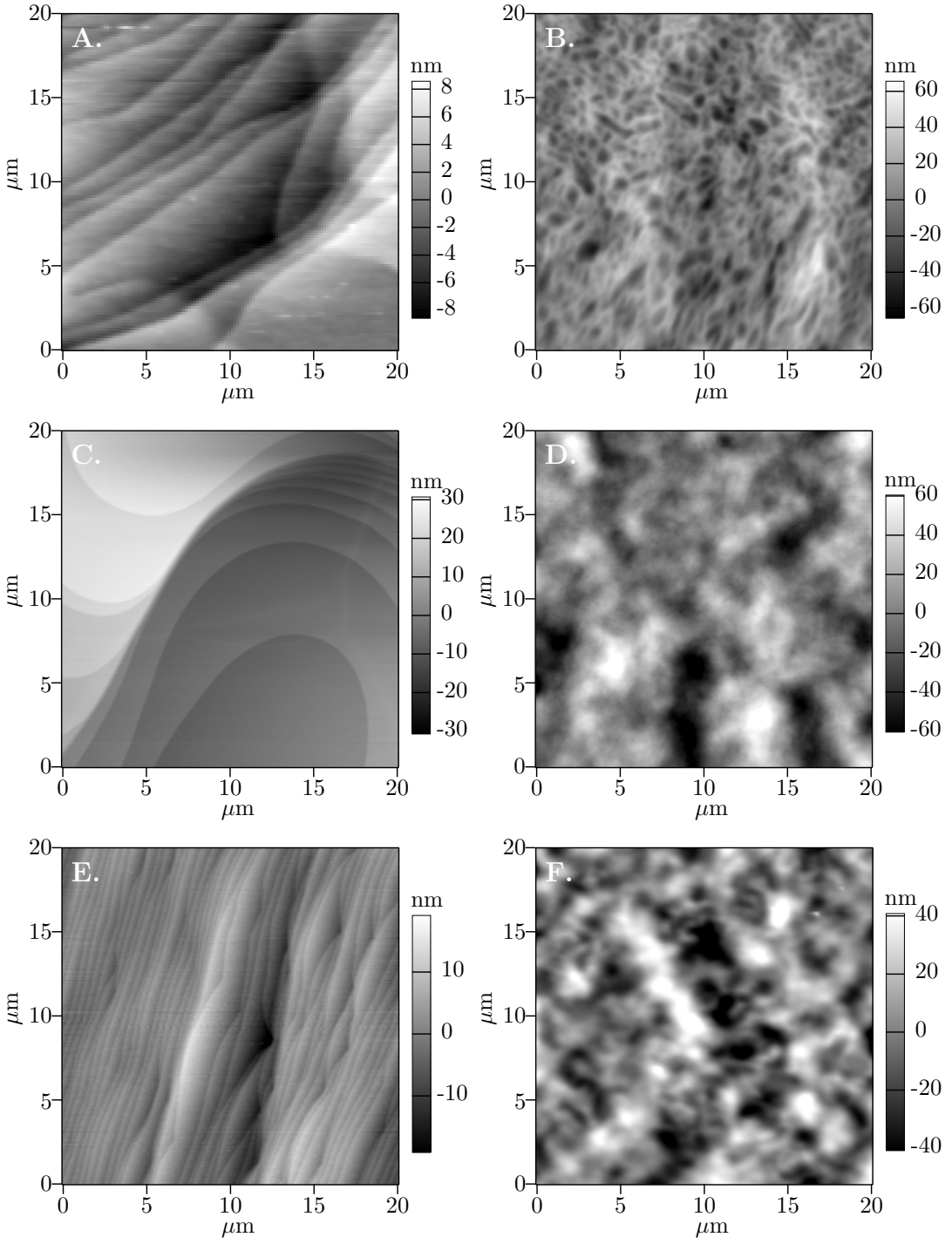

Figure 6.13 – AFM height images of dry peptide/SSM samples in dependence on the lipid composition. **A.** DOPC/Chol, **B.** DOPC/Chol + Ece1-III$_{KR(N)}$, **C.** DOPC/Erg, **D.** DOPC/Erg + Ece1-III$_{KR(N)}$, **E.** DOPC/PS, and **F.** DOPC/PS + Ece1-III$_{KR(N)}$. The lipid-to-lipid ratio of the samples was 9:1 (n/n) and the peptide-to-lipid ratio was $\simeq$ 1:18 ($\approx$ 0.056). The measurements were carried out in room atmosphere using NSG11 (A, B, F) as well as CSG11 (C, D, E) cantilevers. The scanning rate was either set to 0.5 Hz/line (B, D, E) or 1.0 Hz/line (A, C, F). All images were obtained in tapping mode, except for the DOPC/Erg/Ece1-III$_{KR(N)}$ sample, which was imaged in contact-mode.

the bilayers were found to have a thickness of (55.0 ± 2.5) Å. For the pure DOPC stack, the determination of the membrane thickness was impeded, as in these images only large steps corresponding to multiple bilayers were observed. In contrast to the sample's appearance in dry condition, the surface does not show defined holes in the presence of Ece1-III$_{KR(N)}$. It rather exhibits small flat patches with widths of several hundreds of nanometres which are separated from each other by thin pits with a depth of ∼ 50 - 100 Å. A similar surface character is also observed in the DOPC/PS sample with Ece1-III$_{KR(N)}$. Similar to the dry samples, the partially hydrated samples thus show an increased tendency to form some kind of non-lamellar structures in the presence of the peptide. In addition, these samples showed a particular differ-

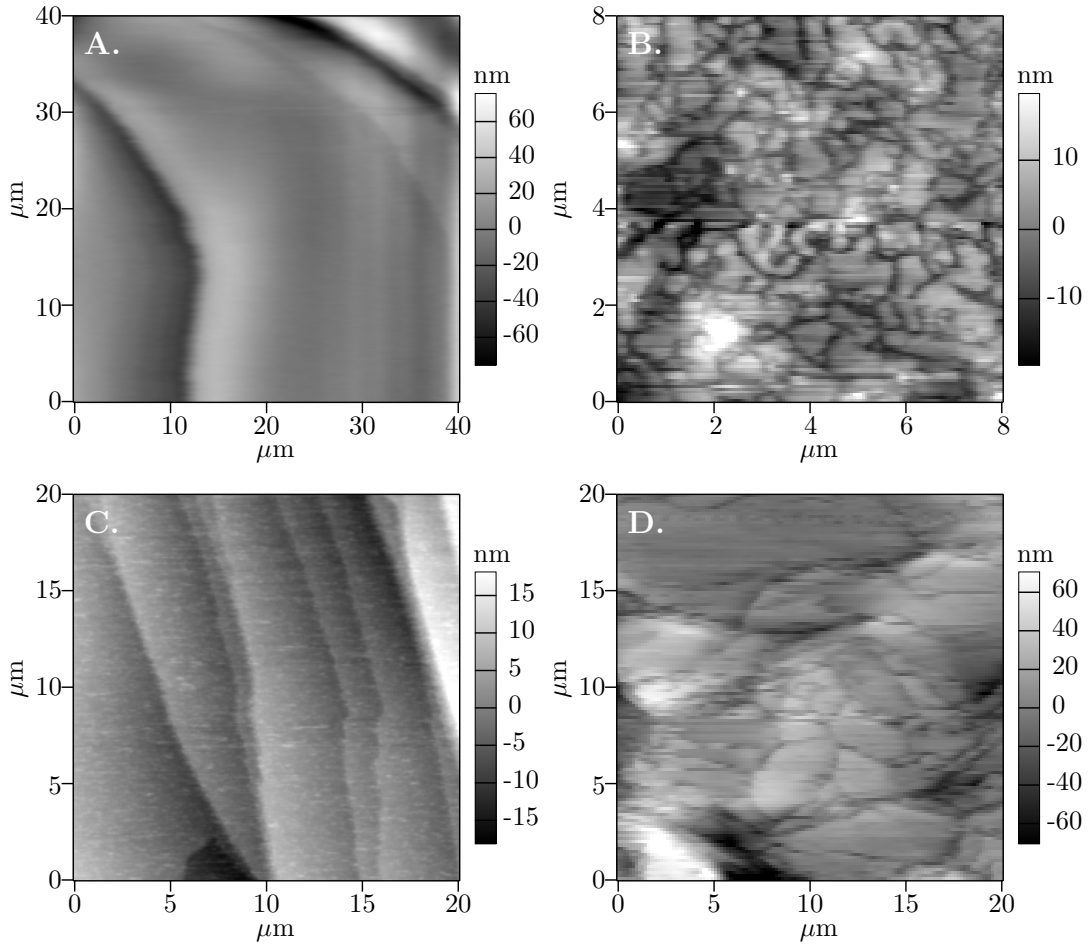

Figure 6.14 – **AFM height images of partially hydrated peptide/SSM samples. A.** DOPC, **B.** DOPC + Ece1-III$_{KR(N)}$ at P/L = 1:50 (= 0.02), **C.** DOPC/PS (9:1, n/n) and **D.** DOPC/PS (9:1, n/n) + Ece1-III$_{KR(N)}$ at P/L = 1:62 (≈ 0.016). Note the differences of the image dimensions: The pure DOPC sample is displayed in a 40 × 40 μm^2 section, whereas its peptide-containing counterpart is pictured with an edge length of only 8 μm. The images were obtained in tapping mode using a NSG11 cantilever for A, a CSG11 type for C and NSG11 cantilevers for B and D. The scanning rate was set to 4.0 Hz/line for A, 2.0 Hz/line for C, 1.0 Hz/line for D and 0.5 Hz/line for B, the temperature was set to 25°C.

ence in their dynamic behaviour. A time series obtained for the hydrated DOPC/PS stack demonstrated a pronounced movement of the bilayers. Such a dynamic movement was absent in the presence of the peptide, suggesting that the broken lateral invariance impedes this dynamics.

6.3.2 Peptide Influence on the Vertical Bilayer Structure

The vertical bilayer organisation is examined with X-ray reflectivity experiments on solid-supported multilayers and bilayers. The latter is only carried out for DOPC bilayers with Ece1-III$_{\mathrm{KR(N)}}$ at 25°C, whereas DOPC/Ece1-III$_{\mathrm{KR(N)}}$ multilayer samples are examined with varying P/L at two temperatures (25°C and 40°C). Complementary studies are also presented for multilayer samples of varying lipid composition and for DOPC samples with either Ece1-III$_{\mathrm{AA(N)}}$ or Ece1-III$_{\mathrm{K(C)}}$ content.

X-Ray Reflectivity of Solid-Supported Multilayers, P/L Dependence

Measurements at 25°C: XRR profiles of a series of DOPC/Ece1-III$_{\mathrm{KR(N)}}$ multilayer samples of varying P/L (0:1, 1:22 $\approx$ 0.045, 1:18 $\approx$ 0.056) are shown in Fig. 6.15. The figures also include the corresponding simulations of the XRR profiles and the resulting electron density reconstructions $\rho_e(z)$. The pure DOPC sample exhibits seven Bragg peaks (from which only the first six are included in the figure for a better comparability). Peaks of higher order are suppressed due the high partial hydration of the stack and the corresponding impact of fluctuations. At P/L = 1:22, the order of detectable Bragg reflections is reduced to six, while at P/L = 18:1 only five Bragg peaks are left. To reproduce the overall reflectivity and the pronounced decay of the higher order peaks with increasing P/L, the roughness σ was increased from $\approx$ 3.2 Å to 4.4 Å and the number of bilayer repetitions was reduced from $\sim$ 200 to $\sim$ 80. Accordingly, the impact of root-mean-square variations increases as well as the disorder of the lamellar lipid/peptide system. With the low number of multilayers, the simulated reflectivity profile exhibits Kiessig fringes at low q_z, which are caused by the interference between the external interfaces of the system as all layers are supposed to be perfectly aligned within the Parratt simulation. The absence of these fringes in the experimental data provides a further indication that the sample surface comprises a certain degree of disorder. In simulations of a higher number of bilayer repetitions, these Kiessig fringes are also absent since their spacing falls below the instrumental resolution.

With respect to the reflectivity of pure DOPC, the Bragg reflections occur at decreased q_z-periodicity at P/L = 1:22 and increased q_z-periodicity at P/L = 1:18. Consequently, no systematic change of the lamellar membrane periodicity d is recog-

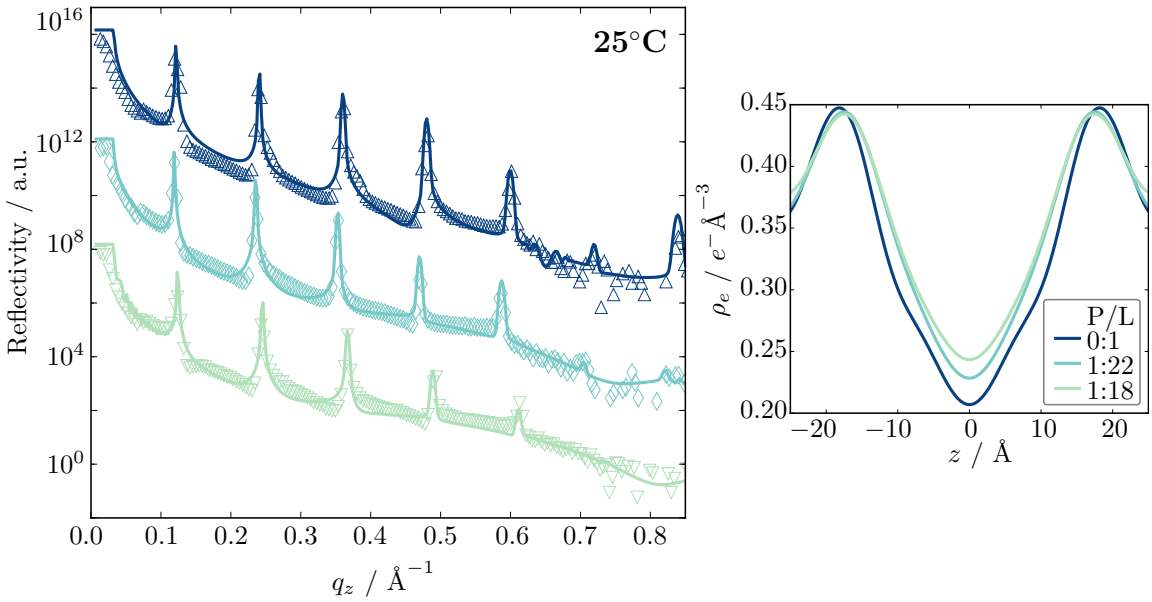

Figure 6.15 – Reflectivities and electron density distributions of DOPC/Ece1-III$_{\mathrm{KR(N)}}$ multilayers with increasing P/L at 25°C. The experimental reflectivities (symbols) and the corresponding simulations (solid lines) are shifted for clarity (left panel). From top to down and from dark to light blue, the P/L was increased 0:1 to 1:22 and 1:18. The electron density profiles $\rho_e(z)$ (right panel) obtained by the fitting are illustrated with the same colour code in the interval $z \in (-25, 25)$ Å. Depicted is an exemplary set of X-ray reflectivities recorded at P08 beamline.

nised. The reconstructions of $\rho_e(z)$, on the contrary, show that the distance between the headgroup maxima (d_{hh}) shrinks as function of the P/L. This thinning is accompanied by the flattening of $\rho_e(z)$, reflected by the decrease in the headgroup maxima $\rho_e(E_h)$ and a concomitant increase in the corresponding minima at both the intermediate hydrocarbon layer and the interlamellar water spacing ($\rho_e(E_c)$ and $\rho_e(E_w)$).

In Fig. 6.16, the analysed parameters of this measurement series taken at P08 and a second one, obtained at I07, are plotted against the P/L. The lamellar periodicities $d = 2\pi/q_z$ differ in both series: the spacings obtained at P08 are up to 2.3 Å larger than those obtained at I07 – with the exception of the samples at P/L = 1:18 (≈ 0.056). Despite their differences in d, both series match well in d_{hh} and reveal a pronounced decrease in it, indicating that the bilayer thins in a linear fashion with increasing peptide content. For the pure DOPC sample, d_{hh} is (36.6 ± 0.5) Å, which is $\simeq 1.0$ Å larger compared to the one found by Salditt and co-workers [203], who also employed solid-supported multilayer samples. However, it is $\simeq 0.5$ Å smaller compared to literature values obtained from vesicle samples [46, 256]. The bilayers thin by $\Delta d_{hh} = (1.7 \pm 0.6)$ Å in the presence of Ece1-III$_{\mathrm{KR(N)}}$ at P/L = 1:18, as obtained from one least-square fit to both data sets. As a consequence from the variances in d, the thicknesses of the water spacings $d_{w'}$ are larger for the P08 measurements.

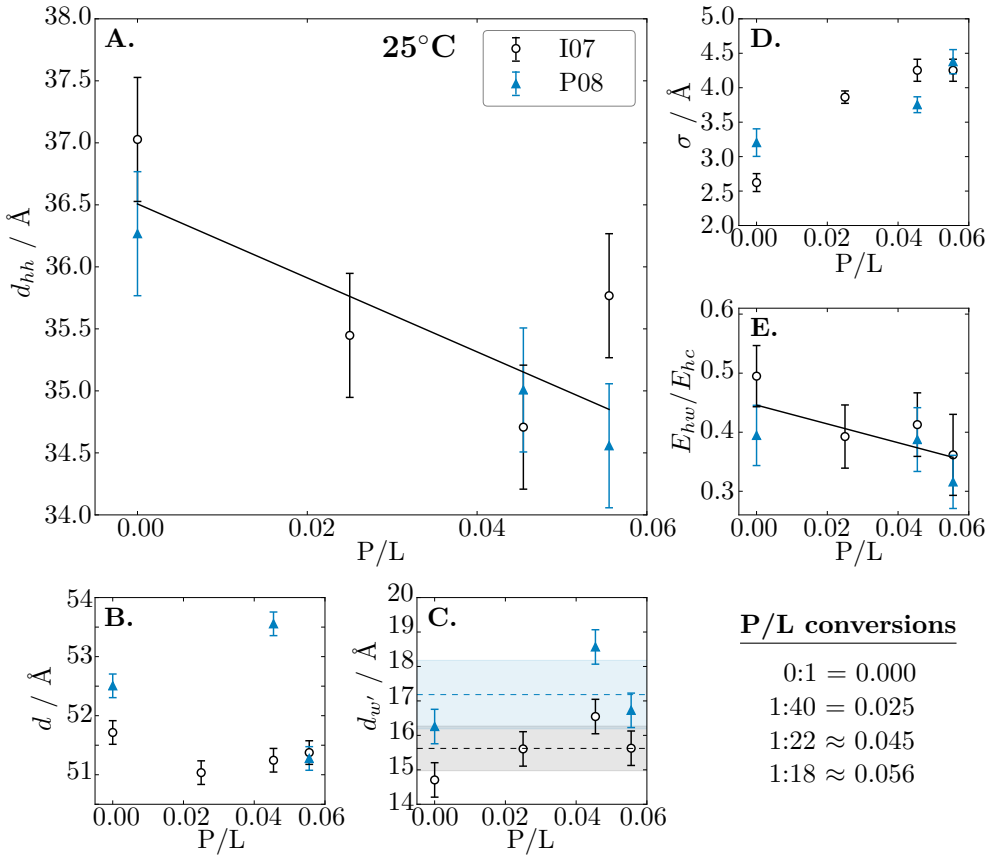

Figure 6.16 – Reflectivity analysis of DOPC/Ece1-III$_{KR(N)}$ multilayers as function of the P/L at 25°C. Illustrated are the parameters of two different measurement series, one obtained at P08 beamline (▲) and the other one at I07 beamline (○). **A.** The headgroup-to-headgroup distance d_{hh} decreases linearly with increasing P/L, which is indicated by a linear fit (solid line). **B.** The lamellar periodicity d exhibits no systematic P/L dependence. **C.** The inter-bilayer water spacings $d_{w'}$ differ for both measurement series, but are approximately constant. The dotted horizontal lines represent the mean values of each series and the shaded area the corresponding standard deviations. **D.** The mean interfacial roughness σ of each layer of the Parratt simulation is observed to increase as function of the P/L. **E.** The shape parameter E_{hw}/E_{hc} decreases with increasing P/L.

For both series, no systematic changes in $d_{w'}$ are observed. Hence, it is assumed that the water thickness exhibits no P/L-dependence. In Fig. 6.16, the constant water thickness is indicated by the horizontal lines and the shaded area, which illustrate the respective mean values and standard deviation of $d_{w'}$ separately for both series. The deviations are most likely explained by variations in the hydration conditions. Near full hydration, the balance of the interbilayer forces is rather delicate which quickly leads to variances of the interlamellar water thickness but does not affect the bilayer structure itself [25]. The samples measured at P08 were allowed to incubate in an atmosphere of 98 % rH water vapour for at least eight hours, whereas the samples utilised at I07 were incubated for only three hours. Consequently, the hydration equilibrium was probably not reached in the latter case. The fifth param-

eter illustrated in Fig. 6.16 is the shape parameter E_{hw}/E_{hc}. It is defined as ratio of the electron density contrast between the local water minimum and the global minimum between both bilayer leaflets $E_{hw}/E_{hc} = (\rho_e(E_h) - \rho_e(E_w))/(\rho_e(E_h) - \rho_e(E_c))$ [203]. This parameter is utilised to quantify the flattening of the electron density profiles which is reflected by its pronounced linear decrease as function of P/L. The progression of E_{hw}/E_{hc} is consistent in both measurement series and the slope of the corresponding least-square fit is (-1.6 ± 0.7).

Measurements at 40°C: Fig. 6.17 illustrates exemplary XRR profiles of a P/L series (0:1, 1:53 ≈ 0.019, 1:40 = 0.025, 22:1 ≈ 0.045, 18:1 ≈ 0.056) of DOPC/Ece1-III$_{\mathrm{KR(N)}}$ multilayers, as well as the corresponding Parratt simulations and the resulting $\rho_e(z)$ reconstructions. The pure DOPC sample exhibits six Bragg peaks. With increasing P/L, the intensities of the Bragg reflections decrease, the peak shapes broaden and higher Bragg orders diminish. At P/L = 1:18 only the first four Bragg peaks remain. Additionally, the peak positions shift to higher q_z values, demonstrating a systematic shrinkage in lamellar periodicity d. Just as for the profiles obtained at 25°C, σ was gradually increased from 2.5 to 4.2 Å and the number of bilayer repetitions was decreased to ~ 80 in order to simulate the XRR profiles. Despite the enhanced bilayer disorder, the samples preserve an overall high degree of orienta-

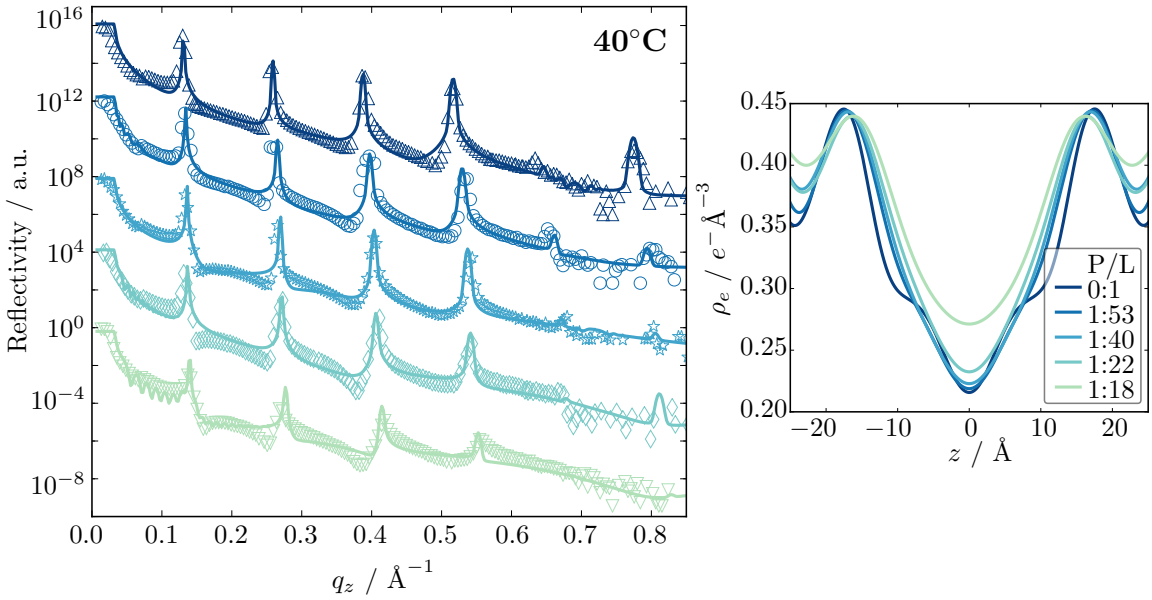

Figure 6.17 – Reflectivities and electron density distributions of DOPC/Ece1-III$_{\mathrm{KR(N)}}$ multilayers with increasing P/L at 40°C. The experimental reflectivities (symbols) and the corresponding simulations (solid line) are shifted for clarity (left panel). From top to down and from dark to light blue, the P/L was increased according to: 0:1, 1:53, 1:40, 1:22, 1:18. The electron density profiles $\rho_e(z)$ (right panel) obtained by the fitting are illustrated with the same colour code in the interval $z \in (-25, 25)$ Å. Depicted is an exemplary set of X-ray reflectivities recorded at P08 beamline.

tional order, which is evidenced by their low mosaicities (cf. Sec. 6.3.3). In the $\rho_e(z)$ reconstructions, the bilayer variations are again expressed as softening of the boundaries between both lipid leaflets and the separating water layer. This flattening is additionally accompanied by a slight increase in the averaged electron density across d, which is also indicative for the peptide association (data not shown). Aside from the shrinking lamellar spacing, also the headgroup-to-headgroup distance decreases as function of P/L.

Fig. 6.18 plots the analysed parameters of this P/L series measured at P08 as well as the ones of a corresponding series obtained at I07. In contrast to the measurements at 25°C, not only d_{hh} but also d and $d_{w'}$ are consistent in both series. This observation is attributed to shorter equilibration times at increased temperature.

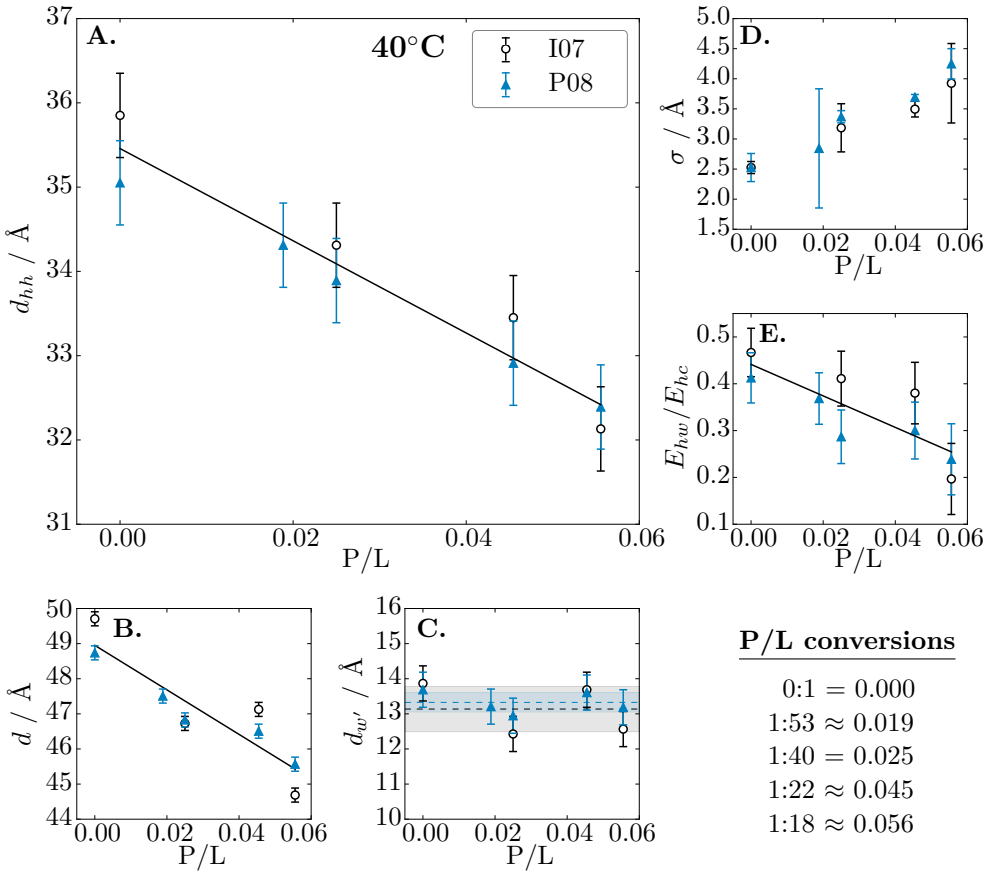

Figure 6.18 – Reflectivity analysis of DOPC/Ece1-III$_{\mathrm{KR(N)}}$ multilayers as function of the P/L at 40°C. Illustrated are the parameters of two different measurement series, one obtained at P08 beamline (▲) and the other one at I07 beamline (○). Both, lamellar periodicity d and headgroup-to-headgroup distance d_{hh} decrease linearly with increasing P/L (**A.** & **B.**), represented by corresponding least-square fits (solid line). The inter-bilayer water spacing $d_{w'}$ exhibits no obvious P/L dependence (**C.**). The horizontal, dotted lines represent the mean value of each series and the shaded area the corresponding standard deviation. With increasing P/L, the mean interfacial roughness σ of each layer of the Parratt simulation increases (**D.**); the shape parameter E_{hw}/E_{hc} decreases linearly (**E.**).

While d_{hh} and d decrease with increasing P/L, $d_{w'}$ is found to adapt a constant level of ≈ 13 Å. Consequently, the thinning of d is directly related to the thinning of d_{hh}, which is also reflected by the slopes of their linear P/L-dependencies. These are (-63.4 ± 11.1) Å and (-54.7 ± 5.3) Å for d and d_{hh}, respectively. Hence, the thinning effect is more pronounced at 40°C than at 25°C. In terms of numbers, the pure DOPC bilayer of $d_{hh} = (35.4 \pm 0.6)$ Å thins by $\Delta d_{hh} = (3.0 \pm 0.4)$ Å for P/L = 1:18 (≈ 0.056). The decrease in the shape parameter E_{hw}/E_{hc} is also more pronounced at 40°C, as it is characterised by a slope of (-3.4 ± 0.9). Both effects can be explained by the adsorption of Ece1-III$_{\mathrm{KR(N)}}$ and an accompanied stress induction on the membrane. In response, the membrane reacts with local thinning. This lateral inhomogeneity then manifests as smoothening of the measured averaged density profile $\rho_e(z)$.

X-Ray Reflectivity of Solid-Supported Multilayers, Lipid Composition

Next, the influence of Ece1-III$_{\mathrm{KR(N)}}$ on lipid multilayers composed of DOPC and 10 % (n/n) Chol, Erg or PS is examined. Since the peptide-induced thinning as well as the flattening of the averaged electron density profile in pure DOPC samples was observed to be stronger at 40°C than at 25°C, the vertical structure of the binary lipid systems is only presented for the higher temperature. The determined parameters of these samples are summarised in Tab. 6.1.

	d [Å]	d_{hh} [Å]	$d_{w'}$ [Å]	E_{hw}/E_{hc}
DOPC/Chol	49.2 ± 0.6	35.3 ± 1.4	13.9 ± 0.4	0.55 ± 0.07
+ Ece1-III$_{\mathrm{KR(N)}}$	45.7 ± 1.2	35.0 ± 0.3	10.7 ± 0.1	0.15 ± 0.02
DOPC/Erg	48.4 ± 0.1	34.6 ± 0.2	13.7 ± 0.1	0.50 ± 0.04
+ Ece1-III$_{\mathrm{KR(N)}}$	46.7 ± 1.4	35.2 ± 0.6	11.5 ± 0.8	0.18 ± 0.03
DOPC/PS	48.5 ± 0.2	34.3 ± 1.4	14.3 ± 1.2	0.47 ± 0.05
+ Ece1-III$_{\mathrm{KR(N)}}$	47.6 ± 0.4	35.2 ± 0.3	12.4 ± 0.1	0.21 ± 0.01

Table 6.1 – Parameters of bilayers of different compositon with Ece1-III$_{\mathrm{KR(N)}}$. The parameters are obtained from electron density reconstructions of lipid multilayer samples composed of DOPC/Chol, DOPC/Erg and DOPC/PS with and without Ece1-III$_{\mathrm{KR(N)}}$ at 40°C. The P/L was 1:18 (≈ 0.056) for each of the samples containing Ece1-III$_{\mathrm{KR(N)}}$ and the lipid-to-lipid ratio was 9:1 (n/n). Each parameter is obtained as mean of duplicate measurements – with the exception of the DOPC/Erg/Ece1-III$_{\mathrm{KR(N)}}$ values which were obtained from triplicate measurements. The given uncertainties reflect the corresponding standard deviations.

DOPC/Chol: Fig. 6.19 plots the reflectivities of an exemplary DOPC/Chol measurement without peptide and one with Ece1-III$_{\mathrm{KR(N)}}$ at P/L = 1:18 ($\approx$ 0.056). The figure also illustrates the best XRR simulations and the corresponding vertical electron density profiles. While in the pure lipid sample seven Bragg reflections are observed (from which only the first six are included in the figure for a better comparability), only four peak orders are clearly visible in the peptide-containing sample. The remaining peaks are of less defined shape and their intensities are remarkably reduced. Accordingly, the sample is further away from being a perfectly well-ordered multilayer system. As a consequence, the fit quality is notably reduced. However, by decreasing the number of bilayer repetitions and increasing the roughness, the essential parameters – i. e. the peak positions and amplitudes – are widely reproduced. Again, the absence of Kiessig fringes at low q_z in the experimental data implies a high degree of disorder of the sample surface.

Although the periodicity decreased by Δd = 3.5 Å (cf. Tab. 6.1), the bilayer thickness itself is not notably affected (the thinning of Δd_{hh} = 0.3 Å lies within the uncertainties). Instead, the thickness of the water layer, which separates two adjacent membranes, is reduced. However, the $\rho_e(z)$ profiles of the DOPC/Chol samples with Ece1-III$_{\mathrm{KR(N)}}$ also exhibit a pronounced flattening, just as it has been

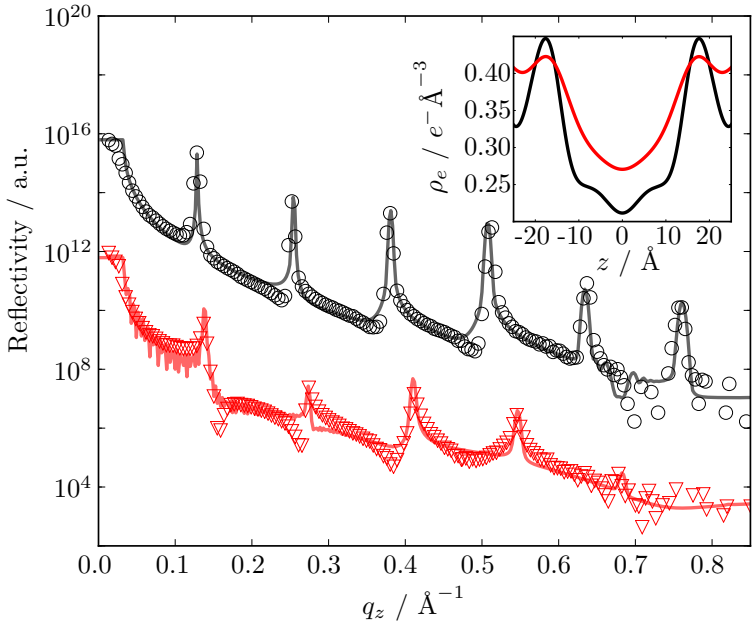

Figure 6.19 – Reflectivity analysis of DOPC/Chol multilayer samples with and without Ece1-III$_{\mathrm{KR(N)}}$. Exemplary X-ray reflectivities (symbols) and simulations (solid lines) of the pure lipid stack (black) and the one containing Ece1-III$_{\mathrm{KR(N)}}$ at P/L = 1:18 ($\approx$ 0.056). Both data sets are shifted for clarity. The inset plots the corresponding electron density reconstructions $\rho_e(z)$ obtained from the simulations. Both measurements were carried out at 40°C, the lipid-lipid ratio was 9:1 (n/n).

observed for the DOPC bilayers. This is also reflected by the decreased shape parameter E_{hw}/E_{hc}. In accordance with that, bilayer variations are also enhanced, but a distinct thinning of the bilayer itself is not observed.

DOPC/Erg: The reflectivities of exemplary DOPC/Erg multilayer samples with and without Ece1-III$_{\mathrm{KR(N)}}$ at P/L = 1:18 ($\approx$ 0.056) are shown in Fig. 6.20. Corresponding simulations and electron density profiles are also included in the figure. The pure lipid sample exhibits six Bragg peaks; in the presence of the peptide only four peak orders appear. In shape and intensity, the remaining peaks are similar to those observed for the corresponding DOPC/Chol/Ece1-III$_{\mathrm{KR(N)}}$ sample (cf. Fig. 6.19). Consequently, not only the determined thicknesses but also the flattening of $\rho_e(z)$ and the related ratio E_{hw}/E_{hc} are comparable (cf. Tab. 6.1). Nevertheless, the DOPC/Erg experiments suggest a marginal bilayer thickening by $\Delta d_{hh} = 0.6$ Å, since the pure lipid sample exhibited a slightly smaller d_{hh} than the one containing Ece1-III$_{\mathrm{KR(N)}}$. However, considering the associated uncertainties, this effect is not significant.

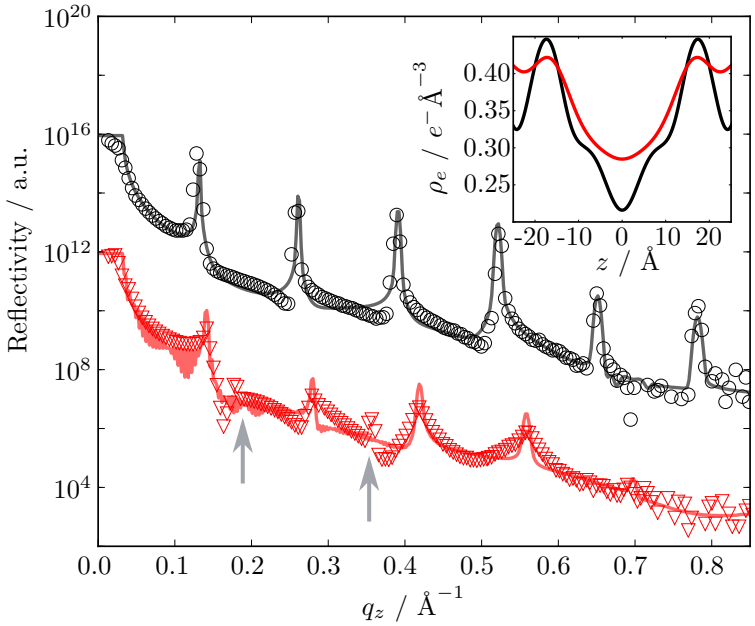

Figure 6.20 – Reflectivity analysis of DOPC/Erg multilayer samples with and without Ece1-III$_{\mathrm{KR(N)}}$. Exemplary X-ray reflectivities (symbols) and simulations (solid lines) of the pure lipid stack (black) and the one containing Ece1$_{\mathrm{KR(N)}}$ at P/L = 1:18 ($\approx$ 0.056). Both data sets are shifted for clarity. The grey arrows indicate additional peaks at $q_z = 0.18$ Å^{-1} and $q_z = 0.35$ Å^{-1}, which appear in the reflectivity profile containing Ece1-III$_{\mathrm{KR(N)}}$. Note that these are in general also present in the one from the pure lipid stack, but not in the particular measurement shown here. The inset plots the corresponding electron density reconstructions $\rho_e(z)$ obtained from the simulations. Both measurements were carried out at 40°C, the lipid-lipid ratio was 9:1 (n/n).

Aside from the Bragg peaks assigned to the lamellar periodicity of the lipid multilayer, additional peaks appear at $q_z = 0.18$ Å^{-1} and $q_z = 0.35$ Å^{-1}. Although the figure suggests that these are only present in the sample with Ece1-III$_{\mathrm{KR(N)}}$, they were in general also present in the pure DOPC/Erg samples. Both width and intensity of these peaks are reduced, indicating that a certain but small amount of the sample has crystalline character. These peaks may be assigned to the presence of ergocalciferol, which is converted from ergosterol in a photochemical reaction. Ergocalciferol is a water-insoluble crystal of orthorhombic structure. The height of its unit cell is 35.3 Å [257] which matches the identified repeat spacing of $\Delta q_z \simeq 0.175$ Å^{-1}. The reaction is either triggered by ultraviolet light and may have happened during the sample preparation, or it is triggered by the synchrotron light. According to that, it is speculative whether the samples are capable to represent the real effect of ergosterol as the remaining amount of it is unknown.

DOPC/PS: Fig. 6.21 plots the reflectivities of exemplary measurements of DOPC/PS with and without Ece1-III$_{\mathrm{KR(N)}}$ at P/L = 1:18 (≈ 0.056). Also included are the corresponding simulations and electron density reconstructions. The pure DOPC/PS sample exhibits eight Bragg reflections (from which only the first

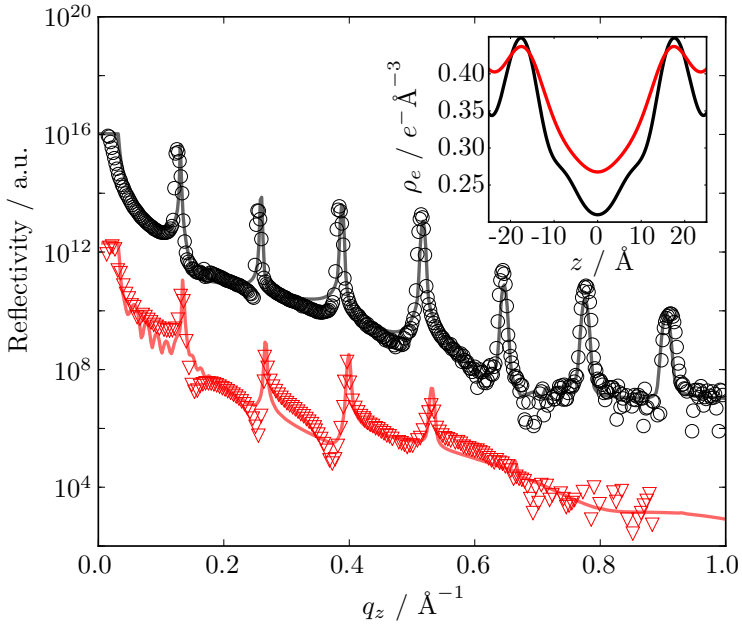

Figure 6.21 – Reflectivity analysis of DOPC/PS multilayer samples with and without Ece1-III$_{\mathrm{KR(N)}}$. Exemplary X-ray reflectivities (symbols) and simulations (solid lines) of the pure lipid stack (black) and the one containing Ece1$_{\mathrm{KR(N)}}$ at P/L = 1:18 (≈ 0.056). Both data sets are shifted for clarity. The inset plots the corresponding electron density reconstructions $\rho_e(z)$ obtained from the simulations. Both measurements were carried out at 40°C, the lipid-lipid ratio was 9:1 (n/n).

seven are included in the figure). This number is drastically reduced in the sample containing Ece1-III$_{\mathrm{KR(N)}}$, where only four Bragg peaks remain. Consequently, the number of Bragg reflections for samples with Ece1-III$_{\mathrm{KR(N)}}$ at P/L = 1:18 is consistent for all lipid samples probed in this work. Again, the remaining peaks are of different shape and decreased intensity. However, the peak degradation is not as pronounced as it was in the other lipid samples.

Nevertheless, the reconstructed electron density is strongly flattened. Accordingly, E_{hw}/E_{hc} decreases as result of the interaction with the peptide (cf. Tab. 6.1). The thicknesses determined from the $\rho_e(z)$ profiles indicate that the slight reduction of $\Delta d \simeq 1$ Å of the repeat spacing basically relates to a marginal thinning of the water layer ($\Delta d_{w'} \simeq 2$ Å) and a simultaneous thickening of the bilayer ($\Delta d_{hh} \simeq 2$ Å). Although these effects are not significant, they may be explained as result of the electrostatic interaction between the cationic Ece1-III$_{\mathrm{KR(N)}}$ and the anionic PS headgroups. The binding of Ece1-III$_{\mathrm{KR(N)}}$ screens the negative charge of PS and leads to a reduced repulsion between adjacent bilayers on the one hand and laterally neighbouring lipids on the other hand [203]. Due to the latter effect, the area per lipid decreases. In response to the tightened packing, the acyl chains stretch out to maintain constant mass density.

X-Ray Reflectivity of Solid-Supported Multilayers, Peptide Variants

To evaluate the influence of C-terminal modifications on the vertical bilayer structure, DOPC multilayer samples containing the peptide variants Ece1-III$_{\mathrm{AA(N)}}$ and Ece1-III$_{\mathrm{K(C)}}$ at P/L = 18:1 (≈ 0.056) were examined. Again, the results discussed in the following were obtained at sample temperatures of 40°C. The respective reflectivities, together with the simulations and electron density reconstructions are illustrated in Fig. 6.22. A summary of the parameters is given in Tab. 6.2. For comparison, the respective parameters obtained for pure DOPC and DOPC/Ece1-III$_{\mathrm{KR(N)}}$ are also included.

The reflectivity of the sample with Ece1-III$_{\mathrm{K(C)}}$ still exhibits five Bragg reflections, although the fifth order is also largely suppressed. In comparison to the pure DOPC sample shown in Fig. 6.18, the peaks are broadened and their intensities are decreased. Accordingly, the order of the vertical stacking is reduced. This is also reflected by the flattening of $\rho_e(z)$ which indicates enhanced bilayer disorder. However, the flattening is not as pronounced as it is for corresponding Ece1-III$_{\mathrm{KR(N)}}$ samples. For these samples, the hydrocarbon minimum adapts a value of $\rho_e(E_c) \simeq 0.27\ e^-\text{Å}^{-3}$. Hence, the minimum is less extensive than the one in the DOPC/Ece1-III$_{\mathrm{K(C)}}$ profile which is $\rho_e(E_c) \simeq 0.25\ e^-\text{Å}^{-3}$. This is also reflected by the shape parameter of the Ece1-III$_{\mathrm{K(C)}}$ sample which is larger than the one observed for

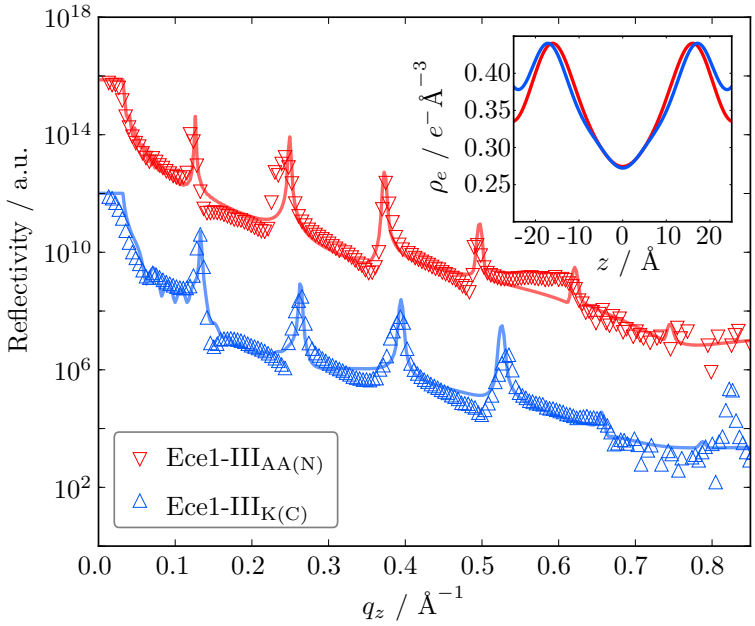

Figure 6.22 – Reflectivity analysis of DOPC multilayer samples with Ece1-III$_{\mathrm{AA(N)}}$ and Ece1-III$_{\mathrm{K(C)}}$. X-ray reflectivities (markers) and simulations (solid lines) of DOPC/$_{\mathrm{AA(N)}}$ (red) and DOPC/Ece1-III$_{\mathrm{K(C)}}$ (blue) at P/L = 1:18 ($\approx$ 0.056). Both data sets are shifted for clarity. The inset plots the corresponding electron density reconstructions $\rho_e(z)$ obtained from the simulations. Both measurements were carried out at 40°C.

Ece1-III$_{\mathrm{KR(N)}}$ but comparable to the one found for the pure lipid stack. Additionally, the membrane thinning effect is less pronounced in this particular lipid/peptide system. Here, d_{hh} shrinks by only 1 Å. As $d_{w'}$ maintains a thickness of $\simeq$ 13.5 Å, this thinning directly affects the periodicity d.

The reflectivity of DOPC/Ece1-III$_{\mathrm{AA(N)}}$ stacks also exhibits four clear Bragg peaks and a largely suppressed fifth order. Compared to the pure DOPC sample (cf. Fig. 6.18), the peak shapes are less defined and the intensities are reduced, indicating a strong reduction in lamellar order. As the peaks are shifted to lower q_z, the lamellar periodicity is increased by $\Delta d = 1.5$ Å which relates to a notable increase in the layer thickness of the water spacing, namely 4.8 Å. Nevertheless, a reduction in d_{hh} is observed. Its extent is similar to the effect of Ece1-III$_{\mathrm{KR(N)}}$. The electron density in the hydrocarbon region is flattened and also the maximum at the headgroup is slightly reduced compared to the pure lipid sample. However, between the headgroup maxima and the water minima, a large electron contrast is preserved which leads to a small increase in E_{hw}/E_{hc}. Consequently, the flattening does not affect the entire repetition unit which is contrary to the findings for Ece1-III$_{\mathrm{KR(N)}}$. The profile suggests that Ece1-III$_{\mathrm{AA(N)}}$ partitions deeper into the membrane, thereby causing a higher electron density in the hydrocarbon region. At the same time,

membrane variations due to local thinning effects are less pronounced. The origin of the enlarged water layer is rather assigned to slight differences in the hydration state than to actual peptide effects. However, this is just a guess as this particular reflectivity measurement could be performed only once. Hence, to prove the validity of this speculation, additional experiments must be carried out.

	d [Å]	d_{hh} [Å]	$d_{w'}$ [Å]	E_{hw}/E_{hc}
DOPC	49.2 ± 0.7	35.4 ± 0.6	13.8 ± 0.1	0.44 ± 0.04
+ Ece1-III$_{\mathrm{KR(N)}}$	45.1 ± 0.6	32.3 ± 0.2	13.6 ± 0.6	0.22 ± 0.03
+ Ece1-III$_{\mathrm{K(C)}}$	48.2 ± 0.5	34.9 ± 0.8	13.3 ± 0.3	0.34 ± 0.05
+ Ece1-III$_{\mathrm{AA(N)}}$	50.7	32.1	18.6	0.63

Table 6.2 – Parameters of DOPC bilayers upon the interaction with different peptide variants. The parameters were obtained from electron density reconstructions of lipid multilayer samples with Ece1-III$_{\mathrm{KR(N)}}$, Ece1-III$_{\mathrm{AA(N)}}$ or Ece1-III$_{\mathrm{K(C)}}$ at 40°C. The P/L was 1:18 (≈ 0.056). Most of the parameters represent the mean of duplicate measurements, except for those of Ece1-III$_{\mathrm{AA(N)}}$, for which the measurement was performed only once. The given uncertainties reflect the corresponding standard deviations.

X-Ray Reflectivity of Solid-Supported Bilayers

In order to have a closer look at the peptide's influence on the structural properties of a bilayer membrane, two independent X-ray reflectivity recordings on single-supported bilayers were performed at 25°C. Fig. 6.23 shows a representative measurement of the reflectivity of a DOPC bilayer on a silicon substrate before and 35 min after the addition of 80 μl Ece1-III$_{\mathrm{KR(N)}}$ (1 mg·ml^{-1} in 0.01 % TFA, final peptide concentration: 11 μM). The reflectivities already indicate that the peptide did not influence the bilayer's thickness since the distances of the Kiessig fringes in both profiles equal one another.

The analysis of the profiles was performed as described in Sec. 3.5.5. The normalised reflectivity $R(q_z)/R_F(q_z)$ was reconstructed up to 0.62 Å^{-1} with a sampling width of 104 Å in real space. The stopping parameter for the iterative algorithm was chosen to be $\tau = 2.1$ resulting in an overall data misfit less than 1.0. The headgroup-to-headgroup distance d_{hh} of the calculated electron density profile (shown in the inset of Fig. 6.23) is about $\simeq$ 35.5 Å for both cases. The overall electron density of the upper DOPC bilayer leaflet is slightly increased by $\simeq 5.6\,\% = 0.8\ e^{-}$Å^{-2} indicating that Ece1-III$_{\mathrm{KR(N)}}$ associates and intercalates into the bilayer. Its lacking influence on the averaged bilayer thickness may have several reasons. On the one hand, it may be explained with the low temperature, at which the bilayer thinning in multilayer samples was also found to be less pronounced than at 40°C. On the

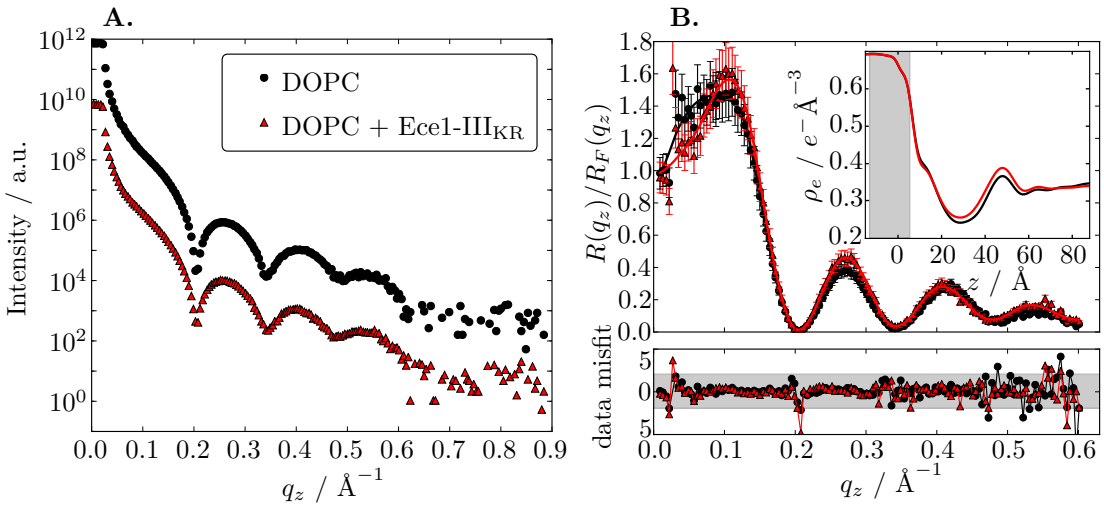

Figure 6.23 – Peptide influence on a DOPC bilayer measured with XRR. A. XRR profiles of a DOPC bilayer before (●) and 35 min after the addition of Ece1-III$_{KR(N)}$ (▲) at a temperature of 25°C. Both scans are shifted vertically by a factor of 10^2 for clarity. **B.** XRR profiles from A, normalised to the Fresnel reflectivity, and the respective reconstructions are shown as solid lines. The data misfit with respect to the experimental data and normalised to the errorbars is shown underneath. The inset depicts the electron density distributions obtained for pure DOPC (black) and for DOPC/Ece1-III$_{KR(N)}$ (red). The final peptide concentration in the sample cell was 11 μM.

other hand, the finding may be explained by a low P/L. Here, the actual P/L value is to some extent uncertain as the distinct substrate coverage of the lipid is obscure and it can not be excluded that the peptide adheres to the hydrophobic walls of the Teflon chamber due to its strong amphiphilicity. Additionally, remaining interactions between the bilayer and the substrate surface may oppose the driving force of the peptide to thin the bilayer.

6.3.3 Peptide Influence on the Lateral Bilayer Structure

In the following section, lateral bilayer changes attributed to the peptide interaction are examined in greater detail. Firstly, the diffuse scattering of a P/L series of DOPC multilayers with Ece1-III$_{KR(N)}$ at 40°C is briefly addressed to obtain information on the lateral coherence lengths in these samples. Secondly, the GID patterns of these samples are analysed for both temperatures, 25°C and 40°C. Here, the analysis also includes different lipid compositions and C-terminal modifications. In the first instance, the small-angle signals are evaluated to determine possible long-range orders in the lipid/peptide stacks. Subsequent to this, the wide-angle scattering range is studied, which provides complementary information on the short-range order of the acyl chains.

Diffuse Scattering of Solid-Supported Multilayers

Firstly, it shall be emphasised that, despite the loss of the well-defined lamellar stacking in DOPC/Ece1-III$_{\mathrm{KR(N)}}$ multilayers, these samples still maintain a high degree of orientational order. This is evidenced by rocking scans around the first Bragg peak. In these scans the sample is tilted from $\alpha_i = 0°$ to $2\alpha_r$ and the detector position is fixed at a constant angle $\alpha_i + \alpha_r = \text{const}$. The central width of the resulting specular peak, i. e. the mosaicity, was in all cases smaller than 0.01°, which is close to the resolution limits of the instrumental setup. Fig. 6.24 A shows an exemplary rocking curve for a multilamellar DOPC/Ece1-III$_{\mathrm{KR(N)}}$ stack at P/L = 1:18 ($\approx$ 0.056) at 40°C. It exhibits a full width at half maximum (FWHM) of 0.0088° of a Gaussian profile. The intensity of the diffuse scattering is two orders of magnitude lower than the specular intensity.

Fig. 6.24 B plots the respective ratios of specular to diffuse intensity of a series of DOPC/Ece1-III$_{\mathrm{KR(N)}}$ samples at 40°C versus the P/L. It can be seen, that the levels of the diffuse background scattering decrease with decreasing peptide content. For these samples, the specular and the diffuse intensity proportions differ by three orders of magnitude. For a better comprehensibility of the individual contributions of the diffuse scattering, the intensity profiles of the first three Bragg peaks are illustrated in Fig. 6.25. Here, the data was obtained by extraction from the 2D

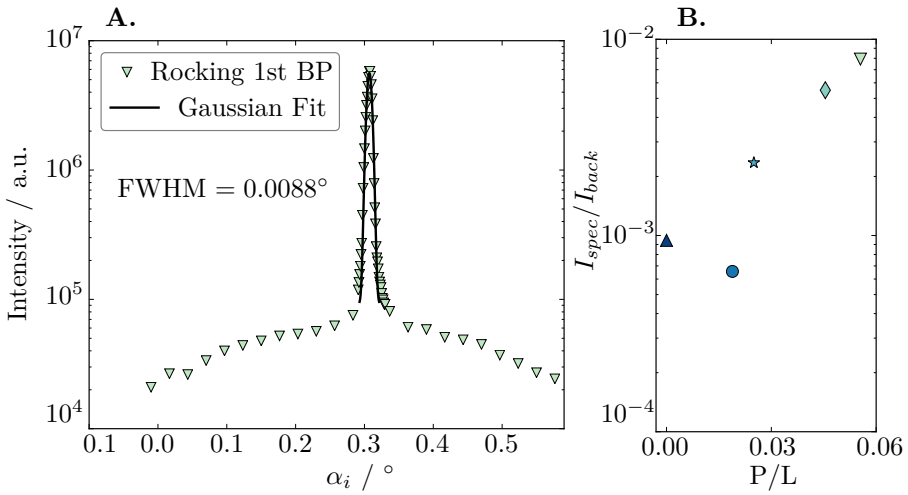

Figure 6.24 – Rocking curve and diffuse scattering contributions at 40°C. A. Exemplary rocking curve around the first Bragg peak of a DOPC/Ece1-III$_{\mathrm{KR(N)}}$ stack at P/L = 1:18 ($\approx$ 0.056) and 40°C. The high degree of the stack orientation is evidenced by the narrow peak width of 0.008° (FWHM). **B.** Relative contribution of the non-specular diffuse background scattering I_{back} with respect to the specular intensity I_{spec}. With increasing P/L, the diffuse scattering contributions reflected by I_{back}/I_{spec} increase. The diffuse scattering ratios are plotted for samples with the following P/L values: 0:1 = 0.000, 1:53 $\approx$ 0.019, 1:40 = 0.025, 1:22 $\approx$ 0.045 and 1:18 $\approx$ 0.056.

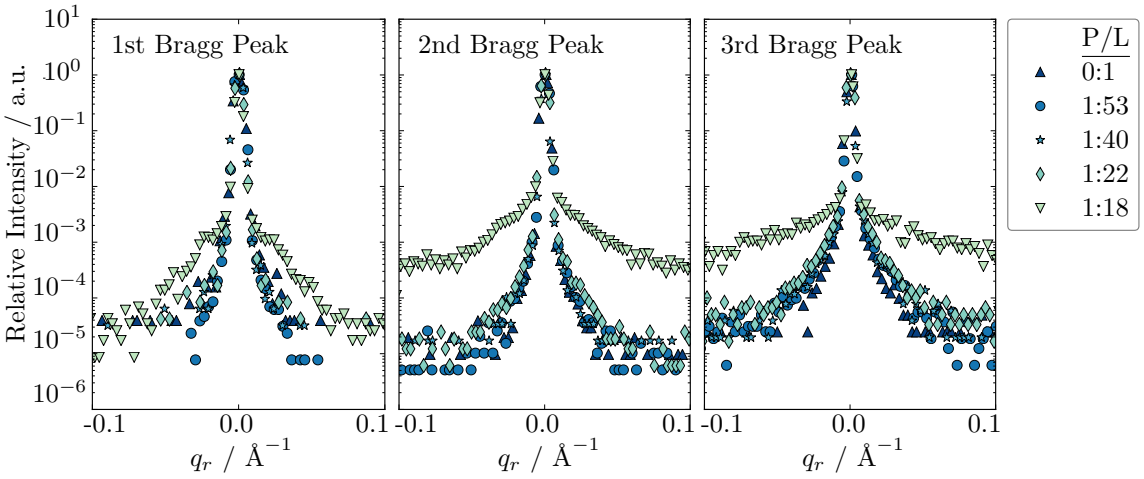

Figure 6.25 – **Specular and non-specular scattering** of a P/L series of DOPC/Ece1-III$_{\mathrm{KR(N)}}$ multilayer samples. Lateral intensity profiles of the first three Bragg orders at 40°C. The profiles were extracted from 2D data sets in reflection geometry. For a better comparability, the specular intensity is normalised to unity. Shown are the profiles obtained from a series of P/L samples: 0:1 = 0.000, 1:53 ≈ 0.019, 1:40 = 0.025, 1:22 ≈ 0.045 and 1:18 ≈ 0.056.

detector images recorded during the corresponding XRR scans which explains the lower resolution compared to the rocking scan.

In aligned lipid multilayers, the non-specular scattering at small q_r may either be caused by thermal fluctuation, static undulation or static disorder [258]. As a consequence of the increasing levels of diffuse scattering, it can be inferred that the peptide enhances such bilayer variations. This is in accordance with the electron profiles obtained from the samples' reflectivities which also indicated a decreasing positional order in the bilayer plane as function of the P/L. It is assumed that the bilayer variations are caused by membrane fluctuation or undulation rather than by true static disorder. This conclusion is supported by findings of Salditt and co-workers [199], who assigned the diffuse Bragg sheets to the coherent scattering contribution from membrane variations. The authors discussed, that truly disordered domains on the contrary would superpose incoherently and lead to circular arcs in the diffraction pattern (see Sec. 6.3.3). However, it can not be revealed whether these variations are of static or thermal nature. Taking into account the small lamellar periodicity in these stacks, however, it is highly likely that the peptide disturbs the membrane in a static manner by imposing stress, which in turn leads to the local thinning effects.

Beyond the evaluation of the relative levels of the non-specular scattering, its decay along q_r may reveal information on the length scale of underlying lateral inhomogeneities. These can be inferred from characteristic transitions of the power-law dependencies of the intensity decay $I(q_r) \propto q_r^{-\gamma}$, which become evident in log-log plots [259]. Fig. 6.26 shows such a plot for the second order Bragg peak of the

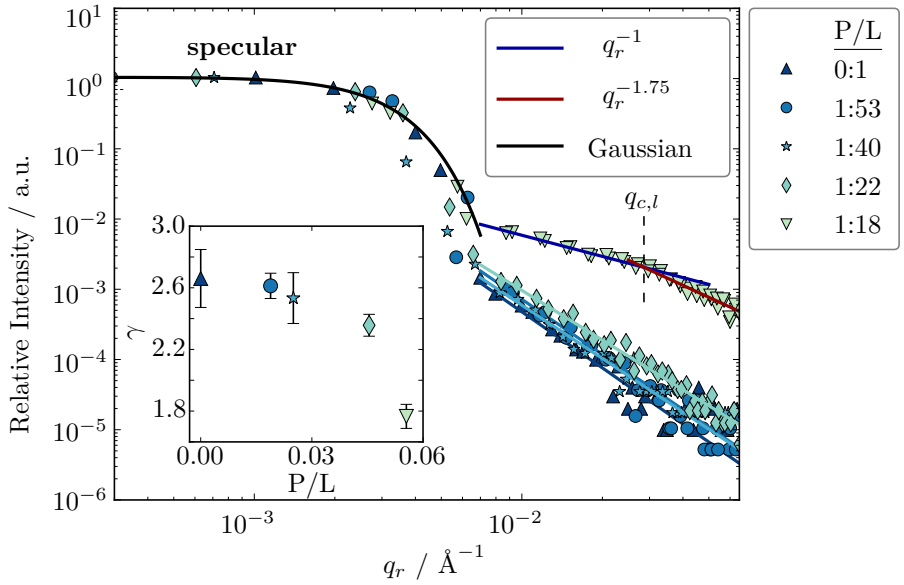

Figure 6.26 – Log-log plot of the diffuse scattering of a P/L series of DOPC/Ece1-III$_{\mathrm{KR(N)}}$ multilayer samples. The figure plots the intensity around the second Bragg peak ($q_z \simeq 0.26$ Å^{-1}) from Fig. 6.25 on double-logarithmic scale. The black line represents a Gaussian fit to the specular peak of the stack with highest peptide content (P/L = 1:18 ≈ 0.056). The remaining solid lines are power-law fits to the diffuse scattering according to $q_r^{-\gamma}$ and the inset shows the fitted exponents γ for $q_r > q_{c,l}$. The diffuse scattering from samples with the following P/L values are plotted: 0:1 = 0.000, 1:53 ≈ 0.019, 1:40 = 0.025, 1:22 ≈ 0.045 and 1:18 ≈ 0.056. Only the sample at P/L = 1:18 shows a characteristic cut-off at $q_{c,l}$ where the power-law dependence changes from q_r^{-1} to $q_r^{-1.75}$ (indicated by a vertical dashed line).

P/L series as an example. For the sample with highest peptide content (P/L = 1:18 ≈ 0.056), the power-law decay changes from $I(q_r) \propto q_r^{-1}$ to $I(q_r) \propto q_r^{-1.75}$. The corresponding cut-off appears roughly at $q_{c,l} = q_r = 0.029$ Å^{-1}. Thus, the lateral coherence translation invariance of the lipid domain structures breaks around $2\pi/q_{c,l} \simeq 22$ nm. The diffuse scattering regimes from the lipid-peptide stacks with P/L > 1:18, however, do not contain such characteristic cut-off kinks. Herein, only single power-law decays with $\gamma \simeq (2.53 \pm 0.13)$ are observable. The respective cut-off edges of these samples are hidden underneath the specular signal, which extends to $\simeq$ 0.007 Å^{-1}, owing to the limited resolution given by pixel size and horizontal beam size. Hence, the lateral coherence length is larger than 90 nm, consistent with the AFM measurements (cf. Sec. 6.3.1). Yet, the power of the decay shrinks subtly with increasing peptide concentration as shown in the inset of Fig. 6.26. This observation again demonstrates the peptide-dependent increase in diffuse scattering.

Grazing Incidence Diffraction: Small-Angle Region, P/L Dependence

40°C: The small-angle region of the diffraction patterns obtained in grazing incidence, significantly varies with increasing amount of Ece1-III$_{\mathrm{KR(N)}}$. To highlight the

particular changes, an exemplary image series obtained from DOPC/Ece1-III$_{\mathrm{KR(N)}}$ samples with increasing P/L (0:1, 1:53, 1:40, 1:22, 1:18), at a temperature of 40°C, is depicted in Fig. 6.27. Owing to their lamellar stacking, the pure DOPC samples give only rise to out-of-plane reflections (along q_z). The comparatively narrow in-plane extent (q_r) of these Bragg reflections arises from slight stacking imperfections and small membrane undulations as explained above. At P/L = 1:53, a circular arc around the first Bragg peak is visible which demonstrates the increased impact of in-plane correlations and static defects [141]. On this arc, two additional peaks emerge symmetrically around q_z, each at an angle of $\varphi \simeq 45°$ with respect to the sample horizon. This observation is indicative for the formation of a distinct non-lamellar phase. At P/L = 1:40, the intensity of these two peaks is increased and also higher orders of it emerge, located on an arc around the second order Bragg peak. Even more reflections are detected in case of the P/L = 1:22 and 1:18 samples.

The diffraction patterns at high P/L are assigned to four distinct orientations of a distorted hexagonal phase. In the x-z-plane, this phase is a two-dimensional monoclinic lattice which is represented by two base vectors $\vec{a}$ and $\vec{b}$, both separated by an angle $\gamma \neq 90°$. For the lipid/peptide systems studied here, γ is identified to be 135°. In one of the observed orientations, the long lattice base is aligned parallel to the substrate surface as sketched in Fig. 6.28 A (red lattice). In accordance with the notations in the figure, the base vectors of H_d are

$$\vec{a} = \begin{pmatrix} a \\ 0 \\ 0 \end{pmatrix}, \quad \vec{b} = \begin{pmatrix} a\cos\gamma \\ 0 \\ a\sin\gamma \end{pmatrix} = \frac{\sqrt{2}a}{2}\begin{pmatrix} -1 \\ 0 \\ 1 \end{pmatrix} \quad \text{and} \quad \vec{c} = \begin{pmatrix} 0 \\ -c \\ 0 \end{pmatrix},$$

with a describing the unit cell in the vertical plane, and c the unit cell length of the columns. The corresponding reciprocal lattice vectors are

$$\vec{a}^\star = \frac{2\pi}{a}\begin{pmatrix} 1 \\ 0 \\ 1 \end{pmatrix}, \quad \vec{b}^\star = \frac{2\sqrt{2}\pi}{a}\begin{pmatrix} 0 \\ 0 \\ 1 \end{pmatrix} \quad \text{and} \quad \vec{c}^\star = \frac{2\pi}{c}\begin{pmatrix} 0 \\ -1 \\ 0 \end{pmatrix}.$$

For small l and with the assumption that the columnar dimension c is large compared to a, the reciprocal lattice vector $\vec{Q}_{hkl}$ is reduced to two dimensions $\vec{Q}_{hkl} \approx \vec{Q}_{hk} = h\vec{a}^\star + k\vec{b}^\star$ and the components $Q_{hk,r} = \frac{2\pi}{a}h$ and $Q_{hk,z} = \frac{2\pi}{a}(h + \sqrt{2}k)$ can partly explain the reflections observed in the diffraction patterns. A second set of the detected reflections is explained by a vertically flipped lattice, whose appearance is explained by the random domain orientation in the x-y-plane (cf. Sec. 3.5.1). These mirrored lattice alignments are denoted by H_d in the following. By rotating the two

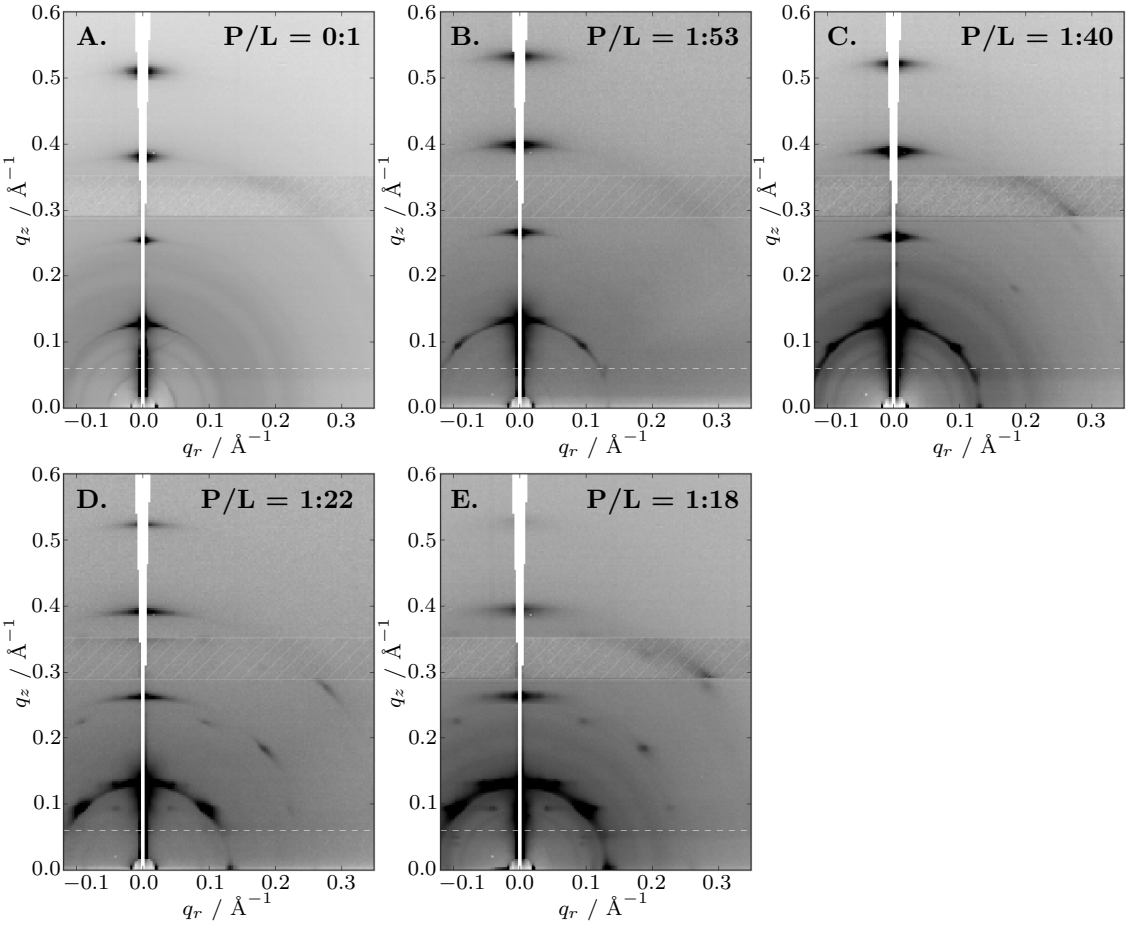

Figure 6.27 – **Small-angle diffraction patterns of a P/L series** of DOPC/Ece1-III$_{\mathrm{KR(N)}}$ multilayer samples at 40°C. From **A.** to **E.**, the peptide concentration is increased from P/L = 0:1 to P/L = 1:18 as indicated. The area below $q_z = 0.06$ Å^{-1} (indicated by the dashed horizontal line) is shaded by the sample horizon. The images represent cut outs of the diffractions patterns obtained at P08 beamline with a Pilatus 300k detector. The hatched section in each image reflects the area of the detectors' sensor gap which is complemented by the data of a second, vertically shifted detector image.

H_d lattices around $\gamma = 135°$, the third and fourth lattice orientations, denoted by H_γ, are obtained (cf. Fig. 6.28 B). While at high peptide concentration (P/L = 1:22 and 1:18) reflections from both H_d and H_γ are registered, at lower P/L only the H_d phase is detected. At high P/L, the peaks originating from this phase are also more pronounced than the ones from H_γ. Consequently, it is inferred that H_d is the predominant form. The unit cell parameter of the distorted hexagonal phase does not exhibit a systematic P/L dependence: While it increases from $a = (66.7 \pm 0.5)$ Å at P/L = 1:53 to $a = (68.2 \pm 0.5)$ Å at P/L = 1:40, it slightly decreases again to $a = (67.5 \pm 0.5)$ Å for P/L = 1:18.

In addition to the reflections explained by the different orientations of the distorted hexagonal phases, a set of orthorhombic reflections at low q_r and $q_z = d$ (lamellar repeat spacing, see Sec. 6.3.2) is observed in the GID patterns associated

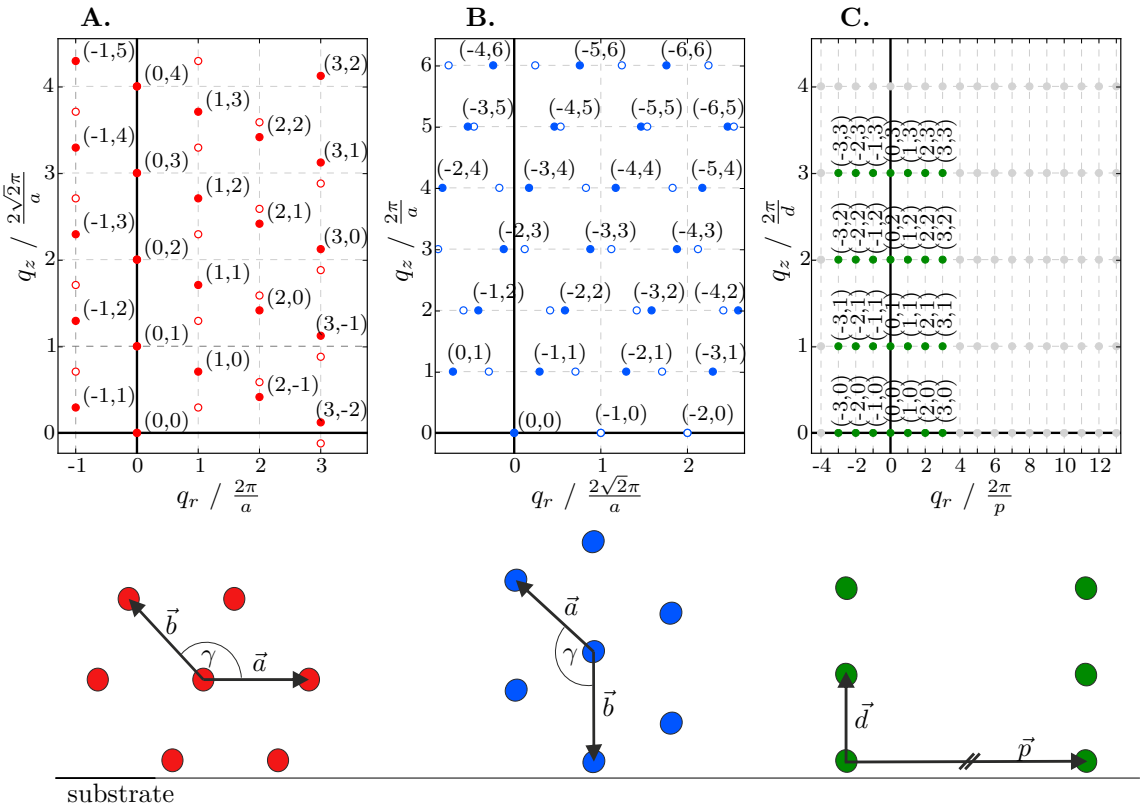

Figure 6.28 – Diffraction patterns of different lipid structures. A. H_d phase with its base aligned parallel to the substrate. **B.** H_γ phase, which is rotated by $\gamma = 135°$ with respect to the H_d phase. **C.** Orthorhombic lattice reflections corresponding to the $P_{\beta'}$ phase. The filled circles illustrate the reflections from the real space lattices drawn below each diffraction pattern. Note that the third lattice dimension is omitted in the drawings. The reflections are additionally indexed with their respective Miller indices (h, k). Reflections from corresponding mirror lattices (with respect to the vertical axis) are indicated by empty circles. For both distorted hexagonal lattices, $|\vec{a}| = |\vec{b}| = a$ applies. In **C.** the indication of the Miller indices is limited to combinations of $(h, k) \in (-3, 3)$ for reasons of clarity. Note that the dimension of the lattice vector $\vec{p}$ of the orthorhombic phase is not drawn to scale. The plot dimensions of the diffraction schemes apply to the patterns depicted in Fig. 6.27 E.

to the lipid/Ece1-III$_{\mathrm{KR(N)}}$ systems. These are described by the reciprocal components $Q_{hk,r} = \frac{2\pi}{p}h$ and $Q_{hk,z} = \frac{2\pi}{d}k$, which trace back to the two-dimensional lattice depicted in Fig. 6.28 C. Again, the third dimension is neglected as it is assumed to be much larger than the unit cell parameters p and d given in the figure. Owing to the limited resolution, the increased intensities of the first and second order Bragg sheets in this particular DOPC/Ece1-III$_{\mathrm{KR(N)}}$ series merely indicate the presence of these reflections. However, they emerge more distinctly in the other lipid mixtures presented in the following. For this reason, this third class of reflections is also introduced at this point. The orthorhombic reflections indicate the presence of an additional rippled phase $P_{\beta'}$, in which the lipid bilayers adapt a symmetric sawtooth shape [260]. In this respect, the unit cell parameter p reflects the 'wavelength' of

the ripples. From the shape of the first order Bragg sheet in the GID patterns corresponding to the samples of P/L = 1:22 and P/L = 1:18, the periodicity of these ripples is estimated to be $\approx$ 155 Å and $\approx$ 238 Å, respectively. A summary on the coexistence of the different phases and their respective unit cell parameters is given in Tab. 6.3.

25°C: The diffraction patterns acquired at 25°C are not depicted as they show a similar emergence of the coexisting phases. However, the peptide-induced phase transition appears to be shifted to higher P/L values since the particular reflections are less intense and the rippled phase is not detectable. The absence or presence of the respective phases, as well as the unit parameters in case of the latter are summarised in Tab. 6.3.

The quantification of the relative proportions of each lattice and the corresponding form factors is not trivial as several reflections from the different lattices coincide. It is further complicated by the lateral inhomogeneity of the sample. Consequently, a quantitative analysis by means of the reconstruction of electron density distributions is omitted and the phase behaviour is only evaluated on a qualitative basis. As mentioned earlier, this is sufficient to evaluate the structural impact of the peptide. Even a reasonable qualitative description of the complex phase coexistence observed here is hard to find. Nevertheless, from the increasing proportions of the H_d phase, it can be concluded that the interaction between the phospholipids and Ece1-III$_{\mathrm{KR(N)}}$ induces a pronounced bilayer curvature which results in the formation of non-lamellar phases.

Grazing Incidence Diffraction: Small-Angle Region, Lipid composition

40°C: Exemplary diffraction patterns of DOPC/Chol, DOPC/Erg and DOPC/PS with and without Ece1-III$_{\mathrm{KR(N)}}$ at P/L = 1:18 and a temperature of 40°C are shown in Fig. 6.29. The patterns caused by the pure DOPC/Chol and DOPC/PS samples are similar to the ones observed for solely DOPC. The in-plane extents of the Bragg sheets are comparatively narrow, confirming a high degree of orientational order. Consistent with the reflectivities of these samples, only the repeat spacings d slightly vary for the different lipid mixtures (cf. Sec. 6.3.2). The DOPC/Erg sample causes stronger circular extensions of the Bragg reflections, demonstrating an increased amount of static defects. Its pattern also shows the additional narrow reflections at $q_z = 0.18$ Å^{-1} and $q_z = 0.35$ Å^{-1} which are attributed to the presence of ergocalciferol (cf. Sec. 6.3.2).

The diffraction patterns caused by the samples containing Ece1-III$_{\mathrm{KR(N)}}$ are also similar to the corresponding DOPC/Ece1-III$_{\mathrm{KR(N)}}$ samples. Reflections from both

	P/L	H_d	H_γ	$P_{\beta'}$	
		a [Å]	a_γ [Å]	d [Å]	p [Å]
25°C					
DOPC	0:1 = 0.000	n/a	n/a	n/a	n/a
+ Ece1-III$_{\mathrm{KR(N)}}$	1:22 ≈ 0.045	n/a	n/a	n/a	n/a
	1:18 ≈ 0.056	71.4	71.4	n. d.	n. d.
DOPC/Chol	0:1 = 0.000	n/a	n/a	n/a	n/a
+ Ece1-III$_{\mathrm{KR(N)}}$	1:18 ≈ 0.056	73.9	73.9	n. d.	n. d.
DOPC/Erg	0:1 = 0.000	n/a	n/a	n/a	n/a
+ Ece1-III$_{\mathrm{KR(N)}}$	1:18 ≈ 0.056	70.5	70.5	236	50
DOPC/PS	0:1 = 0.000	n/a	n/a	n/a	n/a
+ Ece1-III$_{\mathrm{KR(N)}}$	1:18 ≈ 0.056	n/a	n/a	n/a	n/a
DOPC + Ece1-III$_{\mathrm{K(C)}}$	1:18 ≈ 0.056	n/a	n/a	n/a	n/a
DOPC + Ece1-III$_{\mathrm{AA(N)}}$	1:18 ≈ 0.056	76.6	n/a	n/a	n/a
40°C					
DOPC	0:1 = 0.000	n/a	n/a	n/a	n/a
+ Ece1-III$_{\mathrm{KR(N)}}$	1:53 ≈ 0.019	66.7	n/a	n/a	n/a
	1:40 = 0.025	68.2	n/a	n/a	n/a
	1:22 ≈ 0.045	68.2	68.2	292	48.0
	1:18 ≈ 0.056	67.5	67.5	238	47.5
DOPC/Chol	0:1 = 0.000	n/a	n/a	n/a	n/a
+ Ece1-III$_{\mathrm{KR(N)}}$	1:18 ≈ 0.056	69.5	69.5	238	48.7
DOPC/Erg	0:1 = 0.000	n/a	n/a	n/a	n/a
+ Ece1-III$_{\mathrm{KR(N)}}$	1:18 ≈ 0.056	70.2	70.2	238	50.0
DOPC/PS	0:1 = 0.000	n/a	n/a	n/a	n/a
+ Ece1-III$_{\mathrm{KR(N)}}$	1:18 ≈ 0.056	67.2	67.2	240	47.5
DOPC + Ece1-III$_{\mathrm{K(C)}}$	1:18 ≈ 0.056	63.1	n/a	n/a	n/a
DOPC + Ece1-III$_{\mathrm{AA(N)}}$	1:18 ≈ 0.056	72.1	n/a	n/a	n/a

Table 6.3 – Lipid phases observed for different lipid/peptide systems. The table summarises the occurrence of the distorted hexagonal phases H_d and H_γ as well the rippled phase $P_{\beta'}$ at 25°C (upper half) and 40°C (lower half). The absence of a phase is indicated by "n/a". In the presence of the phase, the respective unit cell parameters are given, unless the reflections were only indicated but non-determinable ("n. d."). The uncertainties for the unit cell parameters are estimated to be $\sim 0.8\,\%$ for d, a and a_γ, but almost $5\,\%$ for p. The lipid-lipid ratio was 9:1 (n/n).

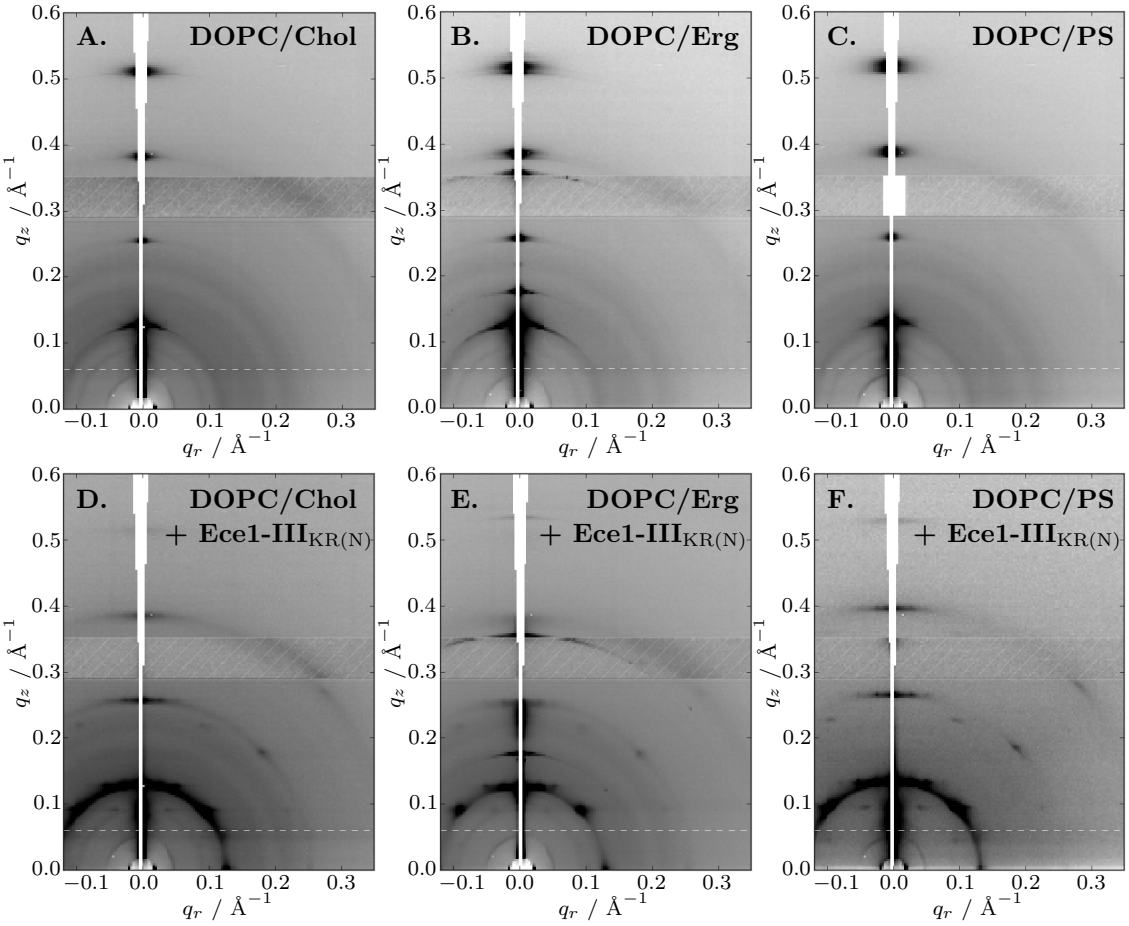

Figure 6.29 – Small-angle diffraction patterns of differently composed lipid/peptide multilayer samples at 40°C. The upper row depicts the patterns obtained for pure lipid samples of DOPC/Chol (**A.**), DOPC/Erg (**B.**) and DOPC/PS (**C.**). The corresponding patterns obtained in the presence of Ece1-III$_{KR(N)}$ at P/L = 1:18 are shown in the lower row (**D.** - **F.**). The lipid-to-lipid ratio of each sample was 9:1 (n/n). The area below $q_z = 0.06$ Å^{-1} (indicated by the dashed horizontal line) is shaded by the sample horizon. The images represent cut outs of the diffractions patterns obtained at P08 beamline with a Pilatus 300k detector. The hatched section in each image reflects the area of the detectors' sensor gap which is complemented by the data of a second, vertically shifted detector image. The additional white space at $q_z \simeq 0.35$ Å^{-1} in C is due to an experimental artefact.

H_d and H_γ phases are registered as well as those from the orthorhombic $P_{\beta'}$ phase. As mentioned earlier, the latter are better resolved in the lipid mixtures than they are in the corresponding pure DOPC samples. This particularly applies for the DOPC/Erg and DOPC/PS mixtures, in which the reflections at $q_z = 2\pi n/d$ and $q_r < 0.06$ Å^{-1} are distinguishable from one another for the first two orders of Bragg peaks (n = 1, 2) – i. e. the reflections with $h \in (-3, 3)$ and $k \in (1, 2)$. Reflexes associated to $(0, 1)$ and $(0, 2)$, however, coincide with the ones from the lamellar bilayer lattice. The angle γ is found to have a constant value of 135°. A summary of the determined phase parameters is included in Tab. 6.3. With a value of $a =$

(67.2 ± 0.3) Å, the unit cell parameter for DOPC/PS is the smallest but compares best to the one found for the equivalent DOPC/Ece1-III$_{\mathrm{KR(N)}}$ samples. With $a = (69.5 \pm 0.4)$ Å and $a = (70.2 \pm 0.4)$ Å, the lattice dimensions of the DOPC/Chol and DOPC/Erg samples are about 2 Å larger. Consistent with that, also the edge length d of the orthorhombic unit cell is the smallest for the peptide-containing DOPC/PS sample, whereas the other two exhibit $\simeq 2$ Å larger edge lengths.

Note that these findings are not consistent with the d-spacings obtained from the XRR experiments listed in Tab. 6.1. Although the XRR recordings have a higher resolution, the deviations between both techniques should basically not exceed a discrepancy of maximal 1 Å. However, for DOPC/Chol and Ece1-III$_{\mathrm{KR(N)}}$, the XRR analysis obtained a value of $d = 45.7$ Å, while here it was found to be $d = 48.7$ Å. Hence, the results differ by 3 Å. While the XRR result was obtained from duplicate measurements on different samples, the GID value was obtained from only one single measurement. This might imply that the discrepancy is due to variations between the different sample preparations. However, for the particular sample presented here, the d-spacing obtained by XRR was 46.9 Å, which is still about 1.8 Å smaller compared to the GID finding. As both experiments were carried out at different lateral sample positions with a distance of 0.5 mm in between, this finding demonstrates that one single sample exhibits a considerable degree of inhomogeneity. However, with regard to the high complexity of the phase behaviour and also the increased disorder of the lipid systems containing Ece1-III$_{\mathrm{KR(N)}}$, this finding is not surprising.

25°C: The phase behaviour observed at 25°C is similar to the one observed for the DOPC/Ece1-III$_{\mathrm{KR(N)}}$ system at 25°C. Again, the complex phase coexistence is not that well marked as it is at higher temperature. While both distorted hexagonal phases, H_d and H_γ, were clearly visible in the DOPC/Chol and DOPC/Erg samples containing Ece1-III$_{\mathrm{KR(N)}}$, the reflections from the orthorhombic $P_{\beta'}$ phase only weakly signified at this temperature. On the contrary, the corresponding DOPC/PS/Ece1-III$_{\mathrm{KR(N)}}$ mixture only exhibited the lamellar phase. The observations are also summarised in Tab. 6.3.

Grazing Incidence Diffraction: Small-Angle Region, Peptide Variants

40°C: The diffraction patterns obtained from DOPC samples with either Ece1-III$_{\mathrm{K(C)}}$ or Ece1-III$_{\mathrm{AA(N)}}$ at P/L = 1:18 and a temperature of 40°C are shown in Fig. 6.30. Together with the corresponding findings for 25°C, the identified phase behaviour is summarised in Tab. 6.3. In the pattern obtained from the DOPC/Ece1-III$_{\mathrm{K(C)}}$, only the $(1, 0)$ reflections of the mirrored H_d phases are identifiable. The

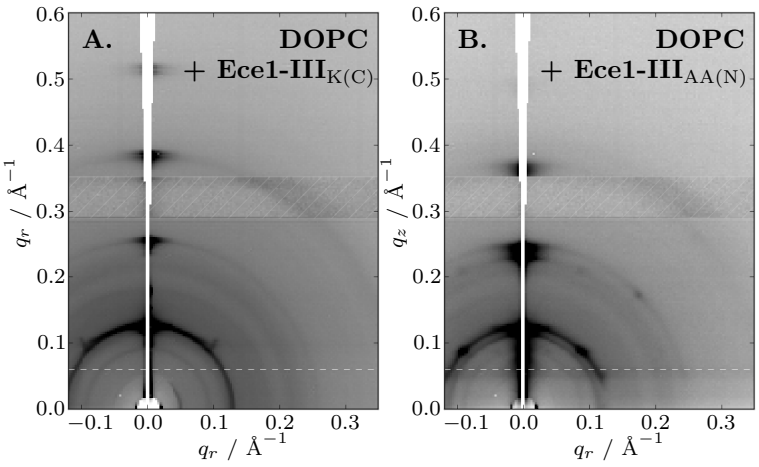

Figure 6.30 – Small-angle diffraction patterns of DOPC multilayers with Ece1-III variants at 40°C. **A.** DOPC + Ece1-III$_{K(C)}$. **B.** DOPC + Ece1-III$_{AA(N)}$. In both measurements, the P/L was 1:18. The images represent cut outs of the diffractions patterns obtained at P08 beamline with a Pilatus 300k detector. The area below $q_z = 0.06$ Å^{-1} (indicated by the dashed horizontal line) is shaded by the sample horizon. The hatched section in each image reflects the area of the detectors' sensor gap which is complemented by the data of a second, vertically shifted detector image.

respective $(0, k)$ reflections, which are also supposed to appear, coincide with the reflections associated to the remaining lamellar L_α phase and cannot be distinguished. With a being (63.1 ± 0.5) Å, the unit parameter of H_d is notably smaller compared to that found for the other systems, but γ is also 135°. In the DOPC/Ece1-III$_{AA(N)}$ sample, a coexistence of the lamellar L_α and the H_d phase is observed. Aside from the $(1, 1)$ reflections, also the $(2, 0)$ reflection is identifiable. However, no reflections from H_γ or $P_{\beta'}$ are detected. The unit cell length of H_d is determined to be $a = (72.1 \pm 0.4)$ Å, which is large in comparison to the other systems at 40°C, but consistent with the observation that it has the largest d spacing (cf. Sec. 6.3.2).

25°C: While in case of Ece1-III$_{K(C)}$ only the L_α phase was present at 25°C, the corresponding Ece1-III$_{AA(N)}$ sample also demonstrates the existence of H_d. The results for both temperatures suggest that the curvature-induction by the peptides is less pronounced for both modified peptide variants as compared to Ece1-III$_{KR(N)}$.

Grazing Incidence Diffraction: Wide-Angle Region, P/L Dependence

The wide-angle data is analysed to examine the acyl chain packing and orientation in response to interactions with Ece1-III$_{KR(N)}$. Fig. 6.31 depicts exemplary raw data of the chain correlation peak obtained for a pure DOPC sample at 40°C and a corresponding DOPC/Ece1-III$_{KR(N)}$ sample at P/L = 1:18 (≈ 0.056). It is obvious that the intensity of the chain correlation peak in the DOPC sample decreases

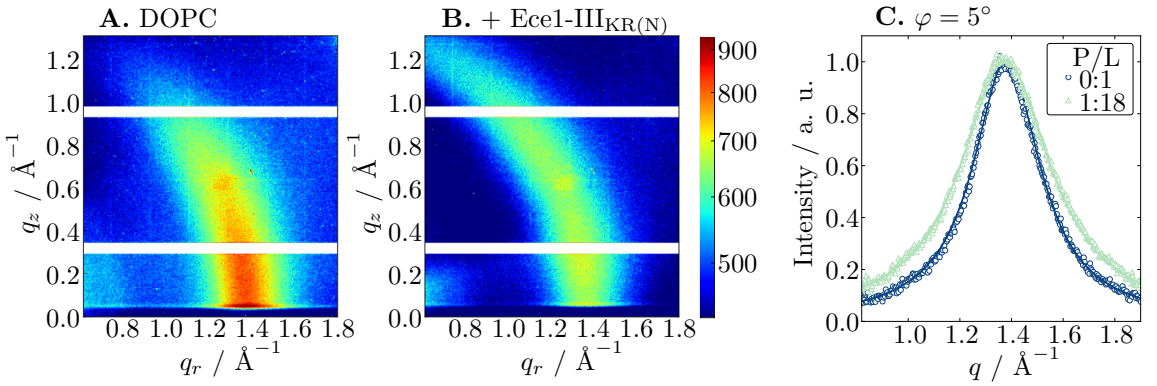

Figure 6.31 – Acyl chain correlation. A. Exemplary chain correlation peak of a DOPC multilayer sample, showing a pronounced decay with increasing azimuthal angle φ. **B.** Chain correlation peak of a binary DOPC/Ece1-III$_{KR(N)}$ sample at P/L = 1:18 (≈ 0.056), demonstrating a broad azimuthal intensity distribution. Both images are cut-outs from the Pilatus 300k images obtained at 40°C at the P08 beamline. Due to the detector's sensor gaps, the GID patterns are incomplete. **C.** Radial peak profiles along $\varphi = 5°$, extracted from the images shown in A and B. For clarity, the fitted background was substracted from the profiles and the data was normalised to the peak maximum. The symbols indicate the experimental data and the solid-lines the Lorentzian fits to the peak profiles.

rapidly with increasing azimuthal angle φ. By contrast, the peak of the peptide-containing sample shows a rather uniform intensity distribution over the arc section probed. Radial profiles along $\varphi = 5°$ of both data sets are illustrated in Fig. 6.31. The chain correlation peaks show a comparatively broad radial width, arising from the absence of long-range order of the fluid acyl chains. The direct comparison between the pure DOPC and the peptide-containing sample, demonstrates that the peak further broadens in the presence of Ece1-III$_{KR(N)}$ which indicates a pronounced chain fluidity. Consequently, the chains' correlation length is reduced.

To study both the peak intensity and the correlation length in greater detail, the parameters are analysed as function of the azimuthal angle. In this context, also the peak position q_0 and the averaged chain-to-chain distance a are evaluated. Fig. 6.32 A illustrates the parameters obtained from Lorentzian fits to the radial profiles from a series of DOPC/Ece1-III$_{KR(N)}$ at different P/L (0:1, 1:53 ≈ 0.019, 1:40 $= 0.025$, 1:22 ≈ 0.045, 1:18 ≈ 0.056). As already inferred from the peaks' appearances in the raw data images, the intensity distribution $L_0(\varphi)$ of the pure lipid sample exhibits a rapid decay. This observation reflects a narrow angular distribution of chain tilts and indicates that the acyl chains adapt a predominant parallel alignment to the bilayer normal. With increasing P/L, the intensity distribution broadens, implying an increasing inclination of the chains. For P/L = 1:22 and P/L = 1:18, $L_0(\varphi)$ adapts a largely uniform distribution over the arc section probed. These findings are consistent with the formation of non-lamellar phase structures,

involving a rearrangement of the acyl chains, that ends up with an isotropic chain distribution in the inverted hexagonal H_{II} phase [212]. Here, the chain tilt distribution is not completely constant, which is attributed to the remaining coexistence of the lamellar and the distorted hexagonal phase populations. The peak position q_0 shifts to slightly higher q-values with increasing φ, which already indicates that the spacing between neighbouring chains is decreased at large tilt angles. Distinct

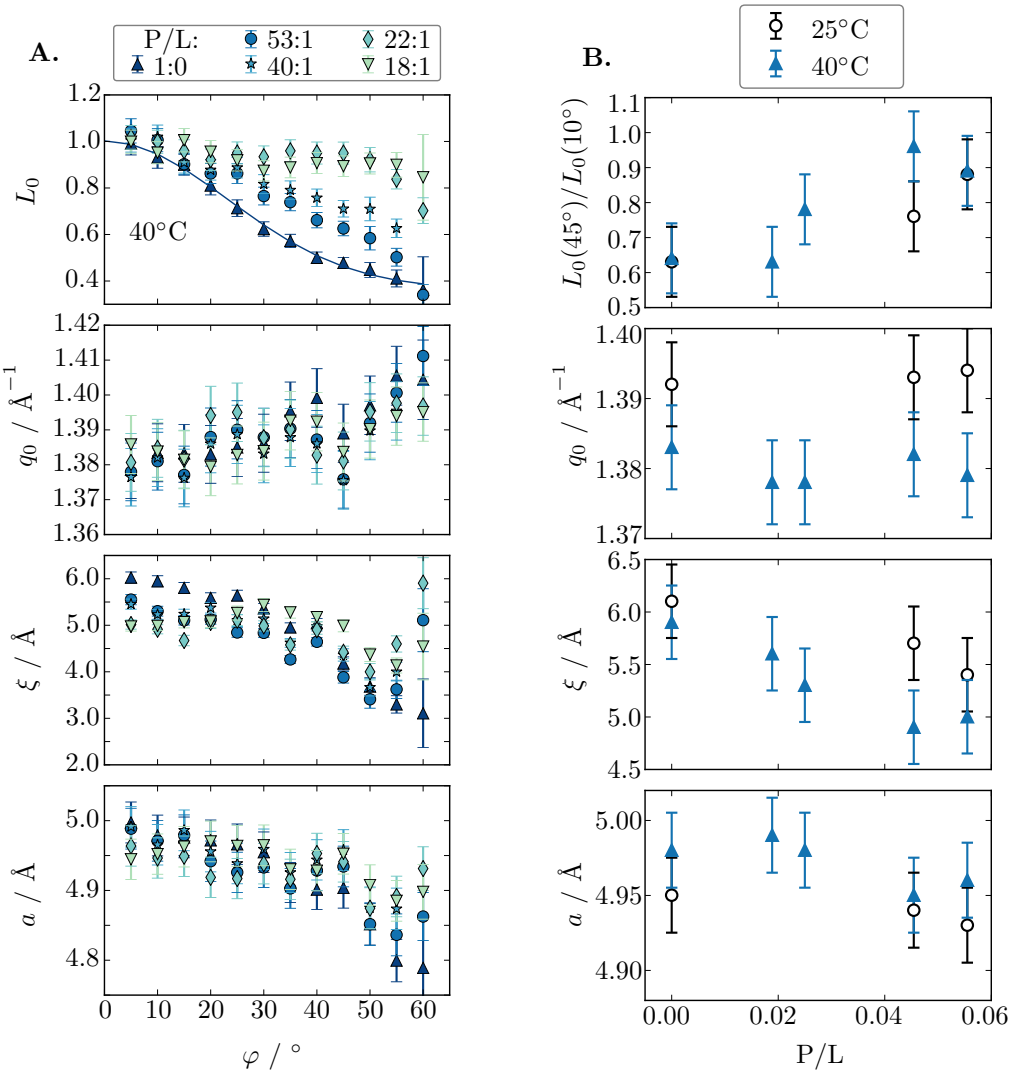

Figure 6.32 – Acyl chain correlations in a P/L series of DOPC/Ece1-III$_{KR(N)}$ multilayers. A. Chain properties at 40°C as function of the azimuthal angle φ. For better comparability, the peak intensity L_0 is normalised to $L_0(5°)$. The solid line represents a Gaussian fit to the angular dependence of the DOPC sample. In the peptide-containing samples, L_0 cannot be represented by such Gaussian profiles. **B.** Comparison of the chain parameters obtained at 25°C (○) and 40°C (▲) as function of the P/L (0:1, 1:53 ≈ 0.019, 1:40 = 0.025, 1:22 ≈ 0.045, 1:18 ≈ 0.056). The parameters q_0 (peak position), ξ (chain correlation length) and a (mean chain-to-chain distance) are given as mean values of the fits obtained for $\varphi = 5°$, 10° and 15°. The errorbars represent the uncertainties estimated by considering the standard deviations from the least-square fitting and the precision of the sample-detector alignment.

differences between the individual samples are not observed. As already deduced from the comparison of the peak profiles shown in Fig. 6.31 C, the correlation length ξ, which is indirectly proportional to the peak width (cf. Sec. 3.5.6), is lower in the peptide-containing samples than in the pure lipid sample. However, this only applies for small φ. Even though ξ shrinks with increasing φ in all samples, the decrease flattens with increasing P/L.

Accordingly, the few highly tilted acyl chains of the pure DOPC bilayers exhibit only little short-range order, whereas the isotropically distributed chains of the non-lamellar phases maintain an almost constant level of short-range order throughout all orientations. The fourth parameter evaluated in Fig. 6.32 A illustrates the averaged lateral chain-to-chain distance a (which is defined in Fig. 3.15 or Sec. 3.5.6). This distance also shrinks for increasing azimuthal angles, but again, the φ-progression flattens as function of the Ece1-III$_{\mathrm{KR(N)}}$ content. Nevertheless, the differences between the samples are not significant as they predominantly vary within the estimated uncertainties. Thus, it may be inferred that the peptide's effect on the interchain distance is negligible.

At lower sample temperature, a similar peptide-dependent chain behaviour is found as shown in Fig. 6.32 B. In this figure, the relative width of the azimuthal orientation distribution is evaluated as ratio of the peak intensities L_0 at 45° and 10°. In order to achieve a better comparability of the acyl chain properties, arithmetic averages of q_0 (peak position), ξ (chain correlation length) and a (mean chain-to-chain distance) at $\varphi = 5°$, 10° and 15° are utilised as representative indicators. Similar to the findings at 40°C, also at 25°C the orientation distribution broadens with increasing P/L. Compared to 40°C, the position is shifted to higher q-values and the interchain distance in enlarged by less than 0.5 Å. Both parameters do not exhibit a systematic P/L dependence, although the mean chain-to-chain distance also indicates a tendency to slightly decrease. The short-range correlation is on average higher at 25°C than at 40°C, but also shrinks with increasing peptide content.

Grazing Incidence Diffraction: Wide-Angle Region, Lipid Composition

The acyl chain correlations observed for lipid systems composed of DOPC/Chol, DOPC/Erg and DOPC/PS are graphically summarised in Fig. 6.33 A. The chain parameters obtained for corresponding samples containing Ece1-III$_{\mathrm{KR(N)}}$ at P/L = 1:18 (≈ 0.056) are also included in this figure. For both sample sets, the chain correlation was probed at 25°C and 40°C. The temperature has no effect on the azimuthal intensity distribution of the chain correlation reflections (represented by $L_0(45°)/L_0(10°)$), but on their maxima positions – these shift to lower q-values by

about 0.01 $Å^{-1}$. Since temperature effects in the acyl chains' correlation lengths are negligible, the shifted peak positions directly reflect the increasing average interchain distances (cf. Eq. 3.26). This in turn implies that the area per lipid also increases.

Comparisons of the chain correlations in pure lipid and in lipid/peptide systems again reveal striking differences in terms of chain orientation. The pure lipid multilayers exhibit comparatively narrow azimuthal intensity distributions, in which

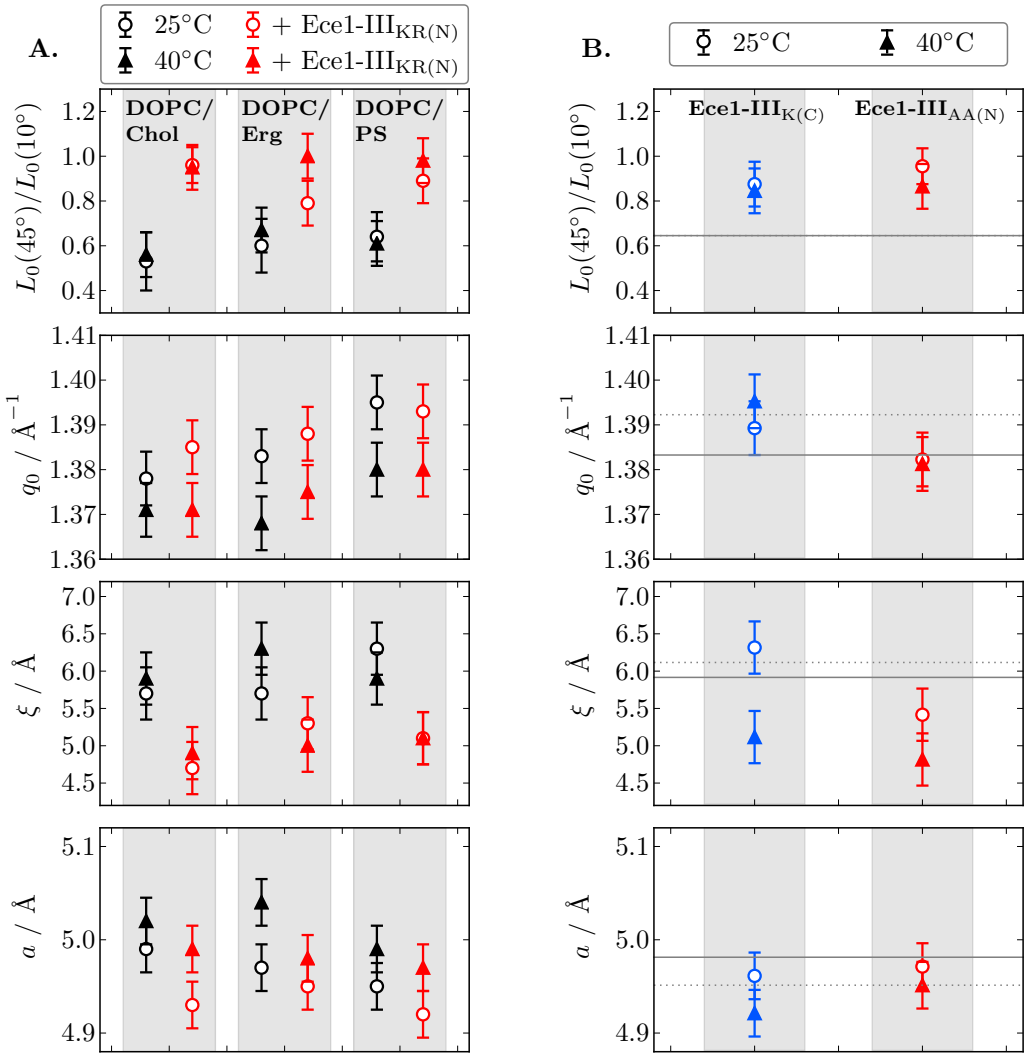

Figure 6.33 – Acyl chain correlations in different lipid/peptide systems. A. Chain properties of differently composed pure lipid multilayers (black symbols) and corresponding samples containing Ece1-III$_{KR(N)}$ at P/L = 1:18 (≈ 0.056, red symbols). The lipid mixtures probed included DOPC/Chol, DOPC/Erg and DOPC/PS, each at a lipid-to-lipid ratio of 9:1 (n/n). **B.** Chain correlations in DOPC multilayers in the presence of either Ece1-III$_{K(C)}$ (blue symbols) or Ece1-III$_{AA(N)}$ (red symbols) at P/L = 1:18. In all panels, the chain correlation parameters obtained at 25°C (empty circles) and 40°C (filled triangles) are compared. In B, the parameters obtained for the pure DOPC sample are additionally illustrated by horizontally dotted lines for 25°C and solid lines for 40°C. The values for q_0 (peak position), ξ (chain correlation length) and a (mean chain-to-chain distance) represent mean values of the fits obtained for $\varphi = 5°$, 10° and 15°.

the peak maxima decrease by a factor of $\simeq 0.5$ from $\varphi = 10°$ to $\varphi = 45°$. In the peptide-containing samples, the corresponding $L_0(45°)/L_0(10°)$ ratios equal almost unity, reflecting uniform intensity distributions and thus, isotropic chain orientations. Again, this is in accordance with the formation of the non-lamellar phases, in which the acyl chains need to adjust their orientation to fill the emerging hydrophobic voids. Note that such a pronounced chain tilt is also observed for the DOPC/PS sample with Ece1-III$_{\mathrm{KR(N)}}$ at 25°C, for which no reflections arising from H_d or H_γ phases have been detected. This observation suggests the existence of an intermediate state, in which the chain rearrangement already started but the final lattice formation has not been completed. The peak positions are independent on the peptide content. The peak widths, however, are clearly broadened in the presence of Ece1-III$_{\mathrm{KR(N)}}$ which is reflected by the decrease of ξ. Again, the peptide seems to have a minor tightening effect on the lipid packing. However, this effect is again negligible as a varies mostly within the boundaries of the estimated uncertainty, i. e. on length scales of ~ 0.03 Å.

Grazing Incidence Diffraction: Wide-Angle Region, Peptide Variants

Fig. 6.33 B plots the determined chain correlation parameters of multilayer mixtures of DOPC/Ece1-III$_{\mathrm{K(C)}}$ and DOPC/Ece1-III$_{\mathrm{AA(N)}}$. For both systems, $L_0(45°)/L_0(10°)$ is $\simeq 0.86$, reflecting a clearly broadened chain tilt distribution compared to the pure DOPC samples, in which $L_0(45°)/L_0(10°)$ was $\simeq 0.64$. Similar to the DOPC/PS sample, no non-lamellar phase was detected for DOPC/Ece1-III$_{\mathrm{K(C)}}$ at 25°C. Thus, the increased occurrence of tilted chains is again assumed to represent some kind of intermediate state. Differences with respect to the peak position and the averaged chain-to-chain distance are not observed. Just as it was observed for the DOPC/Ece1-III$_{\mathrm{KR(N)}}$ sample, the correlation length is found to slightly decrease in the presence of Ece1-III$_{\mathrm{AA(N)}}$. Such an indication for chain fluidisation is not observed for Ece1-III$_{\mathrm{K(C)}}$. Here, the correlation length at 25°C is slightly increased compared to the pure DOPC sample and equal to it at 40°C.

6.3.4 Effect on Lipid Rafts

To get a better understanding of the surface activity of Ece1-III$_{\mathrm{KR(N)}}$ and how it is influenced by specific lipid components, its effect on the nanoscale organisation of lipid domains is investigated. Firstly, FT-IR experiments on domain-forming lipid mixtures are presented to access the averaged acyl chain behaviour in presence of Ece1-III$_{\mathrm{KR(N)}}$. Subsequently, distinct interaction differences with respect to the specific lipid domains are addressed. Therefore, AFM studies on solid-supported single

bilayers are performed to follow the lipid/peptide interaction *in situ*. Additionally, complementary XRR data on similar but static multilamellar samples is obtained to support the real-time data. Two different lipid mixtures, one with and another without PS are employed to examine possible influences of anionic lipids on the interaction behaviour. For the mixtures without PS, no reliable AFM data could be obtained. Therefore, the studies on PS-containing bilayers is presented first and the ones without PS are discussed in the end.

FT-IR Studies

In model bilayers of DOPC/SM/Chol or DOPC/SM/Chol/PS mixtures, the lipids separate into two different phases: the liquid-ordered L_0-phase, enriched in SM and Chol, and the liquid-disordered L_d-phase (alternatively referred to as L_α-phase) which is predominantly composed of DOPC. To study the behaviour of the acyl chain of these two liposome mixtures, the symmetric CH_2 stretching vibrations around 2850 cm^{-1} were examined as function of temperature in the presence and in the absence of Ece1-$III_{KR(N)}$ at P/L = 1:2. Fig. 6.34 depicts the resulting spectral progressions of the maximum position of the corresponding absorption band. The gradual increase to higher wavenumbers reflects the melting of liquid-ordered L_0 domains into the liquid-crystalline L_α state. Given the complex separation in liquid-ordered and liquid-disordered domains in these tertiary and quaternary liposome

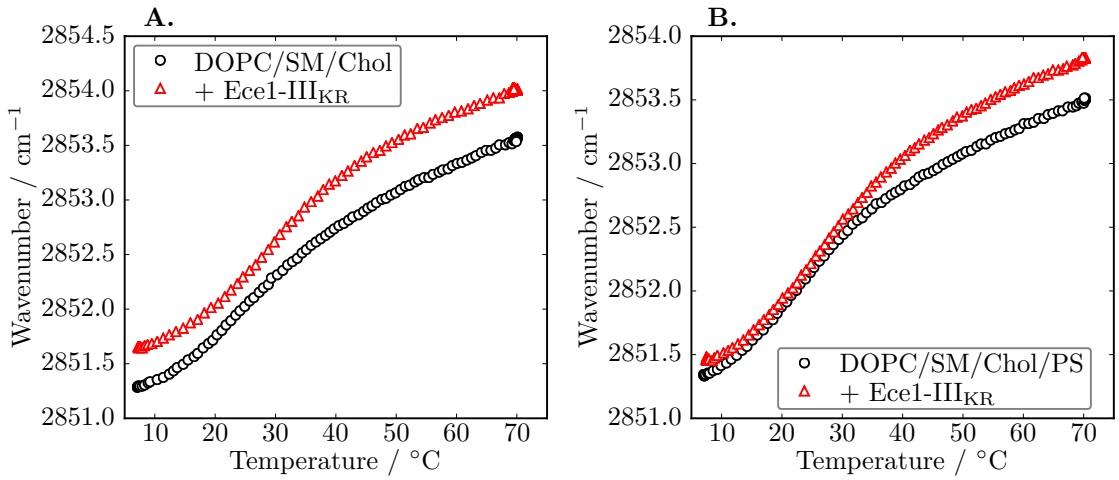

Figure 6.34 – FT-IR examination of lipid mixtures with and without peptide content. A. DOPC/SM/Chol. **B.** DOPC/SM/Chol/PS. The wavenumber of the maximum absorption of the symmetric CH_2 stretching vibrations is given as function of temperature. In both mixtures, liposomes containing Ece1-$III_{KR(N)}$ at a P/L of 1:2 (△) absorb at lower frequencies (lower wavenumbers) than the pure lipid vesicles (○) and the transition is shifted to higher temperatures. Molar lipid-lipid ratios for DOPC/SM/Chol and DOPC/SM/Chol/PS were 9:9:2 and 9:9:2:2, respectively.

compositions (cf. Sec. 6.3.4), the temperature transitions do not occur at one particular temperature but proceed across a broad temperature range. Hence, precise transition temperatures cannot be defined. In the Ece1-III$_{\mathrm{KR(N)}}$/DOPC/SM/Chol mixtures, the absorption frequency is shifted to higher wavenumbers by $\simeq 0.45$ cm^{-1} over the entire temperature range as compared to the pure lipid mix.

In Ece1-III$_{\mathrm{KR(N)}}$/DOPC/SM/Chol/PS mixtures, by contrast, the band is shifted by only $\simeq 0.33$ cm^{-1} and the shift occurs predominantly at higher temperature, i. e. in the L_α-state. These positive shifts reflect increases in the conformational disorder of the chains. Thus, the peptide fluidises the bilayers to a certain degree. In addition, with Ece1-III$_{\mathrm{KR(N)}}$ content, the thermotropic transition itself is retarded as it is shifted to slightly higher temperatures by about $\simeq$ 5 - 10°C.

DOPC/SM/Chol/PS Membranes

The two domains present in phase-separated bilayers exhibit a characteristic height difference as the liquid-disordered L_d-phase, which is predominantly composed of DOPC, is of lower height than the Chol- and SM-rich liquid-ordered L_0-phase. Therefore, both domains can be clearly distinguished in AFM height images. A representative example of such a bilayer image of a DOPC/SM/Chol/PS mixture is shown in Fig. 6.35 A. As determined by height histograms, the L_0 domains extend $\simeq$ 6 Å above the DOPC-rich L_d domains. Keeping in mind, that the images were obtained at constant force in tapping mode, the height representation of these domains might be deluding, depending on whether the imaging was performed in the attractive or repulsive regime. While the latter is found to yield results comparable to those obtained in contact-mode, the attractive mode may lead to inverse images [261]. In the aqueous environment, however, attractive van der Waals potentials are substantially reduced and electrostatic interactions between the cantilever tip and the anionic PS can be neglected due to the tip's neutral charge. Thus, for the pure lipid system, the overall force on the cantilever tip is repulsive and the domains rendered with greater height are indeed the thicker Chol-rich rafts.

After the injection of 10 μl Ece1-III$_{\mathrm{KR(N)}}$ (1 mg·ml^{-1} in 0.01 % TFA, final peptide concentration: $\sim$ 1 μM) to the liquid phase, a film reorganisation is observed as the boundaries of the round-shaped domains start to fray out (Fig. 6.35 B - C). 35 min after the peptide addition, the height difference shrinks to $\simeq$ 4.5 Å. For longer incubation time, precise height determinations are ruled out since the imaging quality worsens dramatically. The system is subjected to increased adhesion forces between tip and sample, i. e. it becomes extraordinarily sticky, which is recognisable by the line smearing apparent in the height images. As can be seen in the images obtained at the time points 65 min and 120 min after the injection (Fig. 6.35 D,

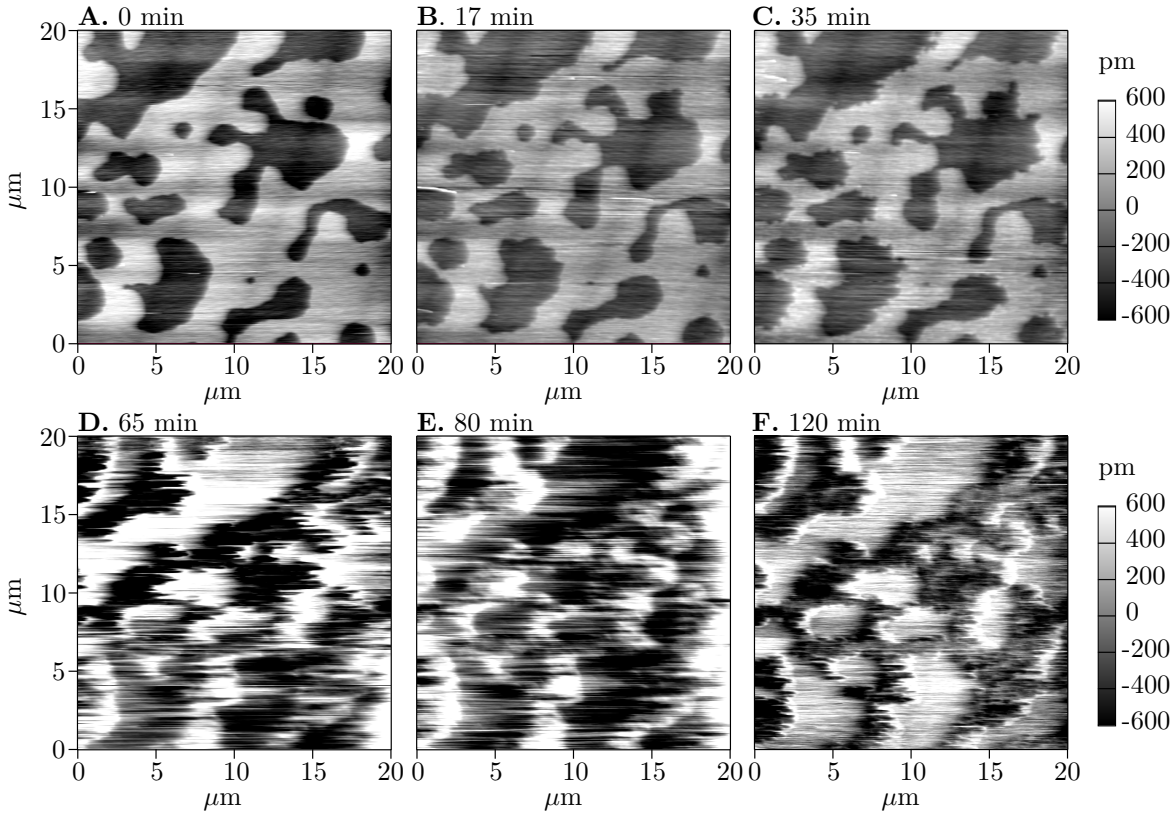

Figure 6.35 – AFM height images of a DOPC/SM/Chol/PS bilayer in the course of the interaction with Ece1-III$_{KR(N)}$. The images visualise **A.** the bilayer before the peptide addition and at different time points after the addition of Ece1-III$_{KR(N)}$: **B.** 17 min, **C.** 35 min, **D.** 65 min, **E.** 80 min and **F.** 120 min. After the peptide injection, the organisation of the domain boundaries alters as function of the incubation time and the imaging quality worsens. Domain shapes and bilayer properties of a control measurement persisted after corresponding additions of 0.01 % TFA. The molar lipid ratio used for the film preparation was DOPC/SM/Chol/PS 2:2:1:1, the final peptide concentration was $\simeq$ 1 μM. The images were obtained in tapping mode with a scanning rate of 1.0 Hz/line at room temperature.

F), the high Chol-rich domains are rendered with a lower height than the DOPC domains. This observations may either originate from a real physical height effect by a peptide assembly at the DOPC domains or from enhanced attraction forces between the cantilever tip and the Chol-rich domains. Due to its sudden appearance and its absence in Fig. 6.35 E at intermediate incubation time, this inversion effect is assumed to originate from the latter case. Such peptide-mediated alterations of the interaction potentials may be explained by occasional functionalisations of the cantilever tip by binding either peptide out of the aqueous phase or lipids solubilised by the peptide.

The associated amplitude images shown in Fig. 6.36 support this conclusion. In absence of the peptide, steady oscillation plateaus are observed for both lipid phases. While this steadiness is preserved throughout the entire experiment for the lower

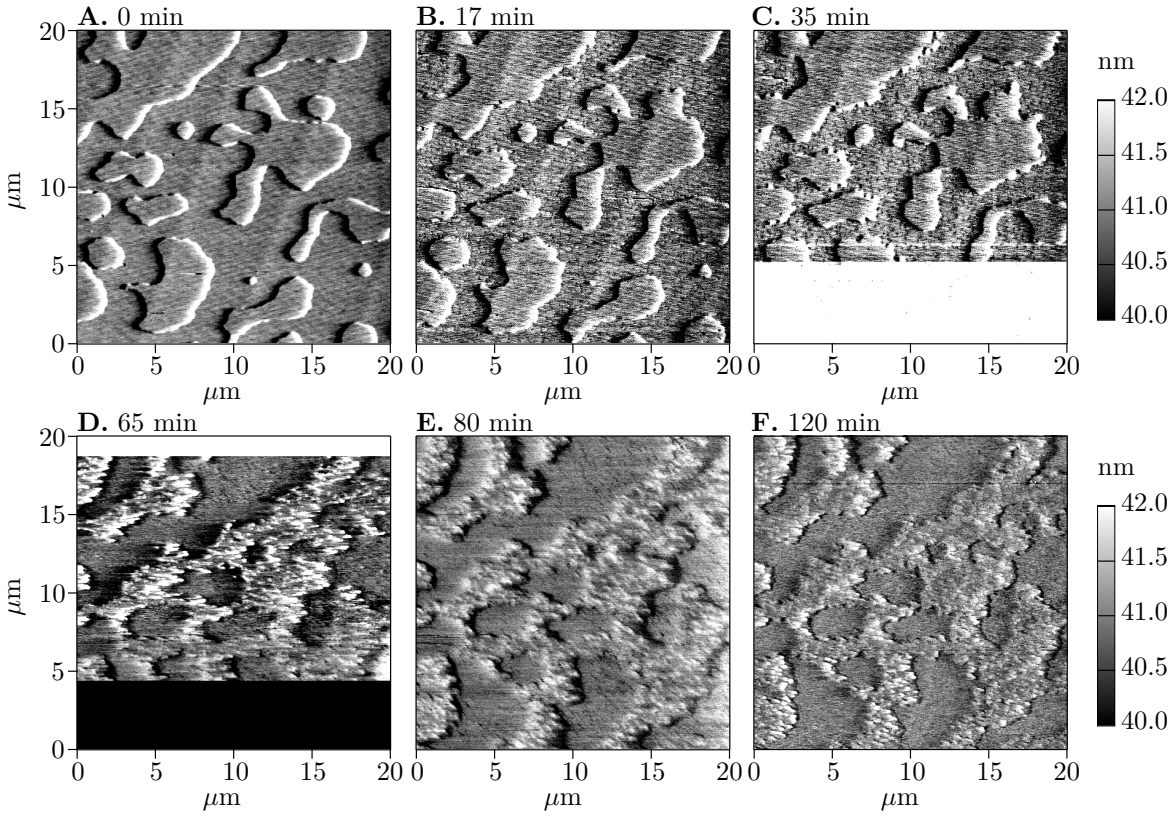

Figure 6.36 – AFM amplitude images of a DOPC/SM/Chol/PS bilayer in the course of the interaction with Ece1-III$_{KR(N)}$. The figure shows the amplitude error renditions of the height images in Fig. 6.35: **A.** Prior to, **B.** 17 min, **C.** 35 min, **D.** 65 min, **E.** 80 min and **F.** 120 min after the injection of Ece1-III$_{KR(N)}$. Though laterally shifted by about 5 μm, it can be seen that the initial domain shapes are largely maintained. The molar lipid mixture used for the film preparation was DOPC/SM/Chol/PS 2:2:1:1, the final peptide concentration was $\simeq$ 1 μM. The amplitude of the free oscillation was 10 nm. The images were obtained with a scanning rate of 1.0 Hz/line at room temperature.

DOPC domains, additional local deviations appear at the raft boundaries and the Chol-rich L_0 domains (Fig. 6.36 B). With increasing time, more and more of these aberrations emerge (Fig. 6.36 C, D), reflecting an increasing surface adhesiveness which requires the feedback loop to continuously adjust the tip-sample separation to maintain a constant amplitude. This can be the effect of a strong attraction between the cationic peptide and the anionic PS if this is present in the Chol-rich domains.

At short incubation time, the amplitude aberrations appear mostly at the domain boundary. Consequently, it is assumed that the peptide favours to insert into the bilayer at locations where irregularities of the lipid packing are present. The time-dependent increase in boundary curvature further represents a reduction of the line tension between the two lipid phases, which is consistent with the disturbance of the intermolecular packing. A similar effect has also been observed for several other surface active peptides as for instance Melittin, hence, it is supposed to be a

fundamental element of the membrane interaction [262]. As a consequence of the reduced interfacial line tension, the miscibility between the Chol-rich and Chol-poor domains is higher in the presence of the peptide. However, both domains do not melt into one continuous phase as the overall domain shapes are still preserved after 120 min.

This finding is also supported by the corresponding X-ray reflectivities shown in Fig. 6.37, where two families of Bragg peaks originating from two different thickness repetitions exist in the absence of Ece1-III$_{\mathrm{KR(N)}}$, but also in its presence. The d-spacing corresponding to the thicker Chol-rich domains is identical in both cases ($d = 2\pi/q_z \simeq 65$ Å), while the smaller repeat spacing ($d = 54.9$ Å) is reduced to $d = 51.9$ Å in the presence of the peptide. The peptide-induced bilayer thinning amounts to $\Delta d_{hh} = 2.2$ Å. Given the respective uncertainty of $\simeq 0.5$ Å, this thinning is consistent with the findings for pure DOPC multilayers (cf. Sec. 6.3.2). Consequently, the XRR data suggests that Ece1-III$_{\mathrm{KR(N)}}$ fluidises the DOPC do-

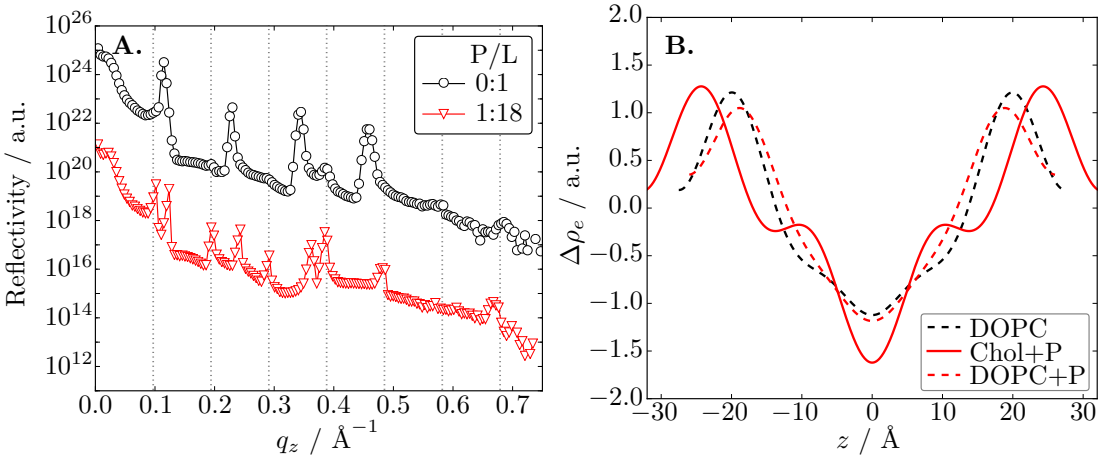

Figure 6.37 – XRR analysis of DOPC/SM/Chol/PS (9:9:2:2, n/n/n/n) multilayers without and with Ece1-III$_{\mathrm{KR(N)}}$ content. A. X-ray reflectivities obtained at 25°C. The reflectivities are plotted against q_z and shifted for clarity. Both XRR profiles show two families of Bragg peaks. The Bragg orders associated to the thicker Chol-rich domains are indicated by dotted lines. In case of the pure lipid stack (black), these were less intense than in the sample containing Ece1-III$_{\mathrm{KR(N)}}$ at P/L = 1:18 (red). The first order Bragg peak is fully superposed by the more intense Bragg peak of the thinner Chol-poor domain. Due to the accompanied lack of information, an electron density reconstruction of this domain was not possible. For the other domains, a Fourier synthesis using the phase combination −1, −1, +1, −1 was employed to obtain the relative electron density profiles $\Delta\rho_e(z)$ depicted in panel **B**. For this analysis, the Lorentz factor q_z^{-2} was applied to correct the specular intensities [141]. The relative electron density of the Chol-poor domains are tagged with "DOPC" (and "DOPC+P" in presence of the peptide) and plotted with dashed lines; the Chol-rich domain of the lipid/peptide sample is plotted with a solid line and tagged with "Chol+P". Again, the data corresponding to the pure lipid stack is depicted in black, the one corresponding to the sample containing Ece1-III$_{\mathrm{KR(N)}}$ is depicted in red.

mains. This conclusion is contrary to the AFM experiment, which on the one hand shows a 1.5 Å-shrinkage of the height difference and on the other hand implies a pronounced peptide interaction with the Chol-rich rafts. As already mentioned, the heights obtained by AFM in tapping mode can strongly depend on the forces between tip and sample which may explain the first deviation. The discrepancy of the preferred interaction domain may result from the different quantity ratios applied in both experiments. The excess amount of peptide compared to domain-forming agents in the multilamellar sample might leave enough peptide for a pronounced interaction with the Chol-poor DOPC domains.

Eventually, it shall be emphasised that none of both experiments does unambiguously evidence that Ece1-III$_{\mathrm{KR(N)}}$ interacts with only one of both phases. It is absolutely possible that it interacts with both domains simultaneously but with different outcomes: Its binding to the Chol-rich rafts may for example modify the attractive forces without affecting the raft thickness, whereas the binding to the Chol-poor domains might not influence the attraction potential but induce a pronounced thinning effect. In order to formulate firm conclusions on the distinct domain preference of the peptide, more extensive studies on varying lipid ratios are required. Here, it could be of advantage to utilise microscopic fluorescence techniques as these are capable to provide the information more straightforwardly than the indirect XRR and AFM experiments.

DOPC/SM/Chol Membranes

Phase separation similar to the one observed above also occurs in membranes composed of DOPC/SM/Chol. However, these liposomes of corresponding molar 2:2:1 mixtures were difficult to immobilise on the mica plate. The imaging of the bilayer and its domains was only successful in a few experiments which made it even harder to obtain meaningful images after the incubation with Ece1-III$_{\mathrm{KR(N)}}$. However, as the imaging quality was also dramatically impeded by a sudden onset of an extraordinarily high adhesiveness, the experiments support the conclusion that the peptide acts on the bilayer in a similar manner as is does in the presence of PS.

Additional XRR measurements were carried out using multilayer samples composed of this lipid mixture (Fig. 6.38). The reflectivity recording for the sample without peptide shows two distinct families of Bragg peaks. One has a characteristic repeat spacing of (61.6 ± 0.7) Å (SM- and Chol-rich domain) and the other one a smaller spacing of (56.2 ± 0.2) Å (DOPC domains). The sample with Ece1-III$_{\mathrm{KR(N)}}$ at P/L = 18:1, also shows a peak splitting, corresponding to repeat spacings of (60.7 ± 0.6) Å and (51.9 ± 0.4) Å. The larger spacing is identical to the Chol-rich region of the pure lipid stack. Thus, the smaller ones are identified with the DOPC-

domains. These are subjected to a peptide-induced thinning. Consequently, the XRR data implies that, again, the peptide interaction is dominated by a fluidisation of the DOPC-rich domains and does not lead to a complete lipid mixing.

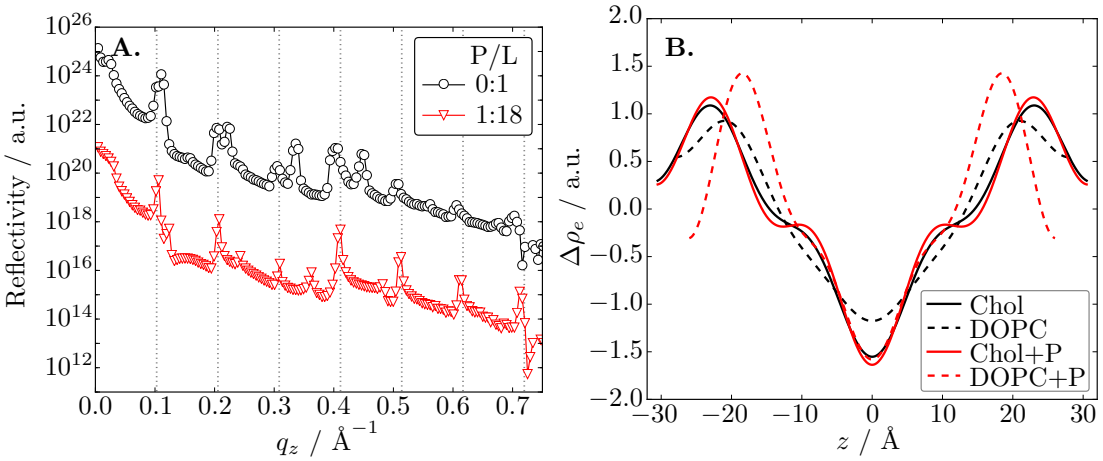

Figure 6.38 – XRR analysis of DOPC/SM/Chol (2:2:1, n/n/n) multilayers without and with Ece1-III$_{KR(N)}$ content. A. X-ray reflectivities obtained at 25°C. The reflectivities are plotted against q_z and shifted for clarity. Both XRR profiles show two families of Bragg peaks. The Bragg orders associated to the thicker Chol-rich domains are indicated with dotted lines. **B.** Relative electron density profiles $\Delta\rho_e(z)$ obtained from a Fourier synthesis with the phase combination −1, −1, +1, −1. For this analysis, the Lorentz factor q_z^{-2} was applied to correct the specular intensities [141]. The relative electron densities of the Chol-rich domains are tagged with "Chol" (or "Chol+P" in presence of the peptide) and plotted with solid lines. The electron densities of the Chol-poor domains are tagged with "DOPC" or "DOPC+P", respectively, and plotted with dashed lines. The data corresponding to the pure lipid stack is depicted in black, the one corresponding to the sample containing Ece1-III$_{KR(N)}$ at P/L = 1:18 is depicted in red.

6.3.5 Peptide-Induced Fusion

To further characterise the lipid-peptide interaction, a FRET fusion assay is employed, in which the fusogenic potential of the amphipathic peptides Ece1-III$_{KR(N)}$, Ece1-III$_{AA(N)}$ and Ece1-III$_{K(C)}$ is examined. To this end, the lipid mixing is monitored by following changes in the fluorescent yield of donor and acceptor dyes in liposome samples composed of either DOPC, DOPC/Chol, DOPC/Erg or DOPC/PS after the addition of each peptide.

P/L Dependence

In Fig. 6.39, the FRET signals detected upon the addition of Ece1-III$_{KR(N)}$ are shown as function of time and P/L. Initially only the liposome solution with the donor label was present. The liposome solution with the acceptor label was added and mixed after 50 s. This led to a dilution of the donor solution and an accompanied decrease

in the intensity signals in both the donor and the acceptor channel. Starting at 150 s, the peptide concentration was raised by four successive additions in intervals of 100 s. The DOPC, DOPC/Chol and DOPC/Erg samples did not entail any signal changes upon these additions, implying that the differently labelled liposome populations maintain stable. By contrast, the DOPC/PS sample clearly displays a prompt onset of the FRET effect after the first peptide addition which reveals the lipid mixing and therefore evidences the peptide-induced liposome fusion at P/L = 1:13.5. In consequence of the second peptide addition at 250 s, the FRET efficiency decreases again. This is attributed to peptide intercalations into the fused liposomes which dilute the lipid FRET pairs.

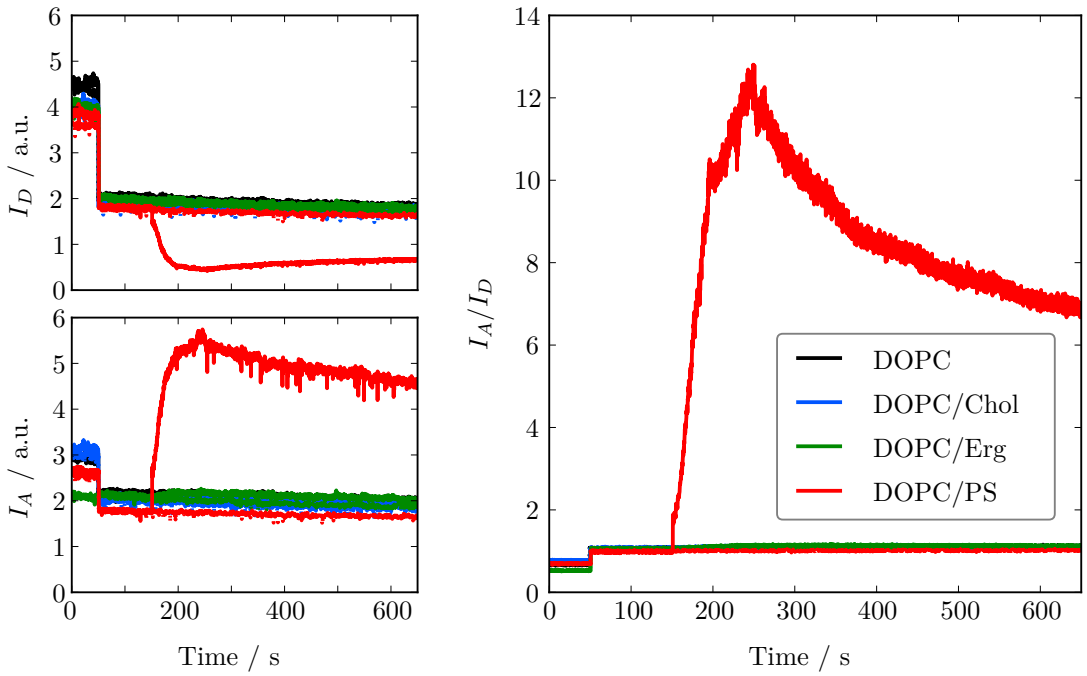

Figure 6.39 – Time dependence of a FRET fusion assay of Ece1-III$_{KR(N)}$. The fluorescence signals of liposome solutions with two differently labelled liposome populations are shown as function of peptide concentration and time. The raw signals of donor and acceptor intensity (I_D and I_A, resp.) are plotted on the left, the calculated ratios I_A/I_D on the right side. Initially, only the liposome solution with NBD-DHPE (donor) was present which was mixed with the Rho-labelled liposomes (acceptor) after 50 s. Starting from 150 s Ece1-III$_{KR(N)}$ (50 μl, 1 mg·ml^{-1} in H_2O) was added every 100 s in four successive steps. Accordingly, the peptide concentration was gradually increased from 0.74 μM (P/L = 1:13.5 $\approx$ 0.074) after the first injection to 3.65 μM (P/L = 1:2.7 $\approx$ 0.37) after the final injection. Liposome fusion is observed for DOPC/PS (red) but not for pure DOPC (black), DOPC/Chol (blue) and DOPC/Erg (green) samples. Lipid-lipid ratio was 9:1 (n/n). The H_2O-controls are plotted with semi-transparent dotted lines. However, they coincide with the DOPC, DOPC/Chol and DOPC/Erg measurements and are, thus, hardly visible. The assay was performed at 37°C.

Peptide Variants

The FRET signals observed after the addition of the variants Ece1-III$_{K(C)}$ and Ece1-III$_{AA(N)}$ are plotted in Fig. 6.40. Starting from 150 s, the peptide concentration was raised by four successive additions in intervals of 100 s. Similar to Ece1-III$_{KR(N)}$, additions of Ece1-III$_{K(C)}$ only induces the FRET effect and the corresponding fusion of liposomes composed of 90 % DOPC and 10 % PS. Its fusogenic activity is, however, reduced which is reflected by the smaller step-wise increase in I_A/I_D.

As the FRET signal for the DOPC/PS mixture increases strongly upon the addition of Ece1-III$_{AA(N)}$, this peptide also exhibits the potential to induce fusion in the presence of PS. The extent and the dynamics of this reaction are similar to the one triggered by Ece1-III$_{KR(N)}$ in liposomes of the same composition. Other than Ece1-III$_{KR(N)}$ and Ece1-III$_{K(C)}$, however, Ece1-III$_{AA(N)}$ also induces the fusion of DOPC, DOPC/Chol and DOPC/Erg liposomes, whereby the efficiency for the fusion of pure DOPC is the lowest.

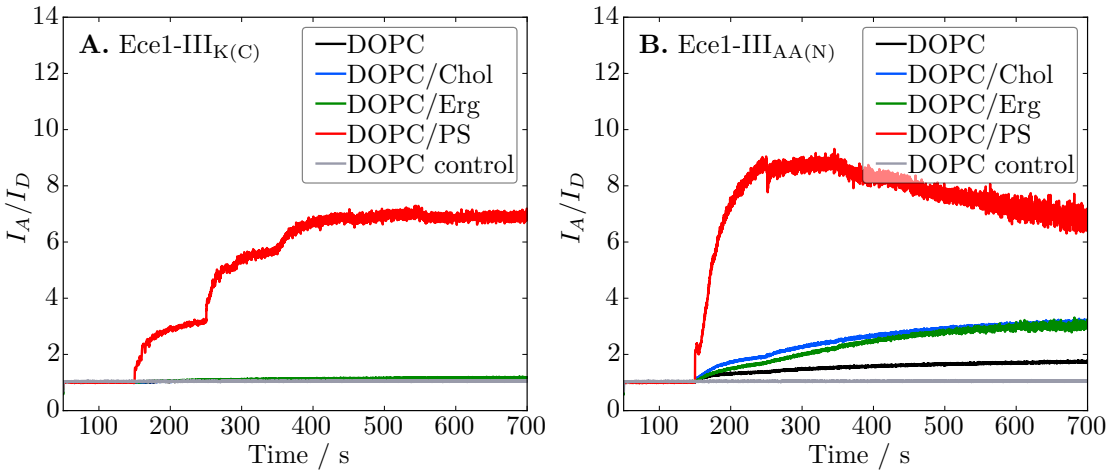

Figure 6.40 – Time dependence of a FRET fusion assay of Ece1-III peptide variants. A. Ece1-III$_{K(C)}$. **B.** Ece1-III$_{AA(N)}$. The figures plot I_A/I_D – i. e. the fluorescence intensity of the acceptor (Rho-DHPE) relative to the donor dye (NBD-DHPE) – upon the addition of the respective peptide. Starting from 150 s, 50 μl of the respective peptide (1 mg·ml^{-1} in H_2O) were titrated every 100 s. Accordingly, the peptide concentration was gradually increased from 0.74 μM (P/L = 1:13.5 $\approx$ 0.074) after the first injection to 3.65 μM (P/L = 1:2.7 $\approx$ 0.37) after the final injection. Ece1-III$_{K(C)}$ triggers liposome fusion only for DOPC/PS vesicles (red), whereas Ece1-III$_{AA(N)}$ also triggers such events in pure DOPC (black), DOPC/Chol (blue) and DOPC/Erg (green) samples. However, the FRET efficiency observed for the liposomes without PS is significantly reduced. The lowest efficiency is observed for the interaction with pure DOPC liposomes. In none of the H_2O-controls a FRET effect is observed. Therefore, only the respective control of DOPC is exemplarily shown in both figures. The measurements were carried out at 37°C and the lipid-to-lipid ratio was 9:1 (n/n).

6.3.6 Summary and Discussion of the Structural Changes

In the presence of Ece1-III$_{KR(N)}$, both erythrocytes (cf. Sec. 4.2) and solid-supported model membranes were found to undergo dramatic structural changes on micro- to nanometre scale. To get a deeper insight into the details of the structural rearrangements, different techniques were used to study the vertical and lateral alterations separately. By the help of AFM and XRR examinations on multilayer samples it was demonstrated that an increasing amount of peptide increases the vertical disorder in the lamellar lipid stacking.

Structural Changes along the Bilayer Normal With regard to the XRR analyses, the increased disorder is inferred from the pronounced flattening of the averaged electron density profiles which corresponds to the emergence of bilayer variations. Since the interaction is also found to be accompanied by a linear bilayer thinning in proportion to the P/L, it is suggested that the variations are caused by locally varying bilayer thicknesses. In other words, they are assumed to be undulations of static nature rather than dynamic fluctuations. The membrane thinning on the other hand, is attributed to the association of the peptide to the amphipathic interfacial region between the phospholipid headgroups and the fatty acyl chains: The shallow intercalation of a peptide expands the membrane area and entails the formation of a void beneath it. This void is in turn filled by the surrounding acyl chains and, thus, leads to local bilayer thinning. A similar linear thickness reduction was also reported for HDPs to which a pore formation according to the two-step model is assigned [253]. It has been described that this thinning represents a source of surface tension which above a threshold value overcomes the energy barrier to open lesions in the membrane. Beyond the thinning and the enhanced bilayer undulations, it is difficult to identify the direct influence of the peptide on the density profiles from the XRR data. Although the reflectivity of the solid supported bilayer suggests that the peptide associates predominantly to the interface and headgroup region, it cannot certainly be inferred where the peptides resides and which particular lipid components have to accommodate the penetration. In order to get a deeper insight into these aspects, neutron reflectivity could be employed as this technique enables isotopic substitution in order to highlight specific parts of the vertical membrane profile.

Structural Changes along the Bilayer Plane In the lateral bilayer direction, it has been observed that the lateral invariance was progressively perturbed with increasing peptide content as Ece1-III$_{KR(N)}$ promoted the formation of non-lamellar phase domains. The corresponding domain sizes decreased from several micrometers

in the pure lipid stacks to a few tens of nanometres at P/L = 1:18. The structural alterations were accompanied by two effects: (1) the fluidisation of the acyl chains, represented by the decreasing length of short-range correlations, and (2) the progressive tilting of the chains to fill the hydrophobic voids of the hexagonal lipid arrangement. The pronounced chain disorder is predominantly attributed to the formation of the non-lamellar phases and the involved chain tilts. Note, however, that the increased local chain fluidity due to the peptide-induced bilayer thinning may also contribute to this observation.

The diffraction patterns have revealed that the non-lamellar structures in the lipid/peptide system are dominated by a two-dimensional monoclinic lattice which resembles a distorted hexagonal phase H_d (or H_γ). With respect to the lipid orientation in this lattice, an inverted type II arrangement rather than a normal type I arrangement is suggested. Thus, similar to the inverted hexagonal H_{II} phase introduced in Sec. 1.3.4, this lipid phase consists of water-filled columns which are aligned parallel to the substrate surface. Although the data obtained here do indeed not allow the discrimination between both the normal and the inverted scenarios, the fact that the type II phase is in general stable under excess water conditions provides a reasonable justification for this conclusion [27]. It is additionally supported by the finding that DOPC/PS vesicles tend to fuse in presence of Ece1-III$_{\mathrm{KR(N)}}$ since this process also entails negative curvature which is characteristic for inverted non-lamellar phases. Moreover, for pure DOPC bilayers, the formation of the negatively curved rhombohedral phase has previously been reported to emerge upon partial dehydration and in combination with Chol, the regular (non-distorted) H_{II} state is observed [212]. Additionally, also PS has been found to impart negative curvature and to promote H_{II} structures [28, 263]. Yet, a distorted hexagonal lattice as it occurs here, is not frequently observed in lipid systems. A similar H_d phase has only been reported by the group of Huang for binary lipid mixtures of DOPC/DOPE or di18:0(9,10dibromo)PC/Chol close to the border between the rhombohedral and the inverted hexagonal phase [264–266]. They have proposed that this distorted hexagonal packing is the result of the demixing of both lipid components in order to achieve states of minimal energy by adjusting the local spontaneous curvature under stress. In both mixtures, the PC lipids were associated to the regions of lower curvature, whereas PS or Chol were found to accumulate in the regions of high curvature. In accordance with these findings, the group concluded that the H_d phase does not occur in lipid systems composed of only a single lipid component.

Adapted to the binary DOPC/Ece1-III$_{\mathrm{KR(N)}}$ system, it is suggested that the lipid-peptide interaction leads to two effects: (1) The lipid headgroups become dehydrated which provokes the formation of hexagonally packed lipid columns. (2) The direct

contact between lipid and peptide generates an even higher negative curvature which leads to the local demixing inside the columnar cross sections and therefore to the distortion of the H_{II} lattice. Aside from the lamellar L_α and the distorted hexagonal H_d and H_γ phases, a third coexisting phase has been identified in the lipid/peptide samples at high P/L, the rippled $P_{\beta'}$ phase, which is assumed to reflect some kind of additional intermediate structure. In addition, it shall be noted that the GID data do not reveal any direct scattering features from a molecular alignment of Ece1-III$_{\mathrm{KR(N)}}$ itself. Accordingly, the data implies that the membrane-associated Ece1-III$_{\mathrm{KR(N)}}$ does not assemble in characteristic oligomeric patterns such as defined barrel-stave or toroidal pores [267, 268].

The Effect of Curvature The detailed interplay between the coexisting lipid mesophases cannot be explained yet. However, regardless of the particular structural appearance, the emergence of the non-lamellar phases clearly signifies that the presence of Ece1-III$_{\mathrm{KR(N)}}$ enhances the lipid curvature. The real-time AFM measurements have additionally suggested, that this effect does not only include the curvature along the bilayer normal but also the curvature of lateral domain boundaries. The observations suggest that Ece1-III$_{\mathrm{KR(N)}}$ mediates a localised increase in positive membrane curvature stress (due to the thinning) that is eventually relieved by the formation of non-lamellar lipid structures of highly negative curvature, in which the acyl chains are splayed to fill the voids. Transferred to real biological systems, this peptide effect would probably entail the disintegration and disruption of a cell membrane. Interestingly, the effects are indicated to enhance with increasing temperature. This may be explained with the expanding interfacial area per lipid (reflected by the increasing average chain distance a), which accompanies the heating and probably promotes the peptide intercalation.

As mentioned before, membrane fusion also entails dramatic changes in bilayer curvature, involving intermediate fusion pores of highly negative curvature. A number of amphipathic peptides are known to induce such processes [96, 269]. Basically, the capability of peptide-induced fusion may be explained by two possible mechanisms: (1) The association of fusion peptides to the membranes directly bends the lipid leaflets which creates curved stalks that develop into fusion intermediates [97]. (2) The association of the peptides to the interfacial region of lipid bilayers primarily perturbs the bilayer by loosening the lipid packing and thereby unveiling the hydrophobic forces arising from the lipid core. In close proximity to a second membrane, this attractive force might alter the free energy balance and promote the formation of fusion pores [37].

The remaining question is why Ece1-III$_{\mathrm{KR(N)}}$ triggered the fusion only for liposomes in the presence of PS although the induction of the highly curved phase structures occurred in all lipid mixtures. An explanation for this is probably found in the inherent differences of both model membrane systems: The solid-supported samples are formed out of dehydrated peptide/lipid stacks which can directly act on hydration with the morphology favoured most. In the fusion experiments, Ece1-III$_{\mathrm{KR(N)}}$ is added to liposomes which are already in aqueous solution and the energetic costs for the formation of fusion pores may diverge for the different mixtures. Owing to electrostatic repulsions, DOPC/PS liposomes have very small radii compared to the zwitterionic mixtures (cf. Sec. 6.2.2). In consequence of the charge screening by the binding of the cationic peptide, the energetic contribution from the highly positive liposome curvature may overcome the energy barrier to form fusion pores. This change in free energy may trigger the fusion of the small liposomes to create larger ones with reduced line tension.

Effects of the Lipid Composition Aside from the fusion effects, no significant differences were observed with respect to the lipid compositions. All membranes have demonstrated that undulations are enhanced in the presence of Ece1-III$_{\mathrm{KR(N)}}$, indicating local thickness variations. In addition, in all mixtures, the L_α, H_d, H_γ and $P_{\beta\prime}$ phases were found to coexist. The observed variations in the unit cell parameters are rather attributed to the local inhomogeneities throughout the sample volume than to actual differences between the lipid systems. The hypothesis that ergosterol might have a membrane-stabilising effect could not be validated from the data. However, due to the obvious degradation of ergosterol to ergocalciferol, it remains obscure whether the intact sterol component might exert such a protective effect after all. The preferred interaction domain with respect to separated liquid-ordered and liquid-disordered phases also remains unclear. Despite the ambiguity of the data presented here, it is proposed that Ece1-III$_{\mathrm{KR(N)}}$ predominantly associates to the liquid-disordered phases. This assumption is also supported by the observed temperature effects. However, the favoured interaction phase remains a matter of speculation and needs to be verified by complementary experiments.

Effects of C-terminal Peptide Modifications Regarding the C-terminal modifications, it was observed that Ece1-III$_{\mathrm{K(C)}}$ has a reduced impact on both the bilayer thinning and the curvature induction. With respect to the solvent-free multilayer model system, this finding confirms that the reduced effects in terms of bilayer penetration and cytotoxicity are not only due to the formation of peptide aggregates in solution. Ece1-III$_{\mathrm{AA(N)}}$ on the other hand, was also found to induce only the

H_d phase which implies that its ability to induce lipid curvature is also reduced compared to Ece1-III$_{\mathrm{KR(N)}}$. However, it also led to a pronounced bilayer thinning and even more remarkable: It triggered the fusion of all liposome mixtures, even though the fusion efficiency in the absence of PS was clearly reduced. With respect to the possible initiation mechanisms for the fusion processes, it is proposed that Ece1-III$_{\mathrm{AA(N)}}$ rather destabilises the bilayers by a comparatively deep intercalation than by a direct induction of curvature. The deeper intercalation on the other hand may be facilitated by the increased hydrophobicity of this peptide variant.

6.4 Permeabilisation

This last section on the lipid-peptide interaction concentrates on the peptides' permeabilisation activity. First, the permeabilisation of DOPC tBLMs by Ece1-III$_{\mathrm{KR(N)}}$ is examined using impedance spectroscopy. This technique is also used to study the peptide's activity with respect to varying lipid composition and to screen general permeabilisation potentials of the amidated peptide variants. The non-amidated variants are studied likewise. Finally, the nature of the lesions induced by Ece1-III$_{\mathrm{KR(N)}}$ and Ece1-III$_{\mathrm{K(C)}}$ is characterised by means of electrophysiological measurements on free-standing DOPC bilayers.

6.4.1 Electrical Impedance of Tethered Bilayer Membranes

DOPC + Ece1-III$_{\mathrm{KR(N)}}$ in 0.01 % TFA

The conductance G_m of differently composed membranes was measured as function of increasing peptide concentration using the tethaPod$^{\mathrm{TM}}$ setup described in Sec. 3.3.1. The conductance change of DOPC membranes upon the addition of Ece1-III$_{\mathrm{KR(N)}}$ is shown in Fig. 6.41. In this figure, ΔG_m, obtained as mean of six independent measurements, is plotted against the peptide concentration (black data points). With increasing peptide concentration, a pronounced increase in ΔG_m is observed, clearly demonstrating that the peptide causes severe membrane defects. However, the particular conductance levels at different concentration stages varied significantly for the individual measurements, thus causing large errorbars. To discuss possible reasons for this observation, two individual examples which contributed to the averaged data set are also shown in the figure.

In one example, the increase in ΔG_m is already observed for the lowest peptide concentration probed, namely 0.5 μM (red data points), whereas in the second one, this increase is not observed until a concentration of 3.0 μM is reached (blue data points). On the one hand, the initial membrane quality obtained from the prepa-

ration may give rise to these deviations. This quality is reflected by the membrane capacitance C_m. This parameter is inverse proportional to the membrane thickness d and it varied strongly for both exemplary measurements. While the presumably thicker membrane with a capacitance of $C_m = 8.194$ nF showed an increased resistance against the peptide-induced permeabilisation, the thinner membrane with $C_m = 21.170$ nF was disrupted at notably lower concentration. Given the fact that the preparation with lower capacitance might arise from multiple membrane layers (or at least remaining secondary patches), its higher resistance can be explained with a surplus of lipid compared to the other preparation. However, this behaviour may also result from a sensitive membrane response to variations in the local peptide concentration. According to that, it is likely that in the second example, the peptide was equally distributed across the sampled volume up to a concentration of $\sim$ 3.0 μM. In the first example, by contrast, the local amount of peptide monomers or aggregates required to trigger the membrane rupture might have happened to appear at lower total peptide concentration. Such variations may result from local fluctuations but also from the physical handling of the syringe during the peptide addition since this process is not automated. Aside from the increase in membrane conductance, also the goodness of fit value increases as function of the peptide

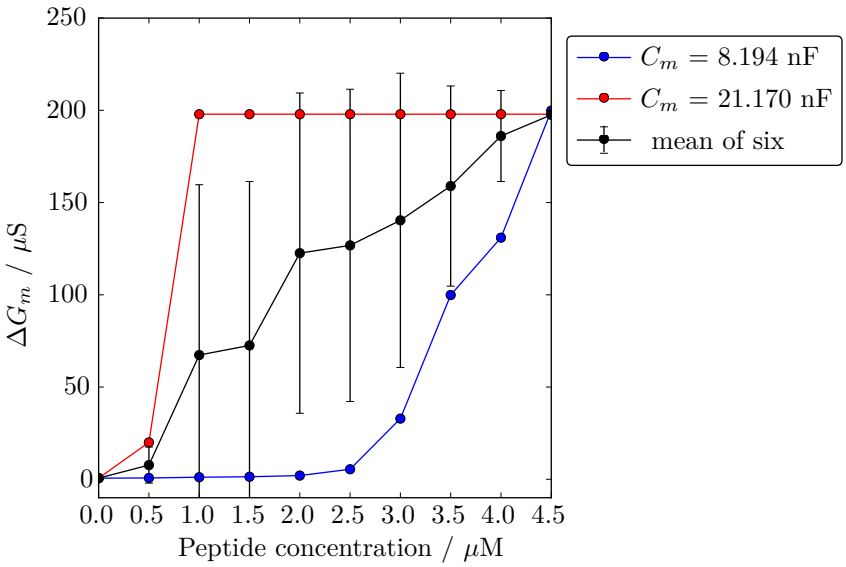

Figure 6.41 – DOPC conductance upon the addition of Ece1-III$_{\mathrm{KR(N)}}$. The change of membrane conductance with respect to the initial conductance (ΔG_m) is plotted as function of the peptide concentration. The figure shows the results from two tBLM preparations with different initial capacitance C_m and the mean of six independent measurements (●). The errorbars represent the standard deviations of the plotted means. Each data set was obtained from 9 subsequent additions of 5 μl peptide (10 μM dissolved in in 0.01 % TFA). The maximal membrane conductance detectable was 200 μS. The membrane with higher initial capacitance (●) is already disrupted at a peptide concentration of 1.0 μM, whereas the tBLM with low capacitance (●) breaks at a concentration of 4.5 μM.

concentration, indicating a reduction of the fit quality. As stated in Sec. 3.3.1, this is caused by the simplistic assumption of a homogeneous membrane featured with a single membrane conductance C_m. Deviations from this model thus suggest that the conductance arises from multiple sites distributed across the tBLM. This may either originate from the formation of peptide pores or a patchy loss of the membrane integrity [143]. Regardless of the specific nature of the lesions, these results clearly demonstrate that the peptide causes severe membrane defects in a concentration-dependent manner. This permeabilisation process takes place in a narrow concentration range between 0.5 and 4.0 μM and it is highly cooperative as the membrane breakdown occurs shortly after initial lesions emerged.

Varying Lipid Composition + Ece1-III$_{\mathrm{KR(N)}}$ in 0.01 % TFA

As shown in Fig. 6.42 A, the potential of Ece1-III$_{\mathrm{KR(N)}}$ to induce membrane permeabilisation was not significantly impeded by neither of the lipid components (cholesterol, ergosterol or PS) added at a 10 % proportion to DOPC (n/n). On average, the maximal measurable value of $G_m = 200$ μS was reached at a peptide concentration of 2.5 μM.

DOPC + peptide variants in 0.01 % TFA

The impedance assay depicted in Fig. 6.42 B implies a pronounced permeabilsation activity of Ece1-III$_{\mathrm{AA(N)}}$. Its extent is comparable to the one induced by Ece1-III$_{\mathrm{KR(N)}}$. By contrast, Ece1-III$_{\mathrm{K(C)}}$ did only slightly affect the membrane conductance in the probed concentration range. This unexpected result might be explained by the formation of large peptide clusters in the buffer phase which impede the integration of monomers into the membrane and therefore reduce the permeabilisation. Such a clustering behaviour has been found to be a general problem with this peptide variant.

Varying Lipid Composition + Ece1-III$_{\mathrm{KR(C)}}$ in H_2O/40 % DMSO

The changes in membrane conductance induced by the non-amidated variant Ece1-III$_{\mathrm{KR(C)}}$ in tBLMs of varied lipid composition are shown in Fig. 6.43 A. All of which lead to an increase in membrane conductance. Thus, the results demonstrate the peptide's concentration-dependent permeabilisation activity and again, none of the added lipid components (cholesterol, ergosterol or PS) was able to reduce this effect.

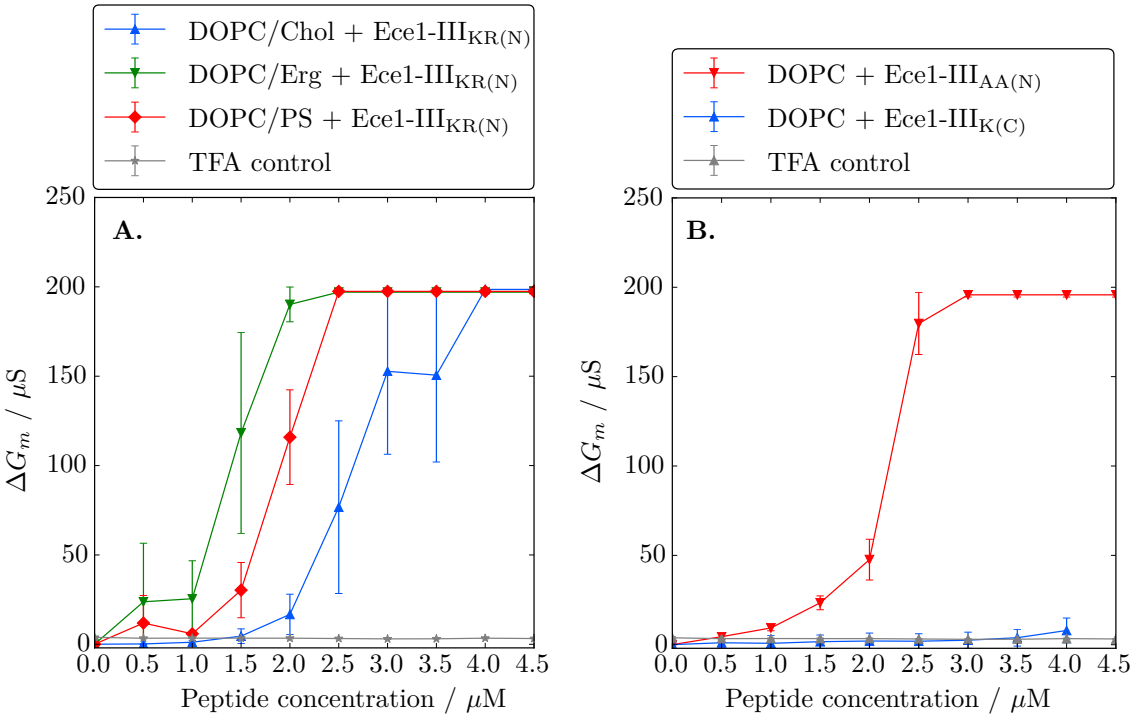

Figure 6.42 – tBLM conductance upon the addition of Ece1-III peptides. The change of membrane conductance with respect to the initial conductance (ΔG_m) is depicted as function of the peptide concentration. **A.** ΔG_m of differently composed tBLMs increases upon the addition of Ece1-III$_{KR(N)}$. Only minor variations in the concentration response are observable for the DOPC/Erg (▼), DOPC/PS (♦) and DOPC/Chol (▲) mixtures (each at a molar ratio of 9:1, n/n). **B.** ΔG_m of DOPC tBLMs as function of Ece1-III$_{AA(N)}$ (▼) and Ece1-III$_{K(C)}$ (▲) concentration. All results were obtained from 9 subsequent additions of 5 μl peptide (10 μM dissolved in 0.01 % TFA). While the concentration-dependent disruption by Ece1-III$_{AA(N)}$ occurred similar to the one induced by Ece1-III$_{KR(N)}$, Ece1-III$_{K(C)}$ did not induce significant increases in ΔG_m (probably due to low solubility, see text). The errorbars represent the standard deviations of the plotted means from duplicate or triplicate measurements. Corresponding additions of 0.01 % TFA served as negative control (★) and did not entail any changes in ΔG_m. The maximal membrane conductance detectable was 200 μS.

DOPC + non-amidated peptide variants in H_2O/40 % DMSO

Fig. 6.43 B depicts the averaged conductance of DOPC tBLMs obtained after the addition of the non-amidated peptide variants Ece1-III$_{KR(C)}$, Ece1-III$_{K(C)}$, Ece1-III$_{A(C)}$ and Ece1-III$_{AA(C)}$, each solved in H_2O/40 % DMSO (v/v). Ece1-III$_{KR(C)}$ causes a strong increase in ΔG_m, similar to its amidated equivalent. The same is true for the non-amidated Ece1-III$_{AA(C)}$ which again showed a pronounced permeabilisation of the tethered DOPC membranes. Compared to these peptide variants, the non-amidated Ece1-III$_{K(C)}$ exhibited a reduced activity which is, however, remarkably stronger than its effect if solved in 0.01 % TFA (see above). The lowest impact on ΔG_m is observed for Ece1-III$_{A(C)}$ which only causes a maximal increase

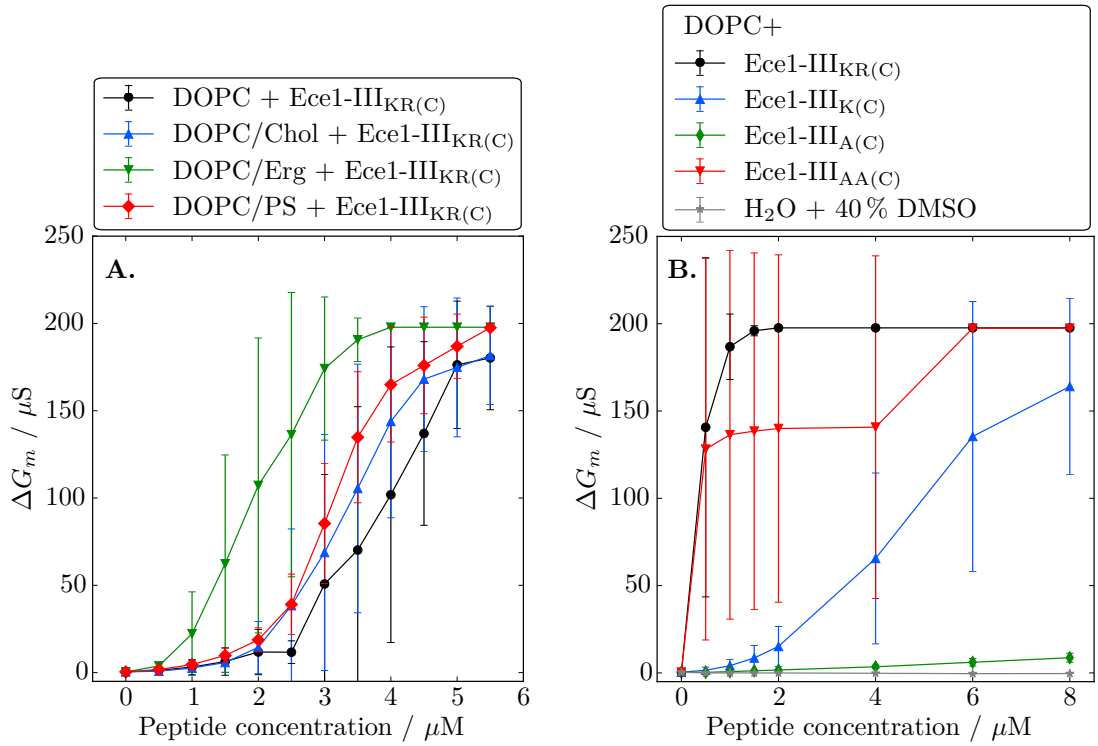

Figure 6.43 – tBLM conductance upon the addition of non-amidated Ece1-III peptides. The change of membrane conductance with respect to the initial conductance (ΔG_m) is shown as function of the peptide concentration. The errorbars represent the standard deviations of the plotted means from triplicate measurements. **A.** ΔG_m of differently composed tBLMs increases upon the addition of Ece1-III$_{KR(C)}$. The figure represents the results from 11 subsequent additions of 5 μl peptide (10 μM dissolved in H_2O + 40 % DMSO). On average, the conductance response is similar in all mixtures probed, i. e. in DOPC (●), DOPC/Chol (▲), DOPC/Erg (▼) and DOPC/PS (♦) at respective lipid-lipid ratios of 9:1 (n/n). **B.** ΔG_m of DOPC tBLMs as function of different Ece1-III peptide variants. The results were obtained from four subsequent additions of 5 μl of a 10 μM peptide solution and three following additions of 5 μl 40 μM-solution. The permeabilisation potential of Ece1-III$_{K(C)}$ (▲) was lower than that observed for the variants Ece1-III$_{KR(C)}$ (●) and Ece1-III$_{AA(C)}$ (▼). By far the lowest permeabilisation potential was observed for Ece1-III$_{A(C)}$ (♦). Again the peptides were dissolved in H_2O + 40 % DMSO (v/v). In addition, the figure contains a negative control with a corresponding titration of H_2O + 40 % DMSO (★) which did not entail any changes in ΔG_m. The maximal membrane conductance detectable was 200 μS.

of $\Delta G_m = (12.0 \pm 2.6)$ μS at 8 μM, the maximum peptide concentration probed in this assay.

6.4.2 Electrophysiological Studies on Free-standing Membranes

Current traces across bilayer membranes were recorded in order to qualitatively evaluate the characteristic nature of the peptide-induced membrane defects evidenced in the previous section. Two representative examples of these recordings are shown in Fig. 6.44. These examples illustrate the current response of solvent-free bilayer

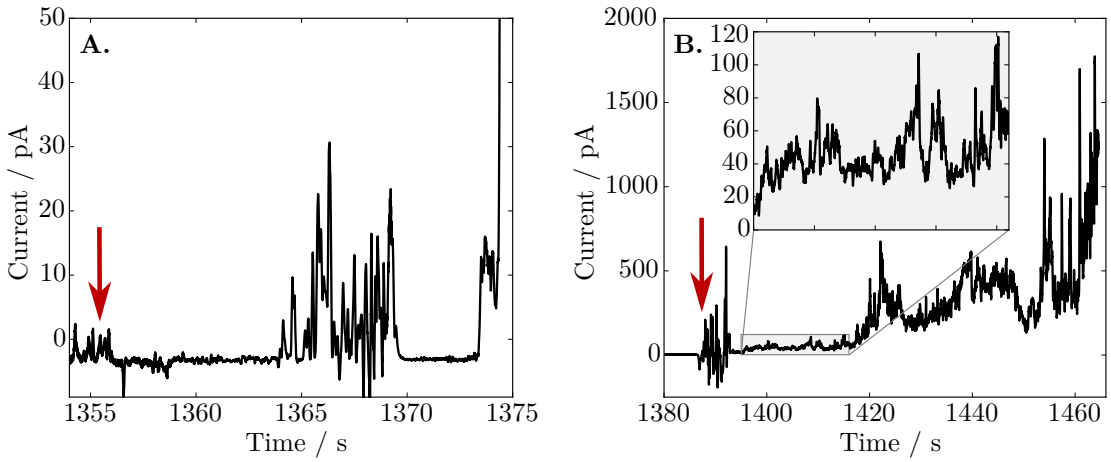

Figure 6.44 – Peptide-induced current fluctuations across a free-standing DOPC membrane. The red arrows indicate the addition of **A.** Ece1-III$_{KR(N)}$ and **B.** Ece1-III$_{K(C)}$. Both peptides induced current fluctuations immediately after this injection and finally entailed the rupture of the membrane. The inset in panel B magnifys the indicated current section. Ece1-III$_{KR(N)}$ and Ece1-III$_{K(C)}$ concentrations were 0.25 μM and 0.4 μM, respectively. For both measurements, a constant voltage of 50 mV was applied and the temperature was set to 37°C.

membranes consisting of DOPC to the addition of Ece1-III$_{KR(N)}$ and Ece1-III$_{K(C)}$, respectively.

Shortly after the injection of Ece1-III$_{KR(N)}$, small current fluctuations, exceeding the noise level of 2 pA, appear, before the membrane ruptures after a short life time of about 20 s. These permeability fluctuations demonstrate a transient disturbance of the membrane integrity. Due to their heterogeneity, the fluctuations additionally imply that they do not derive from stable or metastable pores. Thus, it can be concluded that the peptide induces transient, heterogeneous lesions which readily lead to the collapse of the membrane. This permeabilisation by Ece1-III$_{KR(N)}$ was found to take place at notably low concentration, as similar results were also obtained at concentrations as low as 0.125 μM. This observation again emphasises the extremely high membrane-affinity of Ece1-III$_{KR(N)}$.

The data obtained for Ece1-III$_{K(C)}$ also shows heterogeneous and transient lesions which finally led to the collapse of the membrane. However, here the mean current across the membrane was greater than the one observed for Ece1-III$_{KR(N)}$. In addition, the concentration required to induce these lesions was 0.4 μM and therefore a little higher than that for its longer, amidated analogue.

6.4.3 Discussion of the Permeabilisation Activity

The experiments presented in this section, clearly demonstrate the pronounced permeabilisation effect of both amidation isoforms of Ece1-III$_{KR}$, consistent with their

high cytotoxic activity towards erythrocytes. The permeabilisation proceeds in a concentration-dependent manner and the induced lesions are transient openings, which presumably also enable the translocation of peptides between two bilayer leaflets. The formation of defined membrane pores according to the barrel-stave or the toroidal model can be excluded. Consequently, a carpet-like mechanism is suggested, which leads to localised destabilisations of the lipid packing and results in randomly distributed defects. The results further imply that none of the probed lipid components, shows an increased resistance against the peptide-induced perturbations.

With respect to variations of the C-terminal amino acid sequences, however, substantial differences were observed. Ece1-III$_{\mathrm{AA}}$, whose C-terminal hydrophobicity is increased, also demonstrated a pronounced ability to induce lesions, independent on its amidation state. This is consistent with the peptides' high haemolytic activity found in this work. However, it is in sharp contrast to the findings presented in [1]. In this publication, both an equivalent impedance spectroscopy experiment and a calcium-influx assay have evidenced that Ece1-III$_{\mathrm{AA(C)}}$ is notably less effective in terms of permeabilisation than Ece1-III$_{\mathrm{KR(C)}}$. The considerable discrepancy to the present observations, cannot be explained without further experimental examinations with due regard to external conditions such as the applied solvent.

The membrane activity of the shorter Ece1-III$_{\mathrm{K(C)}}$ variant is approximately halved with respect to that of its longer peptide version Ece1-III$_{\mathrm{KR(C)}}$, consistent with the findings from the haemolytic assay. However, this only applies if H_2O/40 % DMSO is used as solvent. Exposed to 0.01 % TFA, almost no increase in membrane conductance could be detected, implying that its permeabilisation behaviour depends sensitively on the experimental conditions. In this particular case, the results are most likely biased by the peptide's reduced solubility in the highly acidic solvent.

Similar to the activity differences between Ece1-III$_{\mathrm{KR}}$ and Ece1-III$_{\mathrm{K}}$, also the shorter variant of Ece1-III$_{\mathrm{AA}}$, Ece1-III$_{\mathrm{A}}$, exhibited a reduced permeabilisation potential. Indeed, this variant was hardly capable to induce membrane lesions. This observation compares well with the haemolytic assay, in which Ece1-III$_{\mathrm{A}}$ was also found to be the least active of the probed Ece1-III versions.

7 Summary and Future Prospects

The aim of this thesis was to characterise the interaction between the recently identified fungal Ece1-III toxins (or Candidalysines) and lipid membranes. Firstly, the peptide properties were examined using a combination of theoretical and experimental approaches. Following this, different aspects of the lipid-peptide interaction were studied employing model membranes and a variety of biophysical techniques. From these individual aspects, a principal mode of action is derived which is described in this final chapter. Additionally, the influence of the particular type of the lipid component and the C-terminal amino acid sequence are briefly reviewed. Finally, a strategy on how to assess the yet missing aspects of the derived model is outlined.

7.1 The Interaction Model

The results obtained throughout this work imply that the membrane degradation induced by the Candidalysines Ece1-III$_{KR}$ and Ece1-III$_{K}$ basically proceeds in four consecutive steps. Fig. 7.1 illustrates the individual stages of this interaction mechanism and the different techniques employed to obtain the respective snapshots. The foundation for this model is defined by the structural properties of the peptides, namely their amphiphilic α-helical secondary structures. This characteristic essential enables Ece1-III$_{KR}$ and Ece1-III$_{K}$ to directly interact with lipid bilayers. The influence of charge does not significantly contribute to the interaction which could be demonstrated by means of C-terminal modified peptides with reduced cationicity. As a consequence, Ece1-III$_{KR}$ and Ece1-III$_{K}$ have the remarkable virtue to interact with both, anionic and zwitterionic lipids.

It is suggested that the basic membrane interaction for each Candidalysine proceeds as follows: In the presence of a lipid membrane, the peptide binds to the bilayer (step 1) and subsequently partitions its hydrophobic side partly into the bilayer core (step 2) without significantly changing its own α-helical conformation. In the initial binding state, the peptide accumulates parallel at the bilayer surface, but as soon as a critical concentration P/L > 1:100 is reached, it starts to penetrate the bilayer in an oblique alignment. In this T-state orientation, the peptide perturbs the lipid packing near the hydrophobic/hydrophilic interface and causes structural

deformations of the bilayer (thinning and negative curvature, step 3). Thereby, the bilayer is destabilised which in turn leads to conditions that promote local collapses by the formation of time-dependent lesions (step 4). Consequently, the carpet-like disintegration of the bilayer structure is induced which leads to the the disruption of the entire membrane.

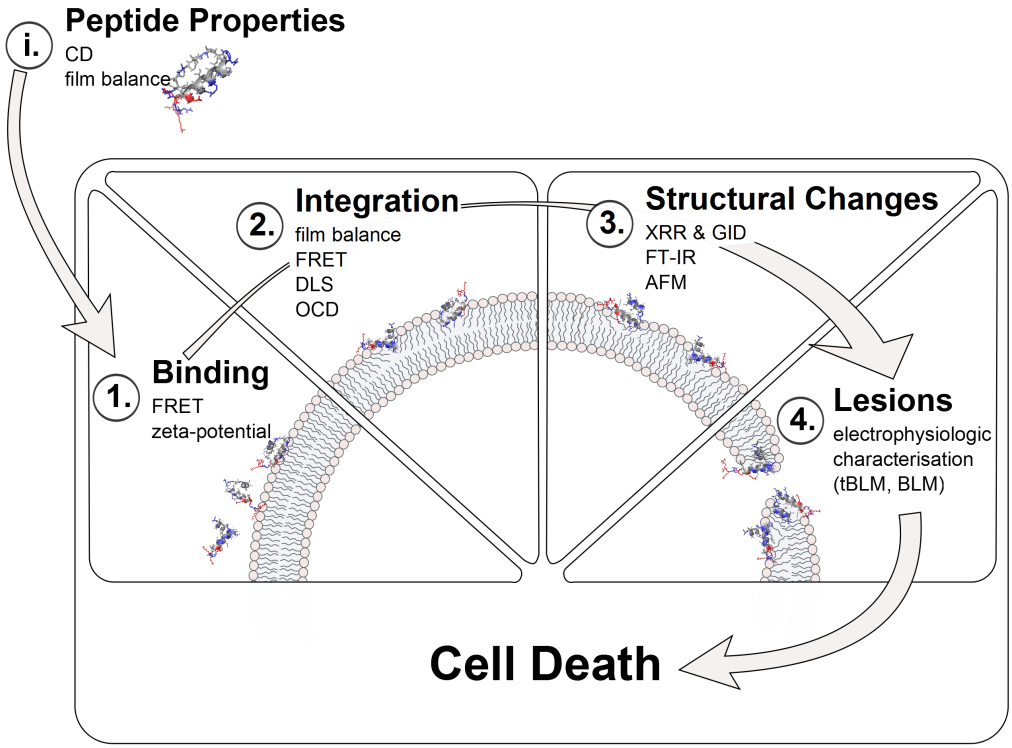

Figure 7.1 – Interaction between Candidalysines and lipid membranes. The figure illustrates the interaction stages of the Candidalysines with lipid membranes as they are proposed in the thesis. It also lists the individual techniques used to study each of these stages. As the cytotoxicity of the peptides is supposed to specifically depend on their structural properties, this aspect is illustrated as initial precondition. Aside from the experimental approaches, namely CD and film balance experiments, also theoretical aspects of the peptide's secondary structure and hydrophobicity were considered. The interaction is then proposed to be initialised by the peptide binding to the lipid surface, which was studied utilising the FRET effect and the zeta potential of liposomes. Subsequent to the binding, the peptide intercalates into the lipid matrix. This membrane penetration was studied using FRET and film balance experiments as well as dynamic light scattering and OCD. In response to the peptide adhesion and intercalation, the structural membrane constitution alters. The structural changes were studied using X-ray reflectivity, grazing incidence diffraction, AFM imaging and FT-IR spectroscopy. Although not listed, also the fusogenic peptide properties, studied with FRET, contributed to the conclusions at this stage. The structural changes then lead to the destabilisation of the membrane integrity and thus provoke the formation of defects, which were evidenced by electrophysiologic techniques. The lesions arising from these defects eventually lead to the collapse of the entire membrane. In a biological system, this is reflected by the death of the cell.

7.2 Lipid composition

Aside from pure DOPC membranes, membranes with a 10 % proportion of cholesterol or ergosterol were employed to identify possible selectivity mechanisms. In addition to these zwitterionic membranes, also mixtures of DOPC with 10 % of the anionic PS were employed to study the influence of electrostatic interactions. The latter membrane composition indicated to promote the binding of the cationic Ece1-III_{KR}. However, a consequent enhancement of the permeabilisation activity could not be recognised. Similar observation were made for the sterol-containing membranes: Both demonstrated that the penetration potential of Ece1-III_{KR} is reduced (which was attributed to steric hindrances), but again, no significant differences were observable with respect to structural bilayer changes or the bilayers' resistance against the induction of lesions. According to that, the working hypothesis that the fungal sterol ergosterol might be responsible for the self-protection of *C. albicans* could not be verified. However, this result may be biased by a possible degradation of ergosterol to ergocalciferol, evidenced in the X-ray measurements. It also remains uncertain if this conversion reaction was induced by the X-ray or the ambient light, so that ergosterol might have stayed intact throughout the other experiments. To clarify the uncertainty around the intactness of the ergosterol component, mass spectroscopy may be employed as this technique is capable to probe the true sample composition.

The absence of the expected differences in the resistance against permeabilisation may also have several other explanations. First of all, the effects may be of rather small influence and the techniques used to study them are probably not suited to resolve such small differences. Secondly, the proportion of the sterols employed here was comparatively low with regard to their relative occurrence in biological membranes (cf. Fig. 1.5). A third explanation may be found in the sterols' effect on the structural membrane properties – while cholesterol is well-known to stiffen membranes consisting of at least one saturated hydrocarbon chain (e. g. POPC or DMPC), it does not stiffen membranes of di-unsaturated hydrocarbon chains such as DOPC [252]. In other word, the absence of the stiffening effect may also entail the absence of resistance effects. After all, it may also be possible that there are no such differences in resistance. For now, however, the inhibiting co-factors and therefore also the mediators of the cell selectivity can not be identified.

Additionally, it shall be noted that the Candidalysines might exhibit a different permeabilisation mode in other lipid systems than the ones probed in this thesis. This has for example been observed for the peptides PGLa and magainin II. For both peptides, a carpet-like mechanism was suggested in the presence of PS as acidic

lipid component but the presence of phosphatidylglycerol led to the formation of toroidal pores [270]. Which kind of interaction occurs depends sensitively on the lipid curvature. For the formation of stable toroidal pores, positive curvature is required as the lipids have to bend around the bilayer normal. The lipid components employed throughout this work rather tend to exhibit negative curvature, which might prohibit this pore mechanism.

7.3 C-terminal Modifications

7.3.1 Peptide Length and Amino Acid Composition

The interaction model proposed here is valid for the Candidalysines Ece1-III$_{\mathrm{K}}$ and Ece1-III$_{\mathrm{KR}}$. However, both show notable differences in terms of their membrane activity. In order to identify relations between the molecular structure of the peptides and their toxicity, particular modifications of the peptide structure were examined. The results obtained in this thesis indicate that the C-terminal amino acid motif is of crucial importance to the peptide's mode of action. However, the precise details of the structure-activity relationship are still unclear. The ultimate membrane activity appears to be a matter of length rather than of hydrophobicity or charge, since both Ece1-III$_{\mathrm{KR}}$, with its polar cationic KR motif, and Ece1-III$_{\mathrm{AA}}$, with its neutral hydrophobic AA motif, were found to induce severe membrane defects. By contrast, the toxicities of the shorter variants Ece1-III$_{\mathrm{K}}$ and Ece1-III$_{\mathrm{A}}$ were notably reduced. This observation indicates that the peptides exhibit differences with respect to penetration depth and accompanied inclination angle.

The proposed disruption mechanism explains that the peptide-induced bilayer destabilisation results from perturbations at the interfacial region between the headgroups and the acyl chains. With regard to this mechanism, a deep penetration with a concomitant large tilt angle would less strongly disturb the lipid packing than a superficial penetration with shallower peptide inclination. This is in accordance with the proposed snorkelling mechanism for Ece1-III$_{\mathrm{K}}$ and Ece1-III$_{\mathrm{KR}}$ – the latter may anchor both its K and R residues inside the hydrophobic lipid core while snorkelling its charged side chains towards the headgroups. The shorter peptide, by contrast, has only one single K residue which could fulfil this task. Consequently, the effective area perturbed at the headgroup interface is assumed to be smaller for Ece1-III$_{\mathrm{K}}$ and the efficiency of the anchoring effect is probably reduced, which is indicated by its more pronounced tilt into the membrane core (cf. Sec. 6.2.4). It is further speculated that the interface perturbation entails a stronger degree of lipid bilayer curvature. This is also consistent with the observed differences between Ece1-III$_{\mathrm{KR}}$

and Ece1-III$_{\mathrm{K}}$, whose structural impact on multilayer membranes is reduced. The same applies for Ece1-III$_{\mathrm{AA}}$. This peptide variant is assumed to partition its hydrophobic AA residues inside the bilayer. Yet, it has no polar side chains which could snorkel towards the headgroups and additionally perturb the interface. Apart from Ece1-III$_{\mathrm{AA}}$'s reduced structural impact on solid-supported multilayer membranes, three aspects are found which still indicate a pronounced disruption of the lipid interface: (1) It demonstrated a permeabilisation activity comparable to the one observed for Ece1-III$_{\mathrm{KR}}$. (2) It proved a pronounced capability to induce states of high lipid curvature, as it triggered fusion processes even in the zwitterionic membranes. (3) Its T-state inside the membrane was found to be similar to the one of Ece1-III$_{\mathrm{KR}}$ and thus also implies an oblique orientation.

What stands out with respect to the structure-activity relationship of the different peptide variants is the behaviour of Ece1-III$_{\mathrm{A}}$: It exhibits a high intercalation potential but yet an extremely low permeabilisation activity. This finding clearly demonstrates the absence of a direct penetration-permeabilisation relationship. In other words, the peptide integration into lipid bilayers does not necessarily lead to its disintegration.

Eventually, the data implies that the peptides' membrane activity depends sensitively on its C-terminal motif. However, the details of this dependence remain uncertain since they are not simply explained by means of hydrophobicity or charge. To resolve this point, complementary experimental studies on the peptide structures and their location inside the bilayer matrix are required.

7.3.2 Amidation State

To further complete the picture of the interaction mechanism, the influence of the C-terminal amidation state was investigated. The comparison of both the amidated and the non-amidated isoforms of Ece1-III$_{\mathrm{KR}}$ revealed no distinct difference in their permeabilisation efficiency, although the membrane association of the amidated Ece1-III$_{\mathrm{KR(N)}}$ was notably increased. This is in accordance with the speculations discussed in Sec. 5.1.4. The same applies for both isoforms of Ece1-III$_{\mathrm{AA}}$. Here, the amidation of Ece1-III$_{\mathrm{AA(N)}}$ also increased its membrane association notably compared to its non-amidated isoform Ece1-III$_{\mathrm{AA(C)}}$. However, their efficiencies with respect to induce membrane lesions were comparable. Finally, it may be concluded that the absence of a C-terminal amidation may alter a peptide's properties with respect to solubility and membrane penetration without significantly affecting the final disruption mechanism.

7.4 Outlook

The thesis provides a comprehensive outline on the basics of the peptide mechanism. In search of factors which mediate cell-selectivity or inhibit the membrane interaction, further details on the particular interaction stages will be necessary. On the one hand, more extensive studies on the lipid composition are required, including further variations of the lipid compositions, such as differing lipid-to-lipid ratios or systematic investigations on the influence of headgroup size or acyl chain length (or saturation). On the other hand, the influences of the buffer system and the peptide solvents should be investigated systematically, since the results of this work suggest that salt concentration and pH strongly impact the peptide's membrane activity. A systematic analysis on the external parameters is also necessary to unravel the discrepancy between the high cytolytic acitivity of Ece1-III$_{\mathrm{AA}}$ observed in this thesis and its previously reported lower activity [1]. This can for instance be achieved by means of electrophysiologic studies using the planar bilayer setup. It is also of interest to study the increase in membrane permeabilisation induced by Ece1-III$_{\mathrm{A}}$ in this setup. These measurements might reflect the permeabilisation in slowed motion, as this peptide was found to be less active than the other variants probed.

To identify further details of the binding process, tethered bilayers can be studied by means of surface acoustic waves. Using this technique the binding to the membrane and the assumed concomitant fluidisation of the acyl chains can be verified at the same time. In addition, isothermal titration calorimetry can be applied to give information on the binding stoichiometry.

Microscopic fluorescence studies employing designated GUV preparations may further be used to reveal whether the Candidalysines favour the binding to Chol-rich or Chol-poor domains. Similar studies may also be used to examine the liposome fusion in greater detail. For a better understanding of the intermediate steps between binding, surface accumulation, intercalation and reorientation of the α-helical axis, more extensive OCD studies can be correlated to equivalent investigations on the intercalation behaviour using for example FRET assays. Even more details with respect to peptide intercalation and alignment may be revealed by other techniques such as solid-state NMR, infra-red reflection-absorption spectroscopy or neutron reflectometry. It is further suggested that molecular dynamic simulations have the potential to provide insights into all single interaction steps, especially on the mechanism which finally evokes the lesion formation.

Moreover, it might be of interest to study also the other peptide fragments of the parent protein Ece1p and possible synergism effects between them. In addition, investigations on the interaction with bacteria are of high interest. Such studies are

assumed to have the potential to reveal new insights into the immune regulation by enlightening competitive mechanisms between *C. albicans* and colocalised bacterial members of the human microbiota [7].

Due to their high haemolytic activity, both Candidalysines, Ece1-III$_{\mathrm{KR(C)}}$ and Ece1-III$_{\mathrm{K(C)}}$, have no potential for pharmaceutical applications. However, appropriate amino acid substitutions may result in peptides with diminished cytotoxic activity but conserved antibacterial or anticancer activity. In order to act as next-generation therapeutics, the interaction forces driven by hydrophobicity have to be decreased, while the interactions due to electrostatic attractions need to be improved, since usually both the cell envelopes of bacteria and the outer cell leaflet of tumour cells express a high density of negative surface charges.

Bibliography

[1] D. L. Moyes, D. Wilson, J. P. Richardson, S. Mogavero, S. X. Tang, J. Wernecke, S. Höfs, R. L. Gratacap, J. Robbins, M. Runglall, C. Murciano, M. Blagojevic, S. Thavaraj, T. M. Förster, B. Hebecker, L. Kasper, G. Vizcay, S. I. Iancu, N. Kichik, A. Häder, O. Kurzai, T. Luo, T. Krüger, O. Kniemeyer, E. Cota, O. Bader, R. T. Wheeler, T. Gutsmann, B. Hube, and J. R. Naglik. "Candidalysin is a fungal peptide toxin critical for mucosal infection". *Nature* 532.7597 (2016), pp. 64–68.

[2] D. L. Nelson and M. M. Cox, eds. *Lehninger Principles of Biochemistry*. 4th ed. W. H. Freeman & Company, 2004.

[3] J. M. Conlon, M. Mechkarska, M. L. Lukic, and P. R. Flatt. "Potential therapeutic applications of multifunctional host-defense peptides from frog skin as anti-cancer, anti-viral, immunomodulatory, and anti-diabetic agents". *Peptides* 57 (2014), pp. 67–77.

[4] J.-l. Vincent, J. Marshall, A. Anzueto, C. D. Martin, and C. Gomersall. "International Study of the Prevalence and Outcomes of Infection in Intensive Care Units". *J. Am. Med. Assoc. Med. Assoc.* 302.21 (2009), pp. 2323–2329.

[5] N. Papon, V. Courdavault, M. Clastre, and R. J. Bennett. "Emerging and Emerged Pathogenic Candida Species: Beyond the Candida albicans Paradigm". *PLoS Pathog.* 9.9 (2013).

[6] V. Czaika, P. Nenoff, A. Glöckner, W. Fegeler, K. Becker, and A. F. Schmalreck. "Epidemiology and changes in patient-related factors from 1997 to 2009 in clinical yeast isolates related to dermatology, gynaecology, and paediatrics". *Int. J. Microbiol.* 2013 (2013).

[7] S. Höfs, S. Mogavero, and B. Hube. "Interaction of Candida albicans with host cells: virulence factors, host defense, escape strategies, and the microbiota". *J. Microbiol.* 54.3 (2016), pp. 149–169.

[8] J. Delaloye and T. Calandra. "Invasive candidiasis as a cause of sepsis in the critically ill patient." *Virulence* 5.1 (2014), pp. 161–9.

[9] G. D. Brown, D. W. Denning, N. a. R. Gow, S. M. Levitz, M. G. Netea, and T. C. White. "Hidden Killers: Human Fungal Infections". *Sci. Transl. Med.* 4.165 (2012), 165rv13.

[10] J. E. Berdal, R. Haagensen, T. Ranheim, and J. V. Björnholt. "Nosocomial candidemia; risk factors and prognosis revisited; 11 years experience from a Norwegian secondary hospital". *PLoS One* 9.7 (2014), pp. 5–10.

[11] I. D. Jacobsen, D. Wilson, B. Wächtler, S. Brunke, J. R. Naglik, and B. Hube. "Candida albicans dimorphism as a therapeutic target." *Expert Rev. Anti Infect. Ther.* 10.1 (2012), pp. 85–93.

[12] C. E. Birse, M. Y. Irwin, W. A. Fonzi, and P. S. Sypherd. "Cloning and characterization of ECE1, a gene expressed in association with cell elongation of the dimorphic pathogen Candida albicans." *Infect. Immun.* 61.9 (1993), pp. 3648–55.

[13] M. Röhm, E. Lindemann, E. Hiller, D. Ermert, K. Lemuth, D. Trkulja, O. Sogukpinar, H. Brunner, S. Rupp, C. F. Urban, and K. Sohn. "A family of secreted pathogenesis-related proteins in Candida albicans". *Mol. Microbiol.* 87.1 (2013), pp. 132–151.

[14] F. L. Mayer, D. Wilson, and B. Hube. "Candida albicans pathogenicity mechanisms." *Virulence* 4.2 (2013), pp. 119–28.

[15] O. Bader, Y. Krauke, and B. Hube. "Processing of predicted substrates of fungal Kex2 proteinases from Candida albicans, C. glabrata, Saccharomyces cerevisiae and Pichia pastoris." *BMC Microbiol.* 8.116 (2008).

[16] M. J. Schmitt and F. Breinig. "Yeast viral killer toxins: lethality and self-protection." *Nat. Rev. Microbiol.* 4.3 (2006), pp. 212–21.

[17] J. C. Skou. "The influence of some cations on an adenosine triphosphatase from peripheral nerves." *J. Am. Soc. Nephrol.* 9.11 (1957), pp. 2170–2177.

[18] S. J. Singer and G. L. Nicolson. "The fluid mosaic model of the structure of cell membranes". *Science* 175.4023 (1972), pp. 720–731.

[19] K. Simons and E. Ikonen. "Functional rafts in cell membranes." *Nature* 387.6633 (1997), pp. 569–572.

[20] B. Brüning, M. C. Rheinstädter, A. Hiess, B. Weinhausen, T. Reusch, S. Aeffner, and T. Salditt. "Influence of cholesterol on the collective dynamics of the phospholipid acyl chains in model membranes." *Eur. Phys. J. E. Soft Matter* 31.4 (2010), pp. 419–28.

[21] E. London. "Insights into lipid raft structure and formation from experiments in model membranes." *Curr. Opin. Struct. Biol.* 12.4 (2002), pp. 480–486.

[22] M. Edidin. "The state of lipid rafts: from model membranes to cells." *Annu. Rev. Biophys. Biomol. Struct.* 32 (2003), pp. 257–283.

[23] S. a. Pandit, S. Vasudevan, S. W. Chiu, R. J. Mashl, E. Jakobsson, and H. L. Scott. "Sphingomyelin-cholesterol domains in phospholipid membranes: atomistic simulation." *Biophys. J.* 87.2 (2004), pp. 1092–100.

[24] G. van Meer, D. R. Voelker, and G. W. Feigenson. "Membrane lipids: where they are and how they behave". *Nat. Rev. Mol. Cell Biol.* 9.2 (2008), pp. 112–124.

[25] J. F. Nagle and S. Tristram-Nagle. "Structure of lipid bilayers". *Biochim. Biophys. Acta - Rev. Biomembr.* 1469.3 (2000), pp. 159–195.

[26] H. Petrache, N. Gouliaev, S. Tristram-Nagle, R. Zhang, R. Suter, and J. Nagle. "Interbilayer interactions from high-resolution x-ray scattering". *Phys. Rev. E* 57.6 (1998), pp. 7014–7024.

[27] M. Rappolt. "Chapter 9 - The Biologically Relevant Lipid Mesophases as 'Seen' by X-Rays". *Adv. Planar Lipid Bilayers Liposomes* 5 (2006), pp. 253–283.

[28] E. F. Haney, S. Nathoo, H. J. Vogel, and E. J. Prenner. "Induction of non-lamellar lipid phases by antimicrobial peptides: a potential link to mode of action". *Chem. Phys. Lipids* 163.1 (2010), pp. 82–93.

[29] J. M. Seddon, J. Robins, T. Gulik-Krzywicki, and H. Delacroix. "Inverse micellar phases of phospholipids and glycolipids". *Phys. Chem. Chem. Phys.* 2.20 (2000), pp. 4485–4493.

[30] S. Aeffner, T. Reusch, B. Weinhausen, and T. Salditt. "Energetics of stalk intermediates in membrane fusion are controlled by lipid composition." *PNAS* 109.25 (2012), E1609–18.

[31] R. M. Epand. "Lipid polymorphism and protein-lipid interactions". *Biochim. Biophys. Acta - Rev. Biomembr.* 1376.3 (1998), pp. 353–368.

[32] V. Luzzati, H. Delacroix, and A. Gulik. "The Micellar Cubic Phases of Lipid-Containing Systems: Analogies with Foams, Relations with the Infinite Periodic Minimal Surfaces, Sharpness of the Polar/Apolar Partition". *J. Phys. Fr. II* 6.3 (1996), pp. 405–418.

[33] H. Delacroix, T. Gulik-Krzywicki, and J. M. Seddon. "Freeze fracture electron microscopy of lyotropic lipid systems: quantitative analysis of the inverse micellar cubic phase of space group Fd3m (Q227)." *J. Mol. Biol.* 258.1 (1996), pp. 88–103.

[34] M. W. Tate, E. Shyamsunder, S. M. Gruner, and K. L. D'Amico. "Kinetics of the lamellar-inverse hexagonal phase transition determined by time-resolved X-ray diffraction." *Biochemistry* 31.4 (1992), pp. 1081–1092.

[35] D. C. Turner and S. M. Gruner. "X-ray diffraction reconstruction of the inverted hexagonal (HII) phase in lipid-water systems." *Biochemistry* 31.5 (1992), pp. 1340–1355.

[36] J. N. Israelachvili, ed. *Intermolecular and Surface Forces*. 3rd ed. Academic Press, 2011, pp. 205–222.

[37] B. R. Lentz, J. R. Wu, L. Zheng, and J. Prevrátil. "The interfacial region of dipalmitoylphosphatidylcholine bilayers is perturbed by fusogenic amphipaths." *Biophys. J.* 71.6 (1996), pp. 3302–3310.

[38] V. Parsegian and B. W. Ninham. "Van der Waals forces in many-layered structures: Generalizations of the lifshitz result for two semi-infinite media". *J. Theor. Biol.* 38.1 (1973), pp. 101–109.

[39] W. Fenzl. "Van der Waals interaction". *Zeitschrift für Phys. B* 97 (1995), pp. 333–336.

[40] V. A. Parsegian. *Van der Waals Forces: A Handbook for Biologists, Chemists, Engineers, and Physicists*. Cambridge University Press, 2006, p. 398.

[41] V. Parsegian. "Reconciliation of van der Waals force measurements between phosphatidylcholine bilayers in water and between bilayer-coated mica surfaces". *Langmuir* 7.11 (1993), pp. 3625–3628.

[42] H. I. Petrache, T. Zemb, L. Belloni, and V. A. Parsegian. "Salt screening and specific ion adsorption determine neutral-lipid membrane interactions". *PNAS* 103.21 (2006), pp. 7982–7987.

[43] R. P. Rand and V. a. Parsegian. "Hydration Forces Between Phospholipid-Bilayers". *Biochim Biophys Acta* 988.3 (1989), pp. 351–376.

[44] T. J. Mcintosh and S. A. Simon. "Hydration and steric pressures between phosopholipid bilayers". *Annu. Rev. Biophys. Biomol. Struct.* 23 (1994), pp. 27–51.

[45] W. Helfrich. "Blocked lipid exchange in bilayers and its possible influence on the shape of vesicles." *Z. Naturforsch. C.* 29C (1974), pp. 510–515.

[46] J. Pan, S. Tristram-Nagle, N. Kucerka, and J. F. Nagle. "Temperature dependence of structure, bending rigidity, and bilayer interactions of dioleoylphosphatidylcholine bilayers." *Biophys. J.* 94.1 (2008), pp. 117–124.

[47] S. A. Tatulian. "Effect of lipid phase transition on the binding of anions to dimyristoylphoshatidylcholine liposomes". *Biochim. Biophys. Acta* 736 (1983), pp. 189–195.

[48] S. A. Tatulian. "Binding of alkaline-earth metal cations and some anions to phosphatidylcholine liposomes." *Eur. J. Biochem.* 170.1-2 (1987), pp. 413–420.

[49] A. Tossi, L. Sandri, and A. Giangaspero. "Amphipathic, alpha-helical antimicrobial peptides." *Biopolymers* 55.1 (2000), pp. 4–30.

[50] M. Zasloff. "Antimicrobial peptides of multicellular organisms." *Nature* 415.6870 (2002), pp. 389–395.

[51] S. R. Dennison, J. Wallace, F. Harris, and D. A. Phoenix. "Amphiphilic alpha-helical antimicrobial peptides and their structure/function relationships." *Protein Pept. Lett.* 12.1 (2005), pp. 31–39.

[52] Y. Chen, C. T. Mant, S. W. Farmer, R. E. W. Hancock, M. L. Vasil, and R. S. Hodges. "Rational Design of Alpha-Helical Antimicrobial Peptides with Enhanced Activities and Specificity / Therapeutic Index". *J. Biol. Chem.* 280.13 (2005), pp. 12316–12329.

[53] M. Dathe, C. Kaduk, E. Tachikawa, M. F. Melzig, H. Wenschuh, and M. Bienert. "Proline at position 14 of alamethicin is essential for hemolytic activity, catecholamine secretion from chromaffin cells and enhanced metabolic activity in endothelial cells". *Biochim. Biophys. Acta - Biomembr.* 1370.1 (1998), pp. 175–183.

[54] B. Leitgeb, A. Szekeres, L. Manczinger, C. Vágvölgyi, and L. Kredics. "The history of Alamethicin: A review of the most extensively studied peptaibol". *Chem. Biodivers.* 4.6 (2007), pp. 1027–1051.

[55] D. G. Lee, D. H. Kim, Y. Park, H. K. Kim, H. N. Kim, Y. K. Shin, C. H. Choi, and K. S. Hahm. "Fungicidal effect of antimicrobial peptide, PMAP-23, isolated from porcine myeloid against Candida albicans." *Biochem. Biophys. Res. Commun.* 282.2 (2001), pp. 570–574.

[56] R. Bucki, J. J. Pastore, P. Randhawa, R. Vegners, D. J. Weiner, and P. a. Janmey. "Antibacterial Activities of Rhodamine B-Conjugated Gelsolin-Derived Peptides Compared to Those of the Antimicrobial Peptides Cathelicidin LL37, Magainin II, and Melittin". *Antimicrob. Agents Chemother.* 48.5 (2004), pp. 1526–1533.

[57] Y. Shai. "Mechanism of the binding, insertion and destabilization of phospholipid bilayer membranes by alpha-helical antimicrobial and cell non-selective membrane-lytic peptides." *Biochim. Biophys. Acta - Biomembr.* 1462.1-2 (1999), pp. 55–70.

[58] S. Jung, A. J. Dingley, R. Augustin, F. Anton-Erxleben, M. Stanisak, C. Gelhaus, T. Gutsmann, M. U. Hammer, R. Podschun, A. M. J. J. Bonvin, M. Leippe, T. C. G. Bosch, and J. Grötzinger. "Hydramacin-1, structure and antibacterial activity of a protein from the basal metazoan hydra". *J. Biol. Chem.* 284.3 (2009), pp. 1896–1905.

[59] M. Michalek, B. Vincent, R. Podschun, Joachim Grötzinger, B. Bechinger, and S. Jung. "Hydramacin-1 in action: Scrutinizing the barnacle model". *Antimicrob. Agents Chemother.* 57.7 (2013), pp. 2955–2966.

[60] L. Zhang, M. G. Scott, H. Yan, L. D. Mayer, and R. E. W. Hancock. "Interaction of polyphemusin I and structural analogs with bacterial membranes, lipopolysaccharide, and lipid monolayers". *Biochemistry* 39.47 (2000), pp. 14504–14514.

[61] M. Wilmes, B. P. a. Cammue, H.-G. Sahl, and K. Thevissen. "Antibiotic activities of host defense peptides: more to it than lipid bilayer perturbation." *Nat. Prod. Rep.* 28.8 (2011), pp. 1350–1358.

[62] R. E. W. Hancock and A. Rozek. "Role of membranes in the activities of antimicrobial cationic peptides". *FEMS Microbiol. Lett.* 206.2 (2002), pp. 143–149.

[63] T. Schneider, T. Kruse, R. Wimmer, I. Wiedemann, V. Sass, U. Pag, A. Jansen, A. K. Nielsen, P. H. Mygind, D. S. Raventós, S. Neve, B. Ravn, A. M. J. J. Bonvin, L. De Maria, A. S. Andersen, L. K. Gammelgaard, H.-G. Sahl, and H.-H. Kristensen. "Plectasin, a fungal defensin, targets the bacterial cell wall precursor Lipid II." *Science* 328.5982 (2010), pp. 1168–1172.

[64] P. Schmitt, M. Wilmes, M. Pugnière, A. Aumelas, E. Bachère, H. G. Sahl, T. Schneider, and D. Destoumieux-Garzón. "Insight into invertebrate defensin mechanism of action: Oyster defensins inhibit peptidoglycan biosynthesis by binding to lipid II". *J. Biol. Chem.* 285.38 (2010), pp. 29208–29216.

[65] De Yang, Q. Chen, a. P. Schmidt, G. M. Anderson, J. M. Wang, J. Wooters, J. J. Oppenheim, and O. Chertov. "LL-37, the neutrophil granule- and epithelial cell-derived cathelicidin, utilizes formyl peptide receptor-like 1 (FPRL1) as a receptor to chemoattract human peripheral blood neutrophils, monocytes, and T cells." *J. Exp. Med.* 192.7 (2000), pp. 1069–1074.

[66] D. M. E. Bowdish, D. J. Davidson, M. G. Scott, and R. E. W. Hancock. "Immunomodulatory activities of small host defense peptides". *Antimicrob. Agents Chemother.* 49.5 (2005), pp. 1727–1732.

[67] M. E. Selsted and A. J. Ouellette. "Mammalian defensins in the antimicrobial immune response." *Nat. Immunol.* 6.6 (2005), pp. 551–557.

[68] K. L. Brown and R. E. W. Hancock. "Cationic host defense (antimicrobial) peptides". *Curr. Opin. Immunol.* 18.1 (2006), pp. 24–30.

[69] A. J. Duplantier and M. L. van Hoek. "The human cathelicidin antimicrobial peptide LL-37 as a potential treatment for polymicrobial infected wounds". *Front. Immunol.* 4.JUL (2013), pp. 1–14.

[70] K. A. Brogden. "Antimicrobial peptides: pore formers or metabolic inhibitors in bacteria?" *Nat. Rev. Microbiol.* 3.3 (2005), pp. 238–250.

[71] H. Sato and J. B. Feix. "Peptide-membrane interactions and mechanisms of membrane destruction by amphipathic α -helical antimicrobial peptides." *Biochim. Biophys. Acta - Biomembr.* 1758.9 (2006), pp. 1245–1256.

[72] K. J. Hallock, D.-K. Lee, and A. Ramamoorthy. "MSI-78, an analogue of the magainin antimicrobial peptides, disrupts lipid bilayer structure via positive curvature strain." *Biophys. J.* 84.5 (2003), pp. 3052–3060.

[73] M. S. Sansom. "The biophysics of peptide models of ion channels." *Prog. Biophys. Mol. Biol.* 55.ii (1991), pp. 139–235.

[74] J. Pan, S. Tristram-Nagle, and J. F. Nagle. "Alamethicin aggregation in lipid membranes". *J. Membr. Biol.* 231.1 (2009), pp. 1–36.

[75] K. He, S. J. Ludtke, H. W. Huang, and D. L. Worcester. "Antimicrobial peptide pores in membranes detected by neutron in-plane scattering". *Biochemistry* 34.48 (1995), pp. 15614–15618.

[76] K. He, S. J. Ludtke, W. T. Heller, and H. W. Huang. "Mechanism of alamethicin insertion into lipid bilayers". *Biophys. J.* 71.November (1996), pp. 2669–2679.

[77] D. Constantin, G. Brotons, A. Jarre, C. Li, and T. Salditt. "Interaction of alamethicin pores in DMPC bilayers." *Biophys. J.* 92.11 (2007), pp. 3978–87.

[78] S. Qian, W. Wang, L. Yang, and H. W. Huang. "Structure of the alamethicin pore reconstructed by x-ray diffraction analysis." *Biophys. J.* 94.9 (2008), pp. 3512–22.

[79] W. T. Heller, K. He, S. J. Ludtke, T. a. Harroun, and H. W. Huang. "Effect of changing the size of lipid headgroup on peptide insertion into membranes." *Biophys. J.* 73.1 (1997), pp. 239–244.

[80] K. He, S. J. Ludtke, D. L. Worcester, and H. W. Huang. "Neutron scattering in the plane of membranes: structure of alamethicin pores." *Biophys. J.* 70.6 (1996), pp. 2659–2666.

[81] K. Matsuzaki, O. Murase, N. Fujii, and K. Miyajima. "An antimicrobial peptide, magainin 2, induced rapid flip-flop of phospholipids coupled with pore formation and peptide translocation". *Biochemistry* 35.35 (1996), pp. 11361–11368.

[82] H. W. Huang. "Action of antimicrobial peptides: two-state model". *Biochemistry* 39.29 (2000), pp. 25–30.

[83] B. Bechinger. "The structure, dynamics and orientation of antimicrobial peptides in membranes by multidimensional solid-state NMR spectroscopy". *Biochim. Biophys. Acta - Biomembr.* 1462.1-2 (1999), pp. 157–183.

[84] L. Yang, T. a. Harroun, T. M. Weiss, L. Ding, and H. W. Huang. "Barrel-stave model or toroidal model? A case study on melittin pores." *Biophys. J.* 81.3 (2001), pp. 1475–85.

[85] D. Allende, S. A. Simon, and T. J. Mcintosh. "Melittin-Induced Bilayer Leakage Depends on Lipid Material Properties: Evidence for Toroidal Pores." *Biophys. J.* 88.3 (2005), pp. 1828–1837.

[86] S. J. Ludtke, K. He, W. T. Heller, T. a. Harroun, L. Yang, and H. W. Huang. "Membrane pores induced by magainin". *Biochemistry* 35.43 (1996), pp. 13723–13728.

[87] K. a. Henzler-Wildman, D.-k. Lee, and A. Ramamoorthy. "Mechanism of Lipid Bilayer Disruption by the Human Antimicrobial Peptide, LL-37". *Biochemistry* 42 (2003), pp. 6545–6558.

[88] K. a. Henzler-Wildman, G. V. Martinez, M. F. Brown, and a. Ramamoorthy. "Perturbation of the hydrophobic core of lipid bilayers by the human antimicrobial peptide LL-37". *Biochemistry* 43 (2004), pp. 8459–8469.

[89] H. Leontiadou, A. E. Mark, and S. J. Marrink. "Antimicrobial peptides in action". *J. Am. Chem. Soc.* 128.37 (2006), pp. 12156–12161.

[90] E. Gazit, a. Boman, H. Boman, and Y. Shai. "Interaction of the mammalian antibacterial peptide cecropin P1 with phospholipid vesicles." *Biochemistry* 34.36 (1995), pp. 11479–11488.

[91] E. Gazit, I. R. Miller, P. C. Biggin, M. S. Sansom, and Y. Shai. "Structure and orientation of the mammalian antibacterial peptide cecropin P1 within phospholipid membranes." *J. Mol. Biol.* 258.5 (1996), pp. 860–70.

[92] H. Jenssen, P. Hamill, and R. E. W. Hancock. "Peptide antimicrobial agents." *Clin. Microbiol. Rev.* 19.3 (2006), pp. 491–511.

[93] B. Bechinger and K. Lohner. "Detergent-like actions of linear amphipathic cationic antimicrobial peptides". *Biochim. Biophys. Acta - Biomembr.* 1758.9 (2006), pp. 1529–1539.

[94] M. T. Lee, F. Y. Chen, and H. W. Huang. "Energetics of Pore Formation Induced by Membrane Active Peptides". *Biochemistry* 43.12 (2004), pp. 3590–3599.

[95] A. Hickel, S. Danner-Pongratz, H. Amenitsch, G. Degovics, M. Rappolt, K. Lohner, and G. Pabst. "Influence of antimicrobial peptides on the formation of nonlamellar lipid mesophases". *Biochim. Biophys. Acta - Biomembr.* 1778.10 (2008), pp. 2325–2333.

[96] R. F. Epand, R. M. Epand, F. Formaggio, M. Crisma, H. Wu, R. I. Lehrer, and C. Toniolo. "Analogs of the antimicrobial peptide trichogin having opposite membrane properties". *Eur. J. Biochem.* 268.3 (2001), pp. 703–712.

[97] B. G. Tenchov, R. C. MacDonald, and B. R. Lentz. "Fusion Peptides Promote Formation of Bilayer Cubic Phases in Lipid Dispersions. An X-Ray Diffraction Study". *Biophys. J.* 104.5 (2013), pp. 1029–1037.

[98] G. Kreil. "Biosynthesis of melittin, a toxic peptide from bee venom. Amino-acid sequence of the precursor." *Eur. J. Biochem.* 33.3 (1973), pp. 558–66.

[99] J. E. Callaway, J. Lai, B. Haselbeck, M. Baltaian, S. P. Bonnesen, J. Weickmann, G. Wilcox, and S. P. Lei. "Modification of the C terminus of cecropin is essential for broad-spectrum antimicrobial activity." *Antimicrob. Agents Chemother.* 37.8 (1993), pp. 1614–9.

[100] E. Strandberg, D. Tiltak, M. Ieronimo, N. Kanithasen, P. Wadhwani, and A. S. Ulrich. "Influence of C-terminal amidation on the antimicrobial and hemolytic activities of cationic α-helical peptides". *Pure Appl. Chem.* 79.4 (2007), pp. 717–728.

[101] S. R. Dennison, F. Harris, T. Bhatt, J. Singh, and D. A. Phoenix. "The effect of C-terminal amidation on the efficacy and selectivity of antimicrobial and anticancer peptides". *Mol. Cell. Biochem.* 332.1-2 (2009), pp. 43–50.

[102] S. H. White and W. C. Wimley. "Hydrophobic interactions of peptides with membrane interfaces". *Biochim. Biophys. Acta - Rev. Biomembr.* 1376.3 (1998), pp. 339–352.

[103] D. E. Shalev, A. Mor, and I. Kustanovich. "Structural consequences of carboxyamidation of dermaseptin S3." *Biochemistry* 41.23 (2002), pp. 7312–7.

[104] M. E. Houston, L. H. Kondejewski, D. N. Karunaratne, M. Gough, S. Fidai, R. S. Hodges, and R. E. Hancock. "Influence of preformed alpha-helix and alpha-helix induction on the activity of cationic antimicrobial peptides." *J. Pept. Res.* 52.2 (1998), pp. 81–8.

[105] S. R. Dennison, M. Mura, F. Harris, L. H. Morton, A. Zvelindovsky, and D. A. Phoenix. "The role of C-terminal amidation in the membrane interactions of the anionic antimicrobial peptide, maximin H5". *Biochim. Biophys. Acta - Biomembr.* 1848.5 (2015), pp. 1111–1118.

[106] S. R. Dennison and D. a. Phoenix. "Influence of C-Terminal Amidation on the Efficacy of Modelin-5". *Biochemistry* 50.9 (2011), pp. 1514–1523.

[107] B. a. Cornell, V. L. Braach-Maksvytis, L. G. King, P. D. Osman, B. Raguse, L. Wieczorek, and R. J. Pace. "A biosensor that uses ion-channel switches." *Nature* 387.6633 (1997), pp. 580–583.

[108] H. M. McConnell. "Structures and Transitions in Lipid Monolayers at the Air-Water Interface". *Annu. Rev. Phys. Chem.* 42 (1991), pp. 171–195.

[109] A. Fischer, M. Lösche, H. Möhwald, and E. Sackmann. "On the nature of the lipid monolayer phase transition". *J. Phys. Lettres* 45.16 (1984), pp. 785–791.

[110] A. Clausell, M. A. Busquets, M. Pujol, A. Alsina, and Y. Cajal. "Polymyxin B-lipid interactions in Langmuir-Blodgett monolayers of Escherichia coli lipids: A thermodynamic and atomic force microscopy study". *Biopolymers* 75.6 (2004), pp. 480–490.

[111] G. Sessa and G. Weissmann. "Phospholipid spherules (liposomes) as a model for biological membranes." *J. Lipid Res.* 9.3 (1968), pp. 310–318.

[112] S. H. Kim, L. Haimovich-Caspi, L. Omer, Y. Talmon, and E. I. Franses. "Effect of sonication and freezing-thawing on the aggregate size and dynamic surface tension of aqueous DPPC dispersions". *J. Colloid Interface Sci.* 311.1 (2007), pp. 217–227.

[113] Y. Okumura, H. Zhang, T. Sugiyama, and Y. Iwata. "Electroformation of giant vesicles on a non-electroconductive substrate." *J. Am. Chem. Soc.* 129.6 (2007), pp. 1490–1.

[114] P. Mueller, D. O. Rudin, H. T. Tien, and W. C. Wescott. "Reconstitution of cell membrane structure in vitro and its transformation into an excitable system." *Nature* 194 (1962), pp. 979–980.

[115] M. Montal and P. Mueller. "Formation of Bimolecular Membranes from Lipid Monolayers and a Study of Their Electrical Properties." *Proc. Natl. Acad. Sci.* 69.12 (1972), pp. 3561–3566.

[116] R. P. Richter, R. R. Escarpit, and P. Cedex. "Formation of Solid-Supported Lipid Bilayers: An Integrated View". *Langmuir* 22.8 (2006), pp. 3497–3505.

[117] L. Tamm and H. McConnell. "Supported phospholipid bilayers". *Biophys. J.* 47.1 (1985), pp. 105–113.

[118] H. McConnell, T. Watts, R. Weis, and A. Brian. "Supported planar membranes in studies of cell-cell recognition in the immune system". *Biochim. Biophys. Acta - Rev. Biomembr.* 864.1 (1986), pp. 95–106.

[119] C. Miller, J. Majewski, T. Gog, and T. Kuhl. "Characterization of Biological Thin Films at the Solid-Liquid Interface by X-Ray Reflectivity". *Phys. Rev. Lett.* 94.23 (2005), p. 238104.

[120] E. Nováková, K. Giewekemeyer, and T. Salditt. "Structure of two-component lipid membranes on solid support: An x-ray reflectivity study". *Phys. Rev. E* 74.5 (2006), p. 051911.

[121] E. Castellana and P. Cremer. "Solid supported lipid bilayers: From biophysical studies to sensor design". *Surf. Sci. Rep.* 61.10 (2006), pp. 429–444.

[122] S. Stanglmaier, S. Hertrich, K. Fritz, J. F. Moulin, M. Haese-Seiller, J. O. Rädler, and B. Nickel. "Asymmetric distribution of anionic phospholipids in supported lipid bilayers". *Langmuir* 28.29 (2012), pp. 10818–10821.

[123] M. Przybylo, J. Sýkora, J. Humpolíčová, A. Benda, A. Zan, and M. Hof. "Lipid diffusion in giant unilamellar vesicles is more than 2 times faster than in supported phospholipid bilayers under identical conditions". *Langmuir* 22.22 (2006), pp. 9096–9099.

[124] R. Tero. "Substrate Effects on the Formation Process, Structure and Physicochemical Properties of Supported Lipid Bilayers". *Materials* 5.12 (2012), pp. 2658–2680.

[125] M. a. Holden, S. Y. Jung, T. Yang, E. T. Castellana, and P. S. Cremer. "Creating fluid and air-stable solid supported lipid bilayers". *J. Am. Chem. Soc.* 126.21 (2004), pp. 6512–6513.

[126] M. Seul and M. J. Sammon. "Preparation of surfactant multilayer films on solid substrates by deposition from organic solution". *Thin Solid Films* 185.2 (1990), pp. 287–305.

[127] U. Mennicke and T. Salditt. "Preparation of solid-supported lipid bilayers by spin-coating". *Langmuir* 18.21 (2002), pp. 8172–8177.

[128] T. Salditt. "Lipid-peptide interaction in oriented bilayers probed by interface-sensitive scattering methods." *Curr. Opin. Struct. Biol.* 13.4 (2003), pp. 467–478.

[129] Y. Lyatskaya, Y. Liu, S. Tristram-Nagle, J. Katsaras, and J. F. Nagle. "Method for obtaining structure and interactions from oriented lipid bilayers". *Phys. Rev. E* 63.011907 (2000).

[130] A. L. Plant. "Self-assembled phospholipid/alkanethiol biomimetic bilayers on gold". *Langmuir* 9.11 (1993), pp. 2764–2767.

[131] J. C. Love, L. a. Estroff, J. K. Kriebel, R. G. Nuzzo, and G. M. Whitesides. "Self-assembled monolayers of thiolates on metals as a form of nanotechnology". *Chem. Rev.* 105.4 (2005), pp. 1103–1169.

[132] J. Jackman, W. Knoll, and N.-J. Cho. "Biotechnology Applications of Tethered Lipid Bilayer Membranes". *Materials* 5.12 (2012), pp. 2637–2657.

[133] H. Lang, C. Duschl, and H. Vogel. "A new class of thiolipids for the attachment of lipid bilayers on gold surfaces". *Langmuir* 10.1 (1994), pp. 197–210.

[134] D. J. McGillivray, G. Valincius, D. J. Vanderah, W. Febo-Ayala, J. T. Woodward, F. Heinrich, J. J. Kasianowicz, and M. Lösche. "Molecular-scale structural and functional characterization of sparsely tethered bilayer lipid membranes." *Biointerphases* 2.1 (2007), pp. 21–33.

[135] F. Heinrich, T. Ng, D. J. Vanderah, P. Shekhar, M. Mihailescu, H. Nanda, and M. Lösche. "A new lipid anchor for sparsely tethered bilayer lipid membranes". *Langmuir* 25.7 (2009), pp. 4219–4229.

[136] S. Shenoy, R. Moldovan, J. Fitzpatrick, D. Vanderah, M. Deserno, and M. Lösche. "In-plane homogeneity and lipid dynamics in tethered bilayer lipid membranes (tBLMs)". *Soft Matter* 2010.6 (2010), pp. 1263–1274.

[137] B. Raguse, V. Braach-Maksvytis, B. A. Cornell, L. G. King, P. D. J. Osman, R. J. Pace, and L. Wieczorek. "Tethered lipid bilayer membranes: formation and ionic reservoir characterization". *Langmuir* 14.3 (1998), pp. 648–659.

[138] D. J. McGillivray, G. Valincius, F. Heinrich, J. W. F. Robertson, D. J. Vanderah, W. Febo-Ayala, I. Ignatjev, M. Lösche, and J. J. Kasianowicz. "Structure of functional Staphylococcus aureus α-hemolysin channels in tethered bilayer lipid membranes". *Biophys. J.* 96.4 (2009), pp. 1547–1553.

[139] A. Junghans and I. Köper. "Structural analysis of tethered bilayer lipid membranes". *Langmuir* 26.13 (2010), pp. 11035–11040.

[140] H. F. Okorn-Schmidt. "Characterization of silicon surface preparation processes for advanced gate dielectrics". *IBM J. Res. Dev.* 43.3 (1999), pp. 351–326.

[141] C. Li, D. Constantin, and T. Salditt. "Biomimetic membranes of lipid-peptide model systems prepared on solid support". *J. Phys. Condens. Matter* 16.26 (2004), pp. 2439–2453.

[142] N. J. Gibson and J. Y. Cassim. "Evidence for an alphaII-type helical conformation for bacteriorhodopsin in the purple membrane." *Biochemistry* 28.5 (1989), pp. 2134–2139.

[143] C. G. Cranfield, B. Cornell, S. L. Grage, P. Duckworth, S. Carne, A. S. Ulrich, and B. Martinac. "Transient potential gradients and impedance measures of tethered bilayer lipid membranes: pore-forming peptide insertion and the effect of electroporation." *Biophys. J.* 106.1 (2014), pp. 182–9.

[144] C. G. Cranfield, T. Bettler, and B. Cornell. "Nanoscale Ion Sequestration To Determine the Polarity Selectivity of Ion Conductance in Carriers and Channels". *Langmuir* 31.1 (2015), pp. 292–298.

[145] S. B. H. Kent. "Chemical synthesis of peptides and proteins". *Ann. Rev. Biochem.* 57.I (1988), pp. 957–989.

[146] R. Pecora, ed. *Dynamic Light Scattering*. New York: Plenum Press, 1985.

[147] R. Pecora. "Dynamic light scattering measurement of nanometer particles in liquids". *J. Nanoparticle Res.* 2 (2000), pp. 123–131.

[148] W. Brown, ed. *Dynamic Light Scattering*. Clarendon Press, 1993.

[149] D. E. Koppel. "Analysis of Macromolecular Polydispersity in Intensity Correlation Spectroscopy: The Method of Cumulants". *J. Chem. Phys.* 57.11 (1972), pp. 4814–4820.

[150] B. J. Frisken. “Dynamic Light-Scattering Data”. *Appl. Opt.* 40.24 (2001), pp. 4087–4091.

[151] B. J. Kirby and E. F. Hasselbrink. “Zeta potential of microfluidic substrates: 1. Theory, experimental techniques, and effects on separations”. *Electrophoresis* 25.2 (2004), pp. 187–202.

[152] a.V. Delgado, F. González-Caballero, R. Hunter, L. Koopal, and J. Lyklema. “Measurement and interpretation of electrokinetic phenomena”. *J. Colloid Interface Sci.* 309.2 (2007), pp. 194–224.

[153] A. C. Adler, N. J. Greenfield, and G. D. Fasman. “Circular dichroism and optical rotatory dispersion of glycogen phosphorylase.” *Methods Enzymol.* 27 (1973), pp. 675–735.

[154] N. J. Greenfield. “Methods to estimate the conformation of proteins and polypeptides from circular dichroism data”. *Anal. Biochem.* 235.1 (1996), pp. 1–10.

[155] G. D. Fasman, ed. *Circular Dichroism and the Conformational Analysis of Biomolecules*. Boston, MA: Springer US, 1996.

[156] N. Berova, K. Nakanishi, and R. W. Woody. *Circular Dichroism: Principles and Applications*. 2nd. New York: Wiley-VCH, 2000.

[157] S. M. Kelly, T. J. Jess, and N. C. Price. “How to study proteins by circular dichroism”. *Biochim. Biophys. Acta - Proteins Proteomics* 1751.2 (2005), pp. 119–139.

[158] N. J. Greenfield and G. D. Fasman. “Computed circular dichroism spectra for the evaluation of protein conformation”. *Biochemistry* 8.10 (1969), pp. 4108–4116.

[159] W. Moffitt. “Optical Rotatory Dispersion of Helical Polymers”. *J. Chem. Phys.* 25.3 (1956), pp. 467–478.

[160] W. Moffitt, D. D. Fitts, and J. G. Kirkwood. “Critique of the Theory of Optical Activity of Helical Polymers.” *Proc. Natl. Acad. Sci. U. S. A.* 43.8 (1957), pp. 723–730.

[161] H. Vogel. “Comparison of the conformation and orientation of alamethicin and melittin in lipid membranes.” *Biochemistry* 26.14 (1987), pp. 4562–4572.

[162] Y. Wu, H. W. Huang, and G. A. Olah. “Method of oriented circular dichroism.” *Biophys. J.* 57.4 (1990), pp. 797–806.

[163] G. a. Olah and H. W. Huang. “Circular dichroism of oriented α helices. I. Proof of the exciton theory”. *J. Chem. Phys.* 89.4 (1988), pp. 2531–2538.

[164] H. de Jongh, E. Goormaghtigh, and J. Killian. "Analysis of circular dichroism spectra of oriented protein-lipid complexes: toward a general application". *Biochemistry* 33.48 (1994), pp. 14521–14528.

[165] S. Brahms and J. Brahms. "Determination of protein secondary structure in solution by vacuum ultraviolet circular dichroism." *J. Mol. Biol.* 138.2 (1980), pp. 149–178.

[166] N. Sreerama and R. W. Woody. "Computation and Analysis of Protein Circular Dichroism Spectra". *Methods Enzymol.* 383 (2004), pp. 318–351.

[167] N. Sreerama and R. W. Woody. "On the analysis of membrane protein circular dichroism spectra". *Protein Sci.* 13.1 (2004), pp. 100–112.

[168] N. J. Greenfield. "Using circular dichroism spectra to estimate protein secondary structure." *Nat. Protoc.* 1.6 (2006), pp. 2876–2890.

[169] W. C. Johnson. "Protein secondary structure and circular dichroism: a practical guide." *Proteins* 7.3 (1990), pp. 205–214.

[170] J. Bürck, S. Roth, P. Wadhwani, S. Afonin, N. Kanithasen, E. Strandberg, and A. S. Ulrich. "Conformation and membrane orientation of amphiphilic helical peptides by oriented circular dichroism." *Biophys. J.* 95.8 (2008), pp. 3872–81.

[171] A. Savitzky and M. J. E. Golay. "Smoothing and Differentiation of Data by Simplified Least Squares Procedures". *Anal. Chem.* 36.8 (1964), pp. 1627–1639.

[172] M. A. Andrade, P. Chacón, J. J. Merelo, and F. Morán. "Evaluation of secondary structure of proteins from UV circular dichroism spectra using an unsupervised learning neural network." *Protein Eng.* 6.4 (1993), pp. 383–390.

[173] a. Lobley, L. Whitmore, and B. a. Wallace. "DICHROWEB: an interactive website for the analysis of protein secondary structure from circular dichroism spectra." *Bioinformatics* 18.1 (2002), pp. 211–212.

[174] L. Whitmore and B. A. Wallace. "DICHROWEB, an online server for protein secondary structure analyses from circular dichroism spectroscopic data". *Nucleic Acids Res.* 32.Web Server issue (2004), pp. 668–673.

[175] L. Whitmore and B. A. Wallace. "Protein secondary structure analyses from circular dichroism spectroscopy: Methods and reference databases". *Biopolymers* 89.5 (2008), pp. 392–400.

[176] J. Bürck, S. Roth, D. Windisch, P. Wadhwani, and A. S. Ulrich. "UV-CD12: synchrotron radiation circular dichroism beamline at ANKA". *J. Synchrotron Radiat.* 22.3 (2015), pp. 844–852.

[177] F.-Y. Chen, M.-T. Lee, and H. W. Huang. "Sigmoidal concentration dependence of antimicrobial peptide activities: a case study on alamethicin." *Biophys. J.* 82.2 (2002), pp. 908–914.

[178] J. C. Sutherland, P. C. Keck, K. P. Griffin, and P. Z. Takacs. "Simultaneous measurement of absorption and circular dichroism in a synchrotron spectrometer". *Nucl. Instruments Methods Phys. Res.* 195.1-2 (1982), pp. 375–379.

[179] R. N. Lewis and R. N. McElhaney. "Membrane lipid phase transitions and phase organization studied by Fourier transform infrared spectroscopy". *Biochim. Biophys. Acta - Biomembr.* 1828.10 (2013), pp. 2347–2358.

[180] T. Förster. "Zwischenmolekulare Energiewanderung und Fluoreszenz". *Ann. Phys.* 437.1-2 (1948), pp. 55–75.

[181] A. B. Schromm, K. Brandenburg, E. T. Rietschel, H. D. Flad, S. F. Carroll, and U. Seydel. "Lipopolysaccharide-binding protein mediates CD14-independent intercalation of lipopolysaccharide into phospholipid membranes". *FEBS Lett.* 399.3 (1996), pp. 267–271.

[182] G. Valincius, T. Meškauskas, and F. Ivanauskas. "Electrochemical impedance spectroscopy of tethered bilayer membranes." *Langmuir* 28.1 (2012), pp. 977–990.

[183] W. K. Chang, W. C. Wimley, P. C. Searson, K. Hristova, and M. Merzlyakov. "Characterization of antimicrobial peptide activity by electrochemical impedance spectroscopy". *Biochim. Biophys. Acta - Biomembr.* 1778.10 (2008), pp. 2430–2436.

[184] T. Gutsmann, T. Heimburg, U. Keyser, K. R. Mahendran, and M. Winterhalter. "Protein reconstitution into freestanding planar lipid membranes for electrophysiological characterization". *Nat. Protoc.* 10 (2014), pp. 188–198.

[185] D. Marsh. "Lateral pressure in membranes". *Biochim. Biophys. Acta - Rev. Biomembr.* 1286.3 (1996), pp. 183–223.

[186] L. D. Mayer, G. L. Nelsestuen, and H. L. Brockman. "Prothrombin association with phospholipid monolayers". *Biochemistry* 22.2 (1983), pp. 316–321.

[187] G. Binnig and C. F. Quate. "Atomic Force Microscope". *Phys. Rev. Lett.* 56.9 (1986), pp. 930–933.

[188] E. Meyer. "Atomic force microscopy". *Prog. Surf. Sci.* 41 (1992), pp. 3–49.

[189] R. García. "Dynamic atomic force microscopy methods". *Surf. Sci. Rep.* 47.6 (2002), pp. 197–301.

[190] P. Eaton and P. West. *Atomic Force Microscopy*. Oxford University Press, 2010.

[191] B. E. Warren. *X-Ray Diffraction*. Reprint Ed. New York, USA: Dover Publications, 1990.

[192] M. Tolan. *X-Ray Scattering from Soft-Matter Thin Films*. Berlin, Heidelberg: Springer, 1999.

[193] J. Als-Nielsen and D. McMorrow. *Elements of Modern X-ray Physics: Second Edition*. 2nd editio. Chichester, UK: John Wiley & Sons, Ltd, 2011.

[194] P. Willmott. *An Introduction to Synchrotron Radiation: Techniques and Applications*. Chichester, UK: John Wiley & Sons, Ltd, 2011.

[195] O. H. Seeck and B. M. Murphy, eds. *X-Ray Diffraction: Modern Experimental Techniques*. Pan Stanford Publishing Pte. Ltd., 2015.

[196] S. Aeffner, T. Reusch, B. Weinhausen, and T. Salditt. "Membrane fusion intermediates and the effect of cholesterol: an in-house X-ray scattering study." *Eur. Phys. J. E. Soft Matter* 30.2 (2009), pp. 205–14.

[197] M. Rappolt, H. Amenitsch, J. Strancar, C. V. Teixeira, M. Kriechbaum, G. Pabst, M. Majerowicz, and P. Laggner. "Phospholipid mesophases at solid interfaces: in-situ X-ray diffraction and spin-label studies." *Adv. Colloid Interface Sci.* 111.1-2 (2004), pp. 63–77.

[198] L. Parratt. "Surface studies of solids by total reflection of X-rays." *Phys. Rev.* 95.2 (1954).

[199] T. Salditt, C. Münster, J. Lu, M. Vogel, W. Fenzl, and V. Souvorov. "Specular and diffuse scattering of highly aligned phospholipid membranes." *Phys. Rev. E* 60.6 (1999), pp. 7285–7289.

[200] A. Spaar and T. Salditt. "Short range order of hydrocarbon chains in fluid phospholipid bilayers studied by x-ray diffraction from highly oriented membranes." *Biophys. J.* 85.3 (2003), pp. 1576–84.

[201] T. Salditt, M. Vogel, and W. Fenzl. "Thermal Fluctuations and Positional Correlations in Oriented Lipid Membranes". *Phys. Rev. Lett.* 90.17 (2003), p. 178101.

[202] J. Katsaras. "Adsorbed to a rigid substrate, dimyristoylphosphatidylcholine multibilayers attain full hydration in all mesophases." *Biophys. J.* 75.5 (1998), pp. 2157–62.

[203] T. Salditt, C. Li, and A. Spaar. "Structure of antimicrobial peptides and lipid membranes probed by interface-sensitive X-ray scattering". *Biochim. Biophys. Acta - Biomembr.* 1758.9 (2006), pp. 1483–1498.

[204] O. H. Seeck, C. Deiter, K. Pflaum, F. Bertam, A. Beerlink, H. Franz, J. Horbach, H. Schulte-Schrepping, B. M. Murphy, M. Greve, and O. Magnussen. "The high-resolution diffraction beamline P08 at PETRA III." *J. Synchrotron Radiat.* 19.Pt 1 (2012), pp. 30–8.

[205] L. Perino-Gallice, G. Fragneto, U. Mennicke, T. Salditt, and F. Rieutord. "Dewetting of solid-supported multilamellar lipid layers". *Eur. Phys. J. E* 8 (2002), pp. 275–282.

[206] J. Katsaras. "X-ray diffraction studies of oriented lipid bilayers." *Biochem. Cell Biol.* 73.5-6 (1995), pp. 209–218.

[207] A. Nelson. "Co-refinement of multiple-contrast neutron/X-ray reflectivity data using MOTOFIT". *J. Appl. Crystallogr.* 39.2 (2006), pp. 273–276.

[208] F. Abelès. "Optical Properties of Thin Absorbing Films". *J. Opt. Soc. Am.* 47.6 (1957), pp. 473–482.

[209] T. Hohage, K. Giewekemeyer, and T. Salditt. "Iterative reconstruction of a refractive-index profile from x-ray or neutron reflectivity measurements". *Phys. Rev. E* 77.5 (2008), p. 051604.

[210] MATLAB. *version 7.13.0 (R2011b)*. Natick, Massachusetts: The MathWorks Inc., 2011.

[211] L. Yang and H. W. Huang. "A rhombohedral phase of lipid containing a membrane fusion intermediate structure." *Biophys. J.* 84.3 (2003), pp. 1808–17.

[212] B. Weinhausen, S. Aeffner, T. Reusch, and T. Salditt. "Acyl-chain correlation in membrane fusion intermediates: x-ray diffraction from the rhombohedral lipid phase." *Biophys. J.* 102.9 (2012), pp. 2121–9.

[213] T. Salditt. "Thermal fluctuations and stability of solid-supported lipid membranes". *J. Phys. Condens. Matter* 17.6 (2005), R287–R314.

[214] Z. Wang and G. Wang. "APD: the Antimicrobial Peptide Database." *Nucleic Acids Res.* 32.Database issue (2004), pp. D590–2.

[215] G. Wang, X. Li, and Z. Wang. "APD2: the updated antimicrobial peptide database and its application in peptide design." *Nucleic Acids Res.* 37.Database issue (2009), pp. D933–7.

[216] J. M. Conlon. "Host-defense peptides of the skin with therapeutic potential: From hagfish to human". *Peptides* 67 (2015), pp. 29–38.

[217] M. Schiffer and A. B. Edmundson. "Use of helical wheels to represent the structures of proteins and to identify segments with helical potential." *Biophys. J.* 7.2 (1967), pp. 121–135.

[218] M. W. MacArthur and J. M. Thornton. "Influence of proline residues on protein conformation". *J. Mol. Biol.* 218.2 (1991), pp. 397–412.

[219] K. Hristova, W. C. Wimley, V. K. Mishra, G. M. Anantharamiah, J. P. Segrest, and S. H. White. "An amphipathic alpha-helix at a membrane interface: a structural study using a novel X-ray diffraction method." *J. Mol. Biol.* 290.1 (1999), pp. 99–117.

[220] E. V. Schow, J. A. Freites, P. Cheng, A. Bernsel, G. von Heijne, S. H. White, and D. J. Tobias. "Arginine in Membranes: The Connection Between Molecular Dynamics Simulations and Translocon-Mediated Insertion Experiments". *J. Membr. Biol.* 239.1-2 (2011), pp. 35–48.

[221] E. Strandberg and J. A. Killian. "Snorkeling of lysine side chains in transmembrane helices: How easy can it get?" *FEBS Lett.* 544.1-3 (2003), pp. 69–73.

[222] Y. Shen, J. Maupetit, P. Derreumaux, and P. Tufféry. "Improved PEP-FOLD Approach for Peptide and Miniprotein Structure Prediction". *J. Chem. Theory Comput.* 10.10 (2014), pp. 4745–4758.

[223] J. Maupetit, P. Derreumaux, and P. Tuffery. "PEP-FOLD: An online resource for de novo peptide structure prediction". *Nucleic Acids Res.* 37.Web Server issue (2009), pp. 498–503.

[224] J. Maupetit, P. Derreumaux, and P. Tufféry. "A fast method for large-scale de novo peptide and miniprotein structure prediction". *J. Comput. Chem.* 31.4 (2010), pp. 726–738.

[225] P. Thévenet, Y. Shen, J. Maupetit, F. Guyon, P. Derreumaux, and P. Tufféry. "PEP-FOLD: An updated de novo structure prediction server for both linear and disulfide bonded cyclic peptides". *Nucleic Acids Res.* 40.Web Server issue (2012), pp. 288–293.

[226] J. Beaufays, L. Lins, A. Thomas, and R. Brasseur. "In silico predictions of 3D structures of linear and cyclic peptides with natural and non-proteinogenic residues". *J. Pept. Sci.* 18.July 2011 (2012), pp. 17–24.

[227] D. Frishman and P. Argos. "Knowledge-based protein secondary structure assignment". *Proteins Struct. Funct. Genet.* 23.4 (1995), pp. 566–579.

[228] J. Y. Suh, Y. T. Lee, C. B. Park, K. H. Lee, S. C. Kim, and B. S. Choi. "Structural and functional implications of a proline residue in the antimicrobial peptide gaegurin". *Eur. J. Biochem.* 266.2 (1999), pp. 665–674.

[229] D. E. Kim, D. Chivian, and D. Baker. "Protein structure prediction and analysis using the Robetta server". *Nucleic Acids Res.* 32.Web Server issue (2004), W526–W531.

[230] Y. Song, F. Dimaio, R. Y. R. Wang, D. Kim, C. Miles, T. Brunette, J. Thompson, and D. Baker. "High-resolution comparative modeling with RosettaCM". *Structure* 21.10 (2013), pp. 1735–1742.

[231] J. E. Deane, P. Roversi, F. S. Cordes, S. Johnson, R. Kenjale, S. Daniell, F. Booy, W. D. Picking, W. L. Picking, A. J. Blocker, and S. M. Lea. "Molecular model of a type III secretion system needle: Implications for host-cell sensing". *Proc. Natl. Acad. Sci.* 103.33 (2006), pp. 12529–12533.

[232] D. Eisenberg, R. M. Weiss, T. C. Terwilliger, and W. Wilcox. "Hydrophobic moments and protein structure". *Faraday Symp. Chem. Soc.* 17 (1982), p. 109.

[233] D. Eisenberg, E. Schwarz, M. Komaromy, and R. Wall. "Analysis of membrane and surface protein sequences with the hydrophobic moment plot." *J. Mol. Biol.* 179.1 (1984), pp. 125–142.

[234] F. Harris, J. Wallace, and D. A. Phoenix. "Use of hydrophobic moment plot methodology to aid the identification of oblique orientated alpha-helices." *Mol. Membr. Biol.* 17.4 (2000), pp. 201–207.

[235] D. a. Phoenix, F. Harris, O. a. Daman, and J. Wallace. "The prediction of amphiphilic alpha-helices." *Curr. Protein Pept. Sci.* 3 (2002), pp. 201–221.

[236] J. Wallace, O. a. Daman, F. Harris, and D. a. Phoenix. "Investigation of hydrophobic moment and hydrophobicity properties for transmembrane alpha-helices". *Theor. Biol. Med. Model.* 1.5 (2004).

[237] R. Brasseur, T. Pillot, L. Lins, J. Vandekerckhove, and M. Rosseneu. "Peptides in membranes: tipping the balance of membrane stability". *Trends Biochem. Sci.* 22.5 (1997), pp. 167–171.

[238] O. Pérez-Méndez, B. Vanloo, A. Decout, M. Goethals, F. Peelman, J. Vandekerckhove, R. Brasseur, and M. Rosseneu. "Contribution of the hydrophobicity gradient of an amphipathic peptide to its mode of association with lipids". *Eur. J. Biochem.* 256.3 (1998), pp. 570–579.

[239] D. Mao and B. a. Wallace. "Differential light scattering and absorption flattening optical effects are minimal in the circular dichroism spectra of small unilamellar vesicles." *Biochemistry* 23.12 (1984), pp. 2667–2673.

[240] B. A. Wallace and C. L. Teeters. "Differential absorption flattening optical effects are significant in the circular dichroism spectra of large membrane fragments." *Biochemistry* 26.1 (1987), pp. 65–70.

[241] N. E. Zhou, C. M. Kay, and R. S. Hodges. "Synthetic model proteins: the relative contribution of leucine residues at the nonequivalent positions of the 3-4 hydrophobic repeat to the stability of the two-stranded alpha-helical coiled-coil." *Biochemistry* 31.25 (1992), pp. 5739–46.

[242] T. J. Graddis, D. G. Myszka, and I. M. Chaiken. "Controlled formation of model homo- and heterodimer coiled coil polypeptides". *Biochemistry* 32 (1993), pp. 12664–12671.

[243] M. Cascio and B. Wallace. "Effects of Local Environment on the Circular Dichroism Spectra of Polypeptides". *Anal. Biochem.* 227.1 (1995), pp. 90–100.

[244] Y. Chen and B. A. Wallace. "Secondary solvent effects on the circular dichroism spectra of polypeptides in non-aqueous environments: Influence of polarisation effects on the far ultraviolet spectra of alamethicin". *Biophys. Chem.* 65.1 (1997), pp. 65–74.

[245] B. A. Wallace, J. G. Lees, A. J. W. Orry, A. Lobley, and R. W. Janes. "Analyses of circular dichroism spectra of membrane proteins". *Protein Sc.* 12 (2003), pp. 875–884.

[246] J. Kim, M. Mosior, L. a. Chung, H. Wu, and S. McLaughlin. "Binding of peptides with basic residues to membranes containing acidic phospholipids." *Biophys. J.* 60.1 (1991), pp. 135–48.

[247] M. Mosior and S. McLaughlin. "Binding of basic peptides to acidic lipids in membranes: effects of inserting alanine(s) between the basic residues." *Biochemistry* 31.6 (1992), pp. 1767–73.

[248] H. I. Petrache, S. Tristram-Nagle, K. Gawrisch, D. Harries, V. A. Parsegian, and J. F. Nagle. "Structure and fluctuations of charged phosphatidylserine bilayers in the absence of salt." *Biophys. J.* 86.3 (2004), pp. 1574–1586.

[249] A. J. Miles, R. W. Janes, A. Brown, D. T. Clarke, J. C. Sutherland, Y. Tao, B. A. Wallace, and S. V. Hoffmann. "Light flux density threshold at which protein denaturation is induced by synchrotron radiation circular dichroism beamlines". *J. Synchrotron Radiat.* 15.4 (2008), pp. 420–422.

[250] P. Tremouilhac, E. Strandberg, P. Wadhwani, and A. S. Ulrich. "Conditions affecting the re-alignment of the antimicrobial peptide PGLa in membranes as monitored by solid state 2H-NMR". *Biochim. Biophys. Acta - Biomembr.* 1758.9 (2006), pp. 1330–1342.

[251] S. Afonin, S. L. Grage, M. Ieronimo, P. Wadhwani, and A. S. Ulrich. "Temperature-dependent transmembrane insertion of the amphiphilic peptide PGLa in lipid bilayers observed by solid state 19F NMR spectroscopy". *J. Am. Chem. Soc.* 130.49 (2008), pp. 16512–16514.

[252] J. F. Nagle. "Introductory Lecture: Basic quantities in model biomembranes". *Faraday Discuss.* 161 (2013), pp. 11–29.

[253] H. W. Huang. "Molecular mechanism of antimicrobial peptides: The origin of cooperativity". *Biochim. Biophys. Acta - Biomembr.* 1758.9 (2006), pp. 1292–1302.

[254] M.-T. Lee, W.-C. Hung, F.-Y. Chen, and H. W. Huang. "Many-body effect of antimicrobial peptides: on the correlation between lipid's spontaneous curvature and pore formation." *Biophys. J.* 89.6 (2005), pp. 4006–4016.

[255] K. Bhargava and J. B. Feix. "Membrane binding, structure, and localization of cecropin-mellitin hybrid peptides: a site-directed spin-labeling study." *Biophys. J.* 86.1 Pt 1 (2004), pp. 329–36.

[256] Y. Liu and J. F. Nagle. "Diffuse scattering provides material parameters and electron density profiles of biomembranes". *Phys. Rev. E* 69 (2004), pp. 1–11.

[257] S. E. Hull, I. Leban, P. Main, P. S. White, and M. M. Woolfson. "The crystal and molecular structure of ergocalciferol (vitamin D2)". *Acta Crystallogr. Sect. B Struct. Crystallogr. Cryst. Chem.* 32.8 (1976), pp. 2374–2381.

[258] G. Brotons, D. Constantin, A. Madsen, and T. Salditt. "Coherent X-ray scattering and speckle pattern of solid-supported multilayers of surfactant bilayers". *Phys. B Condens. Matter* 357.1-2 (2005), pp. 61–65.

[259] M. Tolan, O. Seeck, J.-P. Schlomka, W. Press, J. Wang, S. Sinha, Z. Li, M. Rafailovich, and J. Sokolov. "Evidence for Capillary Waves on Dewetted Polymer Film Surfaces: A Combined X-ray and Atomic Force Microscopy Study". *Phys. Rev. Lett.* 81.13 (1998), pp. 2731–2734.

[260] J. Katsaras, S. Tristram-Nagle, Y. Liu, R. L. Headrick, E. Fontes, P. C. Mason, and J. F. Nagle. "Clarification of the ripple phase of lecithin bilayers using fully hydrated, aligned samples." *Phys. Rev. E* 61.5 (2000), pp. 5668–5677.

[261] S. Roes, U. Seydel, and T. Gutsmann. "Probing the properties of lipopolysaccharide monolayers and their interaction with the antimicrobial peptide polymyxin B by atomic force microscopy". *Langmuir* 21.15 (2005), pp. 6970–6978.

[262] J. E. Shaw, R. F. Epand, J. C. Y. Hsu, G. C. H. Mo, R. M. Epand, and C. M. Yip. "Cationic peptide-induced remodelling of model membranes: Direct visualization by in situ atomic force microscopy". *J. Struct. Biol.* 162.1 (2008), pp. 121–138.

[263] N. Fuller, C. R. Benatti, and R. Peter Rand. "Curvature and Bending Constants for Phosphatidylserine-Containing Membranes". *Biophys. J.* 85.3 (2003), pp. 1667–1674.

[264] L. Yang, L. Ding, and H. W. Huang. "New phases of phospholipids and implications to the membrane fusion problem". *Biochemistry* 42.22 (2003), pp. 6631–6635.

[265] L. Ding, T. M. Weiss, G. Fragneto, W. Liu, L. Yang, and H. W. Huang. "Distorted hexagonal phase studied by neutron diffraction: Lipid components demixed in a bent monolayer". *Langmuir* 21.11 (2005), pp. 203–210.

[266] W. Wang, L. Yang, and H. W. Huang. "Evidence of cholesterol accumulated in high curvature regions: implication to the curvature elastic energy for lipid mixtures." *Biophys. J.* 92.8 (2007), pp. 2819–2830.

[267] C. Münster, A. Spaar, B. Bechinger, and T. Salditt. "Magainin 2 in phospholipid bilayers: peptide orientation and lipid chain ordering studied by X-ray diffraction". *Biochim. Biophys. Acta - Biomembr.* 1562.1-2 (2002), pp. 37–44.

[268] A. Spaar, C. Münster, and T. Salditt. "Conformation of peptides in lipid membranes studied by x-ray grazing incidence scattering." *Biophys. J.* 87.1 (2004), pp. 396–407.

[269] J. E. Cummings and T. K. Vanderlick. "Aggregation and hemi-fusion of anionic vesicles induced by the antimicrobial peptide cryptdin-4". *Biochim. Biophys. Acta - Biomembr.* 1768.7 (2007), pp. 1796–1804.

[270] K. Matsuzaki, K. I. Sugishita, N. Ishibe, M. Ueha, S. Nakata, K. Miyajima, and R. M. Epand. "Relationship of membrane curvature to the formation of pores by magainin 2". *Biochemistry* 37.98 (1998), pp. 11856–11863.

List of Figures

1.1 Cross section of a plasma membrane. 1
1.2 Sketch of a biological membrane. 5
1.3 General structure of phospholipids. 7
1.4 Structures of sphingomyelin, cholesterol and ergosterol. 9
1.5 Lipid composition of eukaryotic cells. 10
1.6 Three-dimensional lipid/water phases. 12
1.7 Effective molecular lipid shape and packing parameter P. 14
1.8 Interaction potentials for two DOPC bilayers at 30°C in excess water. 18
1.9 Possible mechanisms of pore formations in lipid bilayers induced by amphipathic peptides. 24

2.1 Model Membrane Systems. 28
2.2 Molecular structure of the tether and spacer molecules. 41

3.1 Surface potentials within the electrochemical double layer of a charged particle. 47
3.2 Energy levels of the molecular orbitals of a carbonyl group and possible electronic transitions. 49
3.3 Far-UV CD spectra of various types of secondary structure. 50
3.4 Principle of a FRET binding assay. 58
3.5 Principle of a FRET intercalation assay. 58
3.6 Principle of a FRET fusion assay. 59
3.7 Equivalent circuit of the tBLM system. 61
3.8 Measurement principle of the tethaPod™ system. 63
3.9 Basic layout of a film balance. 66
3.10 Illustration of a scattering experiment at a sample with electron density $\rho_e(\vec{r})$. 72
3.11 Two-dimensional character of oriented lipid multilayers. 75
3.12 Diffraction from oriented lipid model membranes. 76
3.13 Refraction and reflection at an ideal smooth interface. 78
3.14 X-ray reflectivity of aligned lipid membranes. 81
3.15 Scattering geometry of GID experiments. 83

3.16 Experimental setup at beamline I07. 86
3.17 Experimental setup at beamline P08. 87
3.18 Horizontal intensity profile of an XRR scan at the position of a Bragg peak. 89
3.19 Geometrical illustration of the illumination correction. 89
3.20 Electron density distribution of a lipid bilayer including distance definitions. 91
3.21 Normalisation of the experimental reflectivity to Fresnel reflectivity of silicon. 93
3.22 Electron density reconstruction of a single bilayer using iterative regularisation. 94
3.23 Analysis of the chain correlation peak. 97

4.1 Cytotoxic activity of different peptide variants. 100
4.2 Microscopic changes in erythrocytes induced by Ece1-III$_{KR(N)}$. 101

5.1 Helical wheel projection of Ece1-III$_{KR}$. 105
5.2 Helical wheel projections of Ece1-III$_{KR}$ separated in two parts. 105
5.3 Secondary structure prediction of Ece1-III$_{KR}$. 107
5.4 Hydrophobicity analysis of Ece1-III$_{KR}$. 110
5.5 Soluble peptide CD spectra of Ece1-III$_{K(C)}$, Ece1-III$_{KR(N)}$ and Ece1-III$_{AA(N)}$ in 0.01 % TFA and of the amidated and non-amidated isoforms of Ece1-III$_{KR}$ in buffer solution. 112
5.6 Membrane-associated CD spectra of Ece1-III$_{KR(N)}$ in the presence of lipid vesicles at 25°C. 114
5.7 Compression isotherms of peptide monolayers. 116
5.8 Temperature-dependent characteristics of peptide monolayers. 117

6.1 Time dependence of a FRET binding assay of Rho-Ece1-III$_{KR(N)}$. . . . 120
6.2 Zeta potential of different liposomes as function of Ece1-III$_{KR(N)}$ content. 122
6.3 Zeta potential of liposomes as function of increasing P/L. 123
6.4 Absolute area expansion of lipid monolayers in response to their interaction with Ece1-III$_{KR(N)}$. 125
6.5 Liposome diameter as function of Ece1-III$_{KR(N)}$ content. 126
6.6 Liposome diameter as function of increasing P/L. 128
6.7 FRET intercalation assays of amidated Ece1-III variants. 129
6.8 FRET intercalation assays of non-amidated Ece1-III variants. 131

6.9 Normalised SR-OCD spectra, corresponding HT values of the lipid sample with peptide content and calculated absorption spectra of Ece1-III$_{KR(N)}$ in aligned and fully-hydrated DOPC membranes at different P/L ratios. . . . 133
6.10 Normalised OCD spectra of Ece1-III$_{KR(N)}$ in aligned and fully hydrated membranes of different lipid composition at P/L = 1:200 and P/L = 1:18. . . . 135
6.11 Normalised OCD spectra of Ece1-III peptide variants in aligned and fully hydrated DOPC membranes at P/L = 1:18. . . . 136
6.12 AFM height images of dry Ece1$_{KR(N)}$/DOPC multilayers in dependence on the peptide concentration. . . . 141
6.13 AFM height images of dry peptide/SSM samples in dependence on the lipid composition. . . . 142
6.14 AFM height images of partially hydrated peptide/SSM samples. . . . 143
6.15 Reflectivities and electron density distributions of DOPC/Ece1-III$_{KR(N)}$ multilayers with increasing P/L at 25°C. . . . 145
6.16 Reflectivity analysis of DOPC/Ece1-III$_{KR(N)}$ multilayers as function of the P/L at 25°C. . . . 146
6.17 Reflectivities and electron density distributions of DOPC/Ece1-III$_{KR(N)}$ multilayers with increasing P/L at 40°C. . . . 147
6.18 Reflectivity analysis of DOPC/Ece1-III$_{KR(N)}$ multilayers as function of the P/L at 40°C. . . . 148
6.19 Reflectivity analysis of DOPC/Chol multilayer samples with Ece1-III$_{KR(N)}$. . . . 150
6.20 Reflectivity analysis of DOPC/Erg multilayer samples with Ece1-III$_{KR(N)}$. . . . 151
6.21 Reflectivity analysis of DOPC/PS multilayer samples with Ece1-III$_{KR(N)}$. . . . 152
6.22 Reflectivity analysis of DOPC multilayer samples with Ece1-III$_{AA(N)}$ and Ece1-III$_{K(C)}$. . . . 154
6.23 Peptide influence on a DOPC bilayer measured with XRR. . . . 156
6.24 Rocking curve and diffuse scattering contributions at 40°C. . . . 157
6.25 Specular and non-specular scattering of a P/L series of DOPC/Ece1-III$_{KR(N)}$ multilayer samples. . . . 158
6.26 Log-log plot of the diffuse scattering of a P/L series of DOPC/Ece1-III$_{KR(N)}$ multilayer samples. . . . 159
6.27 Small-angle diffraction patterns of a P/L series of DOPC/Ece1-III$_{KR(N)}$ multilayer samples. . . . 161

6.28 Diffraction patterns of different lipid structures. 162
6.29 Small-angle diffraction patterns of differently composed lipid/peptide multilayer samples. 165
6.30 Small-angle diffraction patterns of DOPC multilayers with Ece1-III variants. 167
6.31 Acyl chain correlation. 168
6.32 Acyl chain correlations in a P/L series of DOPC/Ece1-III$_{KR(N)}$ multilayers. 169
6.33 Acyl chain correlations in different lipid/peptide systems. 171
6.34 FT-IR examination of lipid mixtures with and without peptide content. 173
6.35 AFM height images of a DOPC/SM/Chol/PS bilayer in the course of the interaction with Ece1-III$_{KR(N)}$. 175
6.36 AFM amplitude images of a DOPC/SM/Chol/PS bilayer in the course of the interaction with Ece1-III$_{KR(N)}$. 176
6.37 XRR analysis of DOPC/SM/Chol/PS (9:9:2:2, n/n/n/n) multilayers without and with Ece1-III$_{KR(N)}$ content. 177
6.38 XRR analysis of DOPC/SM/Chol (2:2:1, n/n/n) multilayers without and with Ece1-III$_{KR(N)}$ content. 179
6.39 Time dependence of a FRET fusion assay of Ece1-III$_{KR(N)}$. 180
6.40 Time dependence of a FRET fusion assay of Ece1-III peptide variants. 181
6.41 DOPC conductance upon the addition of Ece1-III$_{KR(N)}$. 187
6.42 tBLM conductance upon the addition of Ece1-III peptides. 189
6.43 tBLM conductance upon the addition of non-amidated Ece1-III peptides. 190
6.44 Peptide-induced current fluctuations across a free-standing DOPC membrane. 191

7.1 Interaction between Candidalysines and lipid membranes. 194

List of Tables

2.1 Lipids used in this thesis. 36
2.2 Peptides used in this thesis. 42

3.1 Box model parameters of the silicon wafer. 93

6.1 Parameters of bilayers of different compositon with Ece1-III$_{\mathrm{KR(N)}}$. . . 149
6.2 Parameters of DOPC bilayers upon the interaction with different peptide variants. 155
6.3 Lipid phases observed for different lipid/peptide systems. 164

Abbreviations

a.u. **a**rbitrary **u**nits

AFM **a**tomic **f**orce **m**icroscopy

AMP **a**nti**m**icrobial **p**eptide

BLM **b**lack **l**ipid **m**embrane

CD **c**ircular **d**ichroism

Chol **chol**esterol

CSA **c**amphor**s**ulphonic **a**cid

DHPE 1,2-**di**h**e**xadecanoyl-sn-glycero-3-**p**hospho**e**thanolamine

DLS **d**ynamic **l**ight **s**cattering

DMSO **di**m**e**thyl **s**ulf**o**xide

DOPC 1,2-**di**o**l**eoyl-sn-glycero-3-**p**hospho**c**holine

Ece1-III$_{\mathrm{AA}}$ Ece1-III$_{62-93\mathrm{AA}}$

Ece1-III$_{\mathrm{A}}$ Ece1-III$_{62-92\mathrm{A}}$

Ece1-III$_{\mathrm{KR}}$ Ece1-III$_{62-93\mathrm{KR}}$

Ece1-III$_{\mathrm{R}}$ Ece1-III$_{62-92\mathrm{K}}$

Erg **erg**osterol

GID **g**razing **i**ncidence **d**iffraction

GUV **g**iant **u**nilamellar **v**esicle

HDP **h**ost-**d**efence **p**eptide

HEPES 4-(2-**h**ydroxy**e**thyl)-1-**p**iperazine**e**thane**s**ulfonic acid

HT **h**igh voltage

KCl potassium cloride

KOH potassium hydroxide

LC-MS/MS **l**iquid **c**hromatography-tandem **m**ass **s**pectrometry

LUV **l**arge **u**nilamellar **v**esicle

MLV **m**ulti**l**amellar **v**esicle

NBD N-(7-**n**itro**b**enz-2-oxa-1,3-**d**iazol-4-yl)

OCD **o**riented **c**ircular **d**ichroism

P/L **p**eptide-to-**l**ipid ratio

PDB **p**rotein **d**ata **b**ank

PMT **p**hoto**m**ultiplier **t**ube

PS **p**hosphatidyl**s**erine

rH **r**elative **h**umidity

Rho **rho**damine B

SAXS **s**mall **a**ngle **X**-ray **s**cattering

SM **s**phingo**m**yelin

SSB **s**olid **s**upported **b**ilayer

SSM **s**olid **s**upported **m**ultilayer

SUV **s**mall **u**nilamellar **v**esicle

tBLM **t**ethered **bil**ayer **m**embrane

TFA **t**ri**f**luoroacetic **a**cid

TFE **t**ri**f**luoro**e**thanol

XRR **X**-**r**ay **r**eflectivity

Appendix

Acknowledgements

An dieser Stelle möchte ich allen, die am erfolgreichen Zustandekommen der vorliegenden Arbeit beteiligt waren, meinen herzlichen Dank aussprechen.

Allen voran danke ich Prof. Dr. Thomas Gutsmann, der mir die Möglichkeit gab diese Arbeit unter seiner Leitung anzufertigen. Mit seiner wissenschaftlichen Kompetenz und seinem Enthusiasmus für knifflige Fragestellungen gab er mir stets neue Denkanstöße und fortwährende Motivation. Neben den zahlreichen konstruktiven Hinweisen und Vorschlägen scheute er auch nicht vor eigenhändigen Messungen zurück – sei es im heimischen Labor der Biophysik am Forschungszentrum Borstel oder an den Synchrotronquellen. Sein mir entgegengebrachtes Vertrauen weiß ich sehr zu schätzen.

Bei Prof. Dr. Lars Redecke bedanke ich mich herzlich für die Bereitschaft, das Amt des Koreferenten dieser Dissertation zu übernehmen.

Dr. Oliver H. Seeck danke ich vielmals für all das Wissen, das er mir rund um das Thema Synchrotronstrahlung und deren Anwendung vermittelt hat, sowie seine maßgebliche Unterstützung in wissenschaftlichen und messtechnischen Fragen. Ich freue mich über sein unermüdliches Vertrauen in das Gelingen der Arbeit, die stete Diskussionsbereitschaft, die Motivation (insbesondere in den letzten Monaten des Zusammenschreibens) und das flotte Korrekturlesen.

Auch Prof. Dr. Bernhard Hube möchte ich herzlich dafür danken, dass er uns in das spannende Candidalysin-Projekt involviert hat. Ihm, sowie Rainer Bartels und Julian Naglik danke ich zudem für die Synthese und Bereitstellung der verschiedenen Ece1-III Peptide.

Die vorliegende Arbeit bündelt verschiedene interdisziplinäre Teilaspekte und Methoden in einen Gesamtkontext. Ohne die mir entgegengebrachte Hilfe von Experten der jeweiligen Gebiete, wäre dies in dieser Form nicht möglich gewesen. In diesem Sinne danke ich Prof. Dr. Michael Rappolt für die hilfreichen Diskussionen zu den GID Daten. Prof. Dr. Jörg Andrä möchte ich dafür danken, dass ich in seinem Labor die Messungen am ZetaSizer durchgeführen konnte. Ein herzlicher Dank geht ausßerdem an Dominik Wilms, der mich in die Nutzung des Geräts einführte und mir half, mich in dem fremden Labor zurechtzufinden. Dr. Matthias Michalek danke ich für seine Unterstützung bei den CD Messungen in Kiel und die

umfassenden Diskussionen im Hinblick auf weitere Analysemethoden. Erst das hat mich auf die Idee gebracht, die OCD Messungen anzuregen. Damit bin ich auch direkt beim Team der CD12 Beamline in Karlsruhe, bei denen ich mich herzlich für die gelungene Kooperation bedanken möchte: Vielen Dank an Dr. Jochen Bürck, der sich stets die Zeit nahm, meine zahlreichen Fragen zu beantworten, und an Bianca Posselt für ihre ausgesprochen freundliche und engagierte Unterstützung im Labor. Außerdem möchte ich Siegmar Roth danken, der sich mit seiner badischen Gelassenheit als große Hilfe erwies, als ANKA plötzlich nicht mehr so wollte wie wir.

Darüber hinaus möchte ich allen aus der Biophysik und der Immunbiophysik in Borstel danken, dass sie mich stets sehr freundlich willkommen hießen und mich mit der Durchführung der Messungen maßgeblich unterstützten. Dabei geht mein besonderer Dank an Sabrina Groth für ihre Ausdauer bei den zahlreichen FRET und tethaPod Messungen, an Kerstin Stephan für die Messungen mit Erythrozyten, an Nina Hahlbrock für die FT-IR Messungen und an die beiden motivierten Auszubildenden Chee und Jana für die teils nervenraubenden Messungen an den planaren Membranen. Natürlich darf auch Nadine Gebauer nicht fehlen, die das tethaPod System überhaupt erst etabliert hat. Ein besonderer Dank gebührt zudem Laura Paulowski, Christian Nehls und Dr. Annika Saathoff, die mich engagiert und tatkräftig bei den Synchrotronmesszeiten unterstützen – sei es bei der Probenpräparation, den Nachtschichten oder dem exzessiven Verzehr von Süßkram. Ich hätte mir keine fröhlichere Begleitung vorstellen können!

Außerdem möchte ich mich bei meinen Kollegen am DESY bedanken, mit denen ich (abgesehen von meinem Schreibtisch) am Ende doch die meiste Zeit verbrachte. Vielen Dank an Kathrin Pflaum, Dr. Ann-Christin Dippel, David Reuther, Dr. Peter Walter und René Kirchhoff, die mir nicht nur mit ihrem kompetenten technischen Engagement halfen, sondern auch für jeden anderen Spaß zu haben waren und so den hin und wieder drögen Arbeitsalltag sehr erheiterten. Neben meinen lieben Bürokollegen Dr. Sonia Francoual, Dr. Jose Mardegan, Dr. Arvid Skaugen und Dr. Adeline Buffet möchte ich auch allen anderen Kollegen der PETRA III-Crew für das freundschaftliche und hilfsbereite Arbeitsklima danken. Um sie alle einzeln aufzuzählen sind es jedoch eindeutig zu viele.

Abschließend möchte ich meinen Eltern und besonders Christian von ganzem Herzen für ihre Unterstützung und Geduld danken. Ich verspreche, mich in Zukunft mit der gebührenden Aufmerksamkeit und zahlreichen Abendessen zu revangieren.